THE MEASUREMENT AND PREDICTION OF ROTORDYNAMIC FORCES FOR LABYRINTH SEALS

prepared by

D. W. Childs
D. L. Rhode

prepared for

Air Force Office of Scientific Research
Bolling Air Force Base
Washington, D. C. 20332

Contract F49620-82-K0083

Turbomachinery Laboratory
Mechanical Engineering Department
Texas A&M University
College Station, Texas 77843

March 1988

UNCLASSIFIED UNCLASSIFIED

SECURITY CLASSIFICATION OF THIS PAGE

REPORT DOCUMENTATION PAGE

AD-A197 185

1a. REPORT SECURITY CLASSIFICATION: UNCLASSIFIED	1b. RESTRICTIVE MARKINGS
2a. SECURITY CLASSIFICATION AUTHORITY: Unclassified	3. DISTRIBUTION/AVAILABILITY OF REPORT: unlimited
2b. DECLASSIFICATION/DOWNGRADING SCHEDULE	
4. PERFORMING ORGANIZATION REPORT NUMBER(S)	5. MONITORING ORGANIZATION REPORT NUMBER(S): AFOSR-TR- 88-0662
6a. NAME OF PERFORMING ORGANIZATION: Texas A&M University; 6b. OFFICE SYMBOL (If applicable)	7a. NAME OF MONITORING ORGANIZATION: AFOSR
6c. ADDRESS (City, State and ZIP Code): College Station, Texas 77843-3123	7b. ADDRESS (City, State and ZIP Code): same as 6c.
8a. NAME OF FUNDING/SPONSORING ORGANIZATION: Air Force Office of Scientific Research; 8b. OFFICE SYMBOL (If applicable) NA	9. PROCUREMENT INSTRUMENT IDENTIFICATION NUMBER: F49620-82-K-0033
8c. ADDRESS (City, State and ZIP Code): Bldg 410 I lling Air Force Base, D.C. 20332 6448	10. SOURCE OF FUNDING NOS. — PROGRAM ELEMENT NO. 61102F; PROJECT NO. 2302; TASK NO. B1; WORK UNIT NO.

11. TITLE (Include Security Classification) "THE MEASUREMENT AND PREDICTION OF ROTORDYNAMIC FORCES FOR LABYRINTH SEALS"

12. PERSONAL AUTHOR(S): D.W. Childs and D.L. Rhode

13a. TYPE OF REPORT	13b. TIME COVERED	14. DATE OF REPORT (Yr., Mo., Day)	15. PAGE COUNT
Final	FROM 9/1/82 TO 12/31/87	1988, MARCH	

16. SUPPLEMENTARY NOTATION

17. COSATI CODES		
FIELD	GROUP	SUB. GR.

18. SUBJECT TERMS (Continue on reverse if necessary and identify by block number): Labyrinth Seals, Rotordynamic Forces, TURBINE STATORS (JE) ⇐, Computational Fluid Dynamics.

19. ABSTRACT (Continue on reverse if necessary and identify by block number)

Measurements of rotordynamic (stiffness and damping) coefficients and leakage characteristics were completed for labyrinth-rotor/honeycombe-stator seals. Comparisons to labyrinth-rotor/smooth-stator seals showed no stability improvements. Tests were also carried out on smooth-rotor/honeycombe-stator seals and demonstrated superior stability and leakage performance for this type of seal if the entering flow is pre-rotated in the direction of rotation.

A new "bulk-flow" theory for labyrinth seals has been developed and its predictions compare well with measured results for tooth-on-rotor labyrinths.

Also, a more sophisticated model was developed which solves the 3-D Reynolds-averaged Navier-Stokes equations for compressible flow. Predictions

20. DISTRIBUTION/AVAILABILITY OF ABSTRACT: UNCLASSIFIED/UNLIMITED ☒ SAME AS RPT ☐ DTIC USERS ☐	21. ABSTRACT SECURITY CLASSIFICATION: UNCLASSIFIED
22a. NAME OF RESPONSIBLE INDIVIDUAL	22b. TELEPHONE NUMBER (Include Area Code) 202-767-4917; 22c. OFFICE SYMBOL NE

DD FORM 1473, 83 APR EDITION OF 1 JAN 73 IS OBSOLETE

UNCLASSIFIED

THE MEASUREMENT AND PREDICTION OF ROTORDYNAMIC FORCES FOR LABYRINTH SEALS

prepared by

D. W. Childs
D. L. Rhode

prepared for

Air Force Office of Scientific Research
Bolling Air Force Base
Washington, D. C. 20332

Contract F49620-82-K0083

Turbomachinery Laboratory
Mechanical Engineering Department
Texas A&M University
College Station, Texas 77843

March 1988

TABLE OF CONTENTS

FINAL REPORT
AFOSR CONTRACT NO F49620-82-K-0033
9/1/82 through 12/31/87

I. Experimental Measurements and "Bulk Flow" Model Developments - D. Childs

The work conducted in this portion of the research contract has consisted of the following tasks:

(a) the development of a facility and apparatus for measuring the leakage, axial pressure profiles, and rotordynamic (stiffness and damping) coefficients of labyrinth seals,

(b) the measurement of the test data cited above for a range of labyrinth-seal configurations, and

(c) the development and validation of "bulk-flow" models for the prediction of leakage and rotordynamic coefficients of labyrinth seals.

All of these objectives have been met in full and are documented in the following journal publications:

- Childs, D. W. and Scharrer, J. K., "Experimental Rotordynamic Coefficient and Results for Teeth-On-Rotor and Teeth-On-Stator Labyrinth Gas Seals," *ASME Trans. J. of Engineering for Gas Turbine and Power,* Vol. 108, October 1986, pp. 599-604.
- Childs, D. W., Nelson, C. E., Nicks, C., Scharrer, J., Elrod, D., and Hale, K., "Theory Versus Experiment for the Rotordynamic Coefficients of Annular Gas Seals: Part 1-Test Facility and Apparatus", *ASME Transaction Journal of Tribology,* July 1986, Vol. 108, pp. 426-432.
- Nelson, C., Childs, D., Nicks, C., Elrod, D., and Hale, K., "Theory Versus Experiment for the Rotordynamic Coefficients of Annular Gas Seals: Part 2-Constant-Clearance and Convergent- Tapered Geometry," *ASME Transaction Journal of Tribology,* July 1986, Vol. 108, pp. 433-438.
- Childs, D., and Scharrer, J., "An Iwatsubo-Based Solution for Labyrinth Seals - Comparison to Experimental Results," *ASME Transaction Journal of Engineering for Gas Turbine and Power,* April 1986, Vol. 108, pp. 325-331.
- Childs, D. and Elrod, D., "Rotordynamic Coefficient and Leakage Test Results for Interlock and Tooth-on-Stator Labyrinth Seals," accepted for presentation at the ASME International Gas Turbine Conference, Amsterdam, The Netherlands, under review consideration *ASME Trans. for Power.*

II. Finite Difference Developments and Results - D. Rhode

This portion of the research program involved the following tasks:

(a) the development of a 3-D finite difference computer code, using a generalized body-fitted coordinate system, for predicting forces as well as the distribution of various other flowfield quantities

(b) the development of a procedure for calculating the rotordynamic force for a seal with any arbitrary number of cavities at an affordable CPU expenditure

(c) the computation of forces at various operating conditions

These objectives have been met and are documented in the following:

- Rhode, D. L. and Hensel, S. J., "Three-Dimensional Computation of Rotordynamic Force Distributions in a Labyrinth Seal," accepted for presentation at the ASME/AIAA First National Fluid Dynamics Congress, Cincinnati, OH, 24-28 July 1988.
- Rhode, D. L. and Hensel, S. J., "Labyrinth Seal Rotordynamic Forces Predicted with a Three-Dimensional Navier-Stokes Computer Code," accepted for presentation at the 24th AIAA/ASEE/ASME/SAE Joint Propulsion Conference, Boston, MA, 11-14 July 1988.
- Rhode, D. L. and Nail, G. H., "Computation of Cavity-By-Cavity Flow Development in Generic Labyrinth Seals," submitted for presentation at the ASME International Computers in Engineering Conference, San Francisco, CA, 31 July - 3 August 1988.
- Rhode, D. L. and Sobolik, S. R., "Simulation of Subsonic Flow Through a Generic Labyrinth Seal," *ASME Trans. Journal of Engineering for Gas Turbines and Power,* October 1986, Vol. 108, pp. 674-680.
- Rhode, D. L., Demko, J. A., Traegner, U. K., Morrison, G. L. and Sobolik, S. R., "Prediction of Incompressible Flow in Labyrinth Seals," *ASME Trans. Journal of Fluids Engineering,* March 1986, Vol. 108, pp. 19-25.

Appendix B contains three of the most recent papers:

- Rhode, D. L. and Hensel, S. J., "Three-Dimensional Computation of Rotordynamic Force Distributions in a Labyrinth Seal," accepted for presentation at the ASME/AIAA First National Fluid Dynamics Congress, Cincinnati, OH, 24-28 July 1988.
- Rhode, D. L. and Hensel, S. J., "Labyrinth Seal Rotordynamic Forces Predicted with a Three-Dimensional Navier-Stokes Computer Code," accepted for presentation at the 24th AIAA/ASEE/ASME/SAE Joint Propulsion Conference, Boston, 11-14 July 1988.
- Rhode, D. L. and Nail, G. H., "Computation of Cavity-By-Cavity Flow Development in Generic Labyrinth Seals," submitted for presentation at the ASME International Computers in Engineering Conference, San Francisco, CA, 31 July - 3 August 1988.

The following students have participated in this portion of the AFRAPT program: Steve Sobolik, Steve Hensel, Greg Nail, and Robert Hibbs. Steve Hensel worked at Garrett, one summer, finished his M. S. Thesis in December 1987 and is continuing his studies for a Ph.D. A summer position was not available in time for Steve Sobolik and Greg Nail. Steve finished his M. S. Thesis in August 1984 and went to work for Sandia National Labs. Greg finished his M. S. Thesis in December 1987 and is continuing his education for the Ph.D. degree. Robert Hibbs worked last summer at United Technologies in East Hartford and will soon finish his M. S. Thesis.

We are grateful for the sponsorship of this research program by AFOSR. As with the test facility, the computational capability continues to be unique throughout the world. The value of this widely applicable predictive capability has clearly been demonstrated. Also, previously unavailable values of various shear stress quantities have been computed, which were particularly useful in refining the bulk-flow model mentioned in the previous section.

Further work is important and should include an analysis of the effect of geometric configuration including stepped seals, as well as the effect of rotor orbits whose centers are eccentric with respect to the housing.

Copies of the three most-recent publications are included in Appendix A.

- Hawkins, L., Childs, D., and Hale, K., "Experimental Results for Labyrinth Gas Seals with Honeycomb Stators: Comparisons to Smooth-Stator Seals and Theoretical Predictions," submitted for the 1988 ASME-ASLE Joint Tribology Conference and *ASME Journal of Tribology.*
- Scharrer, J., "Theory versus Experiment for the Rotordynamic Coefficients of Labyrinth Gas Seals: Part I - A Two Control Volume Model," *Rotating Machinery Dynamics,* Vol. 2, ASME 1987, pp. 427-434, accepted for presentation, *ASME Journal of Vibration, Acoustics, Stress, and Reliability in Design.*
- Childs, D. and Scharrer, J., "Theory Versus Experiment for the Rotordynamic Coefficients of Labyrinth Gas Seals: Part II - A Comparison to Experiment," *Rotating Machinery Dynamics,* Vol. 2, ASME 1987, pp. 427-434, accepted for presentation, *ASME Journal of Vibration, Acoustics, Stress, and Reliability in Design.*

The AFRAPT participation in this program has included the students: Joseph Scharrer and Lawrence Hawkins. Joe worked at G.E. Lynn during the summer, completed his Ph.D. in January 1987 and is continuing to work in rotating machinery with Rocketdyne. Larry worked for Garrett during two summers, completed his M.S. degree in January 1988, and is also going to work for Rocketdyne.

The support provided by AFOSR is deeply appreciated. The test apparatus we have developed with AFOSR support continues to be unique in the world. The test results and models have been of extraordinary value in resolving rotordynamics stability issues and have been used directly to develop higher-performance commercial turbomachinery. Considerable work remains to be done! No data or models are available yet for stepped seals, see-through labyrinth seals at reduced L/D ratios, brush seals, etc.

Appendix A

Hawkins, L., Childs, D., and Hale, K., "Experimental Results for Labyrinth Gas Seals with Honeycomb Stators: Comparisons to Smooth-Stator Seals and Theoretical Predictions," submitted for the 1988 ASME-ASLE Joint Tribology Conference and *ASME Journal of Tribology*.

Scharrer, J., "Theory versus Experiment for the Rotordynamic Coefficients of Labyrinth Gas Seals: Part I - A Two Control Volume Model," *Rotating Machinery Dynamics*, Vol. 2, ASME 1987, pp. 427-434, accepted for presentation, *ASME Journal of Vibration, Acoustics, Stress, and Reliability in Design.*

Childs, D. and Scharrer, J., "Theory Versus Experiment for the Rotordynamic Coefficients of Labyrinth Gas Seals: Part II - A Comparison to Experiment," *Rotating Machinery Dynamics*, Vol. 2, ASME 1987, pp. 427-434, accepted for presentation, *ASME Journal of Vibration, Acoustics, Stress, and Reliability in Design.*

EXPERIMENTAL RESULTS FOR LABYRINTH GAS SEALS WITH HONEYCOMB STATORS: COMPARISONS TO SMOOTH-STATOR SEALS AND THEORETICAL PREDICTIONS[1]

LARRY HAWKINS, MEMBER TECHNICAL STAFF
ROCKETDYNE DIVISION, ROCKWELL INTERNATIONAL
CANOGA PARK, CA 91304

DARA CHILDS, PROFESSOR
KEITH HALE, RESEARCH ENGINEER
TEXAS A&M UNIVERSITY
COLLEGE STATION, TEXAS 77843

ABSTRACT

Experimental measurements are presented for the rotordynamic stiffness and damping coefficients of a teeth-on-rotor labyrinth seal with a honeycomb stator. Inlet circumferential velocity, inlet pressure, rotor speed, and seal clearance are primary variables. Results are compared to (a) data for teeth-on-rotor labyrinth seals with smooth stators, and (b) analytical predictions from a two-control-volume compressible flow model. The experimental results show that the honeycomb-stator configuration is more stable than the smooth-stator configuration at low rotor speeds. At high rotor speeds, the stator surface does not affect stability. The theoretical model predicts the cross-coupled stiffness of the honeycomb-stator seal correctly within 25% of measured values. The model provides accurate predictions of direct damping for large clearance seals; however, the model predictions and test results diverge with increasing running speed. Overall, the model does not perform as well for low clearance seals as for high clearance seals.

INTRODUCTION

Modern turbomachines can be subject to problems due to *unstable or self-excited* motion. This type of motion is characterized by a rotor whirling at a natural frequency that is less than its rotational speed. The unstable motion is caused by a tangential force acting on the rotor in its whirl direction. Several excitation mechanisms have been identified for unstable motion (Ehrich and Childs, 1984); one of these is the force developed in a labyrinth seal.

---

[1]This work was supported in part by NASA Grant NAG3-181 from NASA Lewis Research Center (Technical Monitor, Robert Hendricks) and AFOSR Contract F49620-82-K-0033 (Technical Monitor, Tony Amos)

Labyrinth seal forces are characterized by rotordynamic stiffness and damping coefficients. For small motion of a seal rotor about a centered position, the rotordynamic coefficients are defined by the following force-motion model

$$-\begin{Bmatrix} F_X \\ F_Y \end{Bmatrix} = \begin{bmatrix} K & k \\ -k & K \end{bmatrix} \begin{Bmatrix} X \\ Y \end{Bmatrix} + \begin{bmatrix} C & c \\ -c & C \end{bmatrix} \begin{Bmatrix} \dot{X} \\ \dot{Y} \end{Bmatrix} \tag{1}$$

where X and Y define the motion of the seal rotor relative to the seal stator, and F_X and F_Y are the reaction force components acting on the seal rotor. The rotordynamic coefficients (K, k, C, and c) represent the direct stiffness, cross-coupled stiffness, direct damping, and cross-coupled damping respectively.

This report presents experimental measurements of the rotordynamic coefficients for a teeth-on-rotor labyrinth seal with a honeycomb stator. The first systematic test program for measuring seal rotordynamic coefficients was performed at the Technical University of Stuttgart (Benckert and Wachter,1978,1980),(Benckert,1980). Stiffness data were published for three types of seals: (a) teeth-on-stator, (b) teeth-on-rotor and stator, and (c) teeth-on-stator and steps or grooves on the rotor. Wright (1983) published data on equivalent radial and tangential stiffnesses for single-cavity, teeth-on-stator seals. Childs and Scharrer (1986,1987) investigated teeth-on-rotor and teeth-on-stator labyrinth seals at Texas A&M University. They measured stiffness and damping coefficients while varying inlet tangential velocity, rotor speed, inlet pressure, and clearance. Elrod and Childs (1988) investigated smooth-rotor/honeycomb-stator annular seals, and compared the results to data for smooth-rotor/smooth-stator annular seals. They found the honeycomb-stator seals to be more stable than smooth-stator seals throughout the range of variables tested.

The labyrinth-rotor/honeycomb-stator configuration was tested for several reasons: (a) This combination is a common industrial configuration, (b) no test data for this combination exists in the published literature, and (c) the results of Elrod and Childs (1988) indicate that seals with honeycomb stators may have a stability advantage over smooth-stator seals. The last item motivates the comparison in this report of the honeycomb-stator seal data to the data of Childs and Scharrer (1987) for labyrinth-rotor/smooth-stator seals. The honeycomb-stator seal data are also compared to the predictions of Scharrer's (1987) theoretical model.

THEORY

Stability Analysis

As a consequence of equation (1), the radial and tangential forces acting on a seal rotor, which is executing a circular orbit of amplitude A, are defined by

$$F_r = -(K + c\omega)A$$
$$F_t = (k - C\omega)A$$

where ω is the running speed. Thus, K and c produce a radial force on the seal rotor, and k and C produce a tangential force. The radial force F_r in a labyrinth seal is normally small compared to other radial fores acting on a rotor; therefore , K and c are of minor consequence. If positive, the tangential force F_t is destabilizing since it supports the whirling motion of a forward whirling rotor. Both k and C are positive for most practical labyrinth seal applications; hence, the compelling reason for determining the rotordynamic seal coefficients is to determine the relative values of k and C. The whirl frequency ratio, defined by

$$f = k/C\omega,$$

is used in this report to compare k and C. Reducing the value of f improves the stability of a rotor system.

Scharrer's Analysis

Prediction of the rotordynamic coefficients requires a flow field model to predict the axial and circumferential pressure distribution acting on the seal rotor. Most early attempts to model the flow field in a labyrinth seal used a single control volume, concentrating on the circumferential flow components. However, the labyrinth seal is known to have two distinct flow regimes: a jet flow region in the leakage path and a recirculation region in the cavity. Hence, Fujikawa et al. (1984), Wyssmann et al. (1984), and Scharrer (1987) have developed two-control-volume analyses to accurately model the known physics of the flow. Scharrer's model is used in this report to generate theoretical predictions for comparison to experimental data.

In Scharrer's model, the shear stresses at the rotor and stator surfaces (τ_s and τ_r) are modeled using the Blasius formula for turbulent pipe flow

$$\tau = \frac{1}{2}\rho U_m^2 no \left(\frac{U_m D_h}{\nu}\right)^{mo}$$

where U_m is the mean flow velocity relative to the surface upon which the shear stress is cting, and D_h is the hydraulic diameter of the particular control volume. No published data are available for the friction coefficients, *no* and *mo*, for the honeycomb-stator surface used in the tests reported here. The following values were determined empirically from pressure drop versus flow tests for smooth-rotor/honeycomb-stator seals

$$ms = -0.1083 \qquad ns = 0.2820.$$

Scharrer uses a perturbation analysis to linearize the governing equations. Expanding the governing equations in the perturbation variables yields a system of twelve linear algebraic equations per cavity. Solution of these equations yields the pressure distribution along and around the seal. Integration of the pressure distribution leads to the solution for the rotordynamic coefficients.

TEST APPARATUS

The test results reported here were obtained using the Texas A&M Air Seal Test Apparatus. The test apparatus will be described here briefly. A detailed description was provided by Childs et al. (1986). As illustrated in figure 1, the rotor shaft is suspended, pendulum fashion, from an upper, rigidly-mounted, pivot shaft. This arrangement allows horizontal (harmonic) motion of the rotor. A cam within the pivot shaft provides vertical (static) positioning of the rotor. The rotor is excited, horizontally, by a hydraulic-shaker head which acts on the rotor-shaft housing. The design of the test rig, which is further illustrated in figure 2, permits the installation of various rotor/stator combinations. The test apparatus has been modified since the 1986 reference to permit an increase in top operating speeds from 8,000 to 16,000 cpm. Changes include the use of a hydraulically fitted rotor, the introduction of high-speed carbon seals, and the replacement of a roller-element thrust bearing with a Torrington, water-lubricated, swing-pad bearing. The stator of figure 2 is supported in the test section housing by three piezo-electric, quartz, load cells in a trihedral configuration. These load cells measure the pressure-induced forces due to rotor motion within the stator. Accelerometers are provided on the stator to correct for acceleration-induced forces which are measured by the load cell.

TEST PARAMETERS

The parameters varied during the tests were supply pressure, rotor speed, circumferential velocity of the inlet air, and seal configuration. Test results for six teeth-on-rotor labyrinth gas seal configurations are presented. Three of the seals have honeycomb stators, each with a different rotor-to-stator clearance. The other three seals have smooth stators, each with a clearance equal to one of the honeycomb-stator seals. The seals are illustrated in figure 3. Seals 1, 2, 3, and 4 were tested for this study, and the data for these seals are reported here for the first time. Seals 5 and 6 were tested previously and documented by Childs and Scharrer (1987). The data are presented here again to provide comparison to the corresponding honeycomb stator seals (seals 2 and 3).

The test points for the other three variables are shown in table 1. The inlet air pressure and attendant mass flow rate through the seal are controlled with a flow control valve located upstream of the seal. Rotor speed is controlled by a variable speed electric motor with a frequency controller. The inlet circumferential velocities are controlled using the inlet guide vanes shown in figure 4. The guide vanes are contained in sleeves and located immediately upstream of the test seal. The no-prerotation case is obtained without guide vanes. *High* and *low* prerotation velocities are obtained for the different, guide-vane-depths *A* of figure 4. The inlet circumferential velocity is calculated from measured values for the volumetric flow rate, upstream temperature and pressure, and a flow-turning correction in accordance with Cohen et al. (1972). The circumferential velocity can not be varied arbitrarily, because it depends on the supply pressure and the flow resistance of the seal being tested. The inlet circumferential velocity set points for each seal are shown in table 2. Inlet circumferential velocity varies a maximum of $\pm$ 10% with supply pressure and

rotor speed from the values in table 2. When reviewing the following test results, figure 3, table 1, and table 2 should be consulted for the definitions of symbols used. Also, note that circumferential velocity ratio is used to represent inlet circumferential velocity; this is the ratio of inlet circumferential velocity to rotor surface speed.

As noted in table 2, the inlet circumferential velocity test point varies significantly when seal clearance is varied. Therefore, the rotordynamic coefficients cannot be plotted versus clearance because the variation in inlet circumferential velocity with clearance would affect the results. The effect of clearance is displayed by plotting the coefficients versus inlet circumferential velocity for each seal on the same plot. This procedure allows only one rotor speed and one supply pressure per plot.

The uncertainty of the rotordynamic coefficients was calculated using the method described by Holman (1978). For the seal configurations tested, the maximum uncertainties in the stiffness and damping coefficients were 15 N/mm (86 lb/in) and 32 N-s/m (0.18 lb-s/in), respectively. The uncertainty in the cross-coupled damping coefficients are of the same order of magnitude as the coefficients themselves; therefore, cross-coupled damping data are not presented here.

TEST RESULTS

Honeycomb-stator seal data are compared to smooth-stator seal data in figures 5–12. ***In these figures, solid lines represent the honeycomb-stator test results and broken lines represent the smooth-stator test results.*** The smallest clearance seals (seals 1 & 4) and the highest inlet circumferential velocity (swirl 3) are used for plots in which these parameters are not varied. Further data are presented by Hawkins (1988).

Leakage

Leakage is represented by the flow coefficient,

$$\Phi = \frac{\dot{m}\sqrt{RT_r}}{\pi DCrP_r}.$$

Figure 5 is a plot of flow coefficient versus seal clearance for an inlet pressure of 3.08 bar and a rotor speed of 3000 cpm. Curve 1 represents the honeycomb-stator seals and curve 4 represents the smooth stator seals. Leakage did not vary with inlet circumferential velocity, thus the data presented are for inlet circumferential velocity 3 only. Examination of the figure reveals that the honeycomb-stator seal leaks more at the smallest clearance and the smooth-stator seal leaks more at the largest clearance. This result is consistent with Stocker et al. (1977). One would expect the honeycomb-stator seal to leak less than the smooth-stator seal because its greater roughness increases the flow resistance. However, in the honeycomb-stator seal, part of the leakage air may bypass the apparent flow path by passing into and out of honeycomb cells. Thus, relative to the smooth-stator seal, the honeycomb-stator seal has a larger effective leakage area for a given clearance. When the

clearance is small, the increased leakage area results in greater leakage in the honeycomb-stator seal versus the smooth-stator seal.

Figure 6 is similar to figure 5, except that leakage is represented by the dimensional mass flow rate. This figure shows that leakage increases as clearance increases.

Direct Stiffness

Direct stiffness is plotted versus rotor speed for various pressures in figure 7. Again, the solid lines are for the smallest clearance honeycomb-stator seal, and the broken lines are for the smallest clearance smooth-stator seal. Direct stiffness of the honeycomb-stator seal is negative and becomes more negative as rotor speed increases. The smooth-stator seal has a similar characteristic, but has a larger direct stiffness magnitude. Direct stiffness becomes more negative as pressure increases for both stator surfaces.

Cross-Coupled Stiffness

Cross-coupled stiffness is plotted versus rotor speed for various pressures in figure 8. Cross-coupled stiffness increases with rotor speed for both seals. For the honeycomb-stator seal, cross-coupled stiffness is negative at low speed and increases to about 300 N/mm at the highest rotor speed. For the smooth stator seal, cross-coupled stiffness has a small positive value at low rotor speeds, increasing to about 350 N/mm at the highest rotor speed. Due to the results of Elrod and Childs (1988), cross-coupled stiffness was expected to be less positive for the honeycomb-stator seal compared to the smooth-stator seal for all rotor speeds. The data show that the cross-coupled stiffness of the two seals have similar magnitudes at high rotor speeds. This plot also shows that increasing pressure increases the absolute value of cross-coupled stiffness.

Figure 9 illustrates cross-coupled stiffness versus circumferential velocity for the three honeycomb-stator seals (1, 2, 3) and the three smooth-stator seals (4, 5, 6). Figure 9(a) is for an inlet pressure of 3.08 bar and rotor speed of 3000 cpm, and figure 9(b) is for the same pressure and rotor speed of 16,000 cpm. Figure 9(a) shows that cross-coupled stiffness increases roughly linearly as inlet circumferential ratio increases for both stator surfaces. The increase is greater with the smooth-stator seal. In figure 9(b), cross-coupled stiffness increases significantly from zero inlet circumferential velocity to the first positive value of inlet velocity; however, from the first positive inlet velocity to the second positive inlet velocity, the cross-coupled stiffness increases only slightly or in some cases decreases. This trend is present for both stator surfaces. Returning to figure 9(a), for the honeycomb-stator seal, cross-coupled stiffness is much lower in the small clearance seal (seal 1) than in the larger clearance seals (seals 2 & 3). Increasing seal clearance has little effect on the cross-coupled stiffness of the smooth-stator seal. At the higher rotor speed (figure 9(b)), seal clearance has little effect on cross-coupled stiffness in the honeycomb-stator seal. The small clearance smooth-stator seal (seal 4) has a much higher cross-coupled stiffness than

the larger clearance seals (seals 5 & 6). Note that cross-coupled stiffness of the larger clearance smooth-stator seals does not depend on rotor speed.

Direct Damping

Direct damping is plotted versus rotor speed for various pressures in figure 10. Direct damping has essentially the same magnitude for either stator surface. However, damping for the honeycomb-stator seal first increases and then decreases with increasing rotor speed, while damping in the smooth-stator seal does not depend on rotor speed. Also, damping increases with pressure for both stator surfaces, but the increase is greater in the honeycomb-stator seal.

Figure 11 is a plot of direct damping versus inlet circumferential velocity ratio for each seal configuration. Damping does not have a clear dependence on inlet circumferential velocity in the honeycomb-stator seals, but increases with increasing inlet circumferential velocity in the smooth-stator seals. Damping increases somewhat from seal 1 (the smallest clearance seal) to seal 2. However, damping in seal 2 and seal 3 is roughly the same. In the smooth-stator seal, damping first falls and then rises as clearance increases. This plot is for pressure of 3.08 bar and rotor speed of 3000 cpm. The same trends are repeated at other inlet pressures and rotor speeds.

Whirl Frequency Ratio

Figure 12 is a plot of whirl frequency ratio versus rotor speed for the three honeycomb-stator seals and the three smooth-stator seals. As noted previously, lower values of whirl frequency ratio indicate a more stable seal. Note that at the lower rotor speeds, each honeycomb-stator seal is more stable than the comparable smooth-stator seal, and that for a particular stator surface, the small clearance seals are more stable than the larger clearance seals. At the higher rotor speeds, stator surface does not significantly affect stability. Also, the small clearance seals (seals 1 & 4) are less stable than the others at the higher speeds.

COMPARISON TO THEORY

Data for the honeycomb-stator seals are compared to the predictions of Scharrer's model in figures 13–16. *The experimental data are represented by solid lines and theoretical predictions are represented by broken lines in each figure.*

Cross-Coupled Stiffness

Figure 13 is a plot of cross-coupled stiffness versus rotor speed for various pressures for the smallest clearance seal. The theory correctly predicts that cross-coupled stiffness rises as rotor speed rises. The theory does not predict the negative values found at low

rotor speeds. In general, the model predicts positive values of cross-coupled stiffness correctly within 25%. Figure 14 is a plot of cross-coupled stiffness versus inlet circumferential velocity ratio for the three honeycomb-stator seals. The model predicts a larger rise in cross-coupled stiffness with increasing circumferential velocity than is shown in the experimental data. The model also predicts little increase in cross-coupled stiffness with increasing clearance.

Direct Damping

Direct damping is plotted versus rotor speed for various pressures in figure 15. The model predicts that damping increases with increasing rotor speed, whereas the data show that damping first increases and then decreases with increasing rotor speed. The model consistently underpredicts the magnitude of the damping at low rotor speeds, and is accurate at high rotor speeds. However, at the highest rotor speeds tested, the model predictions and the test results are diverging. Figure 16 is a plot of direct damping versus inlet circumferential velocity ratio for the three honeycomb-stator seals. The model correctly predicts that damping does not depend on inlet circumferential velocity ratio. The model also predicts that damping does not increase significantly as clearance increases. This is true only at the larger clearances.

CONCLUSIONS

The test data support the following conclusions for the labyrinth-rotor/honeycomb-stator seals:

1) Cross-coupled stiffness is generally positive. Cross-coupled stiffness increases with rotor speed and with inlet circumferential velocity. At the lower rotor speeds, cross-coupled stiffness is much lower for the smallest clearance seal than for the other two seals. At the higher rotor speeds, cross-coupled stiffness is approximately the same value regardless of clearance.

2) Direct damping is positive, and is much lower in the smallest clearance seal than in the two larger clearance seals.

By comparing the results for the honeycomb-stator and smooth-stator seals, the following conclusions may be drawn:

1) The honeycomb-stator seals leak more than the smooth-stator seals when the clearance is small. The honeycomb-stator seals leak less when the clearance is large.

2) The honeycomb-stator seal is more stable at low rotor speeds. For high rotor speeds stator surface does not affect stability.

By comparison of experimental results and theoretical predictions for honeycomb-stator seals, the following conclusions may be drawn:

1) The model does not predict the negative values measured for cross-coupled stiffness at low rotor speeds.

2) The model consistently predicts the positive values of cross-coupled stiffness of the honeycomb-stator seal correctly within 25% of the measured values. The model correctly predicts the weak dependence of cross-coupled stiffness on clearance for the larger clearances.

3) The model incorrectly predicts that direct damping increases with speed, and does not predict the decrease in damping at small clearance. For the two larger clearance seals the model produces good results for tested rotor speeds above 12,000 cpm. Below 12,000 cpm, the model underpredicts direct damping by 50%.

In general, Scharrer's model gives useful results for cross-coupled stiffness in the labyrinth-rotor/honeycomb-stator seal for the range of variables tested. Scharrer's model can give useful results for direct damping in the labyrinth-rotor/honeycomb-stator seal by applying a rotor-speed correction factor to the predicted damping. Overall, the model produces better results for the larger clearances. The increased significance of unmodeled effects at smaller clearances – such as the unmodeled leakage path through the honeycomb cells – is probably responsible for the reduced performance of the model at smaller clearances.

Values of the rotordynamic coefficients for the two larger clearance seals tend to be much closer together than to the smaller clearance seal. This is true for both the labyrinth-rotor/honeycomb-stator seal and for the previously untested smallest clearance labyrinth-rotor/smooth-stator seal. Since there are many practical applications where labyrinth seals are used with clearances below the tested range, further testing with smaller clearances are required.

REFERENCES

Benckert, H., and Wachter, J., 1978, "Querkrafte aus Spaltdichtungen-Eine mogliche Ursache fur die Laufunruhe von Turbomaschinen," *Atomkernenergie,"*32, Lfg. 4, pp. 239-246.

Benckert, H., 1980, "Stromungsbedinte Federkennwerte in Labyrinthdichtungen," Doctoral dissertation at University of Stuttgart.

Benckert, H., and Wachter, J., 1980, "Flow Induced Spring Coefficients of Labyrinth Seals for Applications in Rotordynamics,," NASA CP 2133, Proceedings from a workshop on Rotordynamic Instability Problems in High-Performance Turbomachinery–1980, held at Texas A&M University, College Station, TX, pp. 189-212.

Childs, D. and Scharrer, J., 1986, "Experimental Rotordynamic Coefficient Results for Teeth-On-Rotor and Teeth-On-Stator Labyrinth Gas Seals," ASME Paper No. 86-GT-12, Also accepted for *ASME Journal of Engineering for Gas Turbines and Power.*

Childs, D., and Scharrer, J., 1987, "Theory Versus Experiment for the Rotordynamic Coefficients of Labyrinth Gas Seals: Part II – A Comparison to Experiment," *Rotating Machinery Dynamics,* Vol. 2, proceedings from the ASME Conference on Mechanical Vibration and Noise, Boston, MA, pp. 427-434.

Childs, D., Nelson, C., Nicks, C., Scharrer, J., Elrod, D., Hale, K., 1986, "Theory Versus Experiment for the Rotordynamic Coefficients of Annular Gas Seals: Part 1, Test Facility and Apparatus," *ASME Trans. J. of Tribology,* Vol. 108, pp. 426–432.

Cohen, H., Rogers, C., and Saravanamutto, H., 1972, *Gas Turbine Theory,* Longman Group Limited.

Ehrich, F., and Childs, D., 1984, "Self-Excited Vibration in High-Performance Turbomachinery," *Mechanical Engineering,*May, pp.66–78.

Elrod, D., and Childs, D., 1988, "Experimental Rotordynamic Coefficient Results for Honeycomb Seals", Texas A&M Turbomachinery Laboratory Report TRC-Seal-1-88.

Fujikawa, T., Kameoka, T., and Abe, T., 1984, "A Theoretical Approach to Labyrinth Seal Forces," NASA CP 2338, Proceedings from a workshop on Rotordynamic Instability Problems in High-Performance Turbomachinery–1984, held at Texas A&M University, College Station, TX, pp. 173-186.

Hawkins, L., 1988, "A Comparison of Experimental and Theoretical Results for Labyrinth Gas Seals," Masters Thesis, Texas A&M University, College Station, TX.

Holman, J., 1978,*Experimental Methods for Engineers,* McGraw-Hill, New York, pp. 45.

Scharrer, J., 1987, "Theory Versus Experiment for the Rotordynamic Coefficients of Labyrinth Gas Seals: Part I – A Two Control Volume Model," *Rotating Machinery Dynamics,* Vol. 2, proceedings from the ASME Conference on Mechanical Vibration and Noise, Boston, MA, pp. 411-426.

Stocker, H., Cox, D., and Holle, G., 1977, "Aerodynamic Performance of Conventional and Advanced Design Labyrinth Seals with Solid-Smooth, Abradable, and Honeycomb Lands," NASA CR-135307, pp. 63-72.

Wright, D., 1983, "Labyrinth Seal Forces on a Whirling Rotor," *Rotor Dynamical Instability,* ASME, New York, pp. 19-31.

Wyssmann, H., Jenny, R., and Pham, T., 1984, "Prediction of Stiffness and Damping Coefficients for Centrifugal Compressor Labyrinth Seals," ASME 84-GT-86. Presented at the 29th International Gas Turbine Conference and Exhibit, Amsterdam, The Netherlands.

NOMENCLATURE

C, c	Direct and cross-coupled damping coefficients (Ft/L)
Cr	Radial clearance (L)
D	Rotor diameter (L)
F	Seal reaction-force magnitude (F)
K, k	Direct and cross-coupled stiffness coefficients (F/L)
f	Whirl frequency ratio
$\dot{m}$	Leakage mass flow rate (M/Lt)
ms, ns	Friction coefficients
P	Fluid pressure (F/L^2)
R	Gas constant for air (L^2/Tt^2)
T	Fluid temperature (T)
X, Y	Rotor-to-stator relative displacement components (L)
ν	Kinematic viscosity (L^2/t)
ρ	Density of fluid (M/L^2)
ω	Shaft angular velocity $(1/t)$

Subscripts

r	Reservoir value, radial component
s	Sump value
t	Tangential component

Table 1. Definition of symbols used in figures.

Supply Pressure	Rotor Speeds	Inlet Circumferential Velocities
1 - 3.03 bar	1 - 3,000 cpm	1 - Zero circumferential velocity
2 - 4.46 bar	2 - 6,000 cpm	2 - Low velocity with rotation
3 - 5.84 bar	3 - 9,500 cpm	3 - High velocity with rotation
4 - 7.22 bar	4 - 13,000 cpm	
5 - 8.25 bar	5 - 16,000 cpm	

Table 2. Inlet circumferential velocity set points.

Seal	Circumferential Velocity (m/s)		
	Swirl 1	Swirl 2	Swirl 3
1	0.0	14.9	38.7
2	0.0	20.9	56.3
3	0.0	24.6	64.1
4	0.0	10.3	28.1
5	0.0	22.8	59.9
6	0.0	28.7	76.3

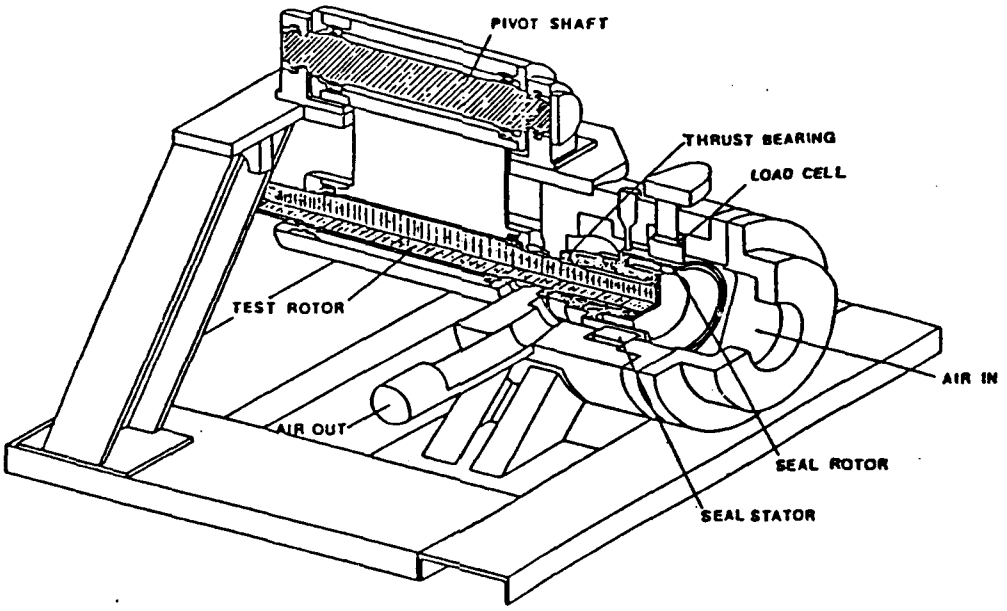

Figure 1. Test apparatus.

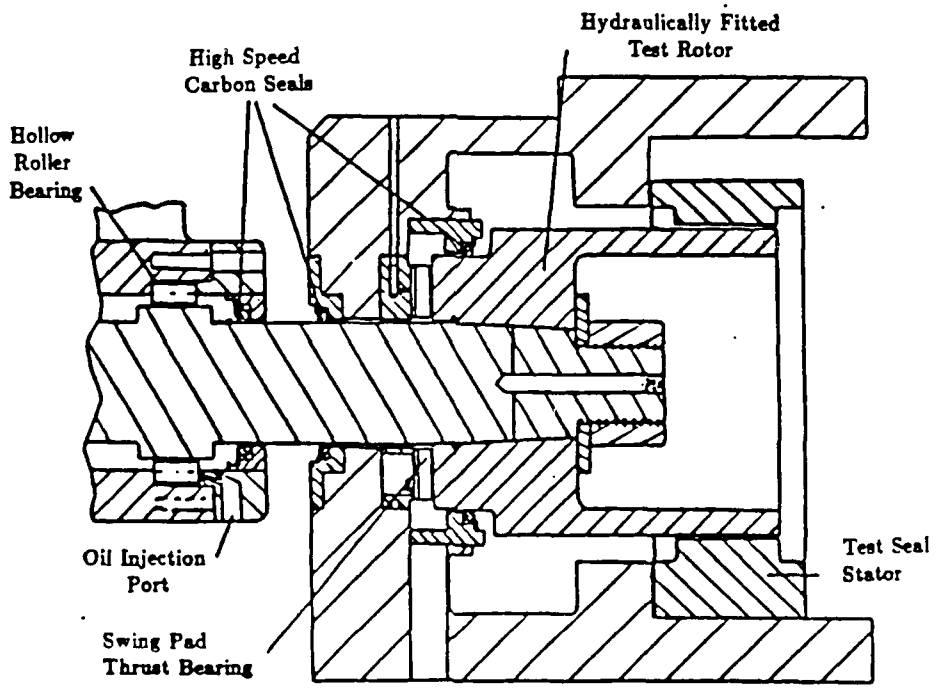

Figure 2. Cross-sectional view of test section.

Honeycomb Stator Seals

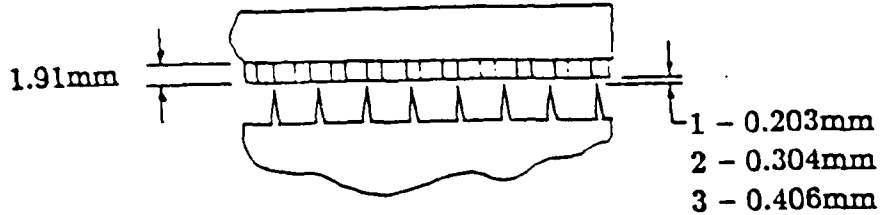

Seal 1, Seal 2, Seal 3

Smooth Stator Seals

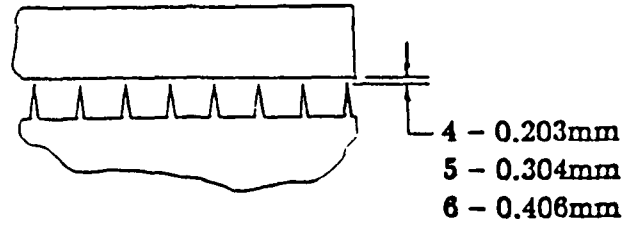

Seal 4, Seal 5, Seal 6

Honeycomb Cell Pattern

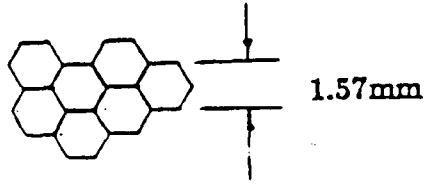

Labyrinth Tooth Detail

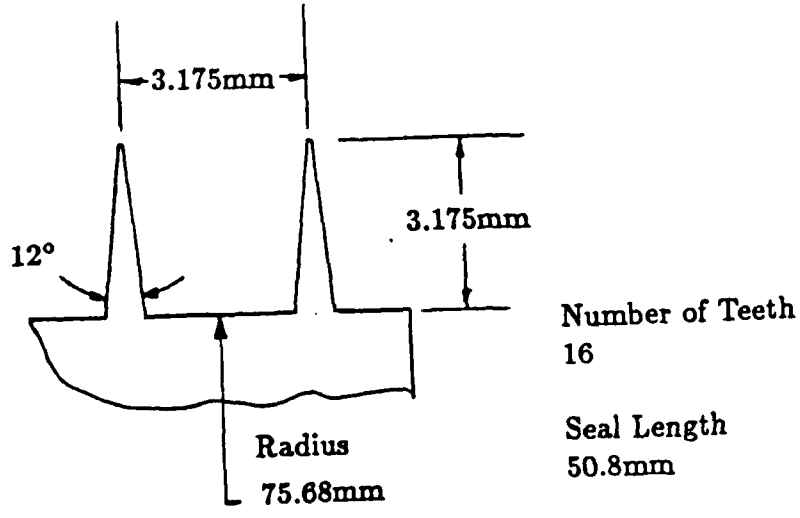

Figure 3. Seal configurations.

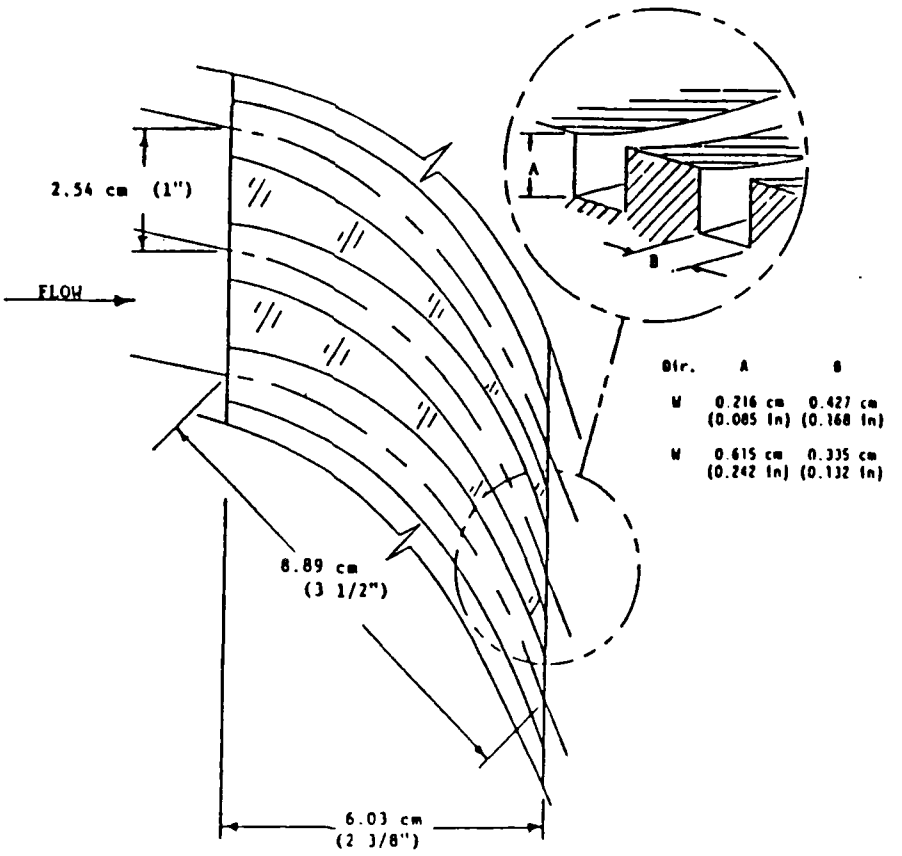

Figure 4. Inlet-guide-vane detail.

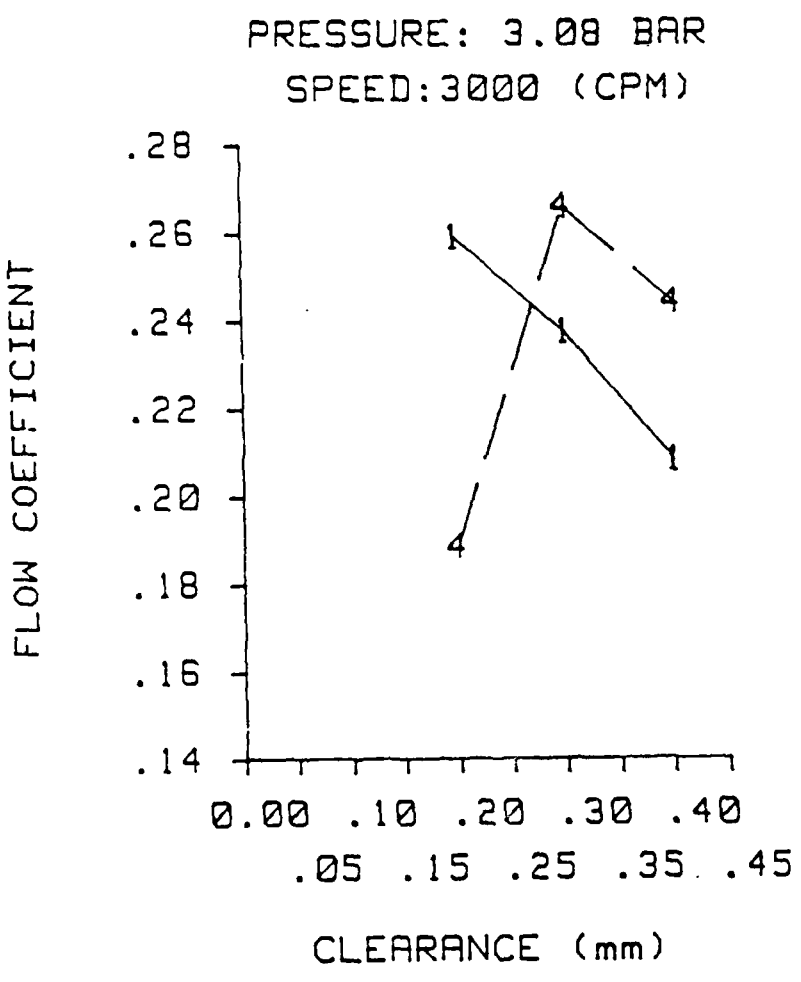

Figure 5. Flow coefficient versus radial seal clearance. Honeycomb-stator seals (curve 1) and smooth-stator seals (curve 4).

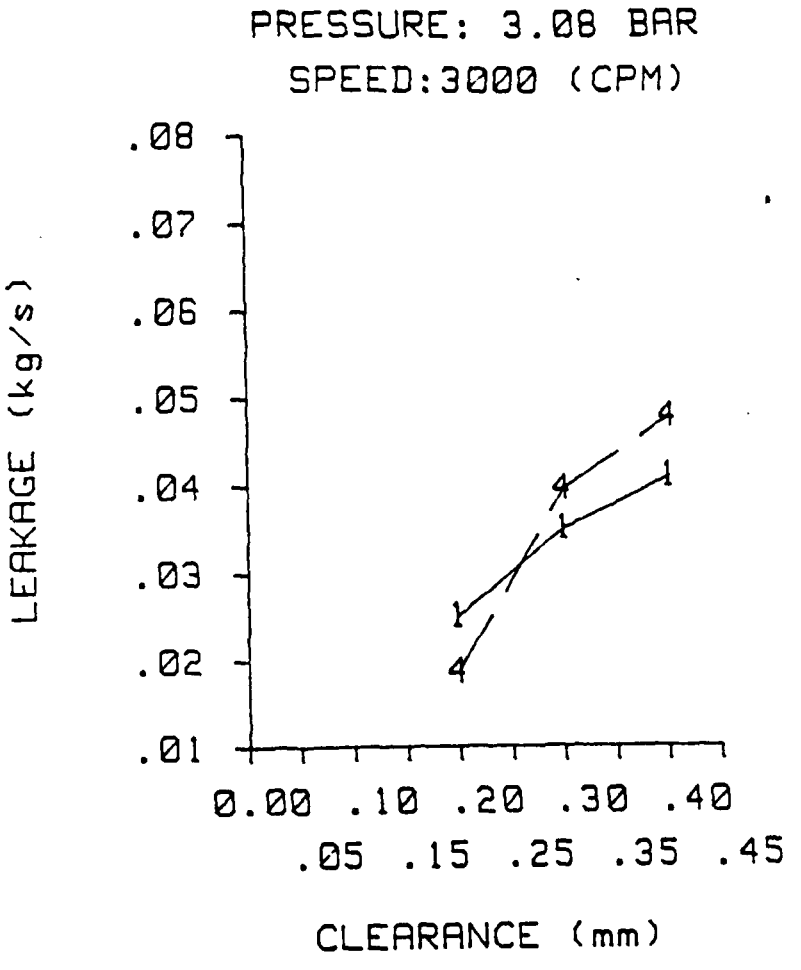

Figure 6. Leakage versus radial seal clearance. Honeycomb-stator seals (curve 1) and smooth-stator seals (curve 4).

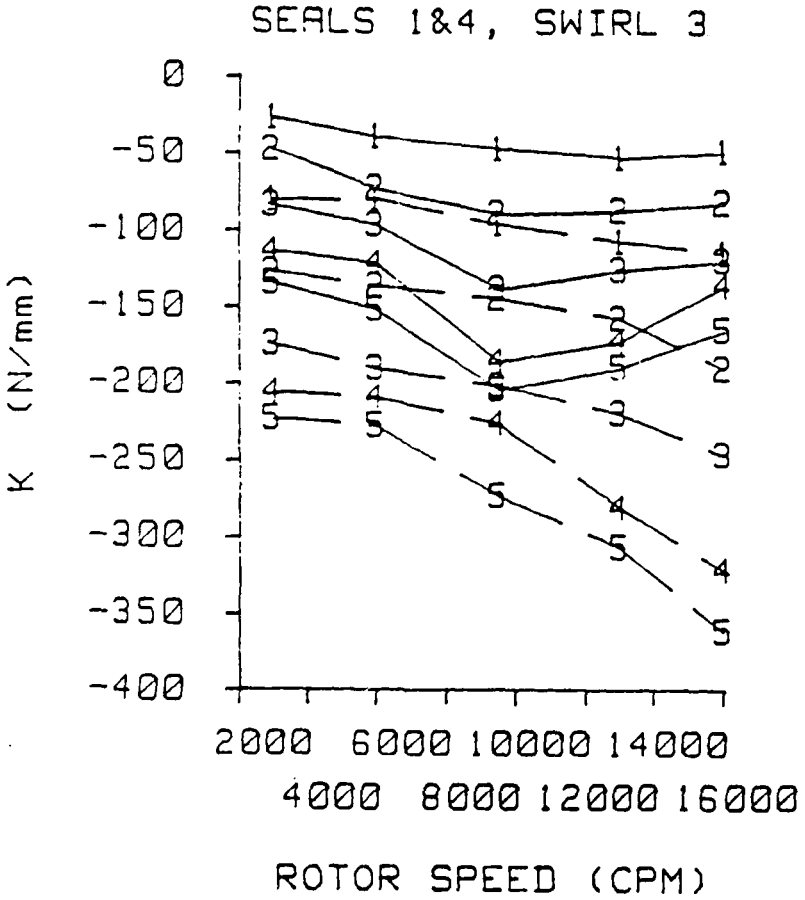

Figure 7. Direct stiffness versus rotor speed for seals 1 & 4 of figure 3.

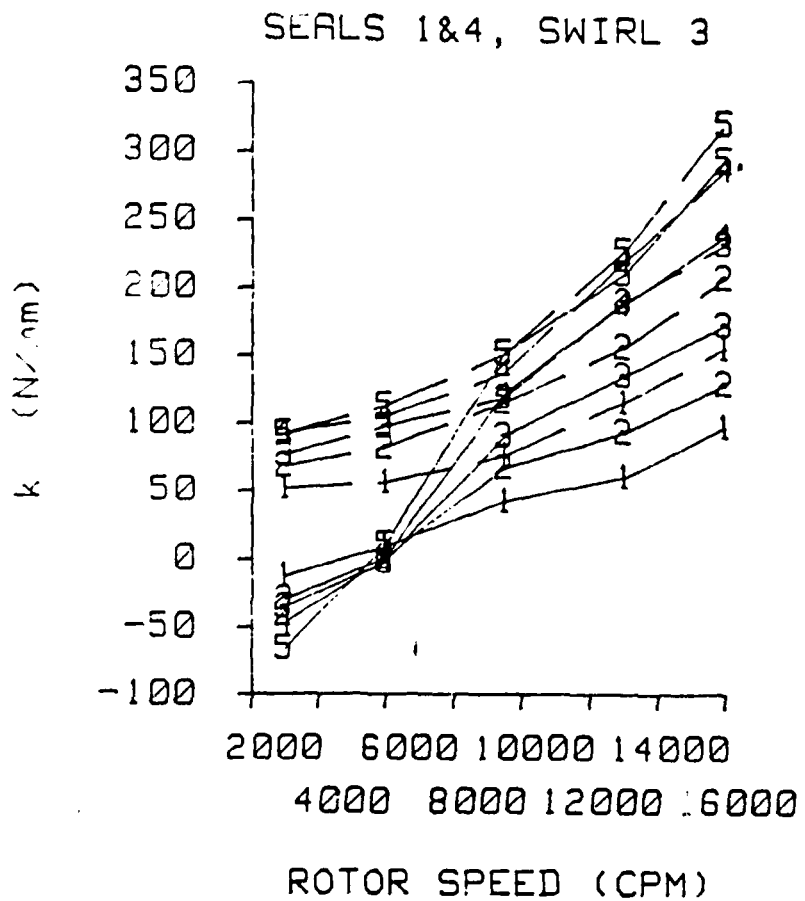

Figure 8. Cross-coupled stiffness versus rotor speed for seals 1 & 4 of figure 3.

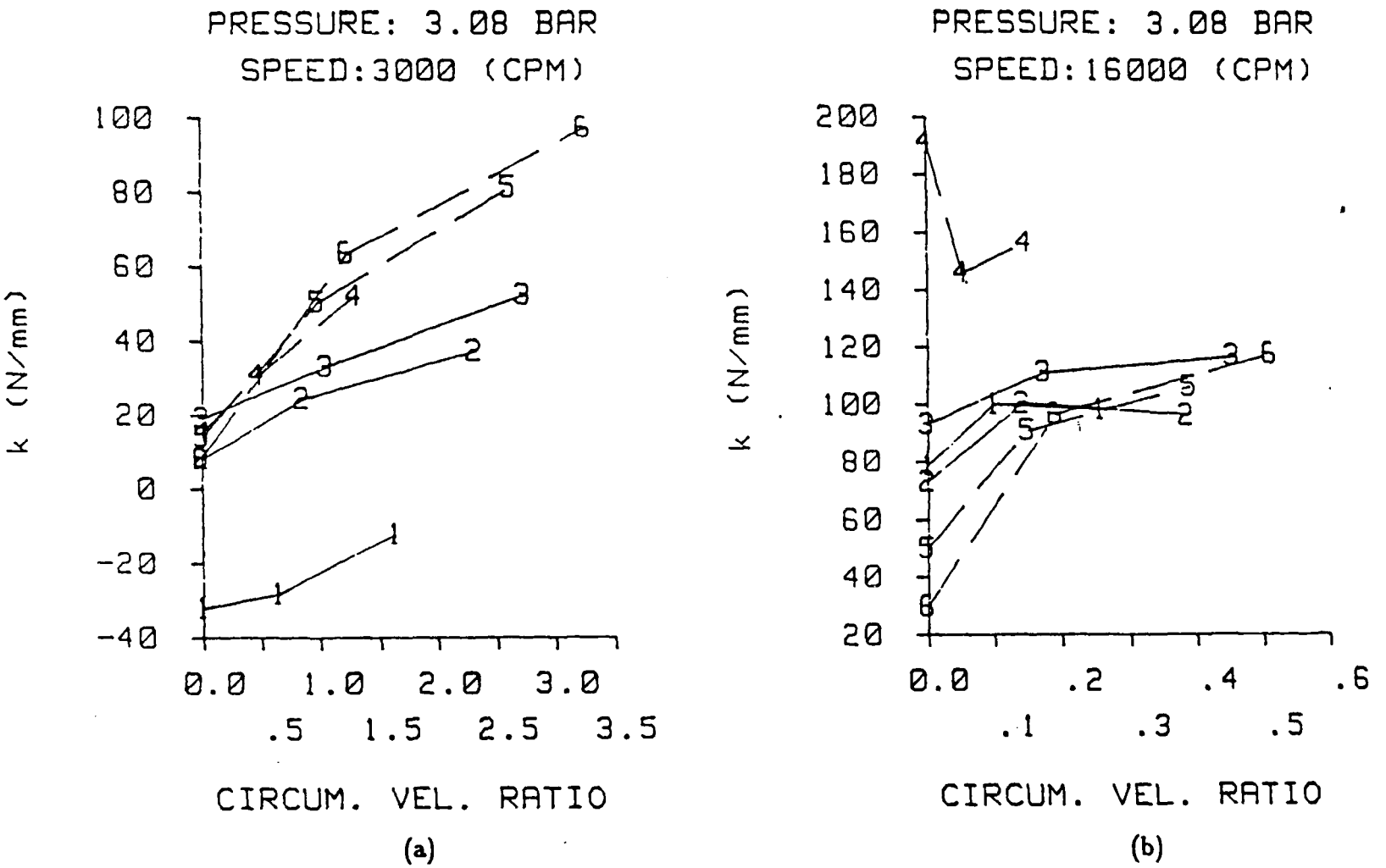

Figure 9. Cross-coupled stiffness versus inlet circumferential velocity ratio for seals 1–6 of figure 3.

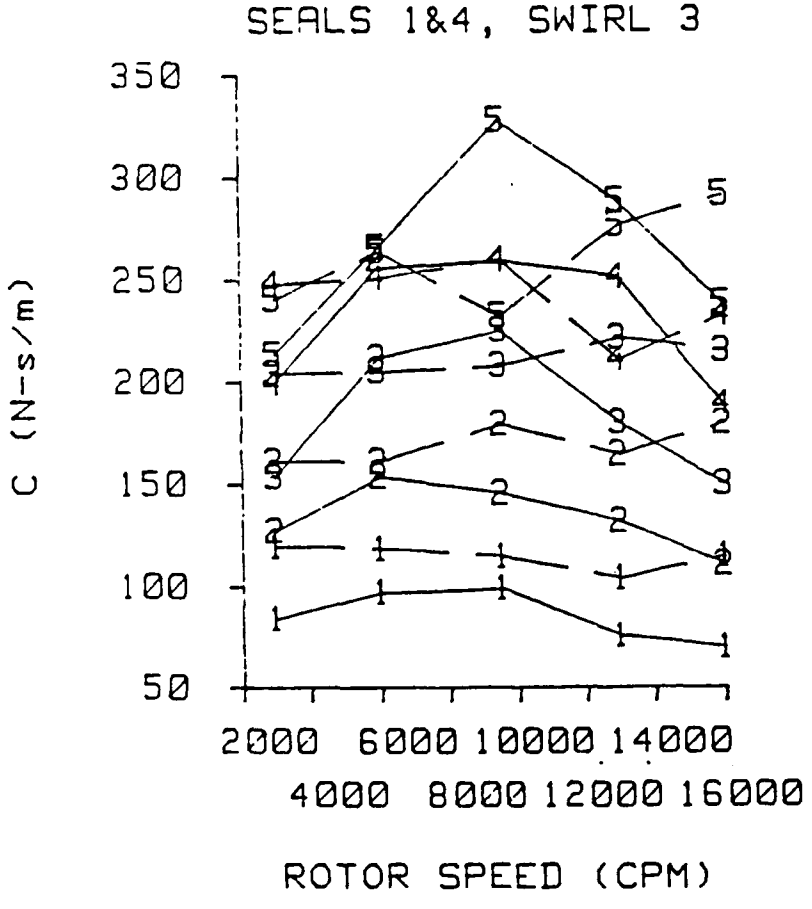

Figure 10. Direct damping versus rotor speed for seals 1 & 4 of figure 3.

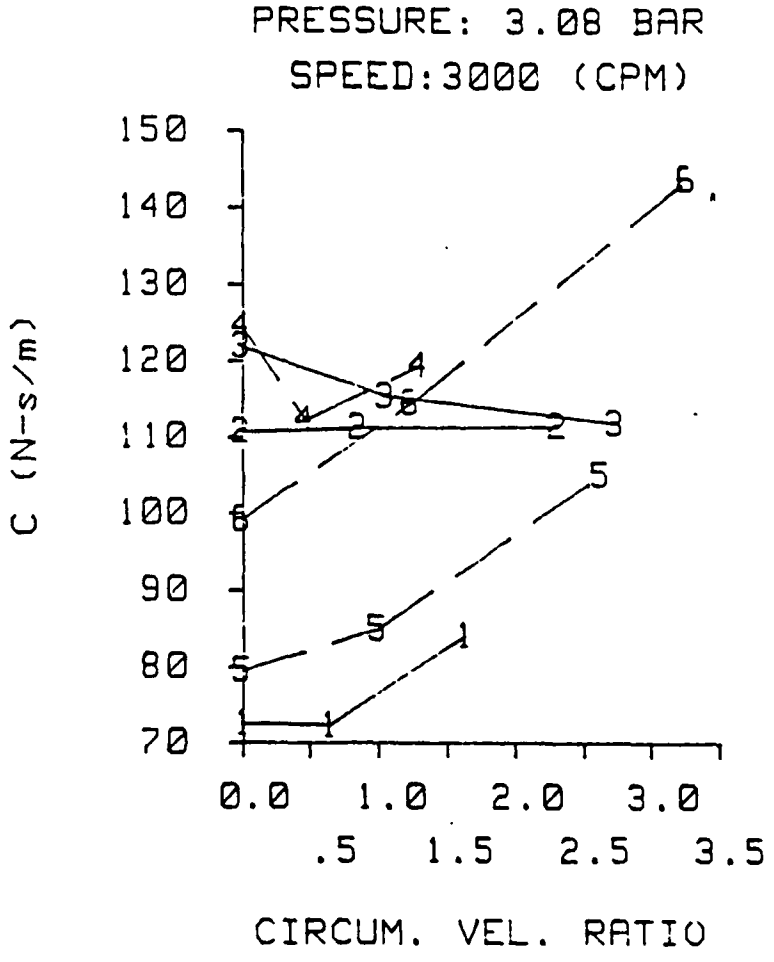

Figure 11. Direct damping versus inlet circumferential velocity ratio for seals 1–6 of figure 3.

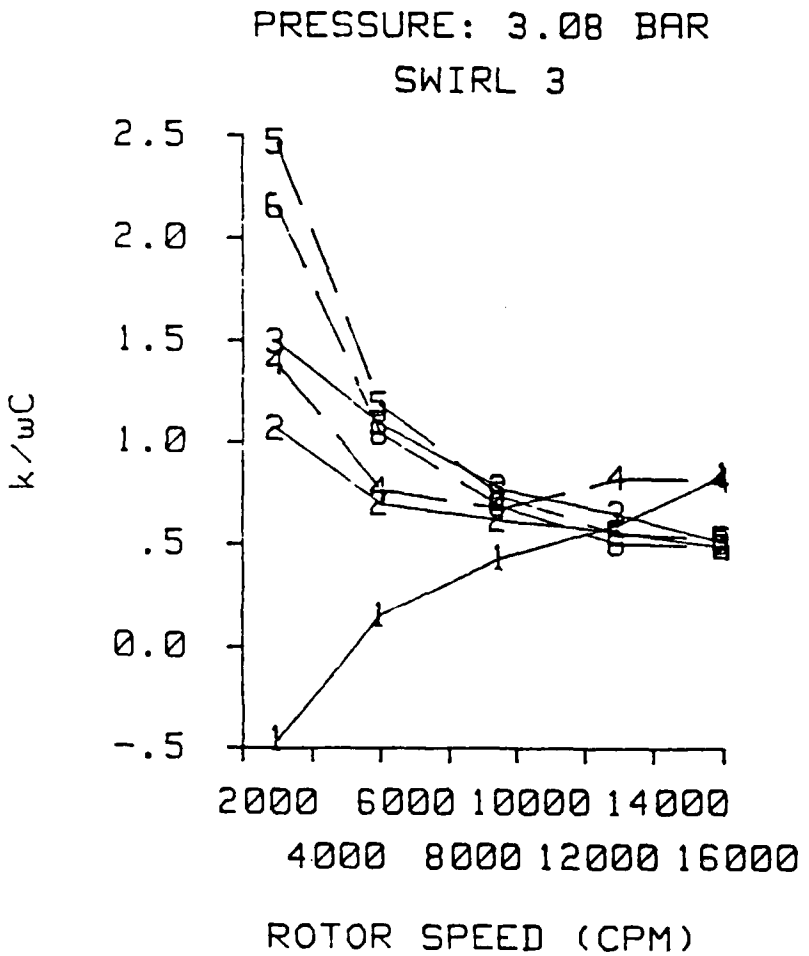

Figure 12. Whirl frequency ratio versus rotor speed for seals 1–6 of figure 3.

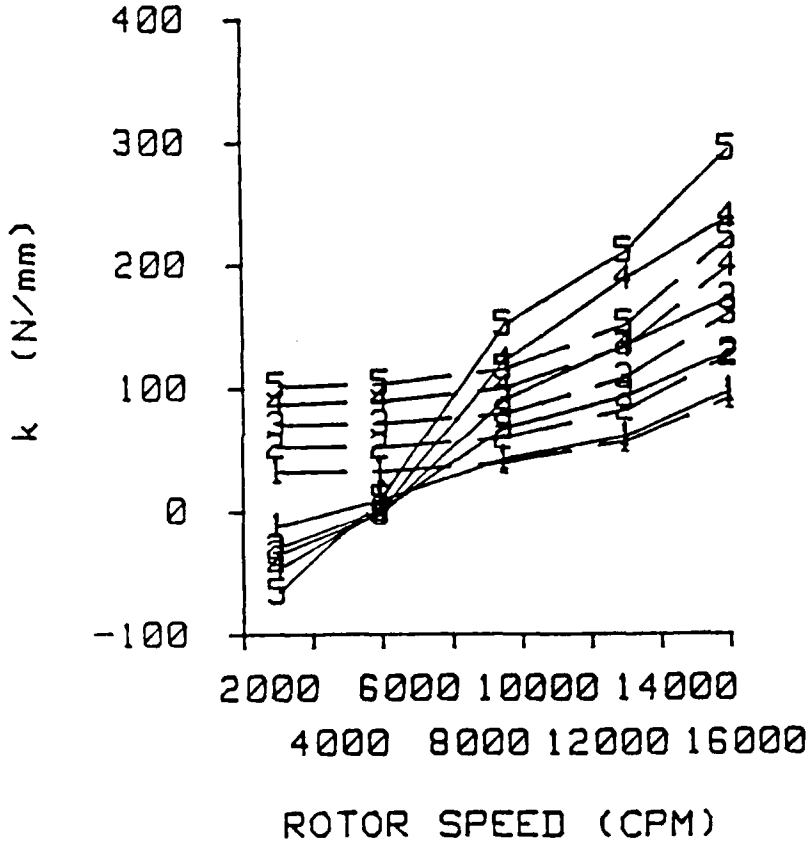

Figure 13. A comparison of experimental and theoretical cross-coupled stiffness versus rotor speed for seal 1 of figure 3.

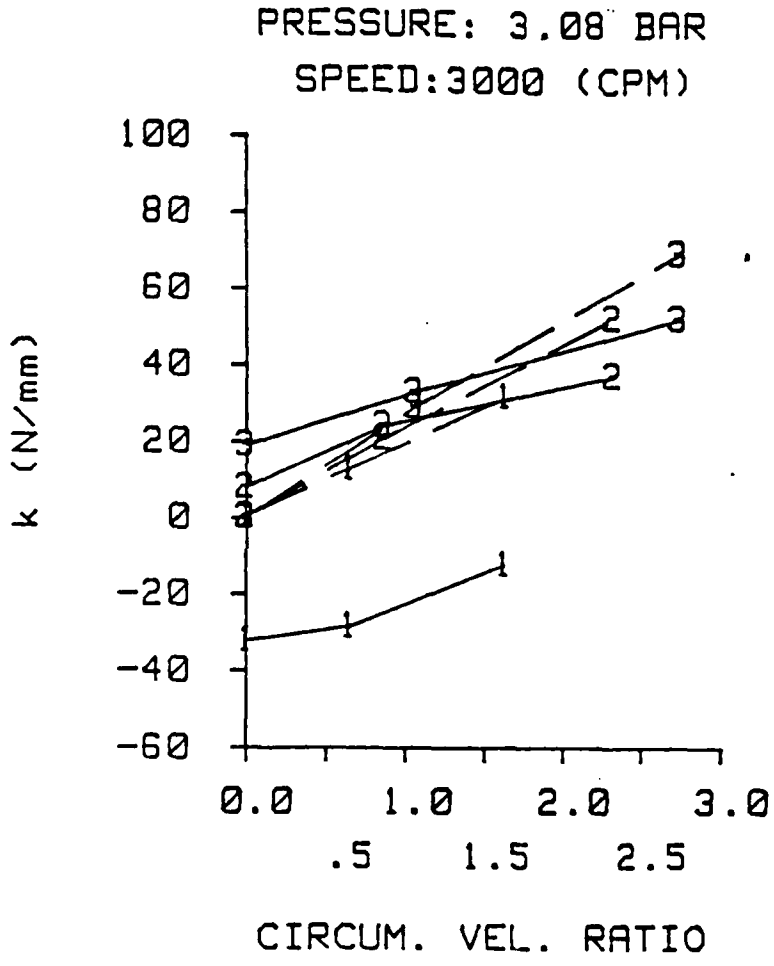

Figure 14. A comparison of experimental and theoretical cross-coupled stiffness versus inlet circumferential ratio for seals 1–3 of figure 3.

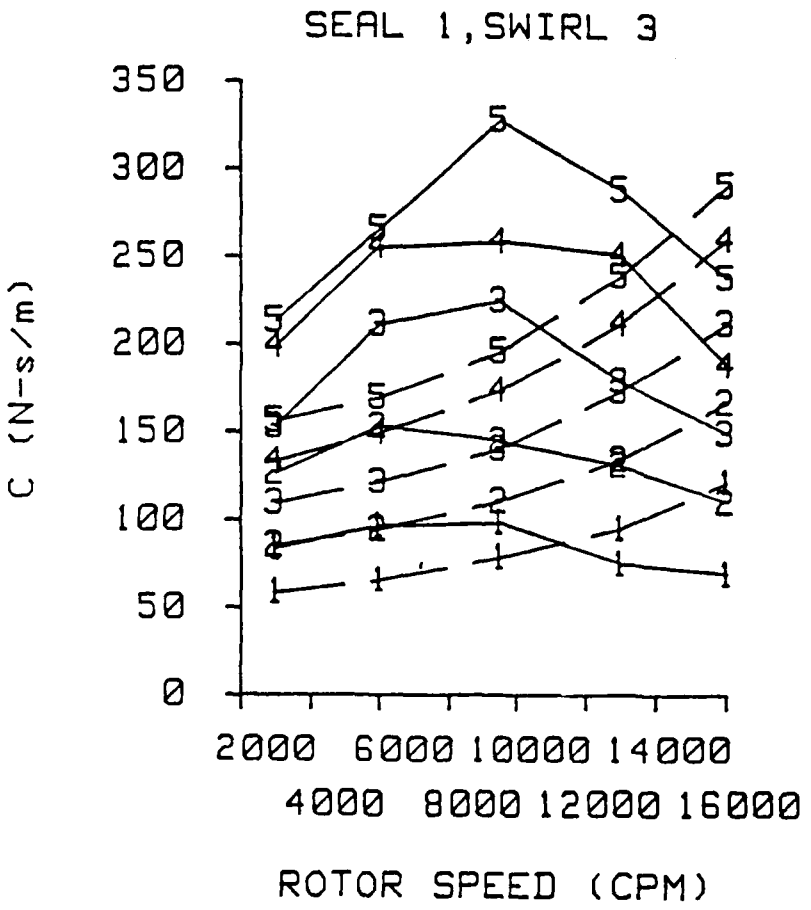

Figure 15. A comparison of experimental and theoretical direct damping versus rotor speed for seal 1 of figure 3.

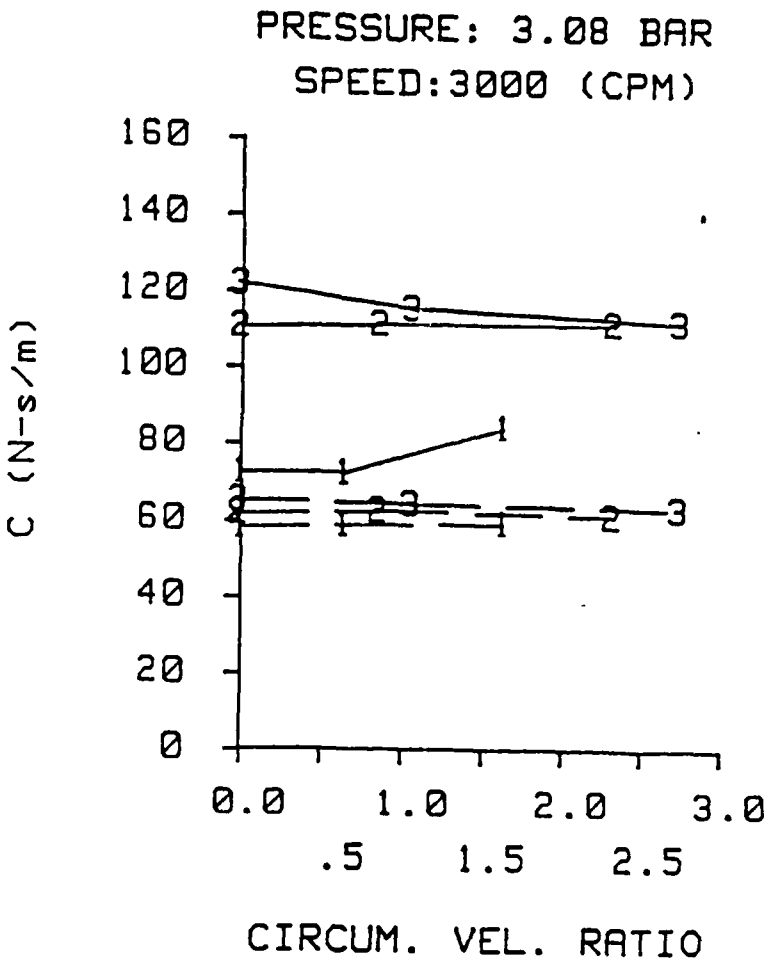

Figure 16. A comparison of experimental and theoretical direct damping versus inlet circumferential velocity ratio for seals 1–3 of figure 3.

THEORY VERSUS EXPERIMENT FOR THE ROTORDYNAMIC COEFFICIENTS OF LABYRINTH GAS SEALS: PART I - A TWO CONTROL VOLUME MODEL[1]

JOSEPH K. SCHARRER
MECHANICAL ENGINEERING DEPARTMENT
TEXAS A&M UNIVERSITY
COLLEGE STATION, TEXAS 77843

SUMMARY

The basic equations are derived for a two-control-volume model for compressible flow in a labyrinth seal. The recirculation velocity in the cavity is incorporated into the model for the first time. The flow is assumed to be completely turbulent and isoenergetic. The wall friction factors are determined using the Blasius formula. Jet flow theory is used for the calculation of the recirculation velocity in the cavity. Linearised zeroth and first-order perturbation equations are developed for small motion about a centered position by an expansion in the eccentricity ratio. The zeroth-order pressure distribution is found by satisfying the leakage equation while the circumferential velocity distribution is determined by satisfying the momentum equations. The first-order equations are solved by a separation of variable solution. Integration of the resultant pressure distribution along and around the seal defines the reaction force developed by the seal and the corresponding dynamic coefficients.

INTRODUCTION

The problems of instability and synchronous response in turbomachines have arisen recently because of the trends in design toward greater efficiency with higher performance. To achieve these design goals, the machines are designed for higher speeds, larger loadings, and tighter clearances. As loadings are increased and clearances decreased, fluid forces increase and can lead to unstable or self-excited vibrations. One of the rotordynamic force mechanisms which has been shown to cause self-excited vibration and synchronous response in centrifugal compressors is that of the forces developed by labyrinth seals.

The flow in a labyrinth seal has been shown by experiment [1] and calculation [2,3,4] to be comprised of two flow regimes: a jet flow region in the leakage path and a recirculating velocity region in the cavity itself (see figure 1). The first attempts at analysis of this system neglected the axial velocity components in the flow and concentrated on the circumferential components. This was the single-control-volume approach, used in refs [5,6]. In an attempt to improve upon the results of these analyses, the two-control-volume approach was introduced. The most notable of the two-control-volume analyses is that of Jenny et al. [7]. Jenny et al. [7] used the two-control-volume approach in conjunction with a 2-D CFD solution to the Navier-Stokes equations to account for the free shear stress between the jet flow and the cavity flow. However, they neglected the recirculating velocity in the cavity and assumed the flow to be incompressible. Further, the present author obtains different signs in the expansion of the continuity equation and different perturbation equations. These discrepancies are explained in detail in Appendix D. The theory of Jenny et al. [7] showed substantial improvement in the prediction of stiffness and damping coefficients, but in the end, correction factors had to be incorporated into the calculation of the shear stress to improve the correlation with test data.

This paper introduces the calculation of the recirculation velocity into the analysis. The model for the recirculation velocity, U_2, used here is illustrated in figure 2. This velocity component is important in the calculation of the cavity shear stresses. The focus is on the shear stresses, because experimental result [8] have shown that the stiffness and damping coefficients are very sensitive to the circumferential velocity in the seal. In the control volume analysis to be presented, the solution to the circumferential momentum equation

[1]This work was supported in part by NASA Grant NAS3-181 from NASA Lewis Research Center (Technical Monitor, Robert Hendricks) and AFOSR Contract F49620-82-K-0033 (Technical Monitor, Tony Amos)

yields the circumferential velocity in the seal. An improvement in the shear stress calculation will yield an improvement in the calculation of the stiffness and damping coefficients. The CFD results of Rhode [2,3] are used to evaluate the models for shear stress and recirculation velocity used in this paper. The results of this analysis are compared to a new set of experimental results for teeth-on-rotor and teeth-on-stator labyrinth seals in Part 2 of this paper.

CONTROL VOLUME MODELLING

Before proceeding with the solution development, the approach taken in modelling the flow will be discussed. As mentioned previously, the flow in a labyrinth seal is known to have two distinct regions: a jet flow region in the leakage path and a recirculating flow region in the cavity itself (see figure 1). Therefore, a two-control-volume model seems appropriate. The choice of control volumes is between the "box-in-a-box" model (see figure 3) of Jenny et al. [7] or a more conventional model with a control volume for the jet flow and one for the recirculating flow in the cavity, as shown in figure 2. The two-separate-control-volume model was chosen since it is suggested by the known physics of the flow. The flow enters the seal and separates into two distinct flow regions which are separated by the dividing streamline.

The final question is whether the control volumes should be defined using a geometric boundary or using the dividing streamline as the boundary. The dividing streamline approach seems, at first, to be the obvious choice. The governing equations would be simplified by the restriction of no flow across a streamline, the free shear stress relations are derived for flow along the dividing streamline, and the solution for the velocity of the recirculating flow may be derived for flow along the dividing streamline. Despite these advantages, the dividing streamline approach was not used, due to mathematical constraints. The mathematical limitations of the dividing streamline approach are dealt with in detail by Scharrer [9]. The geometric boundary approach relies on the assumption that the dividing streamline makes a small angle with the horisontal. As will be shown, this is a good assumption which has been verified experimentally. The geometric boundary approach and solution is provided in the following section.

GEOMETRIC BOUNDARY APPROACH

Assumptions

(1) The fluid is considered to be an ideal gas.

(2) Pressure variations within a chamber are small compared to the pressure differences across a seal strip.

(3) The lowest frequency of acoustic resonance in the cavity is much higher that that of the rotor speed.

(4) The eccentricity of the rotor is small compared to the radial seal clearance.

(5) Although the shear stress is significant in the determination of the flow parameters (velocity etc.), the contribution of the shear stress to the forces on the rotor are negligible when compared to the pressure forces.

(6) The cavity flow is turbulent and isoenergetic.

(7) The recirculation velocity, U_2, is unchanged as it swirls within a cavity.

Procedure

The analysis presented here is developed for the teeth-on-rotor "see-through" labyrinth seal shown in figure 5. The equivalent equations for the teeth-on-stator labyrinth seal are given in Appendix A. The continuity and circumferential momentum equations will be derived for the two-control-volume model shown in figures 2,6,7 and 8. A leakage model will be employed to account for the axial flow. The governing equations are linearised using a perturbation analysis for small motion about a centered position. The seroth-order continuity and momentum equations will be solved to determine the steady state pressure, axial and circumferential velocity for each cavity. The first-order continuity and momentum equations will be reduced to linearly independent, algebraic equations by assuming an elliptical orbit for the shaft and a corresponding harmonic response for the pressure and velocity perturbations. The force coefficients for the seal are found by integration of the first-order pressure perturbation along and around the shaft.

GOVERNING EQUATIONS

Continuity Equation

The control volumes of figures 2 and 6 have a unity circumferential width. Their continuity equations are:

$$\frac{\partial \rho A_1}{\partial t} + \frac{\partial \rho W_1 A_1}{Rs_1 \partial \theta} + \dot{m}_{i+1} - \dot{m}_i + \dot{m}_r = 0 \tag{1}$$

$$\frac{\partial \rho A_2}{\partial t} + \frac{\partial \rho W_2 A_2}{Rs_2 \partial \theta} - \dot{m}_r = 0 \tag{2}$$

For the teeth-on-rotor case, A_1 =LCr, A_2 = LB, Rs_1 = Rs, and $Rs_2 = Rs + B$.

Momentum Equations

The following momentum equations for control volumes I and II are derived using figures 7 and 8 which show the pressure forces and shear stresses acting on the control volumes.

$$\frac{\partial \rho W_1 A_1}{\partial t} + \frac{2\rho W_1 A_1}{Rs_1}\frac{\partial W_1}{\partial \theta} + \frac{\rho W_1}{Rs_1}\frac{\partial A_1}{\partial \theta} + \frac{W_1 A_1}{Rs_1}\frac{\partial \rho}{\partial \theta} + \dot{m}_r W_{\omega i}$$
$$+ \dot{m}_{i+1} W_{1i} - \dot{m}_i W_{i-1} = -\frac{A_1}{Rs_1}\frac{\partial P_i}{\partial \theta} + \tau_{ji} L_i - \tau_{\omega i} as_i L_i \tag{3}$$

$$\frac{\partial \rho W_2 A_2}{\partial t} + \frac{2\rho W_2 A_2}{Rs_2}\frac{\partial W_2}{\partial \theta} + \frac{\rho W_2}{Rs_2}\frac{\partial A_2}{\partial \theta} + \frac{W_2 A_2}{Rs_2}\frac{\partial \rho}{\partial \theta}$$
$$+ \dot{m}_r W_{\omega i} = -\frac{A_2}{Rs_2}\frac{\partial P_i}{\partial \theta} - \tau_{ji} L_i + \tau_{\omega i} ar_i L_i \tag{4}$$

where ar and as are the dimensionless length upon which the shear stresses act and are defined for the teeth-on-rotor labyrinth by

$$as_i = 1 \qquad ar_i = (2B_i + L_i)/L_i \tag{5}$$

$W_{\omega i}$ is the circumferential velocity between the control volumes.

Blasius [10] determined that the shear stresses for turbulent flow in a smooth pipe could be written as

$$\tau = \frac{1}{2}\rho U_m^2 no \left(\frac{U_m D_h}{\nu}\right)^{mo}$$

where U_m is the mean flow velocity relative to the surface upon which the shear stress is acting. The constants mo and no can be empirically determined for a given surface from pressure flow experiments. However, for smooth surfaces the coefficients given by Yamada [11] for turbulent flow between annular surfaces are:

$$mo = -0.25 \qquad no = 0.079$$

Applying Blasius' equation to the labyrinth rotor surfaces yields the following definitions for the rotor shear stress in the circumferential direction. Note that the recirculation velocity, U_2, is included in the definition of the total velocity acting on the rotor.

$$\tau_r = \frac{1}{2}\rho\sqrt{(Rs_2\omega - W_2)^2 + U_2^2}\,(Rs_2\omega - W_2)\,nr \left(\frac{\sqrt{(Rs_2\omega - W_2)^2 + U_2^2}\,D_{h2i}}{\nu}\right)^{mr} \tag{6}$$

where D_{h2i} is the hydraulic diamter of control volume II, defined by

$$D_{h2i} = 2B_i L_i/(B_i + L_i) \tag{7}$$

Similarly, the stator shear stress in the circumferential direction is:

$$\tau_s = \frac{1}{2}\rho\sqrt{W_1^2 + U_1^2}\,W_1 ns \left(\frac{\sqrt{W_1^2 + U_1^2}\,D_{h1i}}{\nu}\right)^{ms} \tag{8}$$

where D_{h1i} is the hydraulic diameter of control volume I, defined by

$$D_{h1i} = 2Cr_i L_i/(Cr_i + L_i) \tag{9}$$

and the axial velocity, U_1, is

$$U_1 = \dot{m}/\rho Cr_i \tag{10}$$

Figure 9 shows a comparison of the predictions from equation (8) and CFD results for stator wall shear stress for seal A of table 1. The figure shows that the comparison is very good. Similar results are obtained for the other seals of table 1. Figure 10 shows a comparison of rotor wall-shear-stress predictions from equation (6), CFD and averaged CFD for seal A of table 1. The averaged CFD results is used here for comparison since the bulk flow model yields a single averaged result for cavity shear stress and is not capable of modelling the complex flowfield.The figure shows that the prediction of equation (6) is close to the CFD results.The dips in the CFD results are the lower corners of the cavity. Similar results are obtained for the other seals of table 1.

Table 1. Seal geometries calculated by Rhode.

	Seal			
	A	B	C	D
Rs	72.5043mm	72.5043mm	72.5043mm	41.780mm
B	3.175mm	3.175mm	3.175mm	0.889mm
L	3.175mm	3.175mm	3.969mm	0.8585mm
Tp	0.35mm	0.35mm	0.35mm	0.15mm
Cr	0.4064mm	0.508mm	0.508mm	0.2159mm

The flow across a labyrinth tooth is very similar to the flow of a turbulent jet issuing from a slot. The problem with using jet-flow results for labyrinth seals is that current jet-flow theory only considers the flow of a jet with a coflowing stream or a crossflowing stream, not both. In the following derivation, the relationships given by Abramovich [12] for the velocity profile of a semi-contained, one-dimensional, turbulent jet with a coflowing stream are assumed to apply for the two-dimensional labyrinth seal flow. According to Abramovich [12], the velocity profile for such a flow can be shown to fit the following function when compared to experimental results:

$$v = v_1 + (v_2 - v_1)\left[1 - \left(\frac{y + y_2}{b}\right)^{1.5}\right]^2 \tag{11}$$

where the coordinate y, the mixing thickness b, and the boundary layer thickness y_2 are defined in figure 11. The relationship between the boundary layer thickness and the mixing thickness was found [12] by comparison to experiment to be:

$$y_2/b = 0.584 - 0.134(v_2/v_1) \tag{12}$$

Once the velocity ratio across the dividing streamline, v_2/v_1, is found, equation (12) reduces to a constant. The total free shear stress is found using Prandtl's mixing length hypothesis [13]:

$$\tau_{jt} = \rho \ell^2 \left|\frac{\partial v}{\partial y}\right| \left(\frac{\partial v}{\partial y}\right) \tag{13}$$

where the mixing length, ℓ, for a labyrinth seal, has been determined from the calculations of Rhode [2,3] to be:

$$\ell = 0.275b \tag{14}$$

Table 1 shows the seal geometries calculated by Rhode [2,3]. The mixing length, ℓ, given in equation (14) is the most sensitive factor in this solution. The large magnitude of the mixing length shows the high

turbulence level of the labyrinth flow as compared to similar flows. The typical values given for the mixing lengths of rectangular and round jet flows, in one dimension, are in the range of 0.07 to 0.09. Without the CFD results, one of these values would have to be used and the results of using ℓ/b in the range [0.07,0.09] would have been disappointing.

Jenny et al. [7] used a 2-D CFD code to obtain a correlation for ℓ/b as a function of clearance and tooth geometry. Their relation is shown below for the teeth-on-rotor case:

$$\ell/b = 0.055(1 + 1.03Cr/L + 0.08\sqrt{Re/L}) \tag{15}$$

However, their shear stress relation neglected the recirculating velocity component, U_2. Upon comparison with the data of Rhode [2,3], the mixing length ratio, ℓ/b, was found to be relatively constant when the shear stress is calculated using all velocity components.

Substituting the differentiated version of equation (11) and equation (14) into equation (13) yields an expression for the total free shear stress. At the interface of the two control volumes (y=0), the total free shear stress is:

$$\tau_{fi} \doteq 0.68\rho|(v_2 - v_1)|\left[1 - \left(\frac{y_2}{b}\right)^{1.5}\right]^2\left(\frac{y_2}{b}\right) \tag{16}$$

The circumferential component of the free shear stress is:

$$\tau_f = 0.68\rho\sqrt{(W_2 - W_1)^2 + (U_2 - U_1)^2}\,(W_2 - W_1)\left[1 - \left(\frac{y_2}{b}\right)^{1.5}\right]^2\left(\frac{y_2}{b}\right) \tag{17}$$

The circumferential component of velocity at the interface, W_{oi}, is obtained from equation (11).

$$W_{oi} = W_1 + (W_2 - W_1)\left[1 - \left(\frac{y_2}{b}\right)^{1.5}\right]^2\left(\frac{y_2}{b}\right) \tag{18}$$

Equations (16,17,18) are all valid along the dividing streamline. Since the control volumes are defined geometrically and not by the dividing streamline, the shear stress calculated using the above equations is assumed to be close to that existing along the geometric boundary line. This is a good assumption considering that the angle of the dividing streamline from the horisontal has been found experimentally to be on the order of 6 degrees by several investigators [14,15].

The analysis to this point is incomplete in that the recirculation velocity , U_2, and the relationship between the mixing thickness and the boundary layer thickness, y_2/b, are undefined. The following section presents the jet flow theory used to determine the recirculation velocity, U_2, and subsequently y_2/b. The discussion is rather lengthy, but the final result is relatively simple.

Determination of the recirculation velocity

As mentioned previously, there is no closed-form solution for the flowfield present in a labyrinth seal cavity. The flow is highly three dimensional and completely turbulent. An approximation for the velocity profile can be obtained using the theory for the flow of a two-dimensional, turbulent, isoenergetic, half-infinite jet. Figure 12 shows the model for this theory. The flow is assumed to enter with one velocity component, in the x-direction, and spread into the cavity developing a y-component of velocity. The model does not account for the circumferential velocity component which, is the same order of magnitude as the axial velocity, in a labyrinth seal flowfield. The solution procedure involves solving the infinitessimal form of the x-momentum equation for the dimensionless velocity profile and then solving the integral form of the continuity and momentum equations in order to determine the dimensionless velocity along the dividing streamline.

The following is a summary of the derivation of the equations necessary to determine the dimensionless velocity along the dividing streamline. A complete discussion of this theory can be found in Korst et al. [16] and Scharrer [9]. The following derivation uses the assumption that the curvature in the dividing streamline is small. The infinitessimal form of the x-momentum equation which has been reduced using the continuity equation is:

$$\rho u\frac{\partial u}{\partial x}+\rho v\frac{\partial u}{\partial y}=\frac{\partial}{\partial y}\left(\epsilon\rho\frac{\partial u}{\partial y}\right) \tag{19}$$

where ϵ is the apparent (turbulent) kinematic viscosity and the x and y velocity components, u and v, respectively, are time averaged. Since the flow illustrated in figure 12 is a quasi-one-dimensional jet flow where there is little or no initial vertical velocity component, equation (19) can be linearised using a small perturbation method. The following simplified equation of motion is obtained:

$$U_1\frac{\partial u''}{\partial x}=\epsilon\frac{\partial^2 u''}{\partial y^2} \tag{20}$$

Here the turbulent viscosity is expressed in a modified form of Prandtl's exchange coefficient, ϵ, so that after introducing the dimensionless variables

$$\begin{aligned}\phi&=\frac{U}{U_e}=\frac{1+u''}{U_e}\\ \varsigma&=\frac{y}{\delta}\\ \psi&=\frac{x}{\delta}\\ \epsilon&=\frac{\psi\delta U_1 f(\psi)}{2\sigma^2}\end{aligned} \tag{21}$$

$$\textit{where}\qquad f(\psi)\longrightarrow 1.0\quad as\quad \psi\longrightarrow\infty$$

and by the transformation

$$\xi=\int_0^{\psi}\frac{\psi f(\psi)d\psi}{2\sigma^2}$$

the following formulation of the equation of motion is obtained

$$\frac{\partial\phi}{\partial\xi}=\frac{\partial^2\phi}{\partial\varsigma^2} \tag{22}$$

with the initial conditions

$$\begin{aligned}\phi=\phi(0,\varsigma)&=0 &&\text{for}\quad -\infty<\varsigma<0\\ \phi=\phi(0,\varsigma)&=\phi_o(\varsigma) &&\text{for}\quad 0<\varsigma<1.0\\ \phi=\phi(0,\varsigma)&=1.0 &&\text{for}\quad 1.0<\varsigma<\infty\end{aligned}$$

and boundary conditions

$$\begin{aligned}\phi=\phi(\xi,-\infty)&=0\quad for\quad \xi<0\\ \phi=\phi(\xi,\infty)&=1.0\quad for\quad \xi>0\end{aligned}$$

Here δ is the initial boundary layer thickness shown in figure 12. σ is the jet spreading parameter which has been found experimentally by Korst and Tripp [17] to fit the following equation:

$$\sigma=12.0+2.758M_e\quad for\quad air \tag{23}$$

The solution to equation (22) for the above initial and boundary conditions is:

$$\phi=0.5[1-erf(\eta_p-\eta)]+\frac{1}{\sqrt{\pi}}\int_{\eta-\eta_p}^{\eta}\frac{\phi(\eta-\beta)}{\eta_p}e^{-\beta^2}d\beta \tag{24}$$

where η_p, the position parameter is given by

$$\eta_p=\frac{1}{2\sqrt{\xi}}\quad and\quad \eta=\varsigma\eta_p$$

The error function, erf(x), is defined by

$$erf(x) = \frac{2}{\sqrt{\pi}} \int_0^x e^{-\beta^2} d\beta$$

$$where \quad erf(-x) = -erf(x)$$

Looking at a limiting case of equation (24):

$$as \quad \frac{x}{\delta} \longrightarrow \infty$$

$$then \quad \psi \longrightarrow \infty$$

$$\xi \longrightarrow \infty$$

$$\eta_p = \frac{1}{2\sqrt{\xi}} \longrightarrow 0$$

This limiting case is for either no initial boundary layer, which is a good assumption for labyrinth seals, or fully developed velocity profiles. Since $\eta_p \rightarrow 0$, the variable η is now undefined. Liepman and Laufer [18] have shown that η for this limiting condition is:

$$\eta = \frac{\sigma y}{x} \tag{25}$$

Goertler [19] has shown that the dimensionless velocity ,ϕ, follows directly from equation (24) when $\eta_p \rightarrow 0$:

$$\phi = 0.5(1 + erf(\eta)) \tag{26}$$

Equation (26) is a solution for the dimensionless velocity profile, ϕ, at any dimensionless position,η. The goal of this development is to determine the dimensionless velocity, ϕ_j, along the dividing streamline whose dimensionless position is η_j. The dimensionless dividing streamline position, η_j, can be obtained by solving the integral form of the continuity and x-momentum equations for the system shown in figure 12. Equations (23,25 and 26) are used to obtain the solution to the integral equations which are to be derived next.

Control Volume Analysis

The coordinate systems and definition of the control surface are shown in figure 12. The (x,y) coordinate system is the intrinsic coordinate system while the (X,Y) coordinate system is the reference system.Equations (25) and (26) are approximate relations; exact relationships, if known, would provide for conservation of momentum for the constant pressure mixing region. The reference coordinate system is the coordinate system in which momentum is conserved. The intrinsic coordinate system is located with respect to the reference coordinate system by a control volume analysis utilising the conservation of momentum principle for this constant pressure mixing region. The relationship between the coordinate systems normal to the jet is:

$$y_m(x) = y - Y \quad with \quad y_m(0) = 0.$$

X-Momentum Equation

The steady flow x-momentum equation for the jet flow shown in figure 12, written for the intrinsic coordinate system and expressed in the previously defined dimensioless variables is:

$$\eta_p \int_0^{1.0} \frac{\rho}{\rho_1} \phi_o^2 d\zeta + \eta_R - \eta_p = \int_{-\infty}^{\eta_R} \frac{\rho}{\rho_1} \phi^2 d\eta + \eta_m \tag{27}$$

where distance R is chosen such that:

$$1 - \phi(\eta_R) <<< 1.0$$

For the momentum equation, the lower control surface is located at $-\infty$. This equation contains no surface forces. This is realistic for a labyrinth seal if location R is chosen far from the stator wall. Applying the condition of no initial boundary condition ($\eta_p \rightarrow 0$) equation (27) is:

$$\eta_m = \eta_R - \int_{-\infty}^{\eta_R} \frac{\rho}{\rho_1}\phi^2 d\eta \tag{28}$$

Continuity Equation

The steady flow continuity equation, written for the intrinsic coordinate system and expressed in the previously defined dimensionless variables is:

$$\eta_p \int_0^{1.0} \frac{\rho}{\rho_1}\phi_o d\zeta + \eta_R - \eta_p = \int_{\eta_j}^{\eta_R} \frac{\rho}{\rho_1}\phi d\eta + \eta_m \tag{29}$$

For the continuity equation,the lower control surface is coincident with the jet dividing streamline. Substituting the results of the momentum equation, equation (27), into equation (28) yields:

$$\int_{\eta_j}^{\eta_R} \frac{\rho}{\rho_1}\phi d\eta = \int_0^{1.0} \frac{\rho}{\rho_1}(1-\phi_o) d\zeta + \int_{-\infty}^{\eta_R} \frac{\rho}{\rho_1}\phi^2 d\eta \tag{30}$$

Making the assumption of no initial boundary layer ($\eta_p \rightarrow 0$), equation (30) becomes:

$$\int_{\eta_j}^{\eta_R} \frac{\rho}{\rho_1}\phi d\eta = \int_{-\infty}^{\eta_R} \frac{\rho}{\rho_1}\phi^2 d\eta \tag{31}$$

The density ratio, (ρ/ρ_1), for isoenergetic flow (constant temperature) is given as:

$$\frac{\rho}{\rho_1} = \frac{(1-Ca^2)}{(1-Ca^2\phi^2)} \tag{32}$$

The final form of the continuity equation becomes:

$$\int_{\eta_j}^{\eta_R} \frac{\phi}{(1-Ca^2\phi^2)} d\eta = \int_{-\infty}^{\eta_R} \frac{\phi^2}{(1-Ca^2\phi^2)} d\eta \tag{33}$$

where Ca is the Crocco number. Equation (33) can be numerically integrated for a given Crocco number using the definition for ϕ given in equation (26). The Crocco number is defined as:

$$Ca^2 = \frac{(\gamma-1)M^2}{(2+(\gamma-1)M^2)} \tag{34}$$

The Crocco number is a dimensionless velocity similar to the Mach number. The Crocco number uses the maximum isentropic speed of a gas while the Mach number uses the local speed of sound. The Mach number varies between 0 andoo while the Crocco number has a range of 0 to 1.

The solution to equation (33),the location of the dividing streamline, can be obtained by the following steps:

0) Calculate the Mach number using the seroth-order leakage value.The seroth-order leakage is discussed in the next section.

1) Calculate the Crocco number using equation (34).

2) Substitute equation (26) into equation (33) and integrate the error function. The value of the error function at the limits R and $-\infty$ is 1.0, leaving an equation in η_j only. This is solved for η_j which is the dimensionless location of the dividing streamline.

3) Insert η_j into equation (26) to obtain the dimensionless velocity along the dividing streamline, ϕ_j.

The results of this solution procedure are tabulated in table 2, for air. For air ($\gamma = 1.4$) flowing in a labyrinth seal, the maximum possible Mach number is 1.0. Therefore, the maximum possible Crocco number is 0.408 or $Ca^2 = 0.167$. The range of solutions is:

$$0.61632 < \phi_j < 0.6263$$

Using an average solution of $\phi_j = 0.62$ gives a maximum error of less th n ± 1 percent. The recirculation velocity at the interface is:

$$U_{2j} = 0.62U_1 \tag{35}$$

The only remaining problem is the numerical definition of y_2/b. Looking back, equation (11) and equation (26) both describe the axial velocity profile in the jet flowfield. If the following observation is made

$$\frac{v_2}{v_1} \approx \phi_j$$

then equation (35) can be substituted back into equation (12) yielding the following numerical definition for y_2/b:

$$\frac{y_2}{b} = 0.584 - 0.134\phi_j = 0.5$$

It is interesting to note that Jenny et al. [7] assumed that $y_2/b = 0.5$.

Figure 13 shows a plot of the dimensionless axial velocity profile in the recirculation region for seal A of table 1 as calculated by Rhode [2,3]. This profile is for the center of the recirculation region to the top of the labyrinth tooth. The intersection of the two dashed lines is the location and value of the theoretical recirculation velocity as calculated using equation (35) and the assumption that the dividing streamline makes an angle of 6° with the horisontal. The agreement is excellent. Again, equation (35) was derived using a 2-D theory which neglects the circumferential velocity component. Equation (35) is actually the velocity at the interface of the two control volumes. The velocity components used in the shear stress equations are all average velocity components. To be consistent, the average recirculation velocity must be used. The CFD results show that the velocity distribution is parabolic in nature. Integrating this yields:

$$U_2 = 0.206U_1 \tag{36}$$

Table 2. Tabulated solution to equation (33).

Ca^2	ϕ_j	Ca^2	ϕ_j
0.00000	0.61632	0.68000	0.67553
0.05000	0.61915	0.72000	0.68188
0.10000	0.62211	0.76000	0.68903
0.15000	0.62523	0.80000	0.69724
0.20000	0.62848	0.84000	0.70689
0.24000	0.63129	0.86490	0.713944
0.28000	0.63405	0.88360	0.719944
0.32000	0.63725	0.90250	0.726834
0.36000	0.64047	0.92160	0.734949
0.40000	0.64387	0.94090	0.744883
0.44000	0.64748	0.96040	0.757869
0.48000	0.65132	0.98010	0.777432
0.52000	0.65543	0.992016	0.798766
0.56000	0.65979	0.998001	0.823427
0.60000	0.66462	1.000000	1.000000
0.64000	0.66982		

Reduced Equations

The solution of the governing equations can be simplified by reducing the number of equations by one. This reduction is accomplished by using equation (2) to eliminate mr from the other equations. The continuity equation for control volume I becomes:

$$\frac{\partial \rho A_1}{\partial t} + \frac{\partial \rho W_1 A_1}{Rs_1 \partial \theta} + \dot{m}_{i+1} - \dot{m}_i + \frac{\partial \rho A_2}{\partial t} + \frac{\partial W_2 A_2}{Rs_2 \partial \theta} = 0 \tag{37}$$

If equation (37) times the circumferential velocity, W_1 is now subtracted from equation (3), the following reduced form of the momentum equation for control volume I is obtained:

$$\rho A_1 \frac{\partial W_1}{\partial t} + \frac{\rho W_1 A_1}{Rs_1}\frac{\partial W_1}{\partial \theta} + \left(\frac{\partial \rho A_2}{\partial t} + \frac{\partial \rho W_2 A_2}{Rs_2 \partial \theta}\right)(W_{oi} - W_{1i}) + \dot{m}_i(W_{i1} - W_{1i-1}) = -\frac{A_1}{Rs_1}\frac{\partial P_i}{\partial \theta} + \tau_{ji} L_i - \tau_{oi} a s_i L_i \tag{38}$$

Similarly, if equation (2) times the circumferential velocity, W_2, is subtracted from equation (4), the reduced momentum equation for control volume II is obtained.

$$\rho A_2 \frac{\partial W_2}{\partial t} + \frac{\rho W_2 A_2}{Rs_2}\frac{\partial W_2}{\partial \theta} + \left(\frac{\partial \rho A_2}{\partial t} + \frac{\partial \rho W_2 A_2}{Rs_2 \partial \theta}\right)(W_{2i} - W_{oi}) = -\frac{A_2}{Rs_2}\frac{\partial P_i}{\partial \theta} + \tau_{ji} L_i - \tau_{ri} a r_i L_i \tag{39}$$

The number of variable is reduced by using the ideal gas law to eliminate the density terms.

$$P_i = \rho_i R T \tag{40}$$

Leakage Equation

To account for the leakage mass flow rate in the continuity and momentum equations, the following model was chosen.

$$\dot{m}_i = \mu_{1i}\mu_{2i} H_i \sqrt{\frac{P_{i-1}^2 - P_i^2}{RT}} \tag{41}$$

where the kinetic energy carryover coefficient, μ_2 is defined by Vermes [20] for straight through seals as:

$$\mu_2 = \frac{1}{(1-\alpha)^{\frac{1}{3}}} \tag{42}$$

$$where \qquad \alpha = \frac{8.52}{\left(\frac{(L_i - T_{Pi})}{Cr_i} + 7.23\right)}$$

and is unity, by definition, for the first tooth of any seal and all the teeth in interlocking and combination groove seals. This definition of the carryover coefficient is a local coefficient which can be perturbed in the clearance. The previous analyses by Childs and Scharrer [6] and Jenny et al [7] used a global definition which could not be perturbed.

The flow coefficient is defined by Chaplygin [21] as:

$$\mu_{1i} = \frac{\pi}{\pi + 2 - 5s_i + 2s_i^2} \qquad where \qquad s_i = \left(\frac{P_{i-1}}{P_i}\right)^{\frac{\gamma-1}{\gamma}} - 1 \tag{43}$$

This flow coefficient yields a different value for each tooth along the seal as has been shown to be the case by Egli [22]. For choked flow, Fliegner's formula [23] will be used for the last seal strip. It is of the form:

$$\dot{m}_{NC} = \frac{0.510\mu_2}{\sqrt{RT}} P_{NC} H_{NC} \tag{44}$$

Perturbation Analysis

For cavity i, the continuity equation (37), momentum equations (38,39) and leakage equation (40) are the governing equations for the variables $W_{1i}, W_{2i}, P_i, \dot{m}_i$. A perturbation analysis of these equations is to be developed with the eccentricity ratio, $\epsilon = e_o/Cr_i$ selected to be the perturbation parameter. The governing equations are expanded in the perturbation variables:

$$P_i = P_{oi} + \epsilon P_{1i} \qquad H_i = Cr_i + \epsilon H_1$$
$$W_{1i} = W_{1oi} + \epsilon W_{11i} \qquad A_i = A_o + \epsilon L_i H_1$$
$$W_{2i} = W_{2oi} + \epsilon W_{21i}$$

where $\epsilon = e_o/Cr_i$ is the eccentricity ratio. The seroth-order equations define the leakage mass flow rate and the circumferential velocity distribution for a centered position. The first-order equations define the perturbations in pressure and circumferential velocity due to radial position perturbation of the rotor. Strictly speaking, results of a first order analysis are only valid for small motion about a centered position.

Zeroth-Order Solution

The seroth-order leakage equation is

$$\dot{m}_{i+1} = \dot{m}_i + \dot{m}_o \tag{45}$$

and is used to determine both the leakage-rate, $\dot{m}_o$ and pressure distribution for a centered position. The leakage-rate and cavity pressures are determined iteratively, in the following manner. First, determine whether the flow is choked or not by assuming that the Mach number at the last tooth is one. Then, knowing the pressure ratio for flow at sonic conditions, the pressure in the last cavity is found. The mass flow can be calculated using equation (44). Working backwards towards the first tooth, the rest of the pressures can be found using equation (41). The final pressure calculation will result in the reservoir pressure necessary to produce the sonic condition at the last tooth. If the actual reservoir pressure is less than this value, then the flow is unchoked. Otherwise, it is choked. If the flow is choked, a similar procedure is followed, but now the pressure in the last cavity is guessed and a mass flow rate calculated using equation (44). The remaining pressures are calculated using equation (41). This is repeated until the calculated reservoir pressure equals the actual reservoir pressure. If the flow is unchoked, the pressure in the first cavity is guessed and a mass flow rate calculated using equation (41). The remaining pressures are calculated with the same equation. This procedure is repeated until the calculated sump pressure equals the actual sump pressure.

The seroth-order circumferential-momentum equations are

$$\dot{m}_o(W_{1oi} - W_{1oi-1}) = (\tau_{joi} - \tau_{ooi} as_i)L_i \tag{46}$$

$$\tau_{joi} L_i = \tau_{roi} ar_i L_i \tag{47}$$

From calculated pressures, the densities can be calculated at each cavity from equation (46), and the only unknowns remaining in equations (46) and (47) are the circumferential velocities W_{1oi} and W_{2oi}. Given an inlet tangential velocity, a Newton-root-finding approach can be used to solve equations (46) and (47) for the i-th velocities, one cavity at a time. This is done starting at the first cavity and working downstream.

First-Order Solution

The governing first-order equations (48,49,50), define the pressure and velocity fluctuations resulting from the seal clearance function. The continuity and momentum equations follow in order:

$$\begin{aligned} &G_{1i}\frac{\partial P_{1i}}{\partial t} + G_{2i}\frac{\partial P_{1i}}{\partial \theta} + G_{3i}\frac{\partial W_{11i}}{\partial \theta} + G_{4i}\frac{\partial W_{21i}}{\partial \theta} + G_{5i}P_{1i} \\ &+ G_{6i}P_{1i-1} + G_{7i}P_{1i+1} = -G_{8i}H_{1i} - G_{9i}\frac{\partial H_{1i}}{\partial t} - G_{10i}\frac{\partial H_{1i}}{\partial \theta} \end{aligned} \tag{48}$$

$$\begin{aligned} &X_{1i}\frac{\partial W_{11i}}{\partial t} + \frac{X_{1i}W_{1oi}}{Rs_1}\frac{\partial W_{11i}}{\partial \theta} + \left[X_{2i} + \frac{X_{3i}W_{2oi}}{Rs_2}\right]\frac{\partial P_{1i}}{\partial \theta} + X_{3i}\frac{\partial P_{1i}}{\partial t} \\ &+ \frac{X_{3i}P_{oi}}{Rs_2}\frac{\partial W_{21i}}{\partial \theta} + X_{4i}P_{1i} + X_{5i}P_{1i-1} + X_{6i}W_{11i} + X_{7i}W_{21i} \\ &- \dot{m}_{oi}W_{11i-1} = X_{8i}H_{1i} \end{aligned} \tag{49}$$

$$\begin{aligned} &Y_{1i}\frac{\partial W_{21i}}{\partial t} + \left[\frac{Y_{2i}P_{oi}}{Rs_2} + \frac{Y_{1i}W_{2oi}}{Rs_2}\right]\frac{\partial W_{21i}}{\partial \theta} + \left[Y_{3i} + \frac{Y_{2i}W_{2oi}}{Rs_2}\right]\frac{\partial P_{1i}}{\partial \theta} \\ &Y_{2i}\frac{\partial P_{1i}}{\partial t} + Y_{4i}P_{1i} + Y_{5i}W_{21i} + Y_{6i}P_{1i-1} + Y_{7i}W_{11i} = Y_{8i}H_{1i} \end{aligned} \tag{50}$$

where the X's, Y's and G's are defined in Appendix B. These perturbation equations are very different from those of Jenny et al. [7] because their analysis neglects pressure perturbations in the leakage and shear stress equations, and assumes that the density is constant.

If the shaft center moves in an elliptical orbit, then the seal clearance function can be defined as:

$$\begin{aligned}\epsilon\bar{H}_1 &= -a\cos\omega t\cos\theta - b\sin\omega t\sin\theta \\ &= -\frac{a}{2}[\cos(\theta-\omega t)+\cos(\theta+\omega t)] - \frac{b}{2}[\cos(\theta-\omega t)-\cos(\theta+\omega t)]\end{aligned} \tag{51}$$

The pressure and velocity fluctuations can now be stated in the associated solution format:

$$P_{1i} = P^+_{ci}\cos(\theta+\omega t) + P^+_{si}\sin(\theta+\omega t) + P^-_{ci}\cos(\theta-\omega t) + P^-_{si}\sin(\theta-\omega t) \tag{52}$$

$$W_{11i} = W^+_{1ci}\cos(\theta+\omega t) + W^+_{1si}\sin(\theta+\omega t) + W^-_{1ci}\cos(\theta-\omega t) + W^-_{1si}\sin(\theta-\omega t) \tag{53}$$

$$W_{21i} = W^+_{2ci}\cos(\theta+\omega t) + W^+_{2si}\sin(\theta+\omega t) + W^-_{2ci}\cos(\theta-\omega t) + W^-_{2si}\sin(\theta-\omega t) \tag{54}$$

Substituting equations (51), (52), (53) and (54) into equations (48), (49) and (50) and grouping like terms of sines and cosines (as shown in Appendix C) eliminates the time and theta dependency and yields twelve linear algebraic equations per cavity. The resulting system of equations for the i-th cavity can be stated:

$$[A_{i-1}](X_{i-1}) + [A_i](X_i) + [A_{i+1}](X_{i+1}) = \frac{a}{\epsilon}(B_i) + \frac{b}{\epsilon}(C_i) \tag{55}$$

where

$$(X_{i-1}) = (P^+_{si-1}, P^+_{ci-1}, P^-_{si-1}, P^-_{ci-1}, W^+_{1si-1}, W^+_{1ci-1}, W^-_{1si-1}, W^-_{1ci-1}, W^+_{2si-1}, W^+_{2ci-1}, W^-_{2si-1}, W^-_{2ci-1})^T$$

$$(X_i) = (P^+_{si}, P^+_{ci}, P^-_{si}, P^-_{ci}, W^+_{1si}, W^+_{1ci}, W^-_{1si}, W^-_{1ci}, W^+_{2si}, W^+_{2ci}, W^-_{2si}, W^-_{2ci})^T$$

$$(X_{i+1}) = (P^+_{si+1}, P^+_{ci+1}, P^-_{si+1}, P^-_{ci+1}, W^+_{1si+1}, W^+_{1ci+1}, W^-_{1si+1}, W^-_{1ci+1}, W^+_{2si+1}, W^+_{2ci+1}, W^-_{2si+1}, W^-_{2ci+1})^T$$

The A matrices and column vectors B and C are given in Appendix C. To use equation (55) for the entire solution, a system matrix can be formed which is block tridiagonal in the A matrices. The size of this resultant matrix is (12NC X 12NC) since pressure and velocity perturbations at the inlet and the exit are assumed to be zero. This system is easily solved by various linear equation algorithms, and yields a solution of the form:

$$\begin{aligned}P^+_{si} &= \frac{a}{\epsilon}F^+_{asi} + \frac{b}{\epsilon}F^+_{bsi} \\ P^-_{si} &= \frac{a}{\epsilon}F^-_{asi} + \frac{b}{\epsilon}F^-_{bsi} \\ P^+_{ci} &= \frac{a}{\epsilon}F^+_{aci} + \frac{b}{\epsilon}F^+_{bci} \\ P^-_{ci} &= \frac{a}{\epsilon}F^-_{aci} + \frac{b}{\epsilon}F^-_{bci}\end{aligned} \tag{56}$$

DETERMINATION OF DYNAMIC COEFFICIENT

The force-motion equations for a labyrinth seal are assumed to be of the form:

$$-\begin{Bmatrix}F_x\\F_y\end{Bmatrix} = \begin{bmatrix}K & k\\-k & K\end{bmatrix}\begin{Bmatrix}X\\Y\end{Bmatrix} + \begin{bmatrix}C & c\\-c & C\end{bmatrix}\begin{Bmatrix}\dot{X}\\\dot{Y}\end{Bmatrix} \tag{57}$$

The solution of equation (57) for the stiffness and damping coefficients is the objective of the current analysis. The solution procedure used for this analysis is the same one used by Childs and Scharrer [6]. The desired solution for the stiffness and damping coefficients is:

$$K = \pi R s \sum_{i=1}^{NC} (F_{aci}^{+} + F_{aci}^{-}) L_i$$

$$k = \pi R s \sum_{i=1}^{NC} (F_{bci}^{+} + F_{bci}^{-}) L_i$$

$$C = -\frac{\pi R s}{\omega} \sum_{i=1}^{NC} (F_{aci}^{+} + F_{aci}^{-}) L_i \qquad (58)$$

$$c = \frac{\pi R s}{\omega} \sum_{i=1}^{NC} (F_{bci}^{+} + F_{bci}^{-}) L_i$$

SOLUTION PROCEDURE SUMMARY

In review, the solution procedure uses the following sequential steps:

a) Determination of whether the flow is choked or not using equations (41) and (44).

b) The steady-state pressure distribution and leakage are found using equation (41) and/or (44).

c) The steady-state circumferential velocity distribution is determined using equations (46) and (47).

d) A system equation is formed for the first-order perturbation variables and solved using the cavity equation (55).

e) Results of this first-order perturbation solution, as defined in equations (56), are inserted into equation (58) to defined the rotordynamic coefficients.

CONCLUSIONS

This paper has presented a new two-control-volume analysis for the rotordynamic coefficients of labyrinth gas seals which, for the first time, accounts for the recirculation velocity in the seal cavity. The analysis was developed in conjunction with a 2-D CFD model which was used to verify the shear stress and jet flow models used. A comparison between the CFD results and the results from the "bulk flow" model of this paper showed the following:

1) The new two-control-volume model accurately predicts the stator wall shear stress for a teeth-on-rotor labyrinth seal cavity.

2) The new model predicts the cavity wall shear stress within 25 percent of the CFD results for a teeth-on-rotor labyrinth seal.

3) The 2-D jet flow theory used in the new model accurately predicts the magnitude of the recirculation velocity along the dividing streamline.

4) The CFD results show that the mixing length parameter, ℓ, used in the free shear stress equation is relatively constant and need not be considered a function of cavity geometry as was assumed by Jenny et al. [7].

The final test of the model, a comparison between experimental results for stiffness and damping coefficients and the predictions of this model, will be carried out in Part 2 of this paper.

NOMENCLATURE

A Cross-sectional area of control volume (L^2); illustrated in figure (6)
B Height of labyrinth seal strip (L); illustratedin figure (5)
C Direct damping coefficient (Ft/L)
Cr Nominal radial clearance (L); illustrated in figure (5)
D_h Hydraulic diameter of cavity (L); introduced in equation (6)
H Local radial clearance (L)
K Direct stiffness coefficient (F/L)
L Pitch of seal strips (L); illustrated in figure (5)
NT Number of seal strips
NC=NT-1 Number of cavities
P Pressure (F/L^2)
R Gas constant (L^2/Tt^2)
Rs Radius of control volume (L); illustrated in figure (5)
$Rs\omega$ Surface velocity of rotor (L/t)
T Temperature (T)
Tp Tooth tip width (L); illustrated in figure (5)
U Average axial velocity for control volume (L/t); in figure (2)
W Average circumferential velocity for control volume (L/t); illustrated in figure (2)
W_o Average circumferential velocity in the interface between control volumes I and II (L/t); introduced in equation (18)
a,b Radial seal displacement components due to elliptical whirl (L); introduced in equation (51)
ar, as Dimensionless length upon which shear stress acts; introduced in equation (3) and (4)
c Cross coupled damping coefficient (Ft/L); in equation (57)
e_o Displacement of the seal rotor from centered position (L)
k Cross coupled stiffness coefficient (F/L); in equation (57)
$\dot{m}$ Leakage mass flow rate per circumferential length (M/Lt)
mr, nr, ms, ns Coefficients for friction factor; in equation (3)
t Time (t)
v Total velocity (L/t); introduced in equation (11)
ω Shaft angular velocity (1/t)
ρ Density of fluid (M/L^3)
ν Kinematic viscosity (L^2/t)
$\epsilon = e_o/Cr$ Eccentricity ratio
ϵ Turbulent viscosity (Ft/L^2); introduced in equation (19)
γ Ratio of specific heats

Subscripts

o Zeroth-order component
1 First-order component, control volume I value
2 Control volume II value
i i-th chamber value
j Value along the dividing streamline
x X-direction
y Y-direction
r Reservoir value
s Sump value

REFERENCES

1. Iwatsubo, T., Matooka, N., and Kawai, R., "Flow Induced Force and Flow Pattern of Labyrinth Seal," NASA CP 225Q Proceedings of a workshop at Texas A&M University 10-12 May 1982, Entitled Rotordynamic Instability Problems in High Performance Turbomachinery, pp. 205-222.

2. Rhode, D., "Simulation of Subsonic Flow Through a Generic Labyrinth Seal Cavity," ASME Paper No. 85-GT-76.

3. Rhode, D., Private correspondence, Texas A&M University, 1985.

4. Stoff, H., "Incompressible Flow in a Labyrinth Seal," *Journal of Fluid Mechanics* , Vol. 100, part 4, pp. 817-829, 1980.

5. Iwatsubo, T., "Evaluation of Instability Forces of Labyrinth Seals in Turbines or Compressors," NASA CP 2133 Proceedings of a workshop at Texas A&M University 12-14 May 1980, Entitled Rotordynamic Instability Problems in High Performance Turbomachinery, pp. 139-167.

6. Childs, D.W., and Scharrer, J.K., "An Iwatsubo Based Solution for Labyrinth Seals: A Comparison to Experimental Results," *ASME Journal of Engineering for Gas Turbines and Power,* April 1986, Vol. 108, pp. 325-331

7. Jenny, R.J., Wyssmann, H.P., Pham, T.C., "Prediction of Stiffness and Damping Coefficients for Centrifugal Compressor Labyrinth Seals," ASME 84-GT-86. Presented at the 29th International Gas Turbine Conference and Exhibit, Amsterdam, The Netherlands, June 4-7, 1984.

8. Childs, D.W. and Scharrer, J.K., "Experimental Rotordynamic Coefficient Results for Teeth-On-Rotor and Teeth-On-Stator Labyrinth Gas Seals," ASME Paper No. 86-GT-12.

9. Scharrer, J.K., "A Comparison of Experimental and Theoretical Results for Labyrinth Gas Seals," PhD Dissertation, Texas A&M University, May 1987.

10. Blasius, H., "Forschungoarb," Ing.-Wes., No 131, 1913.

11. Yamada, Y., Trans. Japan Soc. Mechanical Engineers, Vol. 27, No. 180, 1961, pp. 1267.

12. Abramovich, G.N., *The Theory of Turbulent Jets,* MIT Press, 1963.

13. Schlichting, H., *Boundary Layer Theory,* McGraw-Hill, pp. 579, 1979.

14. Jerie, J., "Flow Through Straight-Through Labyrinth Seals," Proceedings of the 7th International Congress on Applied Mechanics, Vol.2, pp. 70-82, 1948.

15. Komotori, K. and Mori, H., "Leakage Characteristics of Labyrinth Seals," Fifth International Conference on Fluid Sealing, 1971, Paper E4, pp. 45-63.

16. Korst, H.H., Page, R.H., and Childs, M.E., Univ. of Illinois Eng. Exp. Report ME TN 392-1, April 1954.

17. Korst, H.H. and Tripp, W., "The Pressure on a Blunt Trailing Edge Separating Two-Supersonic Two-Dimensional Airstreams of Different Mach Number and Stagnation Pressure But Identical Stagnation Temperature," Proceedings of the 5th Midwestern Conference on Fluid Mechanics, University of Michigan Press, pp. 187-200, 1957.

18. Liepman, H.W. and Laufer, J., NACA TN1257, 1947.

19. Goertler, H., Z. Angew Math. Mech., 22, pp. 244-254, 1942.

20. Vermes, G., "A Fluid Mechanics Approach to the Labyrinth Seal Leakage Problem," *ASME Journal of Engineering for Power,* Vol. 83 No. 2, April 1961, pp. 161-169.

21. Gurevich, M.I., *The Theory Of Jets In An Ideal Fluid,* Pergamon Press, 1966, pp. 319-323.

22. Egli, A., "The Leakage of Steam Through Labyrinth Glands," Trans. ASME, Vol. 57, 1935, pp. 115-122.

23. John, J.E.A, *Gas Dynamics,* Wylie, 1979.

24. Nelson, C.C. and Nguyen, D.T., "Comparison of Hirs' Equation with Moody's Equation for Determining Rotordynamic Coefficients of Annular Pressure Seals," ASME Paper No. 86-TRIB-19, also accepted for the *ASME Journal of Tribology.*

25. Wyssmann, H.R., "Theory and Measurements of Labyrinth Seal Coefficients for Rotor Stability of Turbocompressors," Proceedings of a workshop at Texas A&M University 2-4 June 1986, Entitled Rotordynamic Instability Problems in High Performance Turbomachinery (in press).

APPENDIX A: GOVERNING EQUATIONS FOR TEETH-ON-STATOR SEAL

Reduced Equations

The main difference between the teeth-on-stator equations and the teeth-on-rotor equations occurs in the momentum equations. The shear stresses acting on control volume I are now the rotor shear stress, τ_r, and the free shear stress, τ_j. Similarly, the shear stresses acting on control volume II are now the stator shear stress, τ_s, and the free shear stress, τ_j. These differences are evident in the reduced form of the continuity and circumferential momentum equations given below:

Continuity I

$$\frac{\partial \rho A_1}{\partial t} + \frac{\partial \rho W_1 A_1}{Rs_1 \partial \theta} + \dot{m}_{i+1} - \dot{m}_i + \frac{\partial \rho A_2}{\partial t} + \frac{\partial \rho W_2 A_2}{Rs_2 \partial \theta} = 0 \tag{A1}$$

Momentum I

$$\begin{aligned} &\rho A_1 \frac{\partial W_1}{\partial t} + \frac{\rho W_1 A_1}{Rs_1} \frac{\partial W_1}{\partial \theta} + \left(\frac{\partial \rho A_2}{\partial t} + \frac{\partial \rho W_2 A_2}{Rs_2 \partial \theta} \right) (W_{\alpha i} - W_{1i}) \\ &+ \dot{m}_i (W_{i1} - W_{1i-1}) = -\frac{A_1}{Rs_1} \frac{\partial P_i}{\partial \theta} + \tau_{ji} L_i - \tau_{ri} ar_i L_i \end{aligned} \tag{A2}$$

Momentum II

$$\begin{aligned} &\rho A_2 \frac{\partial W_2}{\partial t} + \frac{\rho W_2 A_2}{Rs_2} \frac{\partial W_2}{\partial \theta} + \left(\frac{\partial \rho A_2}{\partial t} + \frac{\partial \rho W_2 A_2}{Rs_2 \partial \theta} \right) (W_{2i} - W_{\alpha i}) \\ &= -\frac{A_2}{Rs_2} \frac{\partial P_i}{\partial \theta} - \tau_{ji} L_i - \tau_{si} as_i L_i \end{aligned} \tag{A3}$$

where as and ar are defined as:

$$as_i = (2B_i + L_i)/L_i \qquad ar_i = 1.0$$

The rotor shear stress in the circumferential direction is now defined using the smaller hydraulic diameter and the velocity components of control volume I.

$$\tau_r = \frac{1}{2} \rho \sqrt{(Rs_1 \omega - W_1)^2 + U_1^2} \, (Rs_1 \omega - W_1) \, nr \left(\frac{\sqrt{(Rs_1 \omega - W_1)^2 + U_1^2} D_{h1i}}{\nu} \right)^{mr} \tag{A4}$$

where D_{h1i} is the hydraulic diameter of C.V. I, defined by:

$$D_{h1i} = 2Cr_i L_i / (Cr_i L_i) \tag{A5}$$

Similarly, the stator shear stress in the circumferential direction is now defined using the larger hydraulic diameter and the velocity components of control volume II.

$$\tau_s = \frac{1}{2} \rho \sqrt{W_2^2 + U_2^2} \, W_2 ns \left(\frac{\sqrt{W_2^2 + U_2^2} D_{h2i}}{\nu} \right)^{ms} \tag{A6}$$

where D_{h2i} is the hydraulic diameter of C.V. II, defined by:

$$D_{h2i} = 2B_i L_i / (B_i L_i) \tag{A7}$$

The definition of the free shear stress remains the same. However, since CFD results were only available for the teeth-on-rotor configuration, the sensitive mixing length ratio, ℓ/b, may change for a teeth-on-stator seal.

Zeroth-Order Equations
Continuity

$$\dot{m}_{oi+1} = \dot{m}_{oi} \tag{A8}$$

Momentum I and II

$$\dot{m}_o(W_{1oi} - W_{1oi-1}) = (\tau_{joi} - \tau_{soi} as_i)L_i \tag{A9}$$

$$\tau_{joi} L_i = \tau_{roi} ar_i L_i \tag{A10}$$

First-Order Equations
The first-order equations remain exactly the same as before. Since changes were made in the locations and definitions of the rotor and stator shear stress terms, the following changes in the coefficients of the first-order equations are necessary:

$$\begin{aligned}
X_4 =& -\frac{\dot{m}_o(W_{1i} - W_{1i-1})P_{oi}}{P_{oi-1}^2 - P_{oi}^2} + \frac{\dot{m}_o(W_{1i} - W_{i1-1})(\gamma - 1)}{\pi\gamma P_{oi}}\mu_{1i}(4S_{1i} - 5)(S_{1i} + 1) - \frac{\tau_{ji} L_i}{P_{oi}} \\
& - \left[\frac{\tau_{ri}(1 + mr)U_{1i} L_i ar_i}{(Rs_1\omega - W_{1i})^2 + U_{1i}^2} + \frac{\tau_{ji}(U_{2i} - U_{1i})L_i(\phi - 1)}{(W_{2i} - W_{1i})^2 + (U_{2i} - U_{1i})^2}\right] \\
& \times \left[\frac{-U_{1i}}{P_{oi}} - \frac{U_{1i} P_{oi}}{P_{oi-1}^2 - P_{oi}^2} + \frac{\mu_{1i} U_{1i}(4S_{1i} - 5)(\gamma - 1)}{\pi\gamma P_{oi}}(S_{1i} + 1)\right] - \frac{\tau_{ri} ar_i(1 + mr)L_i}{P_{oi}} \\
X_5 =& \frac{\dot{m}_o(W_{1i} - W_{1i-1})P_{oi-1}}{P_{oi-1}^2 - P_{oi}^2} - \frac{\dot{m}_o(W_{1i} - W_{1i-1})(\gamma - 1)}{\pi\gamma P_{oi}}\mu_{1i}(4S_{1i} - 5)\left(\frac{P_{oi-1}}{P_{oi}}\right)^{\frac{\gamma-1}{\gamma}} \\
& - \left[\frac{\tau_{ri} ar_i L_i(1 + mr)U_{1i}}{(Rs_1\omega - W_{1i})^2 + U_{1i}^2} + \frac{\tau_{ji}(U_{2i} - U_{1i})L_i(\phi - 1)}{(W_{2i} - W_{1i})^2 + (U_{2i} - U_{1i})^2}\right] \\
& \times \left[\frac{U_{1i} P_{oi-1}}{P_{oi-1}^2 - P_{oi}^2} - \frac{\mu_{1i} U_{1i}(4S_{1i} - 5)(\gamma - 1)}{\pi\gamma P_{oi}}\left(\frac{P_{oi-1}}{P_{oi}}\right)^{\frac{\gamma-1}{\gamma}}\right] \\
X_6 =& \dot{m}_o + \frac{\tau_{ri} ar_i L_i}{Rs_1\omega - W_{1i}} + \frac{\tau_{ri} ar_i L_i(1 + mr)(Rs_1\omega - W_{1i})}{(Rs_1\omega - W_{1i})^2 + U_{1i}^2} + \frac{\tau_{ji} L_i}{W_{2i} - W_{1i}} + \frac{\tau_{ji}(W_{2i} - W_{1i})L_i}{(W_{2i} - W_{1i})^2 + (U_{2i} - U_{1i})^2} \\
X_8 =& \frac{\dot{m}_o(W_{1i} - W_{1i-1})}{Cr_i}\left[1 + \frac{(L_i - Tp_i)}{17.04 Cr_i}\left(\frac{\mu_{2i}^2 - 1}{\mu_{2i}}\right)^2\right] - \frac{\tau_{ri} ar_i L_i mr D_{h1i}}{2Cr_i^2} \\
Y_4 =& \left[\frac{-U_{1i}}{P_{oi}} - \frac{U_{1i} P_{oi}}{P_{oi-1}^2 - P_{oi}^2} + \frac{\mu_{1i} U_{1i}(4S_{1i} - 5)(\gamma - 1)}{\pi\gamma P_{oi}}(S_{1i} + 1)\right] \\
& \times \left[\frac{\tau_{oi}(1 + ms)\phi U_{2i} L_i as_i}{W_{2i}^2 + U_{2i}^2} + \frac{\tau_{ji}(U_{2i} - U_{1i})L_i(\phi - 1)}{(W_{2i} - W_{1i})^2 + (U_{2i} - U_{1i})^2}\right] + \frac{\tau_{ji} L_i}{P_{oi}} - \frac{\tau_{oi}(1 + ms)as_i L_i}{P_{oi}} \\
Y_5 =& \frac{\tau_{oi} as_i L_i}{W_{2i}} + \frac{\tau_{oi}(1 + ms)W_{2i} as_i L_i}{W_{2i}^2 + U_{2i}^2} + \frac{\tau_{ji} L_i}{W_{2i} - W_{1i}} + \frac{\tau_{ji} L_i(W_{2i} - W_{1i})}{(W_{2i} - W_{1i})^2 + (U_{2i} - U_{1i})^2} \\
Y_6 =& \left[\frac{U_{1i} P_{oi-1}}{P_{oi-1}^2 - P_{oi}^2} - \frac{\mu_{1i} U_{1i}(4S_{1i} - 5)(\gamma - 1)}{\pi\gamma P_{oi}}\left(\frac{P_{oi-1}}{P_{oi}}\right)^{\frac{\gamma-1}{\gamma}}\right] \\
& \times \left[\frac{\tau_{oi}(1 + ms)\phi U_{2i} L_i as_i}{W_{2i}^2 + U_{2i}^2} + \frac{\tau_{ji}(U_{2i} - U_{1i})L_i(\phi - 1)}{(W_{2i} - W_{1i})^2 + (U_{2i} - U_{1i})^2}\right]
\end{aligned}$$

APPENDIX B: DEFINITION OF FIRST-ORDER COEFFICIENTS

$$G_1 = \frac{L_i(Cr_i + B_i)}{RT}; \quad G_2 = \frac{Cr_i W_{1i} L_i}{RTRs_1} + \frac{B_i L_i W_{2i}}{RTRs_2}; \quad G_3 = \frac{P_{oi} L_i Cr_i}{RTRs_1}; \quad G_4 = \frac{P_{oi} B_i L_i}{RTRs_2}$$

$$G_5 = \frac{\dot{m}_o P_{oi}}{P_{oi-1}^2 - P_{oi}^2} + \frac{\dot{m}_o \mu_{1i+1}(\gamma - 1)}{\pi\gamma P_{oi+1}}(5 - 4S_{1i+1}) \left(\frac{P_{oi}}{P_{oi+1}}\right)^{\frac{-1}{\gamma}}$$
$$+ \frac{\dot{m}_o \mu_{1i}(\gamma - 1)}{\pi\gamma P_{oi}}(5 - 4S_{1i})(S_{1i} + 1) + \frac{\dot{m}_o P_{oi}}{P_{oi}^2 - P_{oi+1}^2}$$

$$G_6 = \frac{-\dot{m}_o P_{oi-1}}{P_{oi-1}^2 - P_{oi}^2} - \frac{\dot{m}_o \mu_{1i}(\gamma - 1)}{\pi\gamma P_{oi}}(5 - 4S_{1i}) \left(\frac{P_{oi-1}}{P_{oi}}\right)^{\frac{-1}{\gamma}}; \quad G_9 = \frac{P_{oi} L_i}{RT}$$

$$G_7 = \frac{-\dot{m}_o P_{oi+1}}{P_{oi}^2 - P_{oi+1}^2} - \frac{\dot{m}_o \mu_{1i+1}(\gamma - 1)}{\pi\gamma P_{oi+1}}(5 - 4S_{1i+1})(S_{1i+1} + 1); \quad G_{10} = \frac{P_{oi} W_{1i} L_i}{RTRs_1}$$

$$G_8 = \frac{\dot{m}_o(Cr_i - Cr_{i+1})}{Cr_i Cr_{i+1}} - \frac{\dot{m}_o(L_i - Tp_i)}{17.04Cr_i^2}\left(\frac{\mu_{2i}^2 - 1}{\mu_{2i}}\right)^2 + \frac{\dot{m}_o(L_{i+1} - Tp_{i+1})}{17.04Cr_{i+1}^2}\left(\frac{\mu_{2i+1}^2 - 1}{\mu_{2i+1}}\right)^2$$

$$X_1 = \frac{P_{oi} Cr_i L_i}{RT}; \quad X_2 = \frac{Cr_i L_i}{Rs_1}; \quad X_3 = \frac{B_i L_i}{RT}(W_{oi} - W_{1i})$$

$$X_4 = -\frac{\dot{m}_o(W_{1i} - W_{1i-1})P_{oi}}{P_{oi-1}^2 - P_{oi}^2} + \frac{\dot{m}_o(W_{1i} - W_{i1-1})(\gamma - 1)}{\pi\gamma P_{oi}}\mu_{1i}(4S_{1i} - 5)(S_{1i} + 1) - \frac{\tau_{ji} L_i}{P_{oi}}$$
$$+ \left[\frac{\tau_{oi}(1 + ms)U_{1i} L_i as_i}{W_{1i}^2 + U_{1i}^2} - \frac{\tau_{ji}(U_{2i} - U_{1i})L_i(\phi - 1)}{(W_{2i} - W_{1i})^2 + (U_{2i} - U_{1i})^2}\right]$$
$$\times \left[\frac{-U_{1i}}{P_{oi}} - \frac{U_{1i} P_{oi}}{P_{oi-1}^2 - P_{oi}^2} + \frac{\mu_{1i} U_{1i}(4S_{1i} - 5)(\gamma - 1)}{\pi\gamma P_{oi}}(S_{1i} + 1)\right] + \frac{\tau_{oi} as_i(1 + ms)L_i}{P_{oi}}$$

$$X_5 = \frac{\dot{m}_o(W_{1i} - W_{1i-1})P_{oi-1}}{P_{oi-1}^2 - P_{oi}^2} - \frac{\dot{m}_o(W_{1i} - W_{1i-1})(\gamma - 1)}{\pi\gamma P_{oi}}\mu_{1i}(4S_{1i} - 5)\left(\frac{P_{c\,i-1}}{P_{oi}}\right)^{\frac{-1}{\gamma}}$$
$$+ \left[\frac{\tau_{oi} as_i L_i(1 + ms)U_{1i}}{W_{1i}^2 + U_{1i}^2} - \frac{\tau_{ji}(U_{2i} - U_{1i})L_i(\phi - 1)}{(W_{2i} - W_{1i})^2 + (U_{2i} - U_{1i})^2}\right]$$
$$\times \left[\frac{U_{1i} P_{oi-1}}{P_{oi-1}^2 - P_{oi}^2} - \frac{\mu_{1i} U_{1i}(4S_{1i} - 5)(\gamma - 1)}{\pi\gamma P_{oi}}\left(\frac{P_{oi-1}}{P_{oi}}\right)^{\frac{-1}{\gamma}}\right]$$

$$X_6 = \dot{m}_o + \frac{\tau_{oi} as_i L_i}{W_{1i}} + \frac{\tau_{oi} as_i L_i(1 + ms)W_{1i}}{W_{1i}^2 + U_{1i}^2} + \frac{\tau_{ji} L_i}{W_{2i} - W_{1i}} + \frac{\tau_{ji}(W_{2i} - W_{1i})L_i}{(W_{2i} - W_{1i})^2 + (U_{2i} - U_{1i})^2}$$

$$X_7 = -\frac{\tau_{ji} L_i}{W_{2i} - W_{1i}} - \frac{\tau_{ji}(W_{2i} - W_{1i})L_i}{(W_{2i} - W_{1i})^2 + (U_{2i} - U_{1i})^2}$$

$$X_8 = \frac{\dot{m}_o(W_{1i} - W_{1i-1})}{Cr_i}\left[1 + \frac{(L_i - Tp_i)}{17.04Cr_i}\left(\frac{\mu_{2i}^2 - 1}{\mu_{2i}}\right)^2\right] - \frac{\tau_{oi} as_i L_i ms D_{h1i}}{2Cr_i^2}$$

$$Y_1 = \frac{P_{oi} B_i L_i}{RT}; \quad Y_2 = \frac{B_i L_i(W_{2i} - W_{oi})}{RT}; \quad Y_3 = \frac{B_i L_i}{Rs_2}; \quad Y_8 = 0$$

$$Y_4 = -\left[\frac{\tau_{ri}(1 + mr)\phi U_{2i} L_i ar_i}{(Rs_2\omega - W_{2i})^2 + U_{2i}^2} - \frac{\tau_{ji}(U_{2i} - U_{1i})L_i(\phi - 1)}{(W_{2i} - W_{1i})^2 + (U_{2i} - U_{1i})^2}\right]$$
$$\times \left[\frac{U_{1i}}{P_{oi}} + \frac{U_{1i} P_{oi}}{P_{oi-1}^2 - P_{oi}^2} - \frac{\mu_{1i} U_{1i}(4S_{1i} - 5)(\gamma - 1)}{\pi\gamma P_{oi}}(S_{1i} + 1)\right] - \frac{\tau_{ri} ar_i(1 + mr)L_i}{P_{oi}} + \frac{\tau_{ji} L_i}{P_{oi}}$$

$$Y_6 = \frac{\tau_{ri} ar_i L_i}{Rs_2\omega - W_{2i}} + \frac{\tau_{ri} ar_i L_i(1 + mr)(Rs_2\omega - W_{2i})}{(Rs_2\omega - W_{2i})^2 + U_{2i}^2} + \frac{\tau_{ji} L_i}{W_{2i} - W_{1i}} + \frac{\tau_{ji}(W_{2i} - W_{1i})L_i}{(W_{2i} - W_{1i})^2 + (U_{2i} - U_{1i})^2}$$

$$Y_6 = \left[\frac{U_{1i}P_{oi-1}}{P_{oi-1}^2 - P_{oi}^2} - \frac{\mu_{1i}U_{1i}(4S_{1i}-5)(\gamma-1)}{\pi\gamma P_{oi}}\left(\frac{P_{oi-1}}{P_{oi}}\right)^{\frac{-1}{\gamma}}\right]$$

$$\times - \left[\frac{\tau_{ei}(1+mr)\phi U_{2i}L_i ar_i}{(Re_2\omega - W_{2i})^2 + U_{2i}^2} - \frac{\tau_{ji}(U_{2i}-U_{1i})L_i(\phi-1)}{(W_{2i}-W_{1i})^2 + (U_{2i}-U_{1i})^2}\right]$$

$$Y_7 = -\frac{\tau_{ji}L_i}{(W_{2i}-W_{1i})} - \frac{\tau_{ji}L_i(W_{2i}-W_{1i})}{(W_{2i}-W_{1i})^2 + (U_{2i}-U_{1i})^2}$$

APPENDIX C: SEPARATION OF GOVERNING EQUATIONS

Continuity:

$$cos(\theta+\omega t):(G_1\omega+G_2)P_{oi}^{+}+G_3W_{1oi}^{+}+G_4W_{2oi}^{+}+G_5P_{ci}^{+}+G_6P_{ci-1}^{+}+G_7P_{ci+1}^{+}$$
$$=G_8\left(\frac{a-b}{2}\right)$$

$$sin(\theta+\omega t):-(G_1\omega+G_2)P_{ci}^{+}-G_3W_{1ci}^{+}-G_4W_{2ci}^{+}+G_5P_{oi}^{+}+G_6P_{oi-1}^{+}+G_7P_{oi+1}^{+}$$
$$=\left[\frac{\omega G_9}{2}+G_{10}\right](b-a)$$

$$cos(\theta-\omega t):(-G_1\omega+G_2)P_{oi}^{-}+G_3W_{1oi}^{-}+G_4W_{2oi}^{-}+G_5P_{ci}^{-}+G_6P_{ci-1}^{-}+G_7P_{ci+1}^{-}$$
$$=G_8\left(\frac{a+b}{2}\right)$$

$$sin(\theta-\omega t):(G_1\omega-G_2)P_{ci}^{-}-G_3W_{1ci}^{-}-G_4W_{2ci}^{-}+G_5P_{oi}^{-}+G_6P_{oi-1}^{-}+G_7P_{oi+1}^{-}$$
$$=\left[\frac{\omega G_9}{2}-G_{10}\right](a+b)$$

Momentum I:

$$cos(\theta+\omega t):X_1W_{1oi}^{+}\left[\frac{W_{1i}}{Rs_1}+\omega\right]+\left[\frac{X_3W_{2i}}{Rs_2}+X_2+X_3\omega\right]P_{oi}^{+}+\frac{X_3P_{ci}}{Rs_2}W_{2oi}^{+}+X_4P_{ci}^{+}$$
$$+X_5P_{ci+1}^{+}+X_6W_{1ci}^{+}+X_7W_{2ci}^{+}-\dot{m}_oW_{1ci-1}^{+}=X_8\left(\frac{b-a}{2}\right)$$

$$sin(\theta+\omega t):-X_1W_{1ci}^{+}\left[\frac{W_{1i}}{Rs_1}+\omega\right]-\left[\frac{X_3W_{2i}}{Rs_2}+X_2+X_3\omega\right]P_{ci}^{+}-\frac{X_3P_{ci}}{Rs_2}W_{2ci}^{+}+X_4P_{oi}^{+}$$
$$+X_5P_{oi+1}^{+}+X_6W_{1oi}^{+}+X_7W_{2oi}^{+}-\dot{m}_oW_{1oi-1}^{+}=0$$

$$cos(\theta-\omega t):X_1W_{1oi}^{-}\left[\frac{W_{1i}}{Rs_1}-\omega\right]+\left[\frac{X_3W_{2i}}{Rs_2}+X_2-X_3\omega\right]P_{oi}^{-}+\frac{X_3P_{ci}}{Rs_2}W_{2oi}^{-}+X_4P_{ci}^{-}$$
$$+X_5P_{ci+1}^{-}+X_6W_{1ci}^{-}+X_7W_{2ci}^{-}-\dot{m}_oW_{1ci-1}^{-}=-X_8\left(\frac{a+b}{2}\right)$$

$$sin(\theta-\omega t):-X_1W_{1ci}^{-}\left[\frac{W_{1i}}{Rs_1}-\omega\right]-\left[\frac{X_3W_{2i}}{Rs_2}+X_2-X_3\omega\right]P_{ci}^{-}-\frac{X_3P_{ci}}{Rs_2}W_{2ci}^{-}+X_4P_{oi}^{-}$$
$$+X_5P_{oi+1}^{-}+X_6W_{1oi}^{-}+X_7W_{2oi}^{-}-\dot{m}_oW_{1oi-1}^{-}=0$$

Momemtum II:

$$cos(\theta+\omega t):Y_1\omega W_{2oi}^{+}+\left[\frac{Y_1W_{2i}}{Rs_2}+\frac{Y_2P_{ci}}{Rs_2}\right]W_{2oi}^{+}+\left[Y_2\omega+Y_3+\frac{Y_2W_{2i}}{Rs_2}\right]P_{oi}^{+}$$
$$+Y_4P_{ci}^{+}+Y_5W_{2ci}^{+}+Y_6P_{ci-1}^{+}+Y_7W_{1ci}^{+}=Y_8\left(\frac{b-a}{2}\right)$$

$$sin(\theta+\omega t):-Y_1\omega W_{2ci}^{+}-\left[\frac{Y_1W_{2i}}{Rs_2}+\frac{Y_2P_{ci}}{Rs_2}\right]W_{2ci}^{+}-\left[Y_2\omega+Y_3+\frac{Y_2W_{2i}}{Rs_2}\right]P_{ci}^{+}$$
$$+Y_4P_{oi}^{+}+Y_5W_{2oi}^{+}+Y_6P_{oi-1}^{+}+Y_7W_{1oi}^{+}=0$$

$$cos(\theta-\omega t):-Y_1\omega W_{2oi}^{-}+\left[\frac{Y_1W_{2i}}{Rs_2}+\frac{Y_2P_{ci}}{Rs_2}\right]W_{2oi}^{-}+\left[-Y_2\omega+Y_3+\frac{Y_2W_{2i}}{Rs_2}\right]P_{oi}^{-}$$
$$+Y_4P_{ci}^{-}+Y_5W_{2ci}^{-}+Y_6P_{ci-1}^{-}+Y_7W_{1ci}^{-}=-Y_8\left(\frac{a+b}{2}\right)$$

$$sin(\theta-\omega t):Y_1\omega W_{2ci}^{-}-\left[\frac{Y_1W_{2i}}{Rs_2}+\frac{Y_2P_{ci}}{Rs_2}\right]W_{2ci}^{-}-\left[-Y_2\omega+Y_3+\frac{Y_2W_{2i}}{Rs_2}\right]P_{ci}^{-}$$
$$+Y_4P_{oi}^{-}+Y_5W_{2oi}^{-}+Y_6P_{oi-1}^{-}+Y_7W_{1oi}^{-}=0$$

DEFINITION OF MATRIX ELEMENTS

A_{i-1} MATRIX

$$A_{1,2} = A_{2,1} = A_{3,4} = A_{4,3} = G_6$$
$$A_{5,2} = A_{6,1} = A_{7,4} = A_{8,3} = X_5$$
$$A_{5,6} = A_{6,5} = A_{7,8} = A_{8,7} = -\dot{m}_o$$
$$A_{9,2} = A_{10,1} = A_{11,4} = A_{12,3} = Y_6$$

The remaining elements are zero.

A_i MATRIX

$$A_{1,1} = -A_{2,2} = G_1\omega + G_2$$
$$A_{3,3} = -A_{4,4} = G_1\omega + G_2$$
$$A_{1,2} = A_{2,1} = A_{3,4} = A_{4,3} = G_5$$
$$A_{5,2} = A_{6,1} = A_{7,4} = A_{8,3} = X_4$$
$$A_{5,1} = -A_{6,2} = X_3\omega + X_2 + \frac{X_3 W_{2i}}{Rs_2}$$
$$A_{7,3} = -A_{8,4} = -X_3\omega + X_2 + \frac{X_3 W_{2i}}{Rs_2}$$
$$A_{9,2} = A_{10,1} = A_{11,4} = A_{12,3} = Y_4$$
$$A_{9,1} = -A_{10,2} = Y_2\omega + Y_3 + \frac{Y_3 W_{2i}}{Rs_2}$$
$$A_{11,3} = -A_{12,4} = -Y_2\omega + Y_3 + \frac{Y_3 W_{2i}}{Rs_2}$$
$$A_{1,5} = -A_{2,6} = A_{3,7} = -A_{4,8} = G_3$$
$$A_{5,5} = -A_{6,6} = X_1\left[\omega + \frac{W_{1i}}{Rs_1}\right]$$
$$A_{7,7} = -A_{8,8} = X_1\left[-\omega + \frac{W_{1i}}{Rs_1}\right]$$
$$A_{5,6} = A_{6,5} = A_{7,8} = A_{8,7} = X_6$$
$$A_{9,6} = A_{10,5} = A_{11,8} = A_{12,7} = Y_7$$
$$A_{1,9} = A_{3,11} = -A_{2,10} = -A_{4,12} = G_4$$
$$A_{5,9} = -A_{6,10} = A_{7,11} = -A_{8,12} = \frac{X_3 P_{oi}}{Rs_2}$$
$$A_{5,10} = A_{6,9} = A_{7,12} = A_{8,11} = X_7$$
$$A_{9,9} = -A_{10,10} = Y_1\omega + \frac{Y_1 W_{2i}}{Rs_2} + \frac{Y_2 P_{oi}}{Rs_2}$$
$$A_{11,11} = -A_{12,12} = -Y_1\omega + \frac{Y_1 W_{2i}}{Rs_2} + \frac{Y_2 P_{oi}}{Rs_2}$$
$$A_{9,10} = A_{10,9} = A_{11,12} = A_{12,11} = Y_5$$

The remaining elements are zero.

A_{i+1} MATRIX

$$A_{1,2} = A_{2,1} = A_{3,4} = A_{4,3} = G_7$$

The remaining elements are zero.

B and C Column Vectors

$$B = \begin{Bmatrix} \frac{G_A}{2} \\ \frac{-\psi G_B}{2} - \frac{G_{1B}}{2} \\ \frac{G_A}{2} \\ \frac{\psi G_B}{2} - \frac{G_{1B}}{2} \\ \frac{-X_A}{2} \\ 0 \\ \frac{-X_B}{2} \\ 0 \\ \frac{-Y_B}{2} \\ 0 \\ \frac{-Y_B}{2} \\ 0 \end{Bmatrix} \quad C = \begin{Bmatrix} \frac{-G_A}{2} \\ \frac{\psi G_B}{2} + \frac{G_{1B}}{2} \\ \frac{G_A}{2} \\ \frac{\psi G_B}{2} - \frac{G_{1B}}{2} \\ \frac{X_A}{2} \\ 0 \\ \frac{-X_B}{2} \\ 0 \\ \frac{Y_B}{2} \\ 0 \\ \frac{-Y_B}{2} \\ 0 \end{Bmatrix}$$

APPENDIX D: THE THEORY OF JENNY ET AL. [7]

The theory of Jenny et al. [7] has shown consistently good agreement with measured test results [25] in predictions of cross-coupled stiffness and direct damping. The author had hoped to program their solution and make direct comparison to the present theory; however, as outlined below, unresolvable difficulties arose in deriving the published equations of [7].

The theory of Jenny et al. [7] was derived for the "box-in-a-box" control volume configuration illustrated in figure 5. Thus, a direct comparison of their equations with those presented in this report is not feasible. However, a review of the development of their governing equations is of interest.

The following convention will be used for the control volumes in figure 5: the large control volume is control volume I and the small control volume is control volume II. The continuity equations for the control volumes shown in figure 5 are:

Continuity I:

$$\frac{\partial \rho W_2 A_2}{Rs\partial\theta} + \frac{\partial \rho W_1 A_1}{Rs\partial\theta} + \frac{\partial \rho (A_1 + A_2)}{\partial t} + \dot{m}_{i+1} - \dot{m}_i = 0 \qquad (J1)$$

Continuity II:

$$\frac{\partial \rho W_2 A_2}{Rs\partial\theta} + \frac{\partial \rho A_2}{\partial t} - \dot{m}_{ri} = 0 \qquad (J2)$$

The following assumptions are used by Jenny et al. [7] to simplify equations (J1) and (J2):

a) the flow is incompressible (ρ = constant),

b) $\dot{m}_{i+1} = \dot{m}_i$, and

c) the area of the control volume II is constant.

The first assumption seems questionable, since this is a compressible flow solution and quite often the flow in a labyrinth seal achieves Mach 1 at the exit. Assumption (b) is a valid assumption for the zeroth-order, steady flow solution, but it is questionable for the first-order, unsteady flow solution for an orbiting rotor. Using the chain rule for the expansion of partial derivatives and the above assumptions, equations (J1) and (J2) become:

Continuity I:

$$A_2 \frac{\partial W_2}{\partial\theta} + A_1 \frac{\partial W_1}{\partial\theta} + W_1 L \frac{\partial Cr}{\partial\theta} + Rs \frac{\partial (A_1 + A_2)}{\partial t} = 0 \qquad (J3)$$

Continuity II:

$$\rho A_2 \frac{\partial W_2}{\partial\theta} - Rs\dot{m}_{ri} = 0 \qquad (J4)$$

The equations given by Jenny et al. [7] are:

Continuity I:

$$A_2 \frac{\partial W_2}{\partial\theta} + A_1 \frac{\partial W_1}{\partial\theta} - W_1 L \frac{\partial Cr}{\partial\theta} - Rs \frac{\partial (A_1 + A_2)}{\partial t} = 0 \qquad (J5)$$

Continuity II:

$$\rho A_2 \frac{\partial W_2}{\partial\theta} - \dot{m}_{ri} = 0 \qquad (J6)$$

The difference between equations (J3) and (J5) is in the sign of the third and fourth terms. The second and third terms in equations (J3) and (J5) originate from the same partial derivative, but have opposite signs. The author could not arrive at the same conclusion using the chain rule. The difference between equations (J4) and (J6) is the radius, Rs, in the second term. This may or may not be a problem since the radial mass flow term, $\dot{m}_{ri}$, is not defined by Jenny et al. [7].

The author agreed with the derivation of the momentum equations for the control volumes shown in figure 5 except for the aforementioned assumptions and the following discrepancies:

(a) the axial velocity component is incorporated in the definition of the stator wall shear stress, but neglected in the definition of the Reynold's number which is used to calculate the friction factor term in the shear stress relation.

(b) the perturbation of the friction factor is ignored. This term has been shown [24] to be important in the solution for rotordynamic coefficients.

(c) the leakage equation is a global leakage equation. This means that local perturbations pertaining to a cavity can not be found from this equation. Jenny et al. [7] perturb this global equation for clearance.

(d) the carryover coefficient definition used in the leakage equation is a global equation and cannot be perturbed.

(e) the flow coefficient used in the leakage equation was obtained from a plot of empirical data. No explanation was given for the method used to obtain the dervatives of the flow coefficient used in the perturbation equations.

The aforementioned problems prevented the author from obtaining a solution based on the theory of Jenny et al. [7]. Regrettably, no direct comparison between it and the theory presented in this paper was possible.

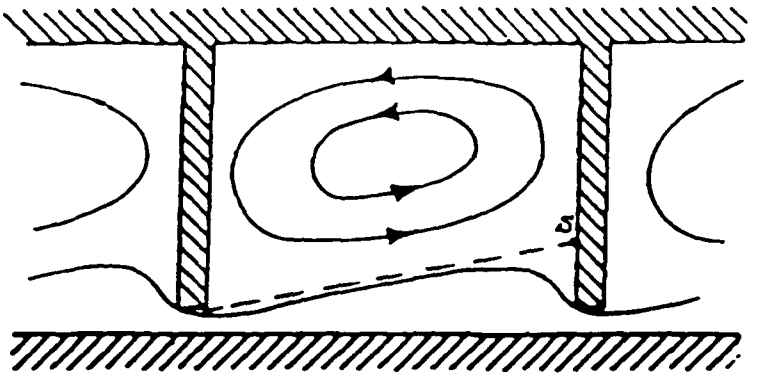

Fig. 1 Flow pattern in labyrinth cavity.

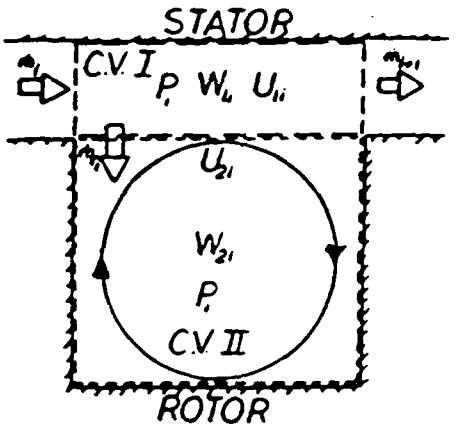

Fig. 2 Control volumes with geometric boundary.

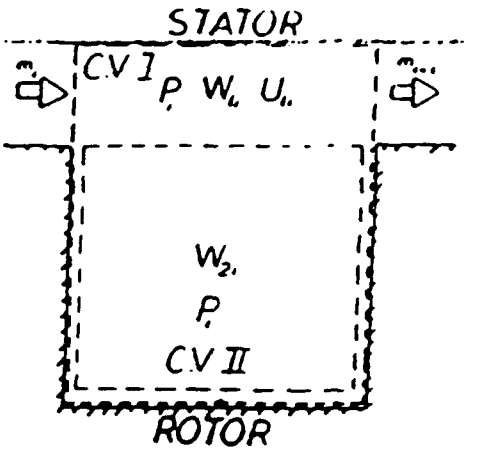

Fig. 3 "Box-in-a-box" model of Jenny et al. 7 .

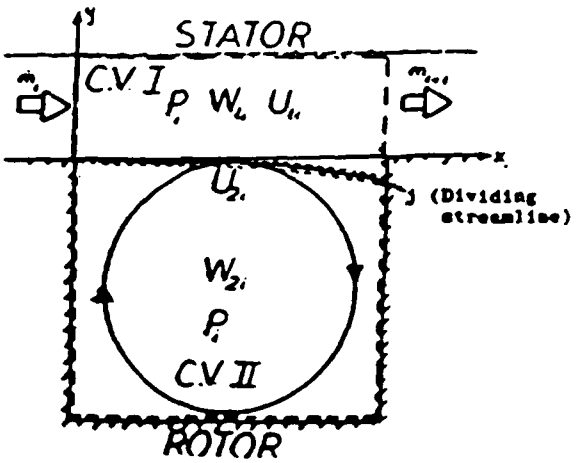

Fig. 4 Control volumes with dividing streamline boundary.

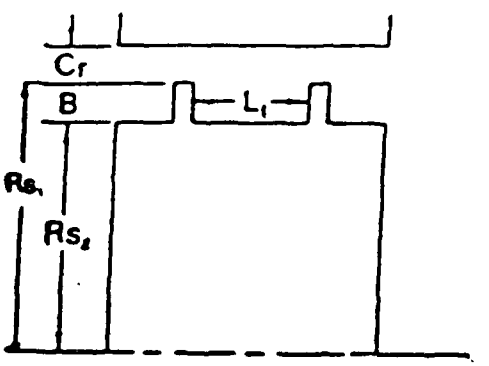

Fig. 5 A typical labyrinth cavity.

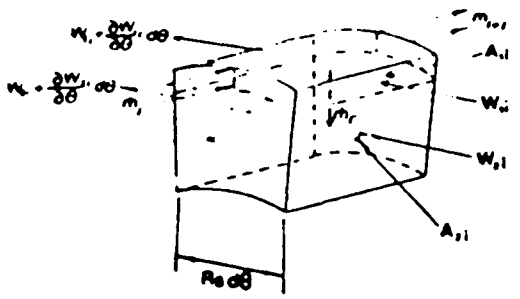

Fig. 6 Isometric view of control volumes.

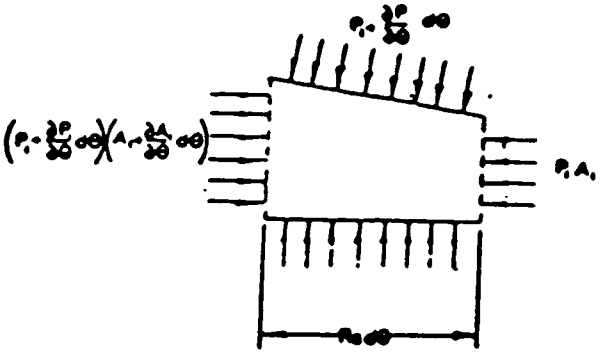

Fig. 7 Pressure forces acting on control volume I.

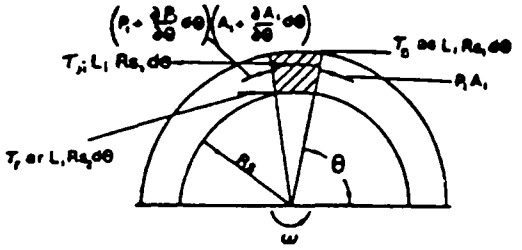

Fig. 8 Forces acting on control volumes.

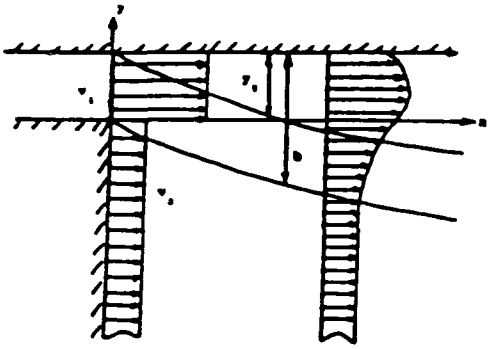

Fig. 11 Model of semi-contained turbulent jet.

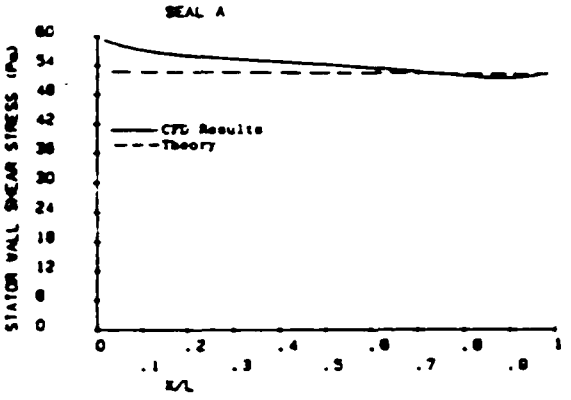

Fig. 9 A comparison of CFD and new model for stator wall shear stress.

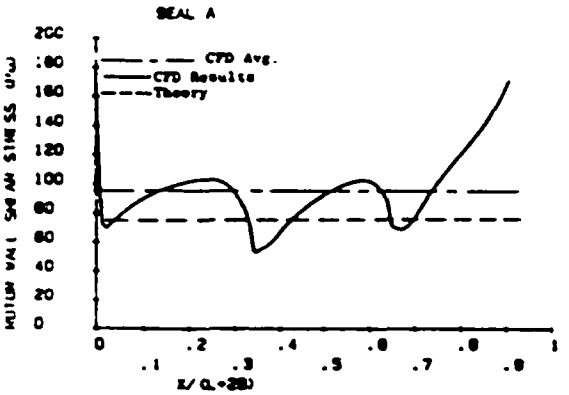

Fig. 10 A comparison of CFD and new model for rotor wall shear stress.

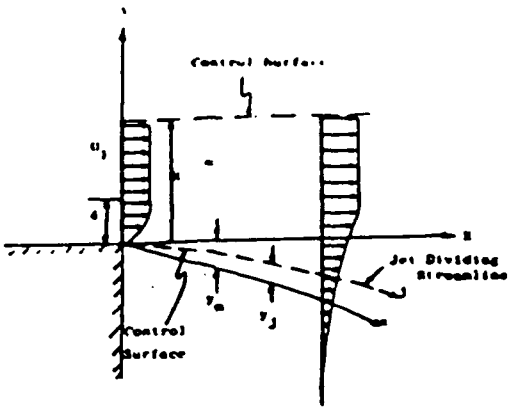

Fig. 12 Model of half-infinite turbulent jet.

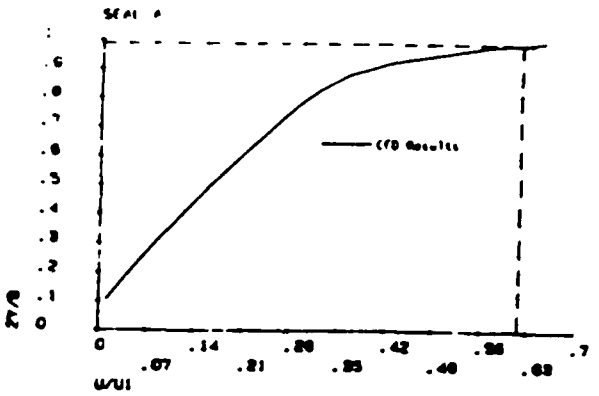

Fig. 13 Comparison of CFD and jet theory results for velocity along dividing streamline.

THEORY VERSUS EXPERIMENT FOR THE ROTORDYNAMIC COEFFICIENTS OF LABYRINTH GAS SEALS: PART II - A COMPARISON TO EXPERIMENT[1]

DARA W. CHILDS
JOSEPH K. SCHARRER
MECHANICAL ENGINEERING DEPARTMENT
TEXAS A&M UNIVERSITY
COLLEGE STATION, TX 77843

SUMMARY

An experimental test facility is used to measure the leakage and rotordynamic coefficients of teeth-on-rotor and teeth-on-stator labyrinth gas seals. The test results are presented along with the theoretically predicted values for the two seal configurations at three different radial clearances and shaft speeds to 16,000 cpm. The test results show that the theory accurately predicts the cross-coupled stiffness for both seal configurations and shows improvement in the prediction of the direct damping for the teeth-on-rotor seal. The theory fails to predict a decrease in the direct damping coefficient for an increase in the radial clearance for the teeth-on-stator seal.

INTRODUCTION

Part 1 of this paper presented a new two-control-volume analysis to predict the rotordynamic coefficients for labyrinth gas seals. This part (Part 2) of the paper provides a comparison of the predictions of the analysis from Part 1 to the new test results for six "see-through" labyrinth gas seals, as shown in figure 1, three with teeth on the rotor and three with teeth on the stator. The design, development, and operation of the test apparatus and facility, which have been developed to measure the leakage and rotordynamic coefficients of annular gas seals, has been described by Childs et al. [1]. The apparatus described in [1] was limited to a top shaft speed of 8,000 cpm. The apparatus has since been redesigned to operate at shaft speeds up to 16,000 cpm. A complete discussion of the redesign of the apparatus can be found in Elrod and Childs [2].

As described in [1], the rotordynamic coefficients for a gas seal are defined by the following linearised force-displacement model.

$$-\begin{Bmatrix} F_X \\ F_Y \end{Bmatrix} = \begin{bmatrix} K_{xx} & K_{yx} \\ K_{xy} & K_{yy} \end{bmatrix} \begin{Bmatrix} X \\ Y \end{Bmatrix} + \begin{bmatrix} C_{xx} & C_{yx} \\ C_{xy} & C_{yy} \end{bmatrix} \begin{Bmatrix} \dot{X} \\ \dot{Y} \end{Bmatrix} \tag{1}$$

Where (X,Y) define the motion of the seal's rotor relative to its stator, (F_x, F_y) are the components of the reaction force acting on the rotor, and $(K_{xx}, K_{yy}, K_{xy}, K_{yx})$ and $(C_{xx}, C_{yy}, C_{xy}, C_{yx})$ are the stiffness and damping coefficients respectively. Equation (1) applies for small motion of the rotor about an arbitrary eccentric position. For small motion about a centered position, the following simpler model applies.

$$-\begin{Bmatrix} F_X \\ F_Y \end{Bmatrix} = \begin{bmatrix} K & k \\ -k & K \end{bmatrix} \begin{Bmatrix} X \\ Y \end{Bmatrix} + \begin{bmatrix} C & c \\ -c & C \end{bmatrix} \begin{Bmatrix} \dot{X} \\ \dot{Y} \end{Bmatrix} \tag{2}$$

Although the test apparatus has the capability of separately identifying the eccentric-position rotordynamic coefficients of equation (1), the results presented here are for the centered-position case only.

PREVIOUS EXPERIMENTAL PROGRAMS

A limited amount of experimental data has been published to date on the determination of stiffness and damping coefficients for labyrinth gas seals. The first published results for stiffness coefficients were those of Wachter and Benckert [3,4,5]. They investigated the following three types of seals: a) teeth-on-stator, b) teeth on the rotor and stator, and c) teeth on the stator and steps or grooves on the rotor. These

[1]This work was supported in part by NASA Grant NAS3-181 from NASA Lewis Research Center (Technical Monitor, Robert Hendricks) and AFOSR Contract F49620-82-K-0033 (Technical Monitor, Tony Amos)

results were limited in that the pressure drop was small, much of the data were for nonrotating seals, no data were presented for seals with teeth on the rotor, the rotor speed was limited, and tests where rotation and inlet tangential velocity existed simultaneously were very scarce. The next investigation was carried out by Wright [6], who measured an "equivalent" radial and tangential stiffness for single-cavity seals with teeth on the stator. Although for a very limited and special case, Wright's results do give insight into the effect of pressure drop, convergence or divergence of the clearance, and forward or backward whirl of a seal. These results could be reduced to direct and cross-coupled stiffness and damping, hence, they are the first published damping coefficients for teeth-on-stator labyrinth seals. Brown and Leong [7,8] investigated the same seal configurations as Wachter and Benckert, in an effort to verify and extend their work. Their results include variations of pressure, geometry, rotor speed, and inlet tangential velocity. Although the investigation was extensive, the published results are limited because of the lack of information concerning operating conditions for the various tests. Childs and Scharrer [9] investigated geometrically similar teeth-on-rotor and teeth-on-stator labyrinth gas seals for stiffness and damping coefficients up to speeds of 8000 cpm. Kanemitsu and Ohsawa [10] investigated multistage teeth-on-stator and interlocking labyrinth seals up to speeds of 2400 cpm. They measured an effective radial and tangential stiffness while varying the whirl frequency of the rotor. These data could be reduced to stiffness and damping coefficients. Hisa et al. [11] investigated teeth-on-stator seals with 2-4 teeth and a teeth-on-stator seal with steps on the rotor up to speeds of 6000 cpm. These data only included static tests for direct and cross-coupled stiffness using steam.

The most extensive comparison of analytical predictions and experimental results was carried out by Scharrer [12] using the theory of Childs and Scharrer [13] and the results of Childs and Scharrer [9]. This comparison showed that the theory [13] predicts cross-coupled stiffness reasonably well, but underpredicts direct stiffness, direct damping and cross-coupled damping.

In reviewing previous experimental programs, there is a clear need for a) more extensive testing of teeth-on-rotor labyrinth seals and b) experimental results showing the effect of radial clearance change on direct damping coefficients. This paper addresses these points in addition to evaluating the new analysis presented in Part 1 of this paper by comparison to the new test results.

TEST APPARATUS AND FACILITY

Introduction

The test results reported here were developed as a part of an extended, joint NASA-USAF funded research program for annular gas seal studies. Tests were carried out on six "see-through" labyrinth seals, three with teeth on the rotor and three with teeth on the stator, each with different radial clearances. The test program had the objective of examining the effects of a change in radial clearance on the leakage and stability performances of a teeth-on-stator and a teeth-on-rotor labyrinth seal. Air is the test fluid.

Test Apparatus

The rotor shaft is suspended pendulum-fashion from an upper, rigidly mounted pivot shaft, as shown in figure 2. This arrangement allows a side-to-side (horisontal) motion of the rotor. A cam within the pivot shaft allows vertical positioning of the rotor. The rotor is both positioned and excited horisontally by a hydraulic shaker head which acts on the rotor-shaft bearing housing and works against a return spring mounted on the opposite side of the bearing housing. The design of the test rig permits the installation of various rotor/stator combinations. The stator is supported in the test section housing by three pieso- electric quarts load cells in a trihedral configuration. The test apparatus measures the reaction-force components and relative seal stator motion. The harmonic components of the motion and force signals are used to identify the stiffness and damping coefficients. Different seal stator designs are obtained by the use of inserts.

The dimensions and pertinent data for each seal configuration are given in table 1. For the remainder of this paper, the seals will be referred to as seal 1, seal 2 and seal 3, as given in table 1, in addition to their respective configuration. The smooth and labyrinth inserts used for the 0.4mm (0.016in.) clearance seals are shown in figure 3. The labyrinth tooth detail for both rotor and stator is shown in figure 4.

Table 1. Dimensions of seals tested in this study

	Teeth-on-rotor	Teeth-on-stator
Seal 1		
Radius, mm	72.5	75.6
Length, mm	50.8	50.8
Clearance, mm	0.3	0.33
Number of teeth	16	16
Seal 2		
Radius, mm	72.5	75.6
Length, mm	50.8	50.8
Clearance, mm	0.4	0.4
Number of teeth	16	16
Seal 3		
Radius, mm	72.5	75.6
Length, mm	50.8	50.8
Clearance, mm	0.55	0.5
Number of teeth	16	16

Test Variables

When shaking about the centered position, the Dynamic-Seal-Apparatus is capable of controlling the following three independent variables:*pressure ratio, rotor speed and inlet circumferential velocity*.Two shake frequencies, 56.8 Hz and 74.6 Hz, were used during testing with essentially the same results. The results to be presented were obtained by shaking at 74.6 Hz at an amplitude between 0.076 mm and 0.1 mm. The actual test points for each of these three independent variables are shown in table 2. When reviewing the following figures, table 2 should be consulted for the definitions of all symbols used.

Table 2. Definition of symbols used in figures

Supply pressure	Rotor speeds	Inlet circumferential velocities
1 3.08 bar	1 3000 cpm	1 High vel. against rotation
2 4.46 bar	2 6000 cpm	2 Low vel. against rotation
3 5.84 bar	3 9500 cpm	3 Zero circumferential vel.
4 7.22 bar	4 13000 cpm	4 Low vel. with rotation
5 8.22 bar	5 16000 cpm	5 High vel. with rotation

The reservoir pressures, as measured upstream of the flowmeter, are given in table 2. These values differ from the actual inlet pressure because of frictional losses and an acceleration of the fluid due to the inlet guide vanes. No tests could be run at zero pressure difference, since a small pressure difference is necessary to keep the rotor from shifting axially and rubbing the inlet guide vanes. Similarly, no zero rotor speed tests were run, since rotor rotation was necessary to prevent damage to the thrust bearing during shaking.

The inlet circumferential velocities are given in figures 5,6 and 7 as a function of pressure ratio. The teeth-on-rotor results are on the left and the teeth-on-stator results are on the right. This convention will be used for all of the results presented in this paper. The figures show that inlet circumferential velocity remains fairly constant over the pressure ratios tested. There were five test points for inlet circumferential velocity; two positive, two negative, and one at zero. The zero inlet circumferential velocity point corresponds to the x-axis in the figures 5,6 and 7. The negative numbers shown in the figures mean that the inlet circumferential velocity was opposed to the direction of rotor rotation. The positive numbers mean that the inlet circumferential velocity was in the same direction as rotor rotation. The two different magnitudes of inlet circumferential velocity, for each direction, correspond to the different inlet guide vane geometries, as discussed in [1]. The ratio of inlet circumferential velocity to rotor surface velocity (inlet circumferential velocity ratio), ranged from about -6 to about 6. Although the larger numbers are practically unrealistic, they do give insight into the effects of inlet circumferential velocity that would have otherwise gone unnoticed.

Normalized Parameters

Before the tests described herein were performed, the TAMU gas seal test apparatus was modified as described by Elrod and Childs [2] to allow operation at running speeds up to 16,000 cpm. As expected, subsequent tests revealed a dependence of the rotor diameter on running speed due to inertia and thermal effects. The rotor growth data, shown in table 3, were obtained from eddy current motion probes positioned at the midspan of the seal. Thus, as the rotor turns faster, the forces in the seal are affected not only by the increased surface speed of the rotor but also by a change in clearance. Theoretically, normalisation would collapse the data and make the presentation simpler and more straight forward. This was not the case with the labyrinth seals tested in this study. The failure of the normalisation is detailed by Scharrer [14].

Table 3. Growth of rotor with rotational speed

Rotor speed (cpm)	Diametrical growth (mm)
3000	0.01
6000	0.02
9500	0.03
13000	0.05
16000	0.11

Dynamic Results

For a circular orbit of amplitude A, the resultant radial and tangential forces developed by the seal model of equation (2) are illustrated in figure 8 and are defined by

$$-F_r/A = K + c\omega$$
$$F_t/A = k - C\omega$$

From a stability standpoint, the destabilising tangential force, F_t, is of most interest. The destabilising influence comes from the cross-coupled stiffness, k, and the stabilising influence comes from the direct damping, C. The radial force usually has little influence on stability, except in rare cases involving multistage "back-to-back" centrifugal compressors with midspan seals where large negative direct stiffness values may reduce the natural frequencies. Since the focus of this study was on stability, the cross-coupled stiffness and direct damping results, which have the most influence, will be presented first. The direct stiffness will follow.

Relative Uncertainty

Before proceeding with the results, a statement must be made concerning the uncertainty present in the experimental results. Using the method described by Holman [15], the uncertainty in the dynamic coefficients can be determined. The uncertainty in the force, excitation frequency, and displacement measurements are 0.89 N (0.2 lb), 0.13 Hs , and 0.0013 mm (0.05 mils), respectively. The resulting calculated uncertainty is 7 N/mm (40 lb/in) for the stiffness coefficients and 0.0875 N-s/mm (0.5 lb-s/in) for the damping coefficients. Since the measured cross-coupled damping results were rarely greater than the uncertainty, test results are not provided here for this parameter.

TEST RESULTS

It might seem obvious, since this paper evaluates the effect on seal performance of varying the radial seal clearance, that the data should be presented as a function of clearance (clearance being the x-axis). However, since the inlet circumferential velocity is directly dependent on seal leakage and the seals leakage a different rates due to differing cross-sectional areas, the inlet circumferential velocity test points for seal 1 differs from those of seals 2 and 3. This is a problem because the rotordynamic coefficients are very sensitive to the inlet circumferential velocity. Therefore the dynamic data will be presented as a function of inlet circumferential velocity ratio at one pressure and one rotor speed. *In the following figures, the solid lines represent the test results and the broken lines represent the analytical predictions.*

Cross-coupled Stiffness Comparison

Figure 9 shows a comparison of experimental and theoretical results for cross-coupled stiffness versus inlet circumferential velocity ratio for the three seal clearances of table 1. The figure shows that the theory does a good job of predicting the cross-coupled stiffness for both the teeth-on-rotor and teeth-on-stator seals, at low rotor speeds. The figure also shows that there is no consistent trend in the cross-coupled results for a change

in clearance. Figure 10 shows a comparison of experimental and theoretical results for cross-coupled stiffness versus rotor speed for seal 1 (minimum clearance seal) of table 1 at the inlet pressures of table 2. The figure shows that the theory correctly predicts a sharp upturn in cross-coupled stiffness at the higher rotor speeds, for the teeth-on-rotor seal. This speed sensitivity was not evident in the low speed results of [9] nor in the results for seals 2 and 3. The figure also shows that the cross-coupled stiffness for the teeth-on-stator seal decreases as rotor speed increases. This decrease in cross-coupled stiffness for an increase in rotor speed was also reported by Hisa et al. [11] for their teeth-on-stator seals. The theory shows the same decrease until the higher rotor speeds are reached, then it shows a sharp upturn. This upturn may appear in the experimental data at higher rotor speeds. The same decrease in cross-coupled stiffness with an increase in rotor speed was evident in the results for seals 2 and 3.

Direct Damping Comparison

Figure 11 shows a comparison of experimental and theoretical direct damping versus inlet circumferential velocity ratio at the three clearances of table 1. The figure shows that the direct damping coefficient for a teeth-on-rotor seal increases as clearance increases. The theory correctly predicts this trend but underpredicts the magnitude of the coefficient by 30 percent. The figure also shows that the direct damping coefficient for a teeth-on-stator seal decreases as clearance increases. The theory shows the opposite trend. Figure 12 shows a comparison of experimental and theoretical direct damping versus rotor speed for seal 1 of table 1 at the inlet pressures of table 2. The figure shows that the test results show little or no sensitivity to rotor speed, for either seal configuration, while the theory shows a sharp upturn at the higher speeds. This upturn may be evident in future test results at higher speeds. The results for seals 2 and 3 showed the same insensitivity to rotor speed.

Direct Stiffness Comparison

Figure 13 shows a comparison of experimental and theoretical direct stiffness versus inlet circumferential velocity for the seal clearances of table 1. The figure shows that, for both seal configurations, the direct stiffness coefficient is negative and increases as radial seal clearance increases. One would expect zero direct stiffness values at sufficiently large clearances. The theory predicts this same trend, for both seal configurations. Figure 13 also shows that the theory underpredicts the direct stiffness magnitudes at high rotor speeds. Figure 14 show a comparison of experimental and theoretical direct stiffness versus rotor speed for seal 1 of table 1 at the inlet pressures of table 2. The figure shows that the test results, for both seal configurations, show little or no sensitivity to rotor speed. The figure also shows that the theory is overly sensitive to rotor speed. The insensitivity to rotor speed was also evident in the test results for seals 2 and 3.

Stability Analysis

One of the main objectives of this test program was an evaluation of the effect on seal performance of varying the radial seal clearance. A comparison of the stability of the two seal configurations at the different radial clearances satisfies that objective. Since a direct comparison of the coefficients of the two seals does not show any clear stability advantage or the overall effect of a change in the radial seal clearance, another method of comparison must be used. One method in which the dynamic coefficients of the two seals can be directly compared is through their respective non-dimensional whirl frequency ratios. Whirl frequency ratio is defined by

$$\text{Whirl frequency ratio} = k/C\omega = \Omega_f$$

where ω is the running speed, and Ω_f is the ratio of the destabilising influence of the cross-coupled stiffness and the stabilising influence of direct damping. From a stability viewpoint, a minimum whirl ratio is desirable. Figure 15 shows the whirl frequency ratio versus inlet circumferential velocity ratio for the seal clearances of table 1. For teeth-on-rotor seals, the figure shows that, as the clearance increases, the seal becomes more stable. For teeth-on-stator seals the opposite is true; as clearance increases the seal becomes less stable, for the positive inlet circumferential velocity case. The figure also shows that the teeth-on-stator seals are more stable that the teeth-on-rotor seals for the positive inlet circumferential velocity ratio, as was found previously [9].

Comparison to theory of [13]

Figures 16 and 17 provide a brief comparison of the present theory to the theory of Childs and Scharrer [13]. Figure 16 shows cross-coupled stiffness versus pressure ratio for a teeth-on-rotor labyrinth seal at 16,000 cpm, and demonstrates that the present theory follows the experimental data more closely than the former theory [13]. Similarly, figure 17 shows that the present theory also follows the experimental data for direct damping more closely than the former theory [13].

CONCLUSIONS

Test results have been presented for stiffness and damping coefficients for six "see-through" labyrinth seals, three with teeth on the rotor and three with teeth on the stator. The seals were tested under identical operating conditions to investigate the influence of rotor speed and the effect of varying the radial seal clearance on the rotordynamic coefficients. These experimental results were compared to the predictions from the new analysis presented in Part 1 of this paper.

The experimental results of the previous section support the following conclusions:

(1) For teeth-on-rotor seals, the direct damping increases as clearance increases; for teeth-on-stator seals, the direct damping decreases as clearances increases.

(2) Direct stiffness is negative and increases as clearances increases, for both seal configurations. Cross-coupled stiffness showed no consistent trend with respect to clearance changes.

(3) Direct stiffness and direct damping show little or no sensitivity to rotor speed up to 16,000 cpm. Cross-coupled stiffness shows a sharp upswing at higher rotor speeds, for a teeth-on-rotor seal. Cross-coupled stiffness decreases as rotor speed increases, for a teeth-on-stator seal.

(4) As clearance decreases, teeth-on-rotor seals become less stable and teeth-on-stator seals become more stable, for positive inlet circumferential velocity.

The theoretical results of the previous section support the following conclusions:

(1) The theory correctly predicts that direct stiffness is negative and increases as clearance increases, for both seal configurations. The theory incorrectly predicts an approximately quadratic increase in the direct stiffness magnitude (becoming more negative) as speed increases. Test results show scant sensitivity.

(2) The theory accurately predicts an increase in cross-coupled stiffness at high speeds, for a teeth-on-rotor seal.

(3) For teeth-on-rotor seals, the theory correctly predicts an increase in direct damping for an increase in clearance. However, the theory incorrectly predicts the same trend for a teeth-on-stator seal.

(4) The theory incorrectly predicts an approximately quadratic increase in direct damping with running speed. Test results show no systematic change in direct damping with running speed.

(5) A comparison with test results for a teeth-on-rotor seal shows that the theory presented in Part 1 of this paper does a better job of predicting cross-coupled stiffness and direct damping than does the theory of Childs and Scharrer [13].

NOMENCLATURE

A Seal orbit radius (L); illustrated in figure 8.
B Tooth height (L); illustrated in figure 1.
C,c Direct and cross-coupled damping coefficients (FT/L)
Cr Radial clearance (L); illustrated in figure 1.
K,k Direct and cross-coupled stiffness coefficients (F/L)
F Seal reaction-force (F)
L Tooth pitch (L); illustrated in figure 1.
Pr Seal inlet pressure (F/L^2)
Rs Seal radius (L); illustrated in figure 1.
X,Y Rotor to stator relative displacement components (L)
Ω_f Whirl frequency ratio
ω Shaft angular velocity (1/T)

Subscripts
i Value in i-th cavity
r Radial component
t Tangential component
x,y Rectangular coordinate directions

REFERENCES

1. Childs, D., Nelson, C., Nicks, C., Scharrer, J., Elrod, Hale, K., "Theory Versus Experiment for the Rotordynamic Coefficients of Annular Gas Seals: Part 1- Test Facility and Apparatus," *ASME Journal of Tribology,* July 1986, Vol. 108, pp. 426-432.

2. Elrod, D and Childs, D., "A Comparison of Experimental and Theoretical Results for Leakage, Pressure Gradients, and Rotordynamic Coefficients for Tapered Annular Gas Seals," Texas A&M Turbomachinery Laboratory Report TRC-SEAL-4-86.

3. Wachter, J., and Benckert, H.,"Querkrafte aus Spaltdichtungen-Eine mogliche Ursache fur die Laufunruhe von Turbomaschinen," *Atomkernenergie,"*32, 1978, Lfg. 4, pp. 239-246.

4. Wachter, J., and Benckert, H., "Flow Induced Spring Coefficients of Labyrinth Seals for Applications in Rotordynamics," NASA CP 2133 Proceedings of a workshop held at Texas A&M University 12-14 May 1980, Entitled Rotordynamic Instability Problems of High Performance Turbomachinery, pp. 189-212.

5. Benckert, H., "Stromungsbedinte Federkennwerte in Labyrinthdichtungen," Doctoral dissertation at University of Stuttgart, 1980.

6. Wright, D.V., "Labyrinth Seal Forces on a Whirling Rotor," *Rotor Dynamical Instability,* ASME, New York, 1983, pp. 19-31.

7. Brown, R.D, and Leong, Y.M.M.S, "Experimental Investigation of Lateral Forces Induced by Flow Through Model Labyrinth Glands," NASA CP 2338, Rotordynamic Instability Problems in High Performance Turbomachinery, proceedings of a workshop held at Texas A&M University 28-30 May, 1984. pp. 187-210.

8. Leong, Y.M.M.S, "Experimental Investigations of Lateral Forces Induced by Flow Through Model Labyrinth Glands," Doctoral Dissertation, Heriot-Watt University, Edinburgh, June 1983.

9. Childs, D. and Scharrer, J, "Experimental Rotordynamic Coefficient Results for Teeth-On-Rotor and Teeth-On-Stator Labyrinth Gas Seals," ASME Paper No. 86-GT-12, Also accepted for *ASME Journal of Engineering for Gas Turbines and Power.*

10. Kanemitsu, Y. and Ohsawa, M., "Experimental Study on Flow Induced Force of Labyrinth Seal," Proceedings of the Post IFToMM Conference on Flow Induced Force in Rotating Machinery, September 18-19, 1986, Kobe University, pp. 106-112.

11. Hisa, S., Sakakida, H., Asatu, S. and Sakamoto, T., "Steam Excited Vibration in Rotor-Bearing System," Proceedings of the International Conference on Rotordynamics, September 14-17, 1986, Tokoyo, Japan, pp. 635-641.

12. Scharrer, J., "A Comparison of Experimental and Theoretical Results for Rotordynamic Coefficients for Labyrinth Gas Seals," TRC Report No. SEAL-2-85, Texas A&M University, May 1985.

13. Childs, D. and Scharrer, J., "An Iwatsubo Based Solution for Labyrinth Seals: A Comparison to Experimental Results," *ASME Journal of Engineering for Gas Turbines and Power,* April 1986, Vol. 108, pp. 325-331.

14. Scharrer, J., "A Comparison of Experimental and Theoretical Results for Labyrinth Gas Seals," Doctoral Dissertation, Texas A&M University, College Station, TX, May 1987.

15. Holman, J.P.,*Experimental Methods for Engineers,* McGraw-Hill, 1978, pp. 45.

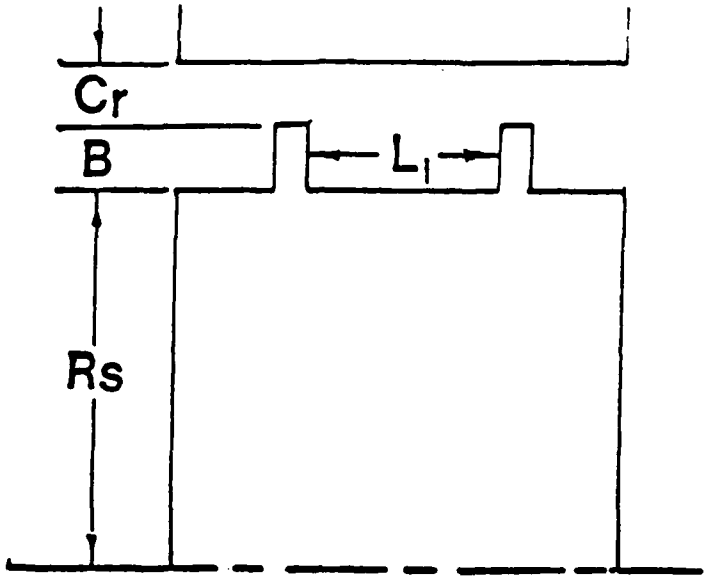

Fig. 1 A typical cavity.

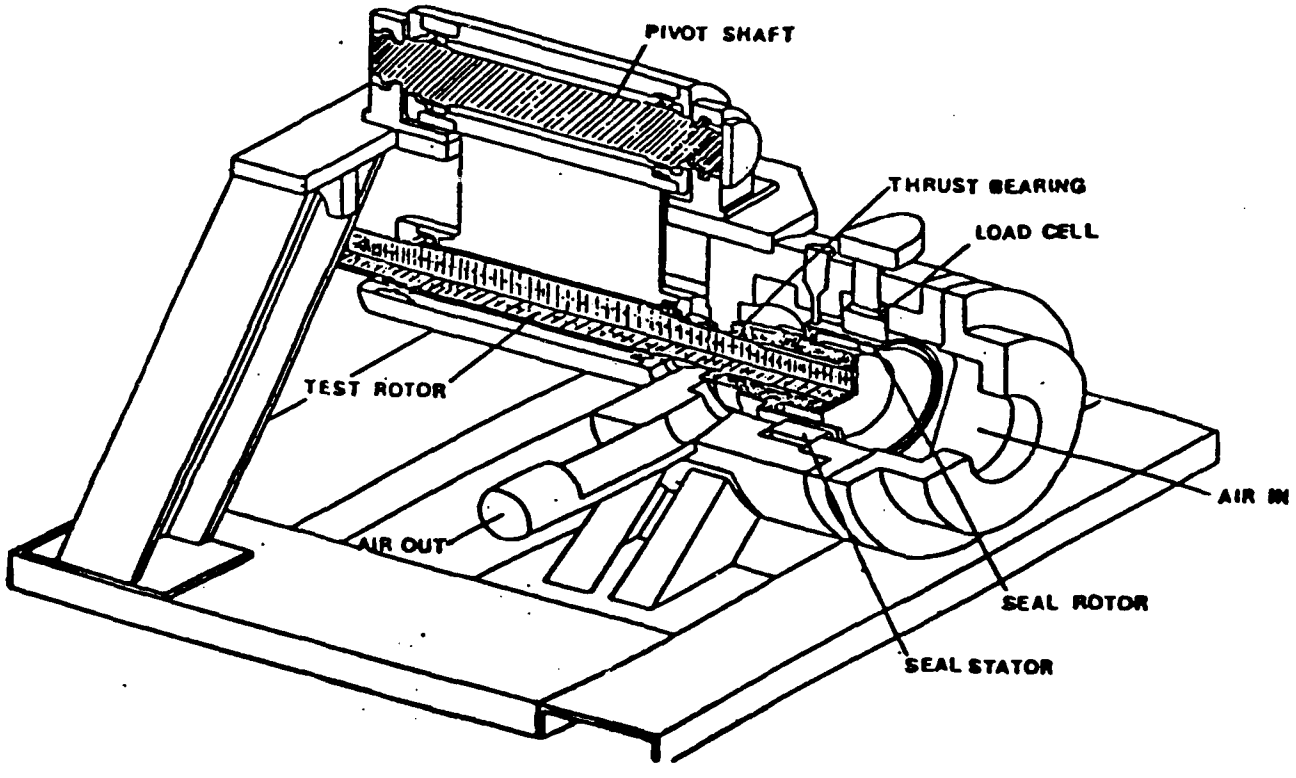

Fig. 2 Test apparatus.

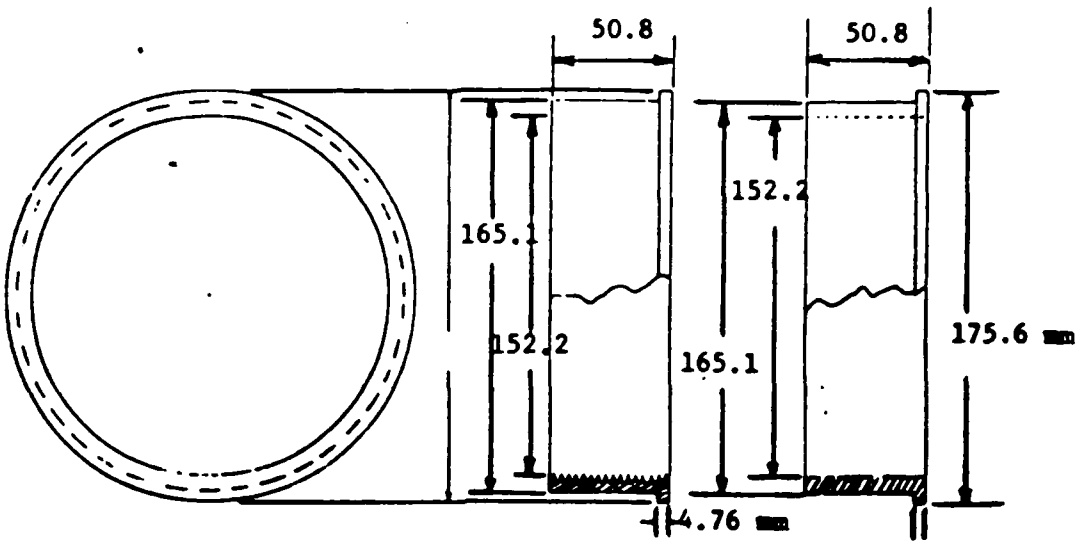

Fig. 3 Smooth and labyrinth stator inserts for seal 2.

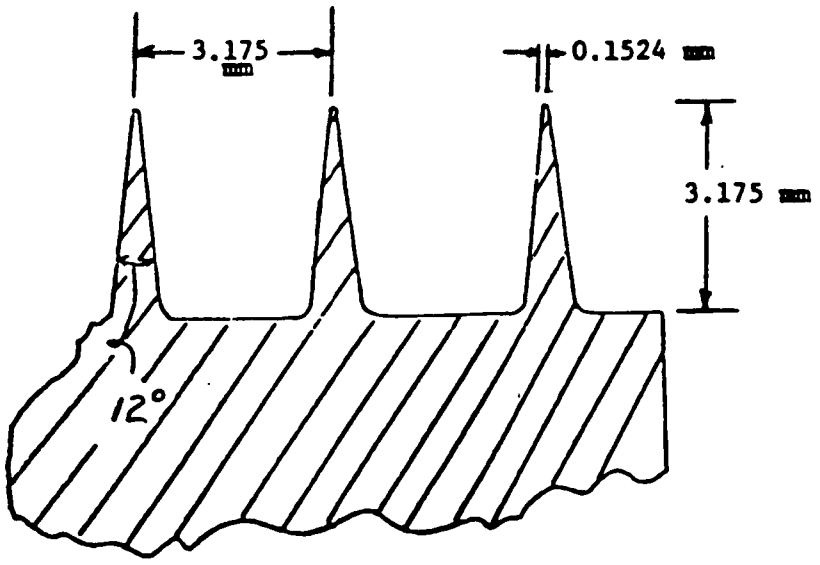

Fig. 4 Detail of labyrinth tooth.

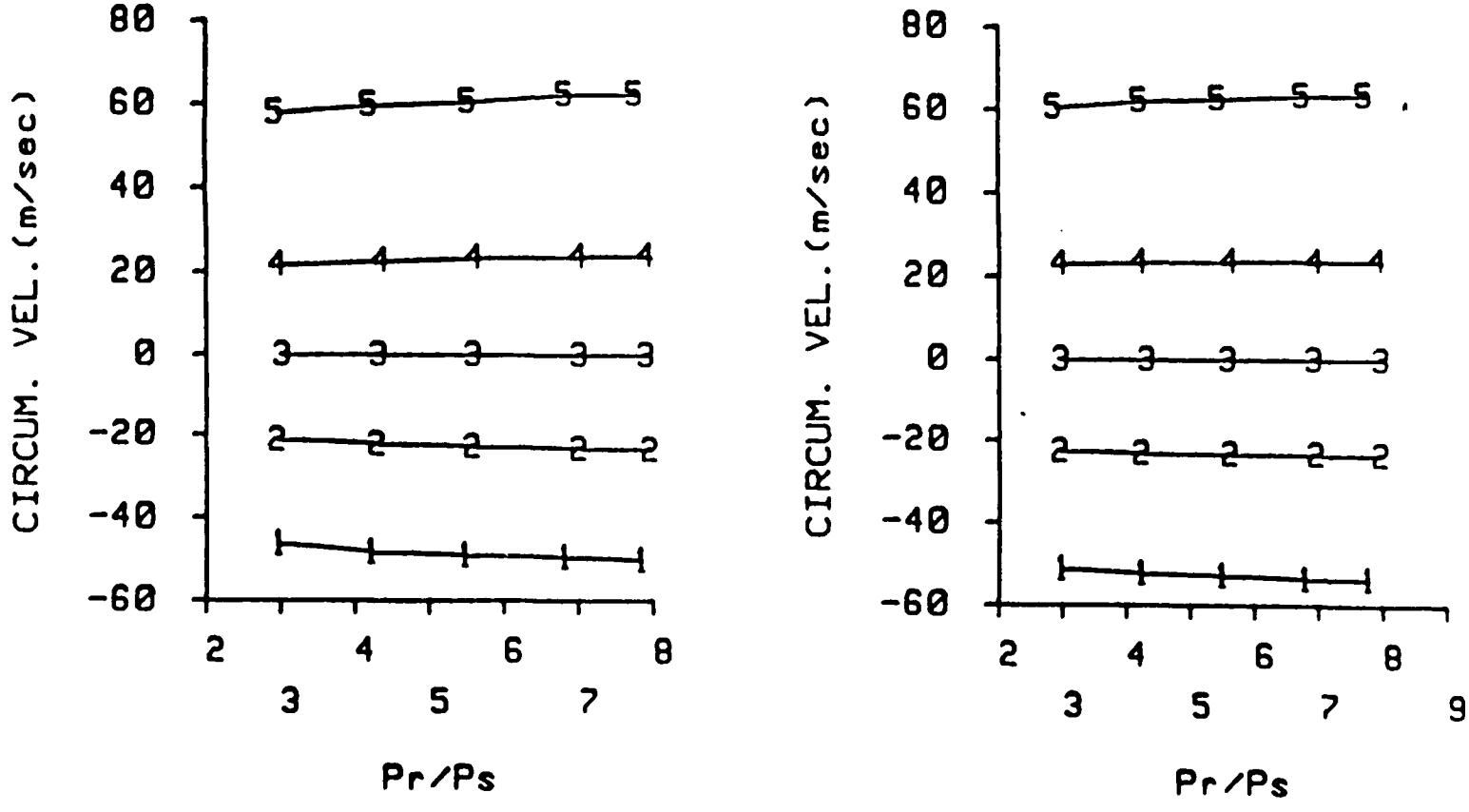

Fig. 5 Inlet circumferential velocities for seal 1. See table 2 for definitions. Teeth-on-rotor (left), teeth-on-stator (right).

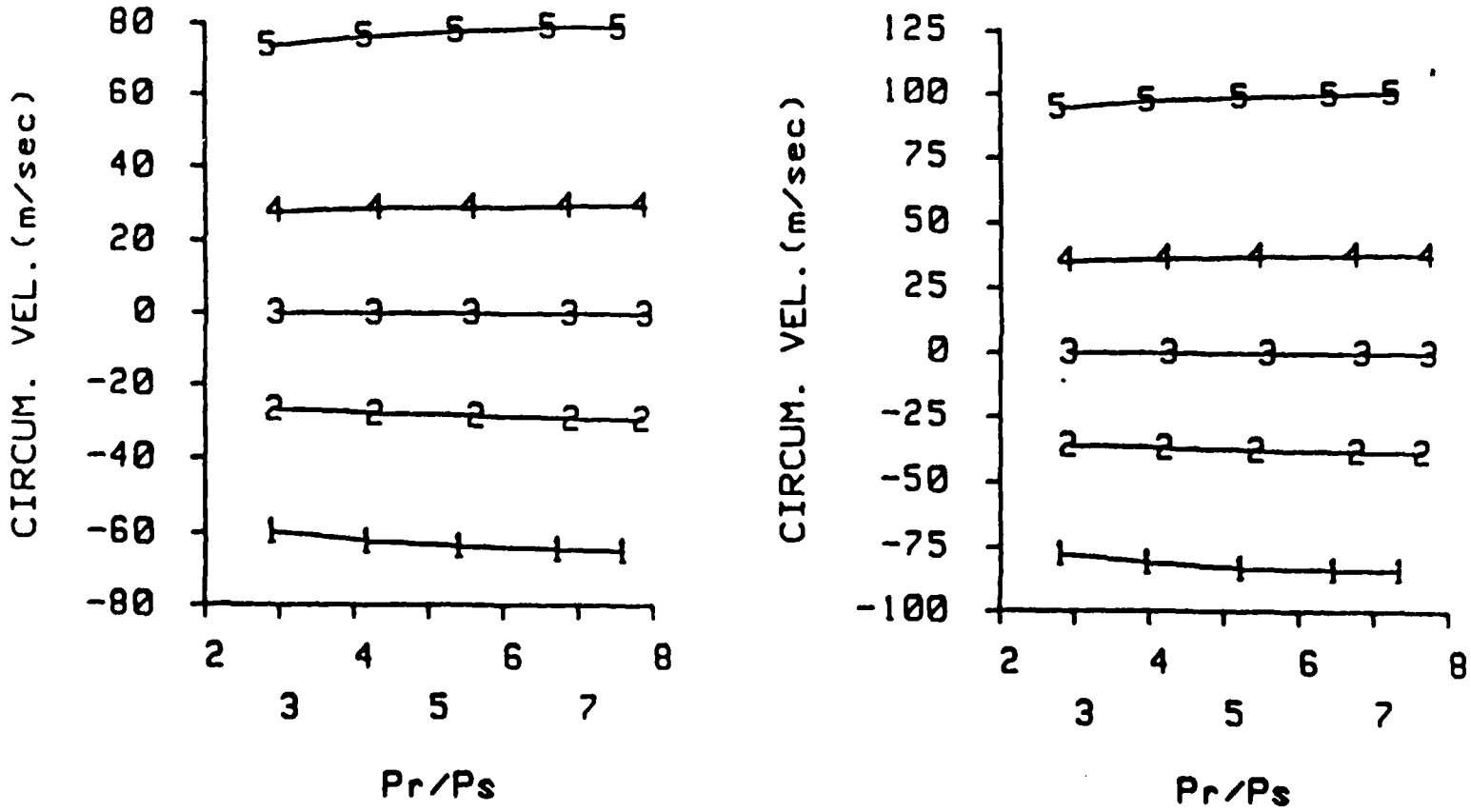

Fig. 6 Inlet circumferential velocities for seal 2. See table 2 for definitions. Teeth-on-rotor (left), teeth-on-stator (right).

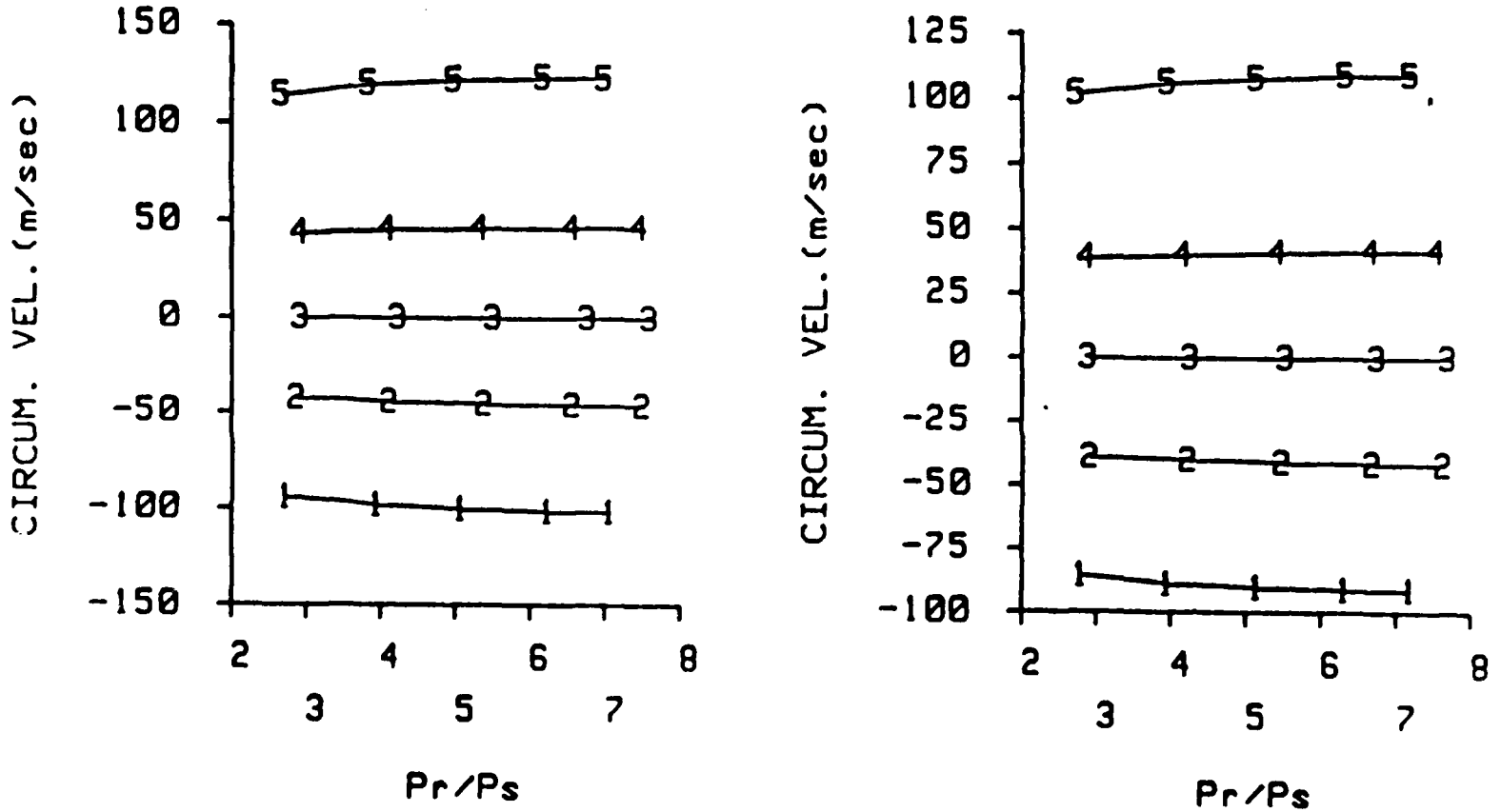

Fig. 7 Inlet circumferential velocities for seal 3. See table 2 for definitions. Teeth-on-rotor (left), teeth-on-stator (right).

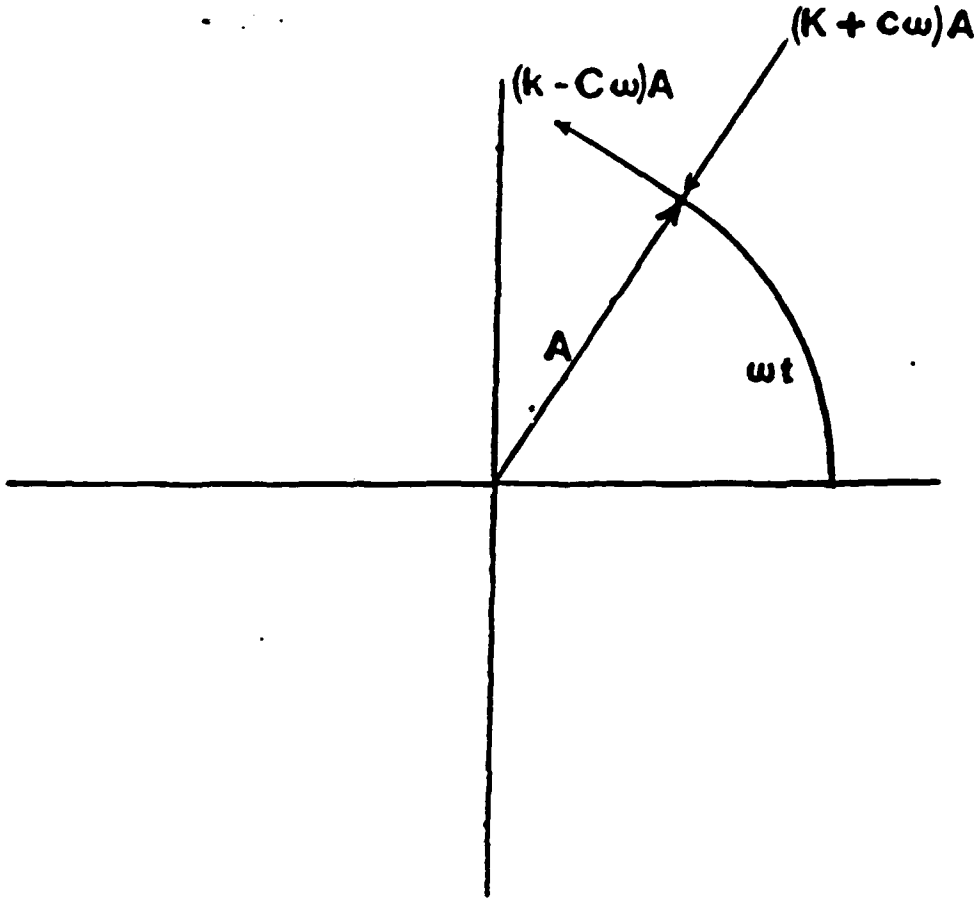

Fig. 8 Forces on a synchronously precessing seal.

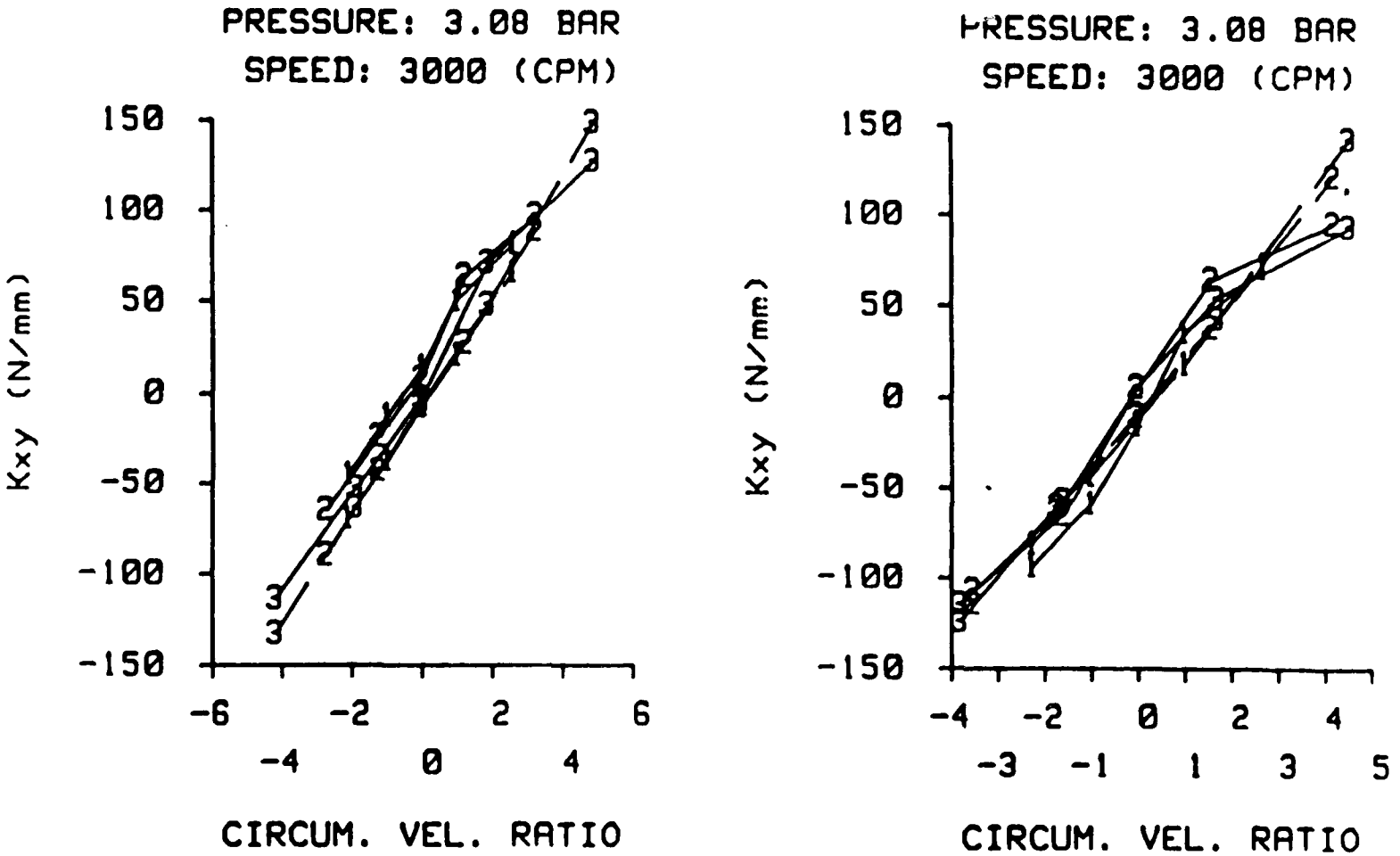

Fig. 9 A comparison of experimental and theoretical cross-coupled stiffness versus inlet circumferential velocity ratio at an inlet pressure of 3.08 bar and rotor speed of 3000 cpm. See table 1 for seal definitions. Teeth-on-rotor (left), teeth-on-stator (right).

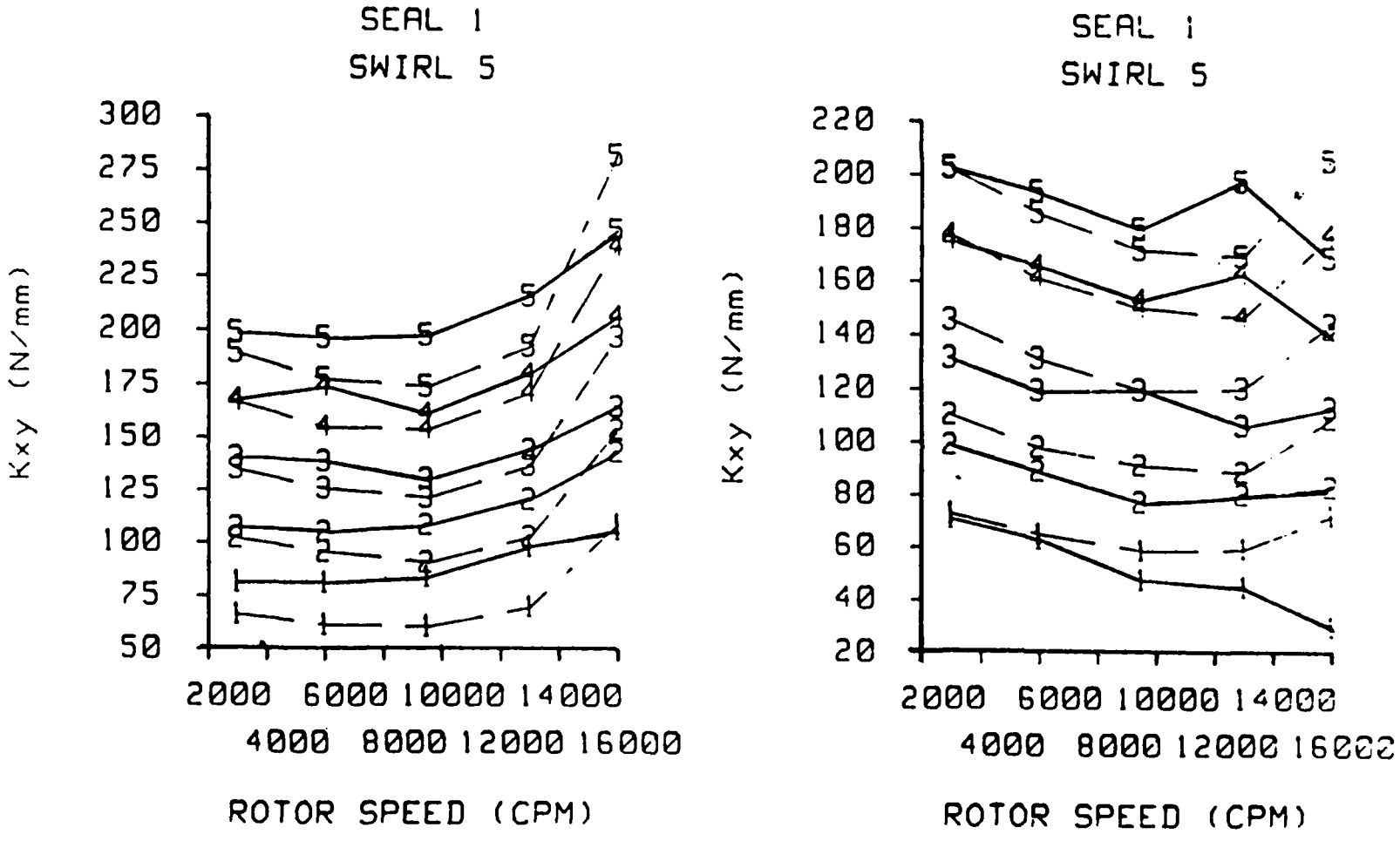

Fig. 10 A comparison of experimental and theoretical cross-coupled stiffness versus rotor speed for seal 1 and inlet circumferential velocity 5. See table 2 for definitions. Teeth-on-rotor (left), teeth-on-stator (right).

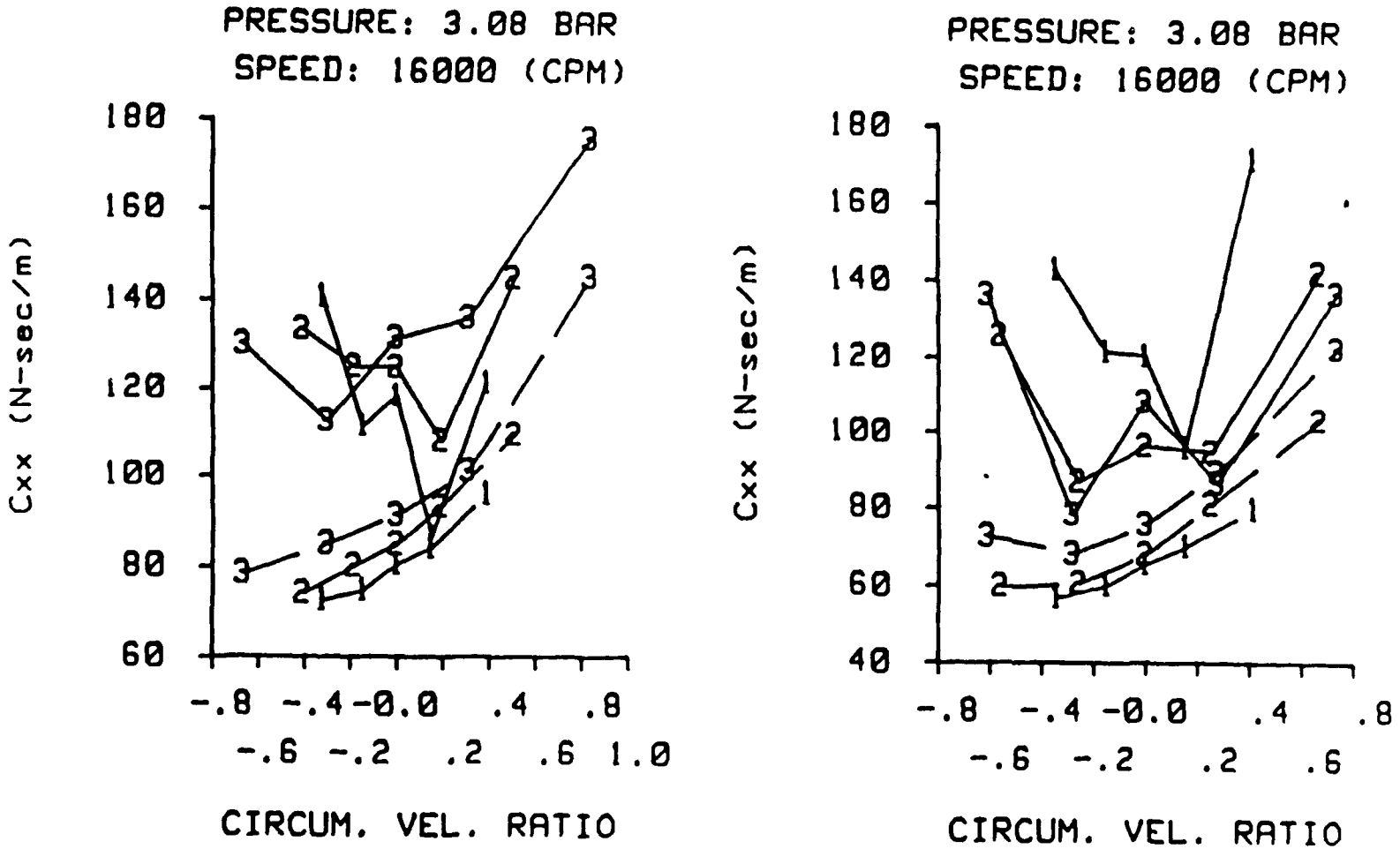

Fig. 11 A comparison of experimental and theoretical direct damping versus inlet circumferential velocity ratio at an inlet pressure of 3.08 bar and rotor speed of 16000 cpm. See table 1 for seal definitions. Teeth-on-rotor (left), teeth-on-stator (right).

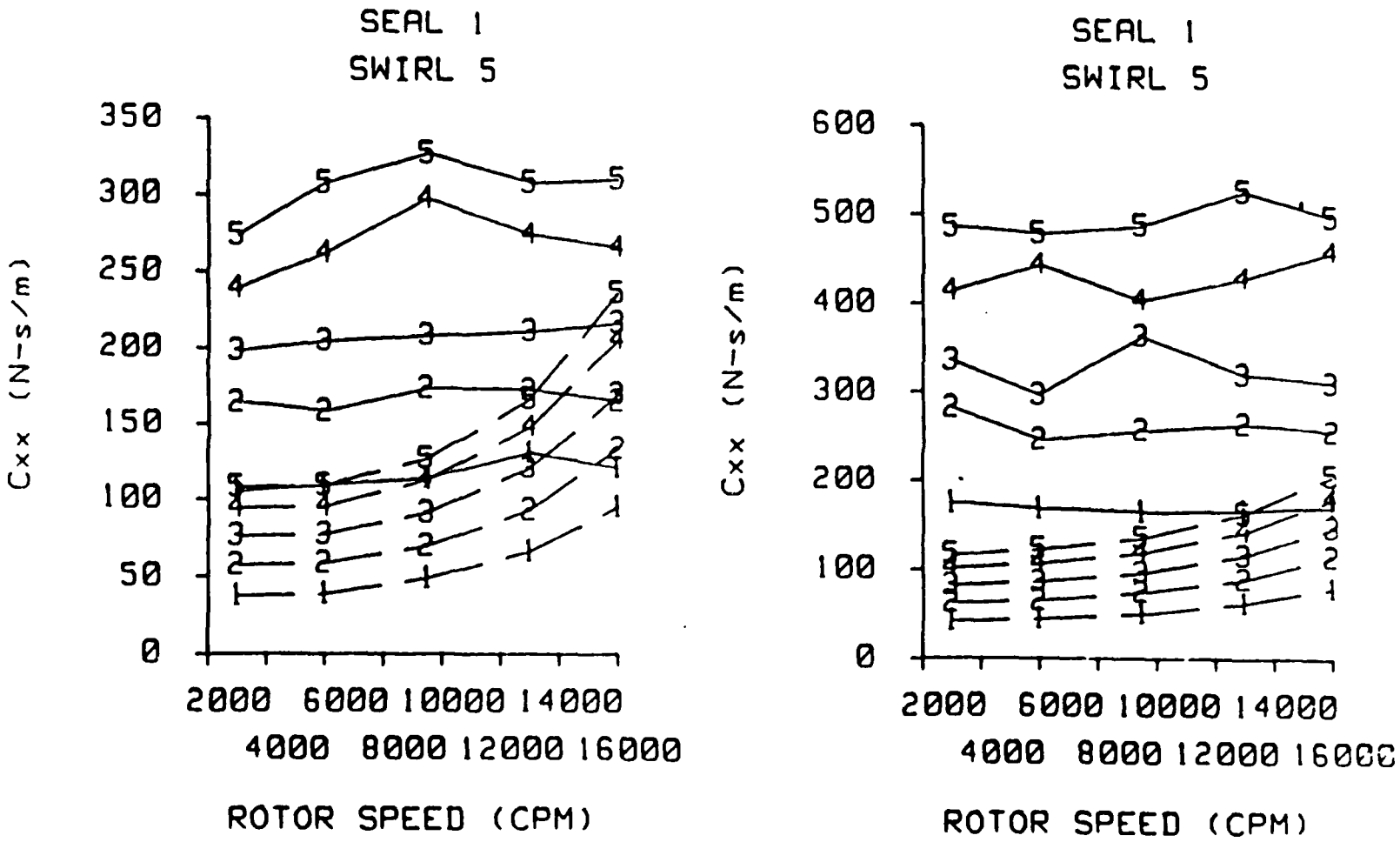

Fig. 12 A comparison of experimental and theoretical direct damping versus rotor speed for seal 1 and inlet circumferential velocity 5. See table 2 for definitions. Teeth-on-rotor (left), teeth-on-stator (right).

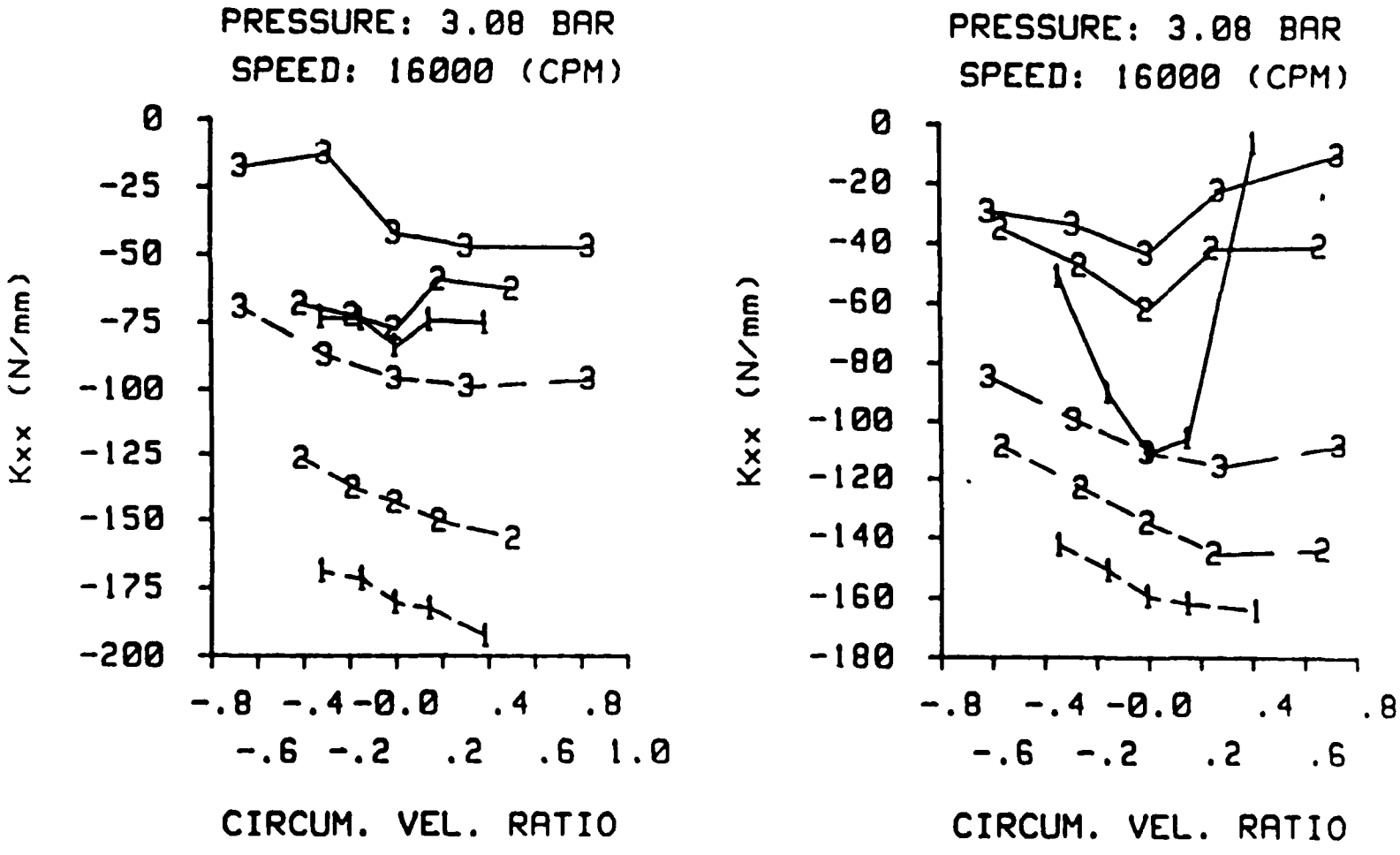

Fig. 13 A comparison of experimental and theoretical direct stiffness versus inlet circumferential velocity ratio at an inlet pressure of 3.08 bar and rotor speed of 16000 cpm. See table 1 for seal definitions. Teeth-on-rotor (left), teeth-on-stator (right).

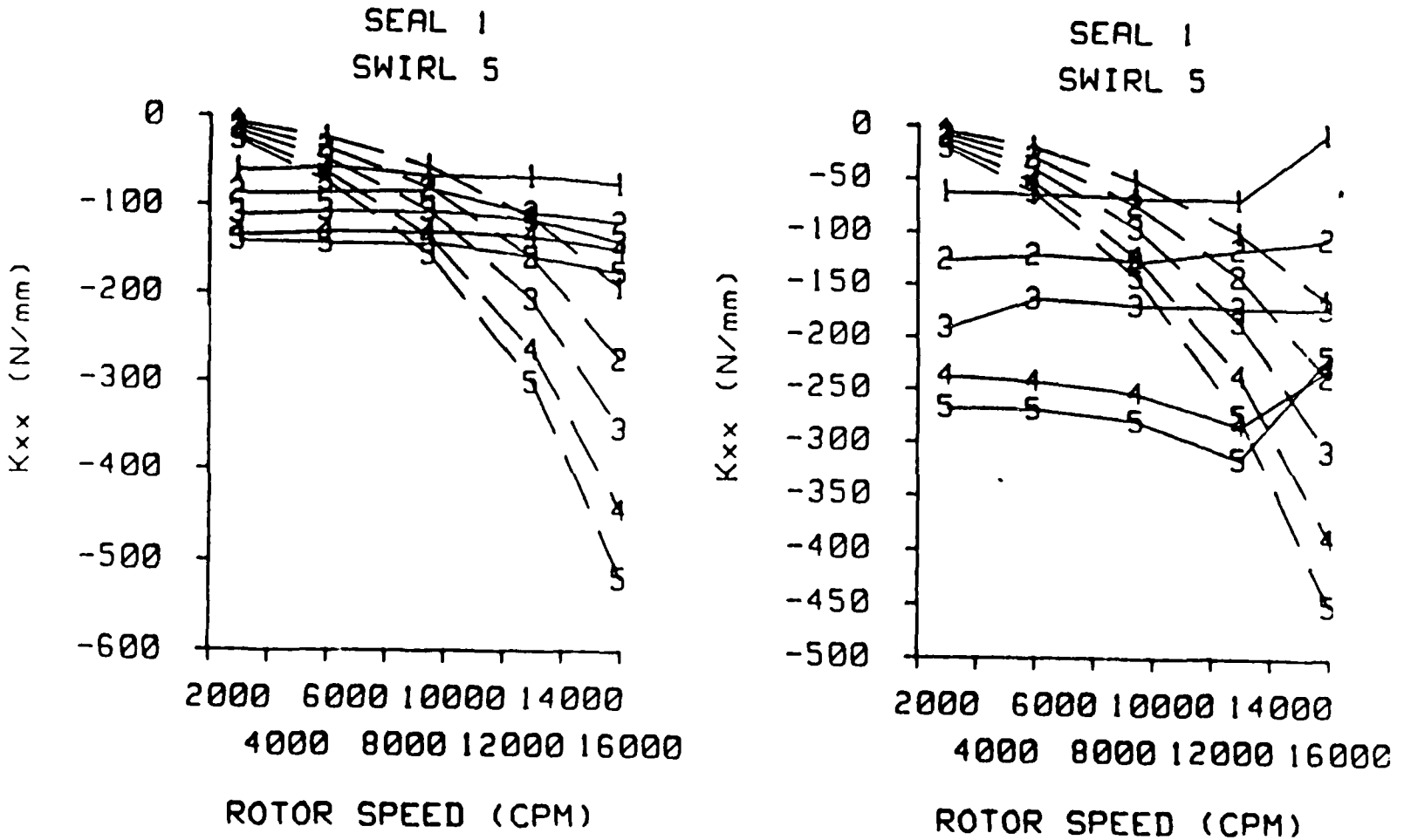

Fig. 14 A comparison of experimental and theoretical direct stiffness versus rotor speed for seal 1 and inlet circumferential velocity 5. See table 2 for definitions. Teeth-on-rotor (left), teeth-on-stator (right).

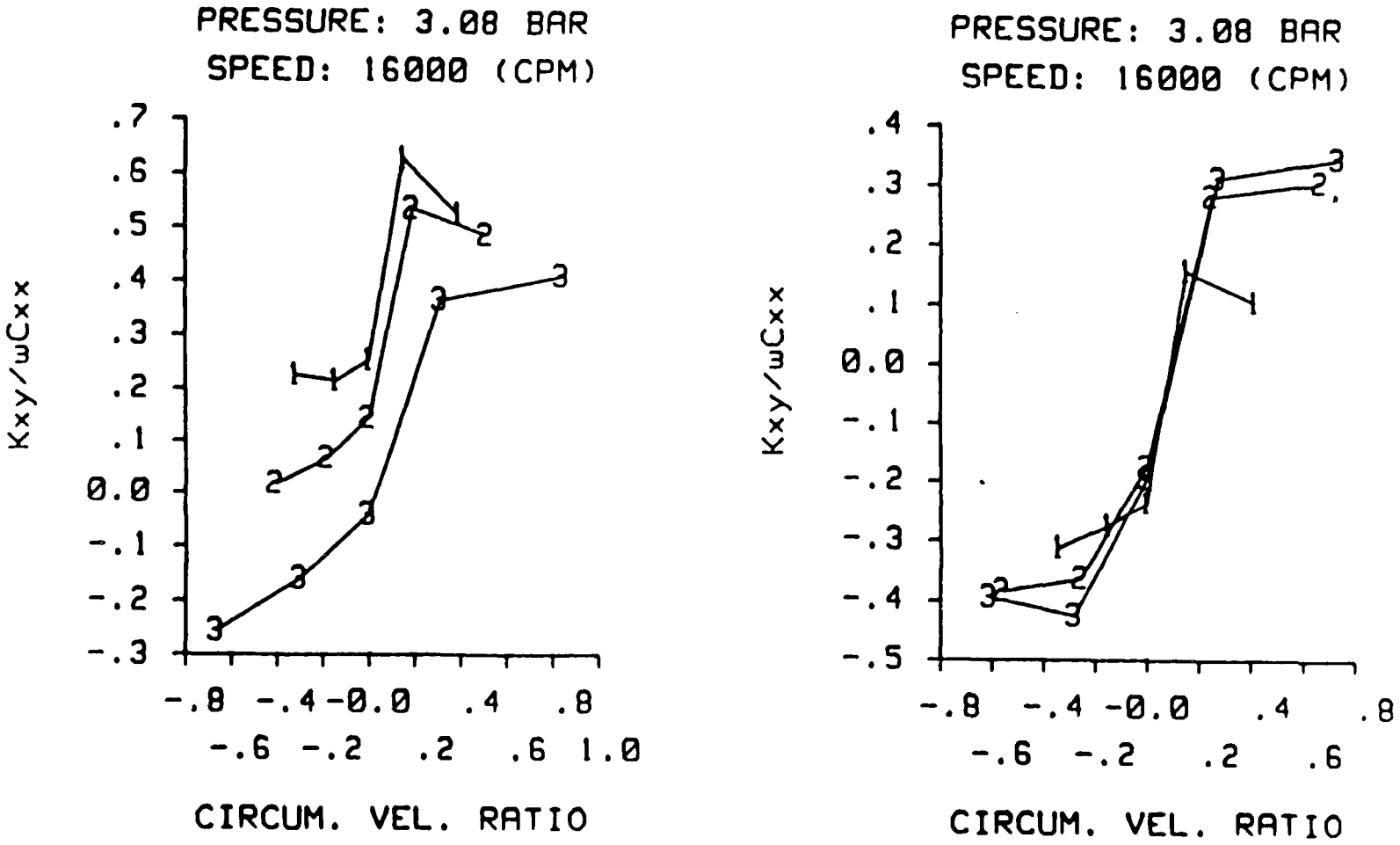

Fig. 15 Whirl frequency ratio versus inlet circumferential velocity ratio at an inlet pressure of 3.08 bar and rotor speed of 16000 cpm. Shake frequency 74.6 Hz. See table 1 for seal clearance definitions. Teeth-on-rotor (left), teeth-on-stator (right).

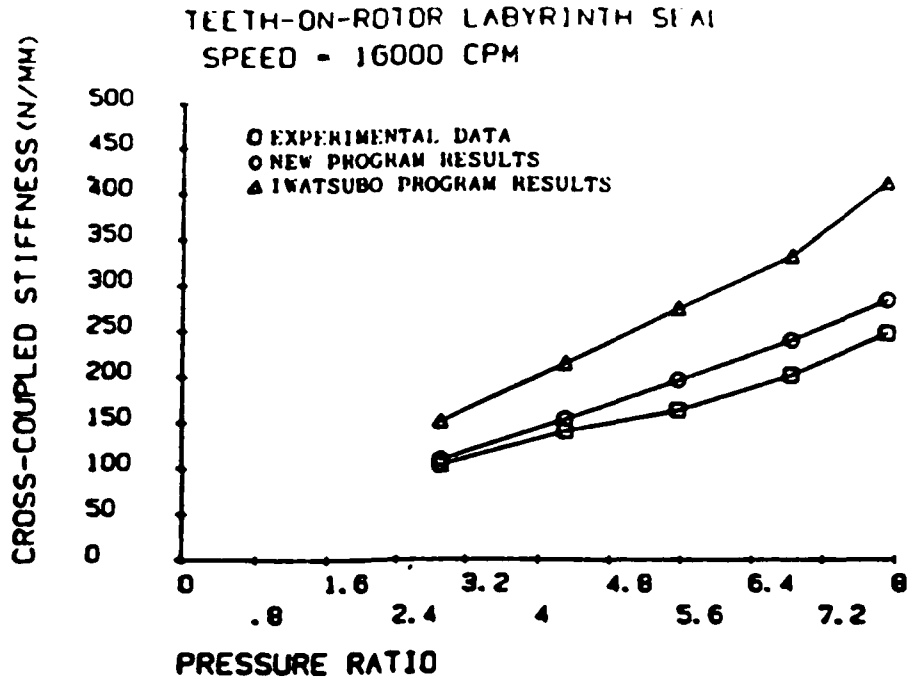

Fig. 16 A comparison of experimental and theoretical results of this report with those of [13] for cross-coupled stiffness.

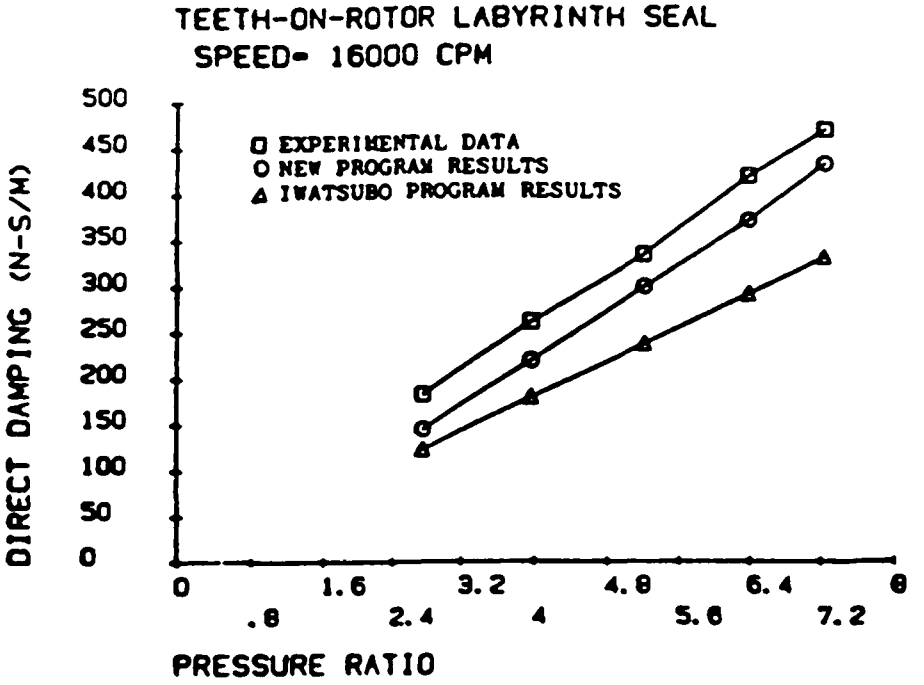

Fig. 17 A comparison of experimental and theoretical results of this report with those of [13] for direct damping.

Appendix B

Rhode, D. L. and Hensel, S. J., "Three-Dimensional Computation of Rotordynamic Force Distributions in a Labyrinth Seal," accepted for presentation at the ASME/AIAA First National Fluid Dynamics Congress, Cincinnati, OH, 24-28 July 1988.

Rhode, D. L. and Hensel, S. J., "Labyrinth Seal Rotordynamic Forces Predicted with a Three-Dimensional Navier-Stokes Computer Code," accepted for presentation at the 24th AIAA/ASEE/ASME/SAE Joint Propulsion Conference, Boston, MA, 11-14 July 1988.

Rhode, D. L. and Nail, G. H., "Computation of Cavity-By-Cavity Flow Development in Generic Labyrinth Seals," submitted for presentation at the ASME International Computers in Engineering Conference, San Francisco, CA, 31 July - 3 August 1988.

THREE-DIMENSIONAL COMPUTATION OF ROTORDYNAMIC FORCE DISTRIBUTIONS IN A LABYRINTH SEAL

D.L. Rhode** and S.J. Hensel*

Turbomachinery Laboratories

Mechanical Engineering Department

Texas A&M University

College Station, Texas 77843

---

* Graduate Student

** Associate Professor

ABSTRACT

A numerical method employing a finite difference approach for calculating the rotordynamic force on eccentric,whirling, labyrinth seals has been developed. The SIMPLER algorithm along with QUICK differencing is used to calculate the flowfield within a seal. A modified bipolar coordinate system accurately describes the geometry of an eccentric seal. The high Reynolds number $k - \epsilon$ turbulence model is utilized, which can handle subsonic compressible or incompressible flows. A three–percent eccentric single labyrinth cavity rotating at 5,000 c.p.m. was investigated with three different inlet swirl conditions, each with and without a whirl orbit frequency of 2500 c.p.m. The fluid was air with an inlet axial velocity near Mach 0.2. Detailed force, pressure and shear stress distributions within the cavity are presented. The results indicate that the pressure component accounts for 99 percent of the rotordynamic force. Whirl seems to have little effect on the force, and the downstream tooth of the cavity makes a very significant contribution to this quantity.

NOMENCLATURE

a	radius of tooth periphery
b	stator radius
c	clearance
C	convection coefficient
$C_{\epsilon 1}$	turbulence constant
$C_{\epsilon 2}$	turbulence constant
C_μ	turbulence constant
D	diffusion coefficient
$dx(i)$	displacement along general orthogonal coordinate lines
F	rotordynamic force
h	scale factor
$H_i(j)$	coordinate variation term
k	turbulence kinetic energy
l	turbulence length scale
L	seal cavity pitch
p	pressure
P_o	reference pressure
p^*	pressure re-defined by Eq. 23
r	polar coordinate
s	distance
U	x^1 velocity component
U_i	velocity expressed in cartesian tensor notation
$U(i)$	velocity expressed in general orthogonal coordinate system
V	x^2 velocity component

W	x^3 velocity component
x_i	general coordinate expressed in cartesian tensor notation
x^i	general orthogonal coordinate
z	transformation variable
A	flux coefficient
C_p	specific heat
e	eccentric distance ratio
H	stagnation enthalpy
P	production of turbulent kinetic energy
Pr	Prandtl number
S_p	source term
S_u	source term
T	temperature
V	total velocity
V^*	reference velocity
α	constant
β	bipolar coordinate parameter
γ	bipolar coordinate parameter
Γ	diffusion coefficient
δ_{ij}	Kronecker delta
ϵ	turbulence energy dissipation
ε	eccentricity ratio
θ	polar coordinate
μ	viscosity
ξ	transformation variable

ρ	bipolar coordinate, density
σ	constant in transport equations
τ	stress
τ^*	anisotropic stress
ϕ	bipolar coordinate
ψ	general transport quantity
ω	rotational frequency
Ω	whirling frequency

Subcripts

eff	effective (laminar plus turbulent)
i	index
in	inlet
j	index
l	index
lam	laminar
out	exit
r	radial
t	tangential
B	bottom face of cell
E	east face of cell
N	north face of cell
P	p-cell node
S	south face of cell
T	top face of cell
W	west face of cell

Superscript

*	nondimensional quantity

INTRODUCTION

Labyrinth seals are usually used in pumps, compressors, and turbines to limit internal leakage. The labyrinth seal was first applied in a steam turbine near the turn of the century. The idea was to create a flow path between high and low pressure zones that would convert pressure head into kinetic energy, which was then dissipated. This was accomplished by a series of cavities. The restriction between each pair of cavities in the flow path converts the pressure head into mean flow kinetic energy, and the expansion in the flow path dissipates the kinetic energy by viscous losses. Figure 1 shows a bank of generic labyrinth cavities and the resulting streamlines due to leakage. Although seals are very successful in limiting internal leakage, they are one of the sources of the self–excited vibration of the turbomachine rotor.

Self–excited vibration is generally subsynchronous, i.e. the rotor whirls within it's housing at a frequency below the rotational frequency. This vibration limits operating speeds and can be extremely destructive to the turbomachine. Although the physics of the shaft vibration is understood, a quantitative analysis of the forces which cause the excitation is not complete. The cause of self vibration is a net force imbalance on the rotor, and this imbalance occurs when the rotor is displaced from the geometric center of its housing.

Numerous attempts to analyze the destabilizing forces due to leakage through labyrinth seals have been made. Analytical, numerical, and experimental investigations have been conducted. Most of the analytical models are complex and use restrictive assumptions. Fujikawa [1] and Jenny [2] used a two–control–volume analytical approach, and both used empirical data extensively. Iwatsubo [3] considered time dependent flow area change, but neglected area change in the circumferential

direction. Recently, Childs [4,5,6] improved Iwatsubo's [3] method and obtained improved results. Kurohashi [7] introduced a variable flow coefficient for annular seals and obtained reasonable results for the cross-coupled force. The fluid mechanics associated with an eccentric labyrinth seal may be too complex to accurately model using an analytical method. Dietzen and Nordman [8] used a finite difference method in conjuction with a perturbation analysis to determine force coefficients for annular seals. Although the method appears to be promising, the author did not compute labyrinth seals. Baumgartner [9] used analytical methods to simplify the equations, which were then solved numerically. Tam and Przekwas [10] used a full three-dimensional finite difference analysis and obtained the most detailed results to date.

Experimental measurements of the rotordynamic coefficients associated with labyrinth seals are quite scarce. Wachter and Benckert [11,12,13] were the first to measure stiffness coefficients, but much of the results are for nonrotating seals. Wright [14] measured single cavity seals with teeth on the rotor. Childs [4,5,6] appears to have obtained the most comprehensive set of measurements. Rotational speed, inlet swirl velocity, and pressure drop across the seals were all varied in these measurements. Seals with teeth on the rotor as well as teeth on the stator were used. Rajakumar [15] measured pressure in the circumferential direction and measured forces at large eccentricities.

COMPUTATIONAL APPROACH

For the present study it has been assumed that the shaft undergoes a circular whirl orbit, the center of which coincides with that of the housing. Further, a single cavity of a multi-cavity seal of teeth-on-rotor design as shown in Figure 1 is considered. Note that the periphery of the teeth and the base of the seal cavity are

concentric. Thus, cylindrical coordinates are well suited to describe the geometry within the seal cavity. However, in the tooth clearance region outside of the cavity, bipolar coordinates are used because of the eccentricity of the shaft. Specifically, it is the modified bipolar coordinates which were choosen because they reduce to cylindrical coordinates in the limit as eccentricity approaches zero. Figure 2 shows such a finite difference grid within the gap region.

Wood [16] used modified bipolar coordinates to solve the fluid dynamics associated with eccentric rotating cylinders in general. Consider two circular cylinders of radii a and b. Let the centers of the two cylinders be a distance ae apart. If the eccentricity ε and the clearance c are defined as

$$\varepsilon = \frac{ae}{c} \tag{1}$$

and

$$c = (b - a) \tag{2}$$

then modified bipolar coordinates are defined by the transformation

$$z = \frac{a(\xi + \gamma)}{1 + \gamma\xi} \tag{3}$$

$$z = re^{i\theta} \tag{4}$$

$$\xi = \rho e^{i\phi} \tag{5}$$

where

$$\gamma = -2\varepsilon[(b/a)^2 - 1 - \varepsilon^2 + \sqrt{(b^2/a^2 - 1 - \varepsilon^2)^2 - 4\varepsilon^2}]^{-1} \tag{6}$$

and

$$\beta = \frac{b/a + \epsilon - \gamma}{1 - (b/a)\gamma - \varepsilon\gamma} \tag{7}$$

Figure 3 shows the geometry and coordinate system associated with modified bipolar coordinates. Curves of constant ρ are circles in the modified bipolar coordinate system. The inner circle is $\rho = 1$, and the outer is $\rho = \beta$. The conformal transformation shown above provides a method to transform any point (ρ, ϕ) in the modified bipolar coordinate system into an equivalent point (r, θ) in the cylindrical coordinate system.

The transport equations to be solved are presented in Cartesian tensor notation. Neglecting body forces, the steady-state continuity and momentum equations are

$$\frac{\partial(\rho U_i)}{\partial x_i} = 0 \tag{8}$$

$$\frac{\partial(\rho U_i U_j)}{\partial x_i} = -\frac{\partial p}{\partial x_j} - \frac{\partial \tau_{ij}}{\partial x_i} \tag{9}$$

where ρ, U_i, and p are the time averaged density, velocity and pressure. The Reynolds stresses are determined by the $k - \epsilon$ turbulence model. The turbulent energy and energy dissipation transport equations are

$$\frac{\partial(\rho U_i k)}{\partial x_i} = \frac{\partial}{\partial x_i}\left(\frac{\mu_{eff}}{\sigma_k}\frac{\partial k}{\partial x_i}\right) + \mathrm{P} - \rho\epsilon \tag{10}$$

$$\frac{\partial(\rho U_i \epsilon)}{\partial x_i} = \frac{\partial}{\partial x_i}\left(\frac{\mu_{eff}}{\sigma_\epsilon}\frac{\partial \epsilon}{\partial x_i}\right) + \frac{\epsilon}{k}(C_{\epsilon 1}\mathrm{P} - C_{\epsilon 2}\rho\epsilon) \tag{11}$$

where the stress is calculated using

$$\tau_{ij} = -\mu_{eff}\left(\frac{\partial U_i}{\partial x_j} + \frac{\partial U_j}{\partial x_i}\right) + \frac{2}{3}(\rho k + \mu_{eff}\frac{\partial U_l}{\partial x_l})\delta_{ij} \tag{12}$$

The production of kinetic energy and the effective viscosity are given by

$$\mathrm{P} = -\left(\frac{\partial U_i}{\partial x_j}\right)\tau_{ij} \tag{13}$$

$$\mu_{eff} = \frac{C_\mu \rho k^2}{\epsilon} + \mu \tag{14}$$

The constants C_μ, $C_{\epsilon 1}$, $C_{\epsilon 2}$, σ_k, and σ_ϵ are given values of $.09, 1.44, 1.92, 1.0,$ and 1.217. This is in accordance with the standard $k-\epsilon$ model investigated by Launder and Spalding [17]. For inlet Mach numbers greater than 0.3, the energy equation must also be employed. The stagnation enthalpy form

$$\frac{\partial(\rho U_i \mathrm{H})}{\partial x_i} - \frac{\partial}{\partial x_j}(\Gamma_\mathrm{H} \frac{\partial \mathrm{H}}{\partial x_j}) = \frac{\partial}{\partial x_j}[U_l \tau_{lj} - \Gamma_\mathrm{H} \frac{\partial}{\partial x_j}(\frac{\mathrm{V}^2}{2})] \tag{15}$$

is included where

$$\Gamma_\mathrm{H} = \frac{\mu_{eff}}{\mathrm{Pr}} \tag{16}$$

Static temperature is calculated using

$$\mathrm{T} = \frac{\mathrm{H} - \frac{\mathrm{V}^2}{2}}{\mathrm{C_p}} \tag{17}$$

The above equations can be transformed into relations using general orthogonal coordinates. Pope [18] suggests such a procedure using general tensor notation. Under this procedure the equations retain their original form and simplicity as much as possible, and they remain in a form where each term has physical significance.

The divergence operator $\nabla(i)$ and coordinate variation term $H_i(j)$ needed to transform the transport equations into general orthogonal coordinates are

$$\nabla(i) = \frac{\mathrm{h}_i}{|\mathrm{h}|} \frac{\partial}{\partial x(i)} \frac{|\mathrm{h}|}{\mathrm{h}_i} \tag{18}$$

$$H_i(j) = \frac{1}{\mathrm{h}_i \mathrm{h}_j} \frac{\partial \mathrm{h}_i}{\partial x_j} \tag{19}$$

Here h_i represent scale factors and $|\mathrm{h}|$ is the product of the scale factors. Following Pope's [18] transformation procedure, the transport equations become

$$\nabla(i)[\rho U(i)] = 0 \tag{20}$$

$$\nabla(i)[\rho U(i)U(j) + \tau^*(ij)] = -\frac{\partial p^*}{\partial x(j)} + H_i(j)[\rho U(i)U(i) + \tau^*(ii)] - H_j(i)[\rho U(i)U(j) + \tau^*(ij)] \tag{21}$$

$$\nabla(i)[\rho U(i)\psi - \frac{\mu_{eff}}{\sigma_\psi}\frac{\partial \psi}{\partial x(i)}] = S_\psi \tag{22}$$

The last equation is a general transport equation for any quantity ψ. Note that the isotropic component of stress has been added to the pressure giving

$$p^* = p + \frac{2}{3}\rho k + \frac{2}{3}\mu_{eff}\nabla(i)U(i) \tag{23}$$

and τ^* has the anisotropic stress as

$$\tau^*(ij) = -\mu_{eff}[\frac{\partial U(i)}{\partial x(j)} + \frac{\partial U(j)}{\partial x(i)} - U(i)H_i(j) - U(j)H_j(i) + 2U(l)H_i(l)\delta_{ij}] \tag{24}$$

The production of turbulent energy becomes

$$\mathrm{P} = -\tau^*(ij)[\frac{\partial U(i)}{\partial x(j)} - U(j)H_j(i) + U(l)H_i(l)\delta_{ij}] - \frac{2}{3}[\rho k + \mu_{eff}\nabla(i)U(i)]\nabla(l)U(l) \tag{25}$$

after the transformation to general orthogonal coordinates. All of the transport equations can be written as

$$\nabla(1)[\rho U(1)\psi - \Gamma_{x(1)}\frac{\partial \psi}{\partial x(1)}] + \nabla(2)[\rho U(2)\psi - \Gamma_{x(2)}\frac{\partial \psi}{\partial x(2)}] + \nabla(3)[\rho U(3)\psi - \Gamma_{x(3)}\frac{\partial \psi}{\partial x(3)}] = S_\psi \tag{26}$$

where all $\Gamma_{x(i)}$ and S_ψ are defined in Table 1 for the appropriate ψ, and U, V, W correspond to $U(1), U(2), U(3)$.

The algebraic finite difference equations can be easily derived by applying the Gauss Divergence theorem to Eq. 26. The integration is performed over the entire

control volume. Figure 4 depicts a general three-dimensional control volume. The variable ψ is stored at nodes P,N,S,E,W,T, and B. Applying the theorem yields

$$\left[\int_{x^3_-}^{x^3_+}\int_{x^2_-}^{x^2_+}\rho U(1)\psi-\Gamma_x\frac{\partial\psi}{\partial x}dx(2)dx(3)\right]_{x^1_-}^{x^1_+}+\left[\int_{x^3_-}^{x^3_+}\int_{x^1_-}^{x^1_+}\rho U(2)\psi-\right.$$
$$\left.\Gamma_y\frac{\partial\psi}{\partial y}dx(1)dx(3)\right]_{x^2_-}^{x^2_+}+\left[\int_{x^2_-}^{x^2_+}\int_{x^1_-}^{x^1_+}\rho U(3)\psi-\Gamma_z\frac{\partial\psi}{\partial z}dx(1)dx(2)\right]_{x^3_-}^{x^3_+}= \tag{27}$$
$$\int_{x^3_-}^{x^3_+}\int_{x^2_-}^{x^2_+}\int_{x^1_-}^{x^1_+}S_\psi dx(1)dx(2)dx(3)$$

where the left side contains convection and diffusion and the right-hand side contains the source term. This form is similar to that for Cartesian coordinates. Note that $dx(1), dx(2)$, and $dx(3)$ are physical lengths in the general orthogonal coordinate system. Thus, the appropriate scale factors are required to compute the integrals. Upon integration the resulting algebraic finite difference equation is of the form

$$\psi_P(A_N+A_S+A_E+A_W+A_T+A_B)=A_N\psi_N+A_S\psi_S$$
$$+A_E\psi_E+A_W\psi_W+A_T\psi_T+A_B\psi_B+(S_\psi)_P vol \tag{28}$$

It is well known that the hybrid differencing scheme produces false diffusion under certain conditions when large control volume Peclet numbers exist. False diffusion occurs if the streamlines of the flowfield are oblique to the grid lines and a nonzero gradient of the dependent variable normal to the flow exists. This false diffusion is a truncation error in the finite difference formulation. The QUICK differencing scheme of Leonard [19] generally reduces false diffusion. Rhode et al [20] have previously implemented QUICK into a two-dimensional labyrinth seal code. Substitution of the corresponding interpolation functions into Eq. 27 , or use

of the hybrid upwind–central differencing scheme, yields

$$\psi_P = \frac{\sum_i A_i \psi_i + Su}{\sum_i A_i - Sp} \tag{29}$$

where i =E,W,N,S,T,B,EE,WW,NN,SS and the last four neighbors are not needed if the hybrid scheme is used.

A system of staggered grids is used to store the variables of interest as is done in the TEACH code [21]. The values of pressure, turbulent kinetic energy, turbulence dissipation, and enthalpy are stored at the intersection points of the primary grid, whereas each velocity component is stored on a separate grid.

The boundary conditions play an extremely important role in determining the solution to flow in the labyrinth seal. Wall functions based on the log law of the wall are used to determine the appropriate shear stress near a wall. Axial velocity, circumferential velocity, turbulence kinetic energy, and turbulence dissipation profiles were prescribed at the inlet. All of these inlet profiles were assumed to be uniform radially. The magnitude of these quantities, except for circumferential velocity, was determined by executing the program with equivalent conditions at the inlet and exit. This case corresponds to a fully developed, i.e. streamwise periodic cavity. From this computer run the circumferential variation of inlet axial velocity, turbulence energy, and energy dissipation, due to eccentricity, were all determined. The inlet circumferential velocity profile was also uniform in the radial direction and varied from case to case. At the circumferential location of largest clearance, this quantity was specified according to the problem of interest. All other circumferential locations were given an inlet value such that the swirl velocity conserved mass in the circumferential direction. The radial velocity was set to zero at the inlet for all circumferential locations. Pressure was prescribed at

AD-A197 185 THE MEASUREMENT AND PREDICTION OF ROTORDYNAMIC FORCES FOR LABYRINTH SEALS (U) TEXAS A AND M UNIV COLLEGE STATION TURBOMACHINERY LABS D W CHILDS ET AL MAR 88 2/3

UNCLASSIFIED AFOSR-TR-88-0662 F49620-82-K-0033 F/G 13/7 NL

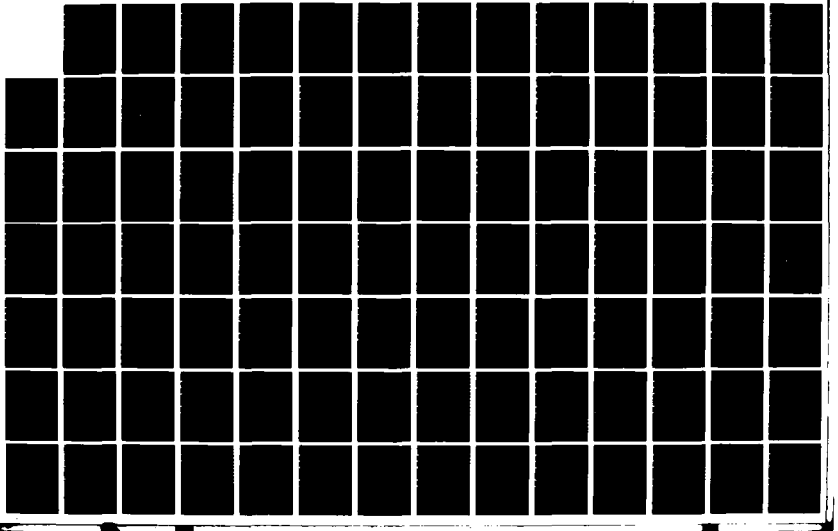

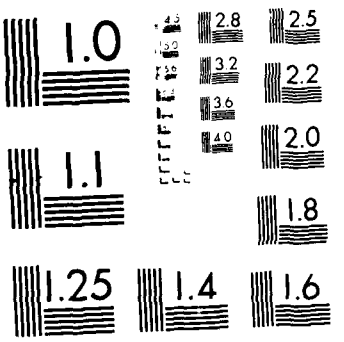

one nodal location and its value held constant during the numerical procedure. At this location pressure had a value of 3 atmospheres. All other pressure nodes were calculated on a relative basis with respect to this node. The stagnation enthalpy at the inlet was calculated using the inlet velocities and temperature.

Convection is dominant over diffusion at the exit, and the Hybrid upwind/central differencing scheme applied there requires no downstream boundary values. The axial velocity at the exit was set equal to the axial velocity at the upstream node plus a uniformly distributed percentage of the axial velocity increment required to conserve mass globally.

RESULTS AND DISCUSSION

The first cavity of a multi-cavity seal is considered throughout this work. Figure 5 depicts the cavity and shows the relevant dimensions. These dimensions were chosen because they constitute a generic cavity which is somewhat similar to those used in high performance turbomachines. Further, this geometry can be modelled with a uniform grid within the cavity. Due to the coordinate system arrangement the grid must be nonuniform in the gap region. Minimizing the grid nonuniformity as much as possible was desireable in aiding convergence. The eccentricity of the rotor was three percent of the clearance c in this analysis.

Computational Characteristics

A total of six converged solutions were obtained. In all six cases the rotational speed of the rotor was 5,000 cpm. The working fluid was air at 3.0 atm. and 294 K at the inlet. The axial Reynolds number $\mathrm{Re} = 2U_{in}c/\nu$ in all cases was 19,200, which corresponds to a Mach number near 0.2. The inlet conditions in all six cases were identical except for swirl velocity. Three different inlet swirl cases were investigated. These were approximately 30,60, and 90 percent of the rotational speed of the cavity, which correspond to tangential Reynolds numbers $\mathrm{Re}_\theta = 2W_{in}c/\nu$ of 1,315, 2,631, and 3,946. Each swirl case was considered with no whirl as well as half-speed forward whirl, i.e. 2,500 cpm.

A grid dependence study revealed that a grid of 22x22x17 nodes in the x-, r-, and θ-directions, respectively was sufficient to simulate the flowfield for this seal problem. Only the number of grid points in the circumferential direction was varied in the present grid independence study. In order to conserve computer resources, the number of grid nodes used in the axial and radial directions, 22x22, was chosen based on extensive previous grid dependence testing [22] at the same Mach number

using a concentric-rotor version of the computer program. Grids of 22x22x11, 22x22x17, and 22x22x25 were all used to solve the eccentric cavity whirling at half speed. All parameters used in the grid dependence study were similar to those used in the final computations. The 22x22x17 grid was required to determine the grid independent value for pressure drop across the cavity. The grid-independent results are presented in Figure 6.

Results

The distribution of the tangential force component within the cavity can be observed in Figure 7. This plot clearly shows that the downstream tooth contributes heavily to the total tangential force. Further, the effect of inlet swirl strength on this force component is only observed at the downstream tooth. This is attributed to the fact that the circumferential flow is developing within the cavity so that there is a different pressure distribution at the downstream tooth.

For the cases considered here, the radial force generally decreases slightly with increasing swirl. Note that this force component is not restoring the rotor to its original position, but is actually pushing it to larger eccentricities. These same general trends were measured by Leong [23] at small eccentricities. As with the tangential force, the flow over the downstream tooth significantly influences the net radial force as seen in Figure 8. Observe that swirl has little effect on the radial force distribution and that this force is smallest in the middle of the cavity, as for the tangential force.

It was determined that the net shear stress contribution to the total net radial force is less than one percent, as is the case with the net tangential force. As expected, the shear contribution to the radial force was a minimum when $W_{in}^{*} = 0.6$ because this is near the asymptotic value in which case there was negligible $\tau_{r\theta}$ stress

on the south wall.

As observed earlier, the pressure force virtually determined the net forces acting on a seal. The variation of pressure (relative to a reference value given below) in the circumferential direction at three locations along the rotor are plotted in Figures 9 through 11. The locations are on the upstream tooth, in the middle of the cavity, and on the downstream tooth. The reference pressures used to nondimensionalize the pressure in the polar plots, are 306,000 Pa, 310,400 Pa, and 321,800 Pa respectively.

As seen in Figure 9, swirl has little effect on pressure at the upstream tooth. The distribution of pressure is somewhat symmetrical about the axis through θ =180 degrees. This symmetry indicates that the tangential force component is smaller than the radial component at the upstream tooth.

In Figure 10 the pressure values are taken at the middle of the south wall of the cavity. Symmetry about the same axis is also observed, and swirl had little effect on this. At this mid-cavity location the tangential and radial forces were earlier seen to be at a minimum. Thus this circumferential pressure distribution is the closest to being perfectly symmetrical about the axis through θ =180 degrees and that through θ =90 degrees.

In Figure 11 the pressure distribution on the downstream tooth is given. Observe that the pressure distribution is not symmetric at all. This shows the large pressure forces on the downstream tooth seen earlier in Figures 7 and 8. Higher inlet swirl values increased this lack of symmetry, which caused an increase in the tangential force.

Although turbomachines frequently whirl at half-speed, the case of no whirl has also been studied previously [11,12,13]. The F_t^* distribution along the cavity

for the no–whirl case was plotted in Figure 12. These results are very similar to those for half–speed whirl shown in Figure 7. This was expected since for such small eccentricities the boundary conditions are nearly the same. Figure 13 is the no–whirl counterpart of Figure 8 for F_r^*. Again, quantitatively as well as qualitatively the results are very similar to the whirling case.

The Shear Stress

The shear stress distributions along the cavity walls provide previously unavailable insight into the basic flowfield. Although they were not found to contribute significantly to the force components, estimates of these are useful in the development of simpler models. Shear stresses are plotted along the wall and in the free shear layer for a specific theta value. The circumferential variation for a specific wall location is also given. Thus Figures 14 through 18 can be used to construct the entire three–dimensional shear stress distribution along the cavity walls and the free shear layer. Figure 14 shows the points labeled E,F,G, and H which are used to denote a specific location in the cavity. For example, wall FG is the south wall of the cavity, and EH is the free shear layer.

The variation of shear stress along the rotor surface at θ=0 degrees for all three inlet swirl cases at half–speed whirl can be seen in Figure 15. Although the τ_{rz} component does not vary with inlet swirl, $\tau_{r\theta}$ varies substantially and is largest for the low inlet swirl case. This is because the $\partial w/\partial r$ term in the expression for $\tau_{r\theta}$ is largest for low inlet swirl, as the shaft tangential velocity is much higher than that of the fluid. For the case of high inlet swirl, $\tau_{r\theta}$ is almost uniform. Note that the stresses are smallest in the corners of the cavity where the turbulence energy and thus the turbulent viscosity is small.

In Figure 16 the free shear layer stresses are shown. Again, τ_{rz} does not vary

with inlet swirl, and stress $\tau_{r\theta}$ is fairly uniform for the high swirl case. The $\tau_{r\theta}$ stress is highest near the upstream tooth, as this is again a region of very large $\partial W/\partial r$.

The shear stresses along the west wall of the cavity at θ=0 degrees can be seen in Figure 17. Stress τ_{xr} does not vary with inlet swirl, and $\tau_{x\theta}$ is largest for the low inlet swirl case as expected. Stress $\tau_{x\theta}$ is rather uniform for high swirl, and the maximum value of $\tau_{x\theta}$ occurs near the shear layer. The shear stresses along the east wall of the cavity at θ=0 degrees are presented in Figure 18. The basic characteristics are generally similar to those in Figure 17. That is τ_{rx} does not vary with inlet swirl, and $\tau_{x\theta}$ is largest for low inlet swirl. The maximum of stress $\tau_{x\theta}$ is near the shear layer due to the high turbulence level there.

CONCLUSIONS

A computer program has been developed for the prediction of rotordynamic forces on an eccentric whirling cavity. Eccentricity, shaft speed, whirl rate, and various inlet conditions can be specified by the user. This work demonstrated that numerical methods can be used to determine rotordynamic forces on labryinth seals, as well as the bulk flow analytic models used in the past. The solution obtained from the computer code appeared to be reasonable and contained the expected flowfield features. Comparison of forces with Leong [22] showed qualitative agreement. Unfortunately, force measurements for a single teeth-on-rotor labyrinth cavity are not available for quantitative comparison. However, multi-cavity predictions for comparison with measurements are forthcoming.

For the present case of one generic cavity at three percent eccentricity, rotating at 5,000 r.p.m., whirling at 2,500 r.p.m., and with an inlet axial velocity near Mach 0.2, the following can be asserted:

1. An increase in inlet swirl velocity increased the tangential force. The direction of the force would accelerate the whirl.

2. The largest contribution by far to the total tangential force was from the pressure imbalance on the periphery of the downstream tooth. It is expected that the tangential force can be affected by altering the geometry of the cavity at the downstream tooth. Specifically, the thickness and/or geometry of the tooth periphery is apparently a very important consideration when one is designing a bank of labyrinth seal cavities in high performance turbomachinery where rotordynamic instabilities are a problem.

3. The radial force was not restoring the shaft, but was pushing the shaft to larger eccentricities.

4. The shear stress made little, nearly one percent, contribution to the total tangential and radial force.

5. Whirl had a very small effect on the forces.

ACKNOWLEDGEMENT

The financial support of AFOSR is gratefully acknowledged.

REFERENCES

1 Fujikawa, T., Kameoka, T., Abe, T., "A Theoretical Approach to Labyrinth Seal Forces," in *Rotordynamic Instability Problems in High Performance Turbomachinery*, Texas A&M University, May 28–30, 1984.

2 Jenny, R. J., Wyssmann, H. P., Pham, T. C., "Prediction of Stiffness and Damping Coefficients for Centrifugal Compressor Labyrinth Seals," in *ASME International Gas Turbine Conference and Exhibit*, Amsterdam, Netherlands, June 4–7, 1984.

3 Iwatsubo, T., "Evaluation of Instability Forces of Labyrinth Seals in Turbines or Compressors," in *Rotordynamic Instability Problems in High Performance Turbomachinery*, Texas A&M University, May 12–14 1980.

4 Childs, D. W. and Scharrer, J. K., "An Iwatsubo–Based Solution For Labyrinth Seals," in *ASME International Gas Turbine Conference*, Houston, 1985.

5 childs, D. W. and Scharrer, J. K., "Theory Versus Experiment For The Rotordynamic Coefficients Of Labyrinth Gas Seals:Part 1–A Two Control Volume Model," in *ASME Bienniel Conference on Mechanical Vibrations and Noise*, Boston, 1987.

6 childs, D. W. and Scharrer, J. K., "Theory Versus Experiment For The Rotordynamic Coefficients Of Labyrinth Gas Seals:Part 2–A Two Comparison To Experiment," in *ASME Bienniel Conference on Mechanical Vibrations and Noise*, Boston, 1987.

7 Kurohashi, M., Inoue, Y., Abe, T. and Fujikawa, T., "Spring and Damping Coefficients of the Labyrinth Seal," in *Second International Conference on Vibrations in Rotating Machinery*, Cambridge, England, 1980.

8 Dietzen, F. J., and Nordman, R., "Calculating Rotordynamic Coefficients of Seals by Finite Difference Techniques," in *Rotordynamic Instability Problems in High Performance Turbomachinery*, Texas A&M University, 1986.

9 Baumgartner, M., "Evaluation Of Exciting Forces In Turbomachinery Induced By Flow In Labyrinth Seals," in *ASME Biennial Conference on Mechanical Vibrations and Noise*, Boston, 1987.

10 Tam, L. T., and Przekwas, A. J., "Numerical And Analytical Study Of Fluid Dynamic Forces In Seals And Bearings," in *ASME Biennial Conference on Mechanical Vibrations and Noise*, Boston, 1987.

11 Wachter, J., and Benckert, H., "Querkrafte aus Spaltdichtungen-Eine Mogliche Ursache fur die Laufunruhe von Turbomaschinen," *Atomkernenergie*, vol. 32, pp. 239-246, 1978.

12 Wachter, J., and Benckert, H., "Flow Induced Spring Coefficients of Labyrinth Seals for Applications in Rotordynamic," in *Rotordynamic Instability Problems of High Performance Turbomachinery*, Texas A&M University, May 12-14, 1980.

13 Benckert, H., "Stromungsbedinte Federkennwerte in Labyrinthdichtungen," *Research Report*, Doctoral dissertation, University of Stuttgart, 1980.

14 Wright, D.V., "Labyrinth Seal Forces on a Whirling rotor," in *ASME Applied Mechanics, Bioengineering, and Fluids Engineering Conference*, Houston, Texas, June 20-22, 1983.

15 Rajakumar, C., "Experimental Investigations Of Rotor Whirl Excitation Forces Induced By Labyrinth Seal Flow," in *ASME Bienniel Conference on Mechanical Vibrations and Noise*, Boston, 1987.

16 Wood, W. W., "The Asymptotic Expansions at Large Reynolds Numbers for Steady Motion Between Non-Coaxial Rotating Cylinders," *Journal of Fluid Mechanics*, vol. 3, pp. 159-175, 1959.

17 Launder, B. E., and Spalding, D. B., *Mathematical Models of Turbulence.* London: Academic Press, 1972.

18 Pope, S. B., "The Calculation of Turbulent Recirculating Flows In General Orthogonal Coordinates," *Journal of Computational Physics*, vol. 26, pp. 197-217, 1978.

19 Leonard, B. P., "A Stable and Accurate Convective Modelling Procedure Based on Quadratic Upstream Interpolation," *Computational Methods Appl. Mech. Engr.*, vol. 19, pp. 59-98, 1979.

20 Rhode, D. L., and Sobolik, S. R., "Simulation Of Subsonic Flow Through A Generic Labyrinth Seal," in *ASME International Gas Turbine Conference*, Houston, Texas, 1985.

21 Gosman, A. D. and Pun, W. M., "Calculation of Recirculating Flows," *Research Report*, Report no. HTS/74/2, Dept. of Mech. Eng., Imperial College, London, England, 1974.

22 Nail, G.H., "Leakage Prediction in Compressible Flow Labyrinth Seals," *Research Report*, Master's Thesis, Texas A&M University, College Station, Texas. December 1986.

23 Leong, Y.M.M.S., "Experimental Forces Induced by Flow Through Model Labyrinth Glands," *Research Report*, Ph.D. Dissertation, Heriot-Watt University, Edinburgh, June 1983.

Table I Diffusion Coefficients and Source Terms in the Transport Equations

ψ	$\frac{\Gamma_{x(i)}}{\mu}$	S_ψ
1	0	0
U	1	$\nabla(2)(\mu\frac{\partial V}{\partial x(1)}) + \nabla(3)(\mu\frac{\partial W}{\partial x(1)}) + \nabla(1)(\mu\frac{\partial U}{\partial x(1)}) - \frac{\partial p^*}{\partial x(1)}$
V	1	$\nabla(2)[\mu\frac{\partial V}{\partial x(2)} + 2\mu W H_2(3)] + \nabla(3)\Big[\mu\big(\frac{\partial W}{\partial x(2)} - VH_2(3) - WH_3(2)\big)\Big]$ $+\nabla(1)[\mu\frac{\partial U}{\partial x(2)}] - \frac{\partial p^*}{\partial x(2)} + H_3(2)\Big[\rho W^2 - 2\mu\big(\frac{\partial W}{\partial x(3)} + VH_3(2)\big)\Big]$ $-H_2(3)\Big[\rho VW - \mu\big(\frac{\partial V}{\partial x(3)} + \frac{\partial W}{\partial x(2)} - VH_2(3) - WH_3(2)\big)\Big]$
W	1	$\nabla(2)\Big[\mu\big(\frac{\partial V}{\partial x(3)} - VH_2(3) - WH_3(2)\big)\Big]$ $+\nabla(3)\Big[\mu\frac{\partial W}{\partial x(3)} + 2\mu VH_3(2)\Big] + \nabla(1)\Big[\mu\frac{\partial U}{\partial x(3)}\Big] - \frac{\partial p^*}{\partial x(3)}$ $+H_2(3)\Big[\rho V^2 - 2\mu\big(\frac{\partial V}{\partial x(2)} + WH_2(3)\big)\Big]$ $-H_3(2)\Big[\rho VW - \mu\big(\frac{\partial V}{\partial x(3)} + \frac{\partial W}{\partial x(2)} - VH_2(3) - WH_3(2)\big)\Big]$
k	$\frac{1}{\sigma_k}$	$\mathrm{P} - \rho\epsilon$
ϵ	$\frac{1}{\sigma_\epsilon}$	$\frac{\epsilon}{k}(C_{\epsilon 1}\mathrm{P} - C_{\epsilon 2}\rho\epsilon)$
H	$\frac{1}{\sigma_H}$	$\mathrm{P} - \frac{1}{2}\big[\nabla(2)\frac{\mu}{\sigma_H}\nabla(2)V^2 + \nabla(3)\frac{\mu}{\sigma_H}\nabla(3)V^2 + \nabla(1)\frac{\mu}{\sigma_H}\nabla(1)V^2\big]$ $+V\Big[\nabla(2)2\mu\big(\frac{\partial V}{\partial x(2)} + WH_2(3)\big)$ $+\nabla(3)\mu\big(\frac{\partial V}{\partial x(3)} + \frac{\partial W}{\partial x(2)} - VH_2(3) - WH_3(2)\big)$ $+\nabla(1)\mu\big(\frac{\partial V}{\partial x(1)} + \frac{\partial U}{\partial x(2)}\big)\Big]$ $+W\Big[\nabla(2)\mu\big(\frac{\partial V}{\partial x(3)} + \frac{\partial W}{\partial x(2)} - VH_2(3) - WH_3(2)\big)$ $+\nabla(3)2\mu\big(\frac{\partial W}{\partial x(3)} + VH_3(2)\big) + \nabla(1)\mu\big(\frac{\partial W}{\partial x(1)} + \frac{\partial U}{\partial x(3)}\big)\Big]$ $+U\Big[\nabla(2)\mu\big(\frac{\partial V}{\partial x(1)} + \frac{\partial U}{\partial x(2)}\big) + \nabla(3)\mu\big(\frac{\partial W}{\partial x(1)} + \frac{\partial U}{\partial x(3)}\big)$ $+\nabla(1)2\mu\frac{\partial U}{\partial x(1)}\Big]$

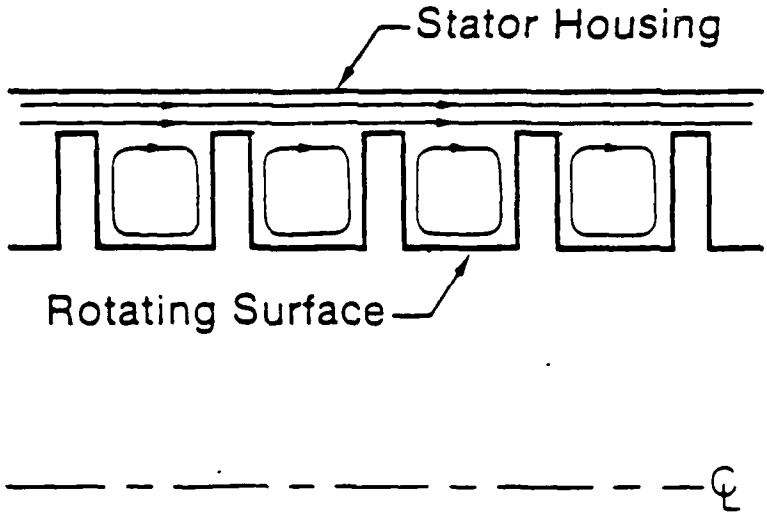

Fig. 1 Resulting streamlines due to leakage flow in a labyrinth seal

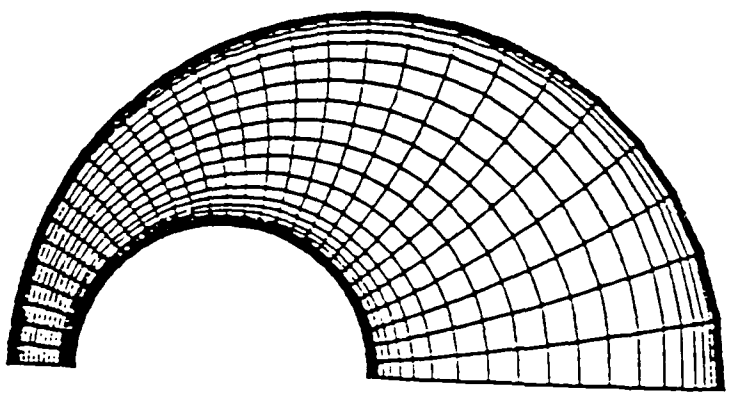

Fig. 2 An example of a finite difference grid in the eccentric region of the seal

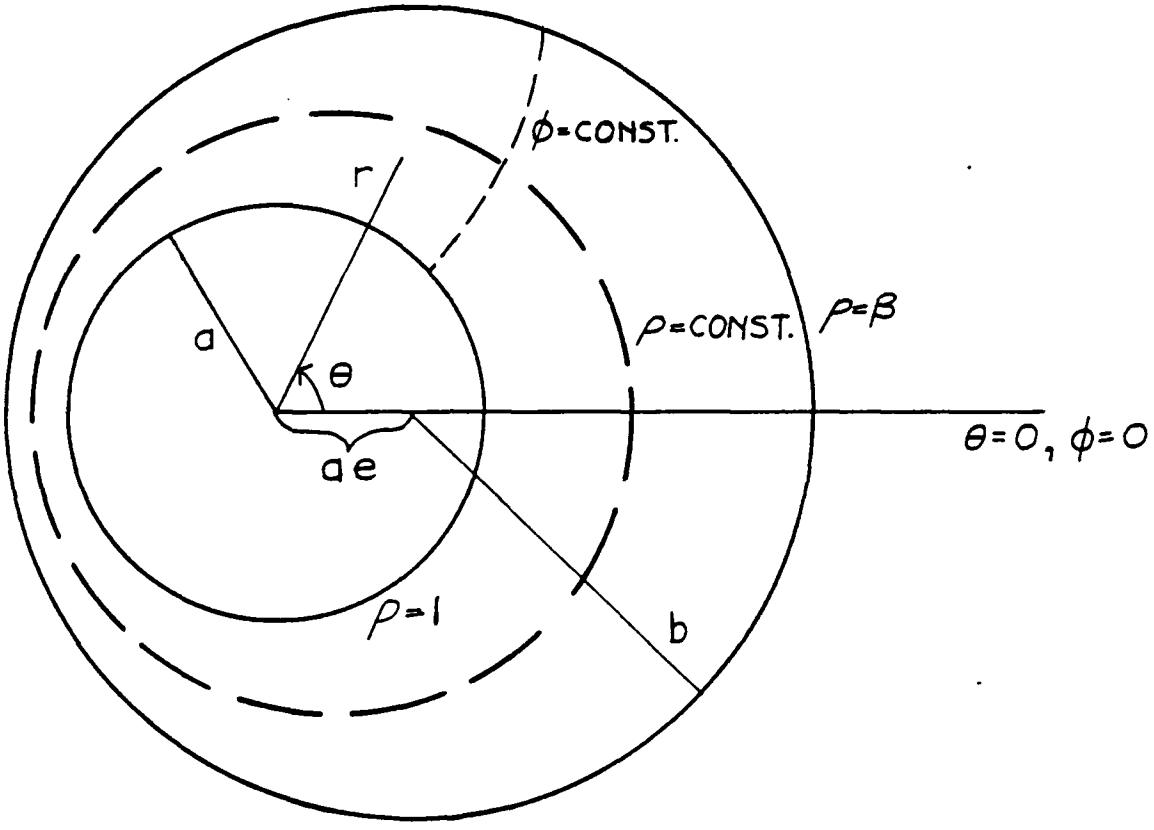

Fig. 3 The modified bipolar coordinate system

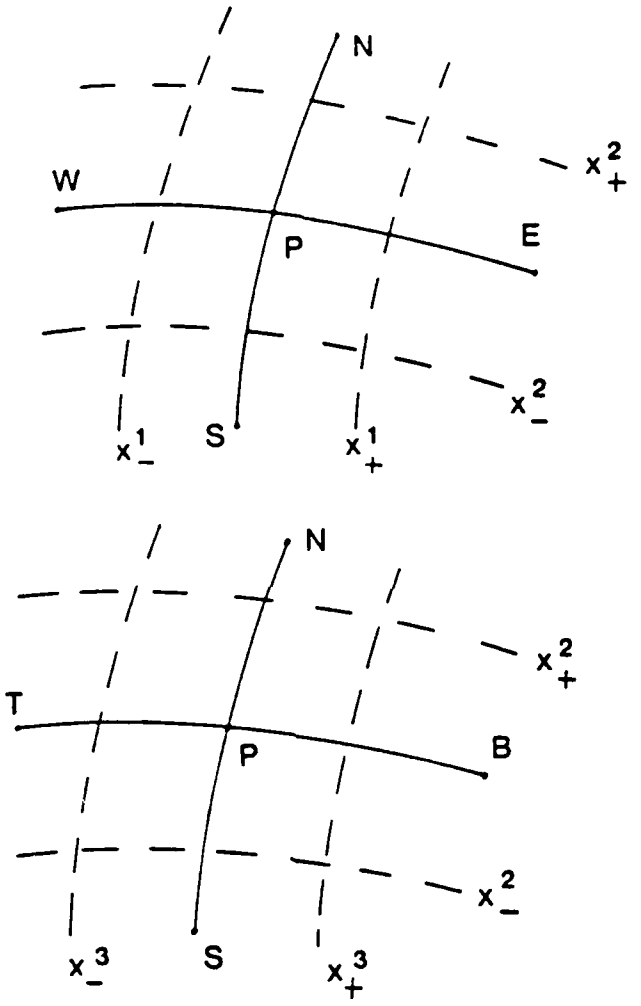

Fig. 4 A general three-dimensional control volume

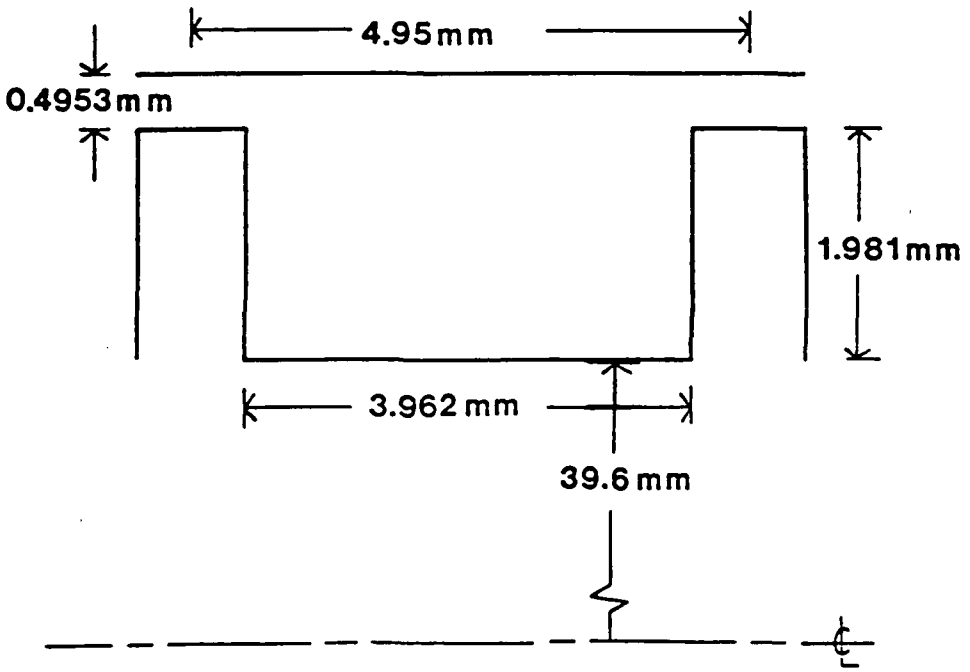

Fig. 5 The seal cavity investigated and its dimensions

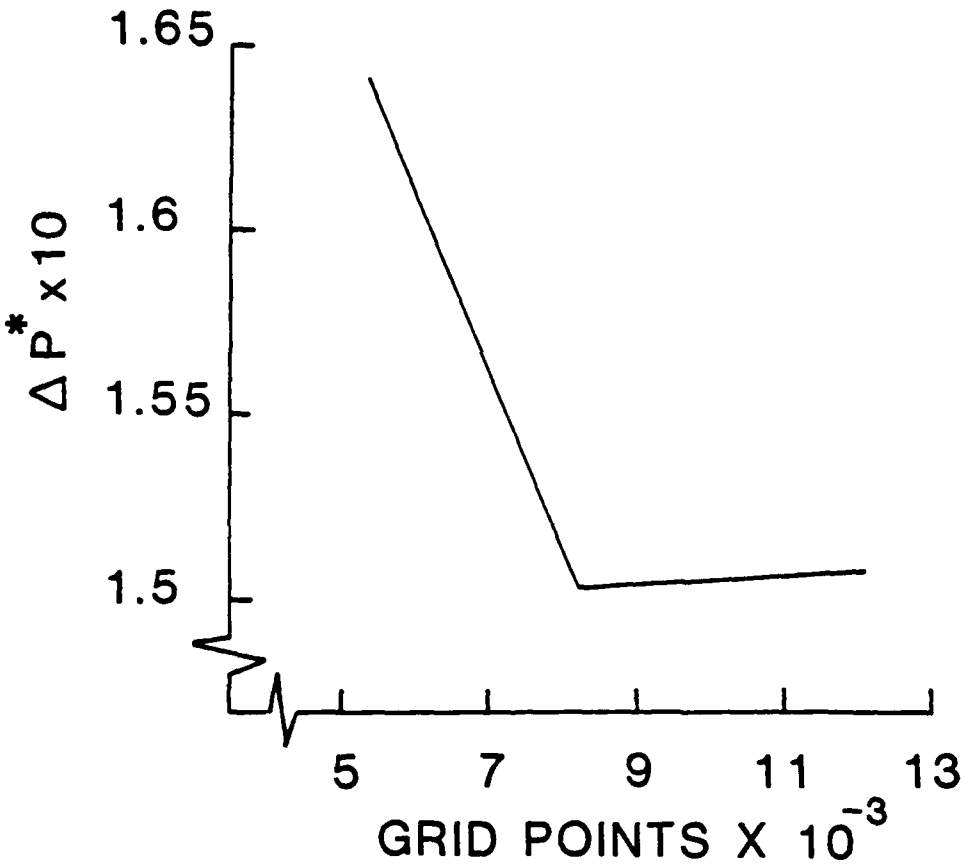

Fig. 6 The effect of the number of grid nodes on cavity pressure drop

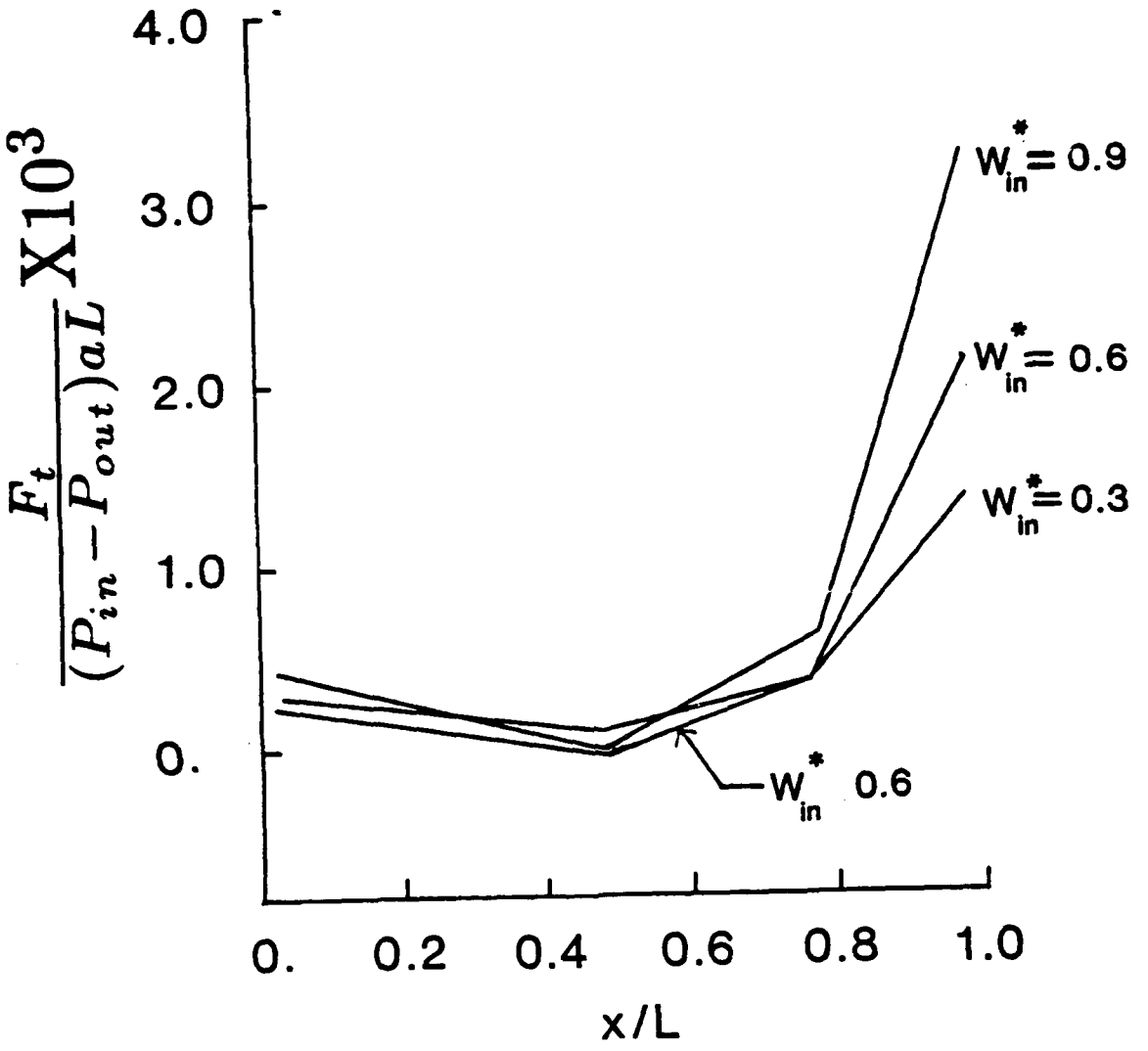

Fig. 7 Variation of total tangential force along the rotating surface for three inlet swirl cases of half-speed whirl

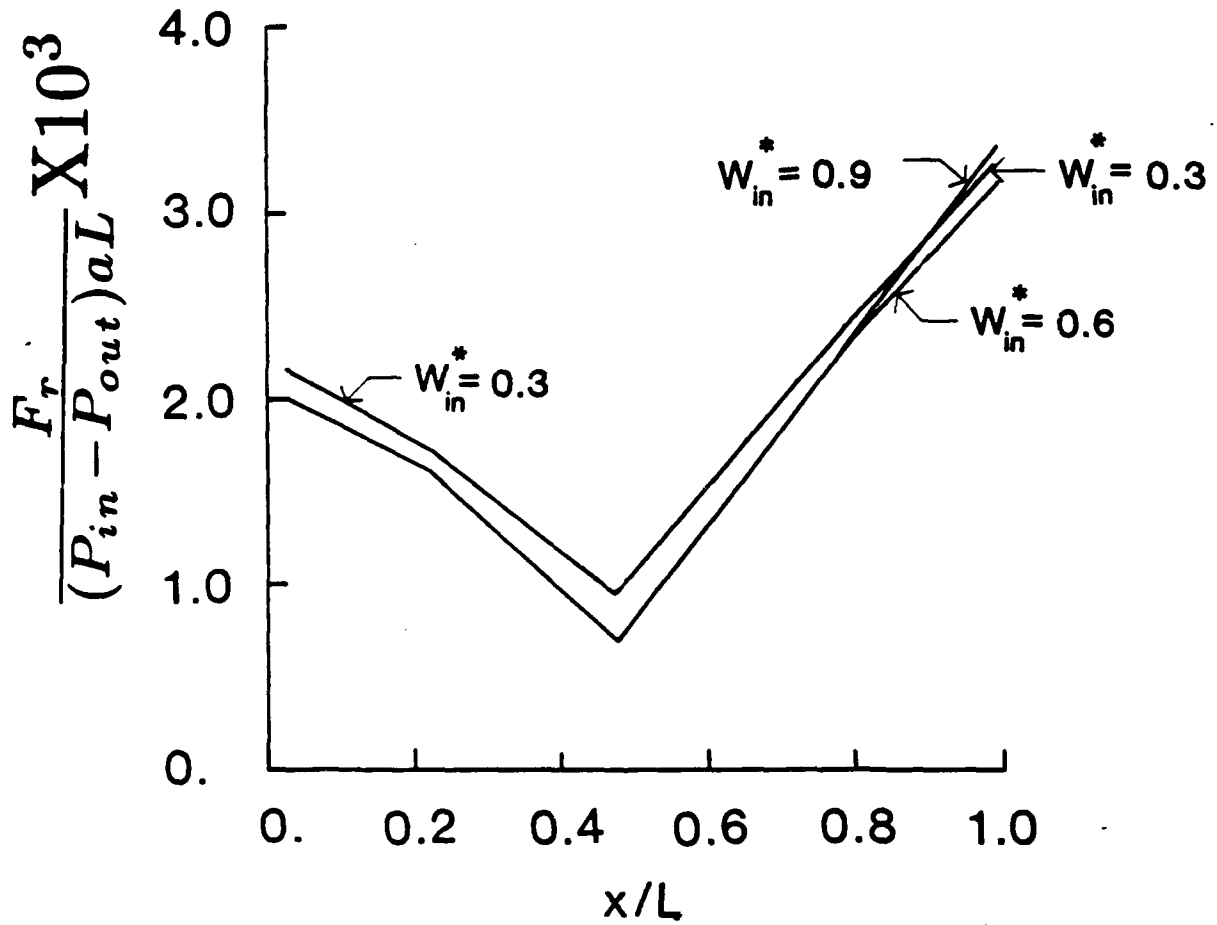

Fig. 8 Variation of total radial force along the rotating surface for three inlet swirl cases of half-speed whirl

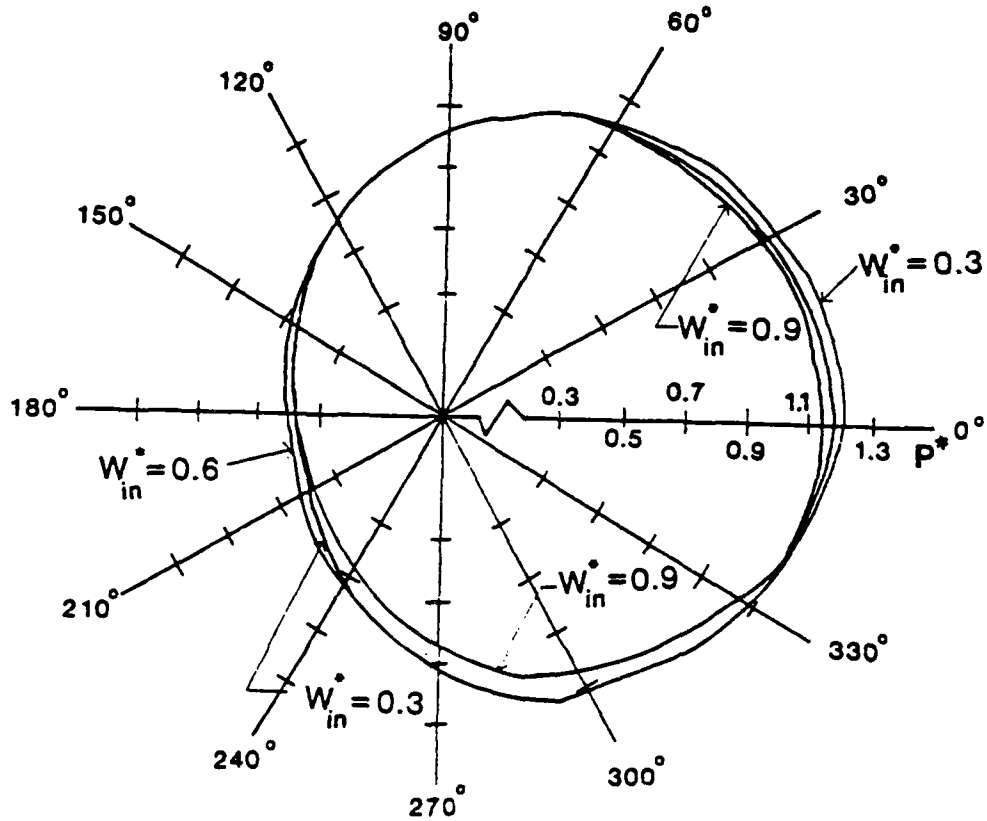

Fig. 9 Polar plot of the variation of relative pressure around the periphery of the upstream tooth for three inlet swirl cases at half-speed whirl

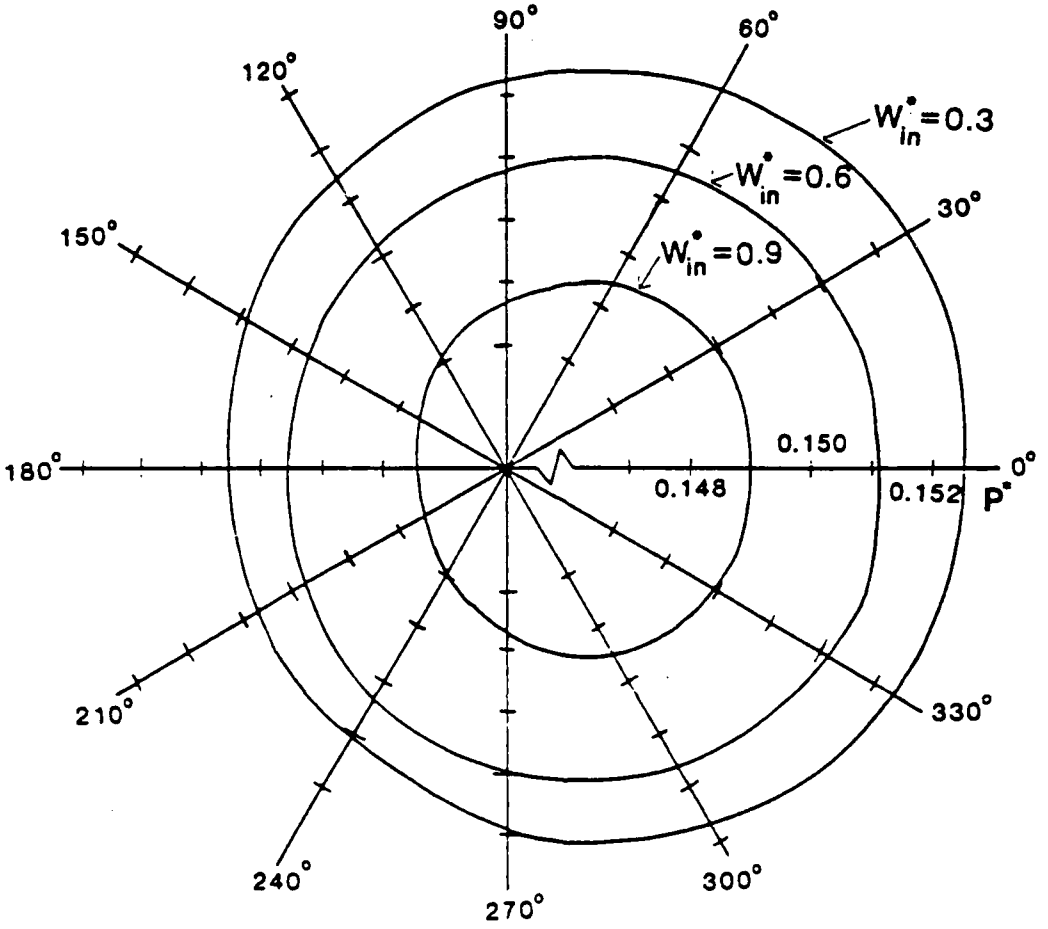

Fig. 10 Polar plot of the variation of relative pressure around the periphery of the rotor at mid-cavity for three inlet swirl cases at half-speed whirl

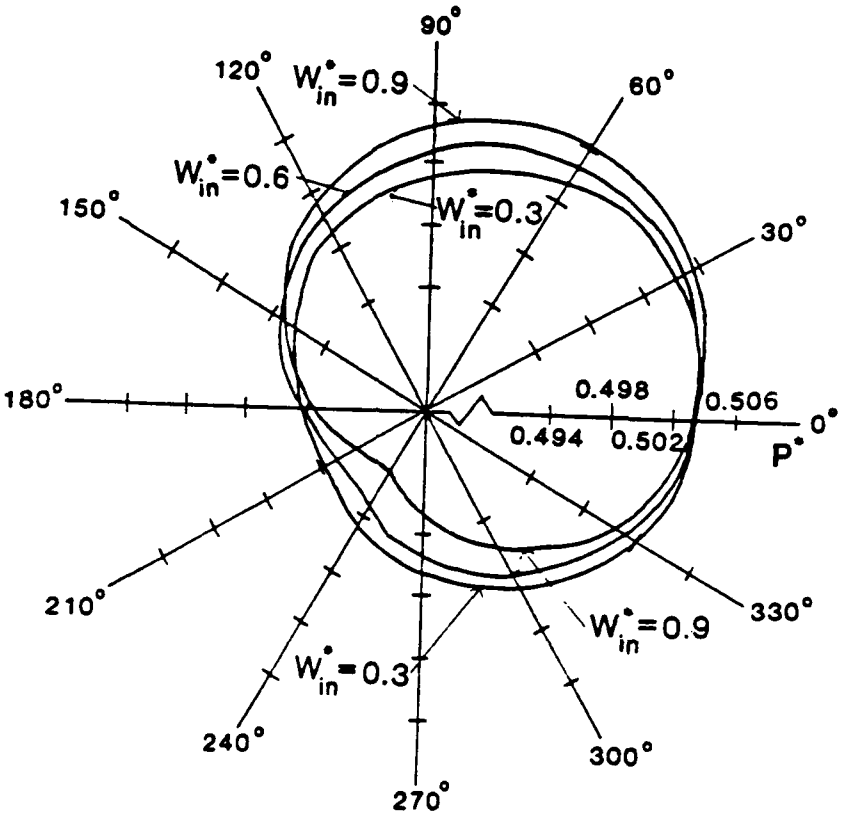

Fig. 11 Polar plot of the variation of relative pressure around the periphery of the downstream tooth for three inlet swirl cases at half-speed whirl

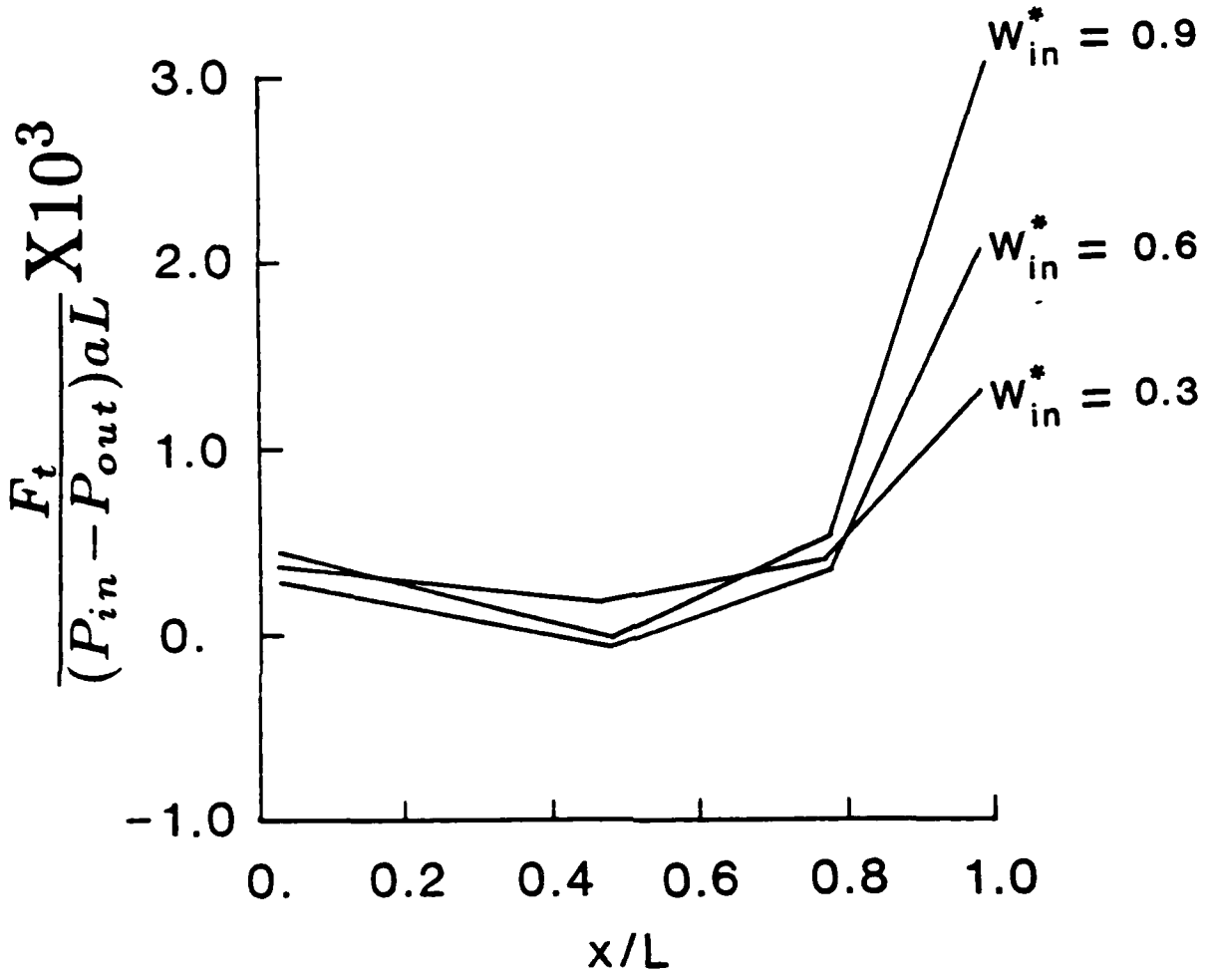

Fig. 12 Variation of total tangential force along the rotating surface for three inlet swirl cases with no whirl

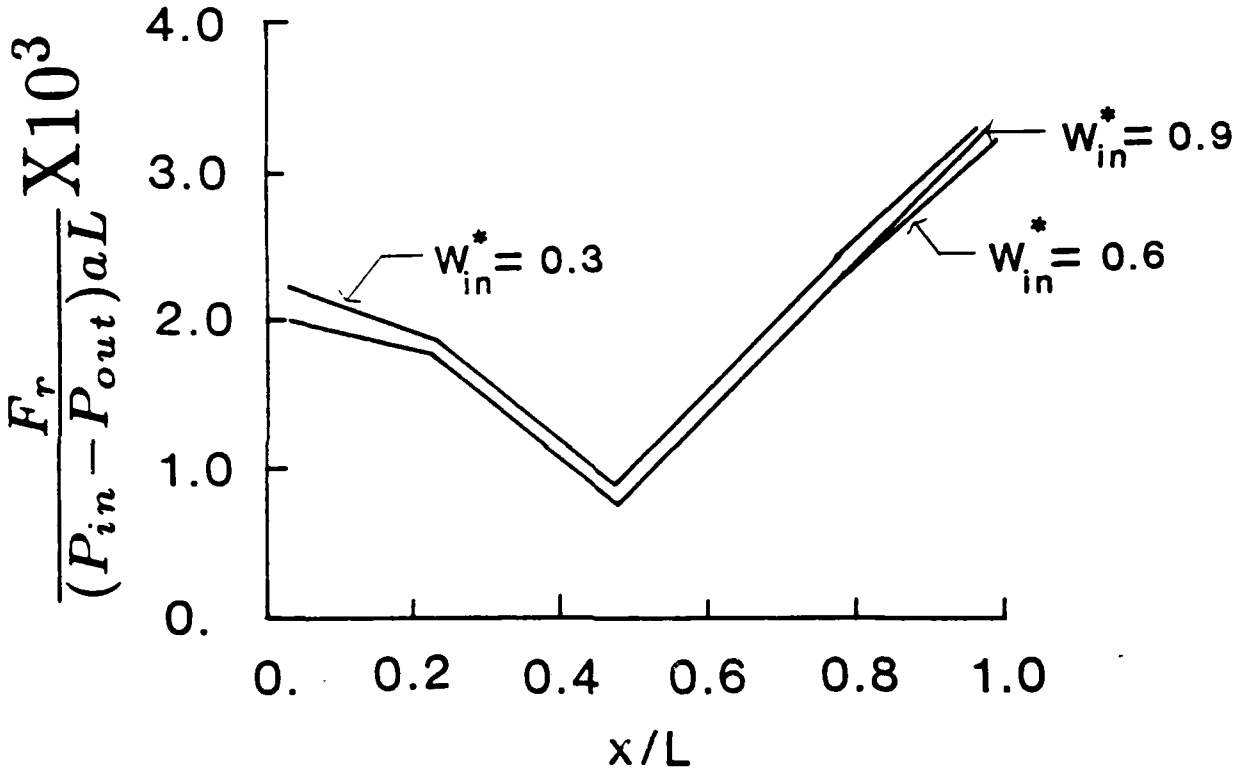

Fig. 13 Variation of total radial force along the rotating surface for three inlet swirl cases with no whirl

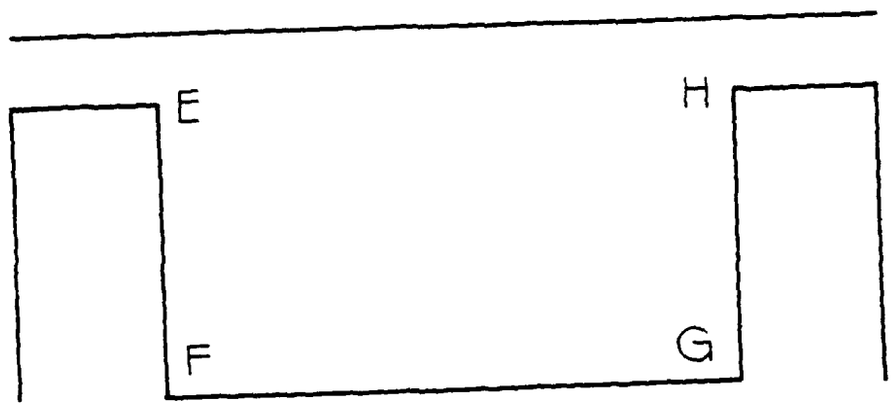

Fig. 14 Nomenclature used to specify location within the cavity

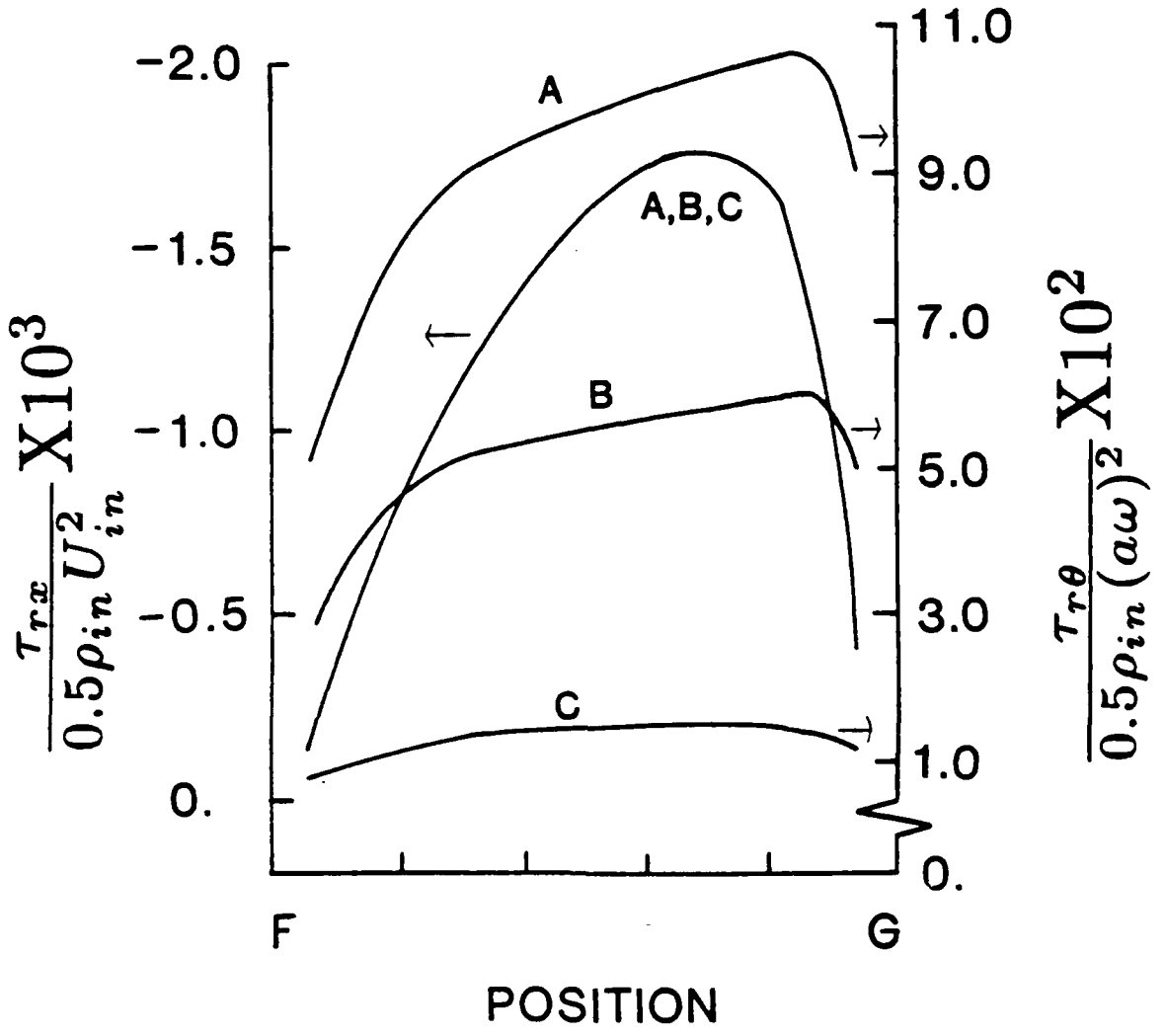

Fig. 15 Variation of shear stress along the rotor surface at $\theta = 0$ degrees for cases A,B, and C ($W_{in}^* = 0.3, 0.6$, and 0.9 respectively) at half-speed whirl

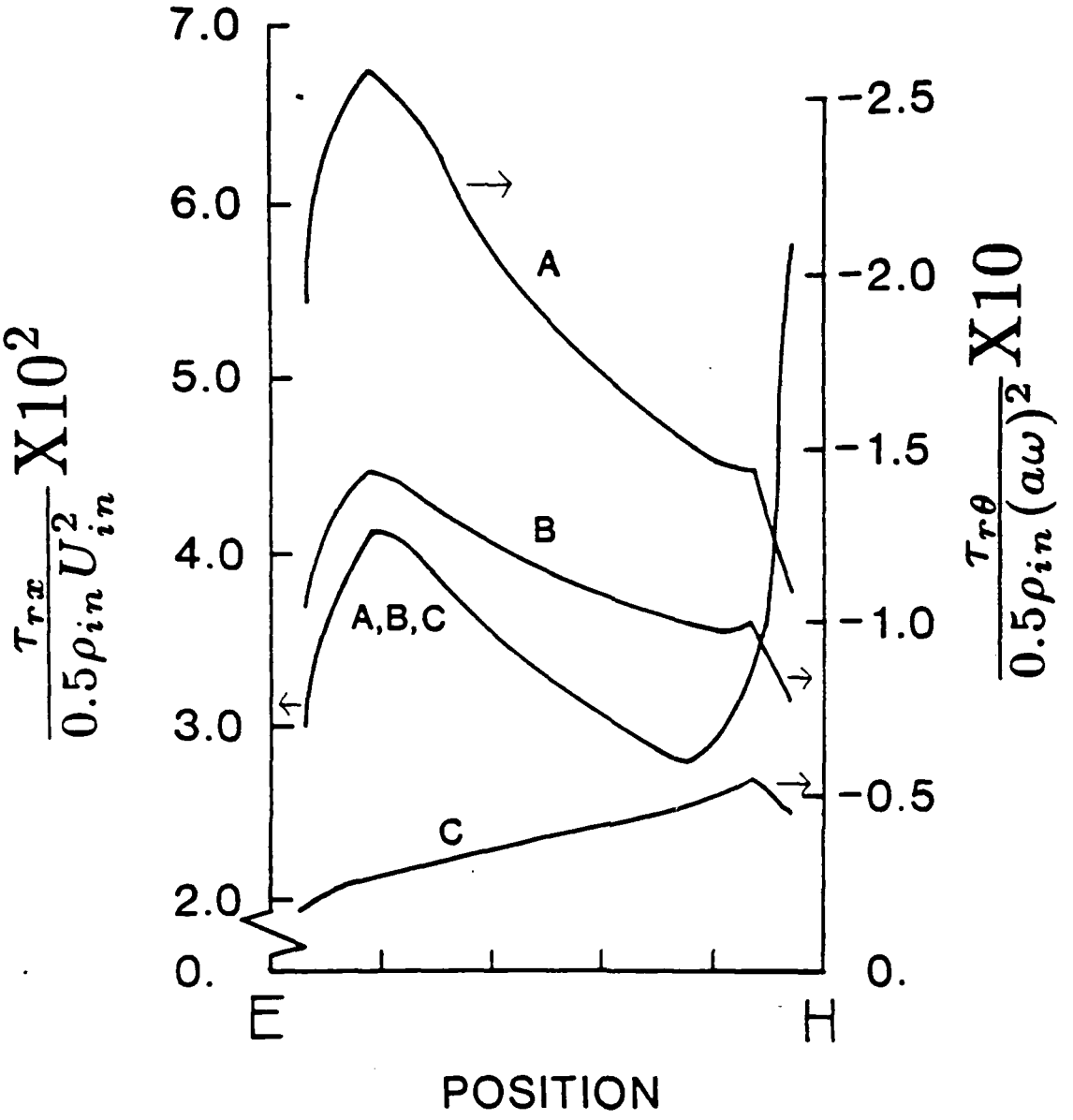

Fig. 16 Variation of shear stresses along the free shear layer at $\theta = 0$ degrees for cases A,B, and C ($W_{in}^* = 0.3, 0.6$, and 0.9 respectively) at half-speed whirl

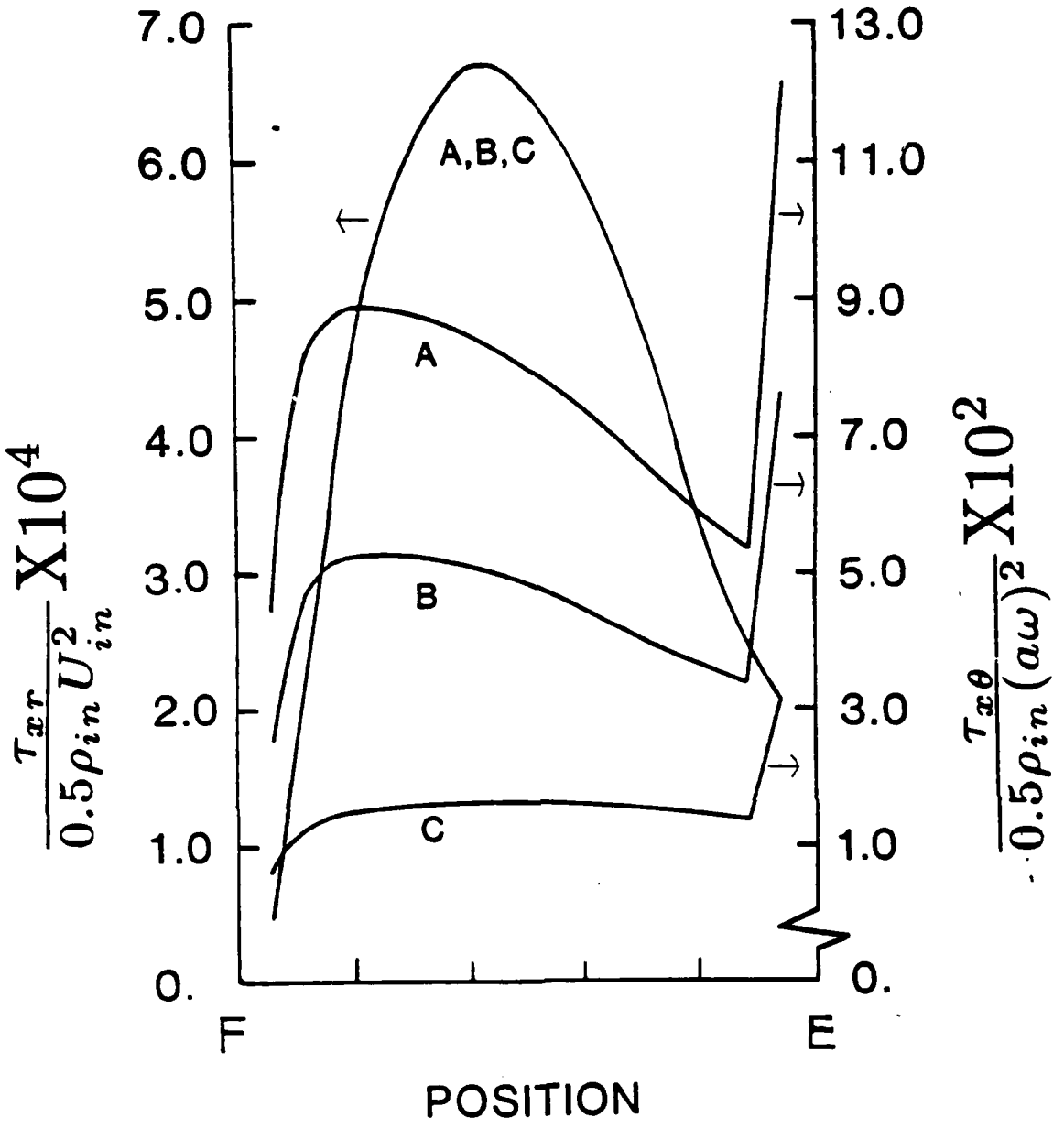

Fig. 17 Variation of shear stresses along the upstream tooth at $\theta = 0$ degrees for cases A,B, and C (W_{in}^* =0.3.0.6. and 0.9 respectively) at half-speed whirl

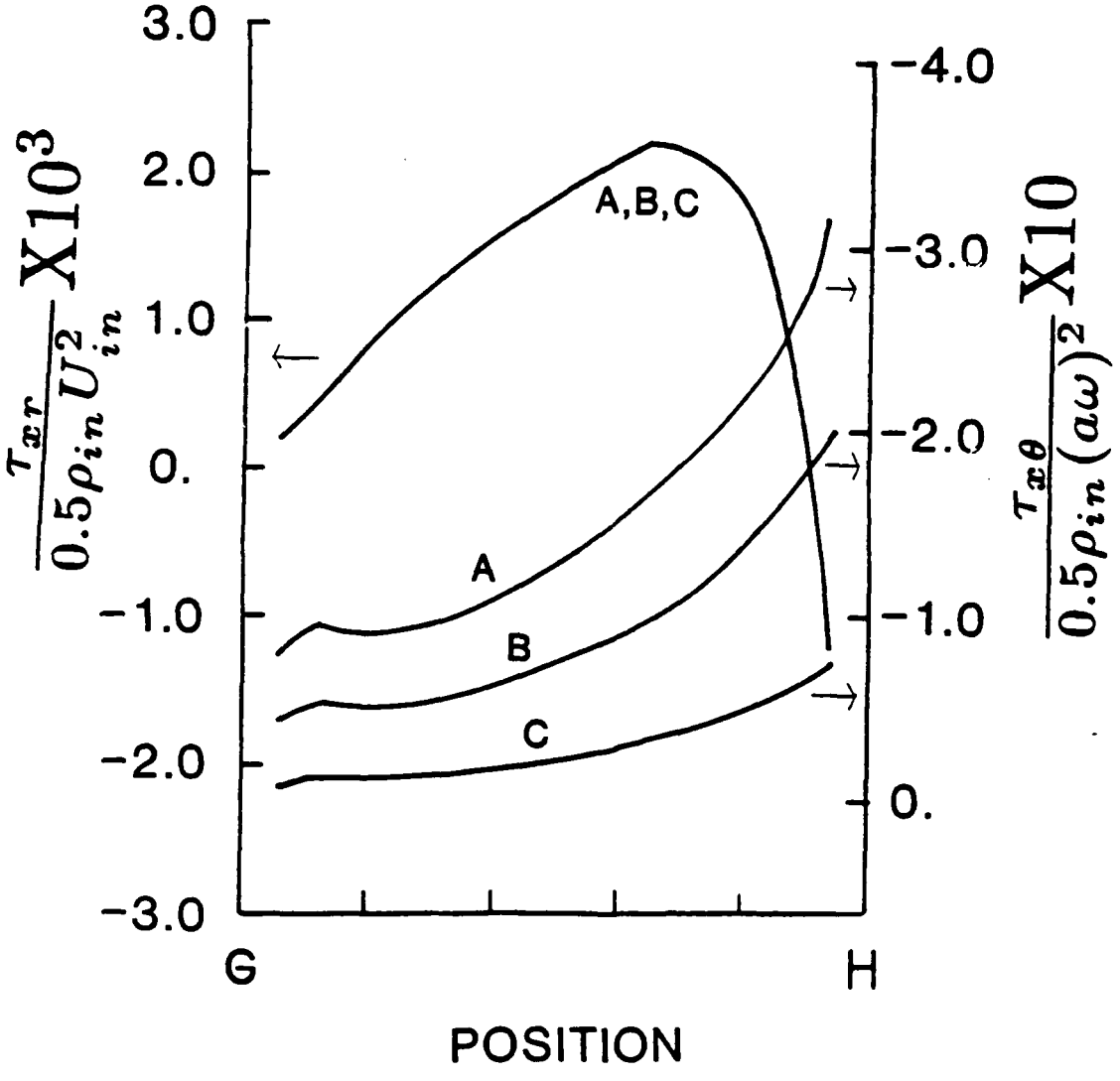

Fig. 18 Variation of shear stresses along the downstream tooth at $\theta = 0$ degrees for cases A,B, and C (W_{in}^* =0.3,0.6, and 0.9 respectively) at half-speed whirl

LABYRINTH SEAL ROTORDYNAMIC FORCES PREDICTED WITH A THREE-DIMENSIONAL NAVIER-STOKES COMPUTER CODE

D.L. Rhode** and S.J. Hensel*

Turbomachinery Laboratories

Mechanical Engineering Department

Texas A&M University

College Station, Texas 77843

---

* Graduate Student

** Associate Professor

ABSTRACT

A finite difference method for determining rotordynamic forces on an eccentric whirling labyrinth cavity has been developed. A coordinate transformation was applied to the turbulent flow Navier–Stokes equations in order to use the modified bipolar coordinate system. The SIMPLER algorithm with QUICK differencing and the high Reynolds number k–ϵ turbulence model are used to compute the complex turbulent flowfield. A circular whirl orbit about the geometric center of the housing was specified for simplicity. For the cases considered, the radial and tangential force components increased and decreased, respectively, with increasing inlet swirl. Also, circumferential pressure variations are included for enhanced insight into the flowfield. Further, the circumferential variation of both shear stress components along each surface of the cavity are presented to allow the developers of various bulk flow models to refine their stress modelling.

NOMENCLATURE

a	radius of tooth periphery
$dx(i)$	displacement along general orthogonal coordinate lines
F	rotordynamic force
h	scale factor
$H_i(j)$	coordinate variation term
k	turbulence kinetic energy
L	seal cavity pitch
p	pressure
p^*	pressure re-defined by Eq. 9
r	polar coordinate
s	distance
U	x^1 velocity component
U_i	velocity expressed in cartesian tensor notation
$U(i)$	velocity expressed in general orthogonal coordinate system
V	x^2 velocity component
W	x^3 velocity component
x_i	general coordinate expressed in cartesian tensor notation
x^i	general orthogonal coordinate
A	flux coefficient
S_p	source term
S_u	source term
Γ	diffusion coefficient
δ_{ij}	Kronecker delta
ϵ	turbulence energy dissipation

θ	polar coordinate
μ	viscosity
ρ	density
τ	stress
τ^*	anisotropic stress
ψ	general transport quantity
ω	rotational frequency

Subscripts

eff	effective (laminar plus turbulent)
i	index
in	inlet
j	index
l	index
out	out
r	radial
sh	shaft
t	tangential
B	bottom face of cell
E	east face of cell
N	north face of cell
P	p–cell node
S	south face of cell
T	top face of cell
W	west face of cell

Superscript

* nondimensional quantity

INTRODUCTION

Self–excited vibration remains a serious problem encountered in high performance turbomachines. A complete quantitative analysis of the excitation forces causing such vibration is still not complete. The excitation forces result from the displacement of the rotor from its geometric center in the housing. This displacement often results from a small mass imbalance on the rotor. The result of the self–excited forces is usually subsynchronous whirl. Subsynchronous whirl (whirling at a frequency below the rotational frequency of the shaft) may occur in the same direction as the shaft rotation or in the opposite direction. One source of these self–excited forces is labyrinth seals.

Labyrinth seals are used to limit internal leakage from high to adjacent low pressure regions in a turbomachine. They consist of a highly frictional flow path between the rotor and stator. The flow path converts pressure head into mean flow kinetic energy, which is dissipated by viscous losses. Figure 1 shows the streamlines within a short bank of labyrinth cavities.

A number of analytical investigations on the destablizing forces generated by the leakage flow through labyrinth seals have been performed. Many of the analytical methods employ bulk flow models and use numerous empirical correlations. The problem was first modelled by Alford [1], who neglected circumferential flow, resulting in no predicted force. The calculations of Kostyuk [2] neglected the change of chamber area due to rotor eccentricity and contradicted various force measurements. Iwatsubo [3,4] extended Kostyuk's model to include this chamber area variation. Childs and Scharrer [5] included this variation and developed improved shear stress relationships. They obtained generally improved predictions. These investigators also presented [6] the first complete set of separate experimental values for the

stiffness and damping coefficients.

Only very recently has Computational Fluid Dynamics CFD been utilized to predict the forces on labyrinth seals. Dietzen and Nordman [7] used it in a hybrid perturbation/CFD model to solve the Navier–Stokes equations for turbulent flow. Wyssman [8] was apparently the first to present pressure distributions for an eccentric–rotor labyrinth cavity from a three–dimensional computation of the turbulent Navier–Stokes equations. These along with velocity distributions given by Wyssman, et al [9] were used to develop a special two–control–volume bulk–flow model. Tam, et al [10] used a three–dimensional CFD code to compute the forces in non–labyrinth, i.e. annular seals.

NUMERICAL MODEL

In this study the whirl orbit has been idealized as circular motion, the center of which coincides with that of the housing. A single cavity of a multi–cavity seal of teeth–on–rotor design is analyzed. Since the tooth perimeter is concentric with the base of the seal cavity, cylindrical coordinates are the natural choice within the seal cavity. However, in the clearance region between the teeth and the stator, bipolar coordinates are used because of the eccentricity of the shaft. Specifically, the modified bipolar coordinate system was selected as it becomes the cylindrical coordinate system in the limit as eccentricity approaches zero. Figure 2 shows such a finite difference grid within the clearance region. Reference [11] gives details concerning the modified bipolar coordinate system.

Neglecting body forces, the steady–state continuity and momentum equations are

$$\frac{\partial(\rho U_i)}{\partial x_i} = 0 \tag{1}$$

$$\frac{\partial(\rho U_i U_j)}{\partial x_i} = -\frac{\partial p}{\partial x_j} - \frac{\partial \tau_{ij}}{\partial x_i} \tag{2}$$

where ρ, U_i, and p are the time–averaged density, velocity and pressure. The Reynolds stresses are determined by the high Reynolds number $k - \epsilon$ turbulence model.

The equations were transformed into relations involving general orthogonal coordinates, using Pope's [12] method. With his transformation procedure the equations retain their original form and simplicity as much as possible.

Consider a general orthogonal coordinate system where the orthogonal coordinates are denoted by x^i. Distances in this system can be related to the Cartesian system by the scale factors h_i,

$$(ds)^2 = (\mathrm{h}_i dx^i)^2 = [dx(i)]^2 \tag{3}$$

where the scale factors h_i are excluded from the summation convention. Thus, the physical displacements along a coordinate line x^i in the general orthogonal coordinate system are $dx(i)$. The scale factors are determined by

$$\mathrm{h}_i^2 = \sum_l \frac{\partial \bar{x}_l}{\partial x^i} \frac{\partial \bar{x}_l}{\partial x^i} \tag{4}$$

where $\bar{x}_l$ are the coordinates in the Cartesian coordinate system. Pope's divergence operator $\nabla(i)$ and coordinate variation term $H_i(j)$ needed to transform the transport equations into general orthogonal coordinates are

$$\nabla(i) = \frac{\mathrm{h}_i}{|\mathrm{h}|} \frac{\partial}{\partial x(i)} \frac{|\mathrm{h}|}{\mathrm{h}_i} \tag{5}$$

$$H_i(j) = \frac{1}{\mathrm{h}_i \mathrm{h}_j} \frac{\partial \mathrm{h}_i}{\partial x_j} \tag{6}$$

Here h_i represent scale factors and |h| is the product of the scale factors. After performing the transformation, the mass and momentum equations become

$$\nabla(i)[\rho U(i)] = 0 \tag{7}$$

and

$$\begin{aligned}\nabla(i)[\rho U(i)U(j) + \tau^*(ij)] = &-\frac{\partial p^*}{\partial x(j)} + H_i(j)[\rho U(i)U(i) + \tau^*(ii)] \\ &- H_j(i)[\rho U(i)U(j) + \tau^*(ij)]\end{aligned} \tag{8}$$

The isotropic component of stress has been added to the pressure giving

$$p^* = p + \frac{2}{3}\rho k + \frac{2}{3}\mu_{eff}\nabla(i)U(i) \tag{9}$$

where τ^* has the anisotropic stress as

$$\tau^*(ij) = -\mu_{eff}[\frac{\partial U(i)}{\partial x(j)} + \frac{\partial U(j)}{\partial x(i)} - U(i)H_i(j) - U(j)H_j(i) + 2U(l)H_i(l)\delta_{ij}] \tag{10}$$

All of the transport equations can be written as

$$\begin{aligned}\nabla(1)[\rho U(1)\psi - \Gamma_{x(1)}\frac{\partial \psi}{\partial x(1)}] + \nabla(2)[\rho U(2)\psi - \Gamma_{x(2)}\frac{\partial \psi}{\partial x(2)}] \\ + \nabla(3)[\rho U(3)\psi - \Gamma_{x(3)}\frac{\partial \psi}{\partial x(3)}] = S_\psi\end{aligned} \tag{11}$$

where all $\Gamma_{x(i)}$ and S_ψ are defined in reference [11] for the appropriate ψ, and U, V, W correspond to $U(1), U(2), U(3)$.

The algebraic finite difference equations can be easily derived by applying the Gauss Divergence theorem to Eq. 11. Further details are available in reference [11]. Figure 2 shows the modified bipolar coordinate portion of the grid. Observe that $dx(1), dx(2)$, and $dx(3)$ are physical lengths in the general orthogonal coordinate system. Upon integration the resulting algebraic finite difference equation is of the form

$$\begin{aligned}\psi_P(A_N + A_S + A_E + A_W + A_T + A_B) = A_N\psi_N + A_S\psi_S \\ + A_E\psi_E + A_W\psi_W + A_T\psi_T + A_B\psi_B + (S_\psi)_P vol\end{aligned} \tag{12}$$

The hybrid upwind/central differencing scheme yields false diffusion under certain conditions when large control volume Peclet numbers occur. False diffusion error arises if the streamlines are oblique to the grid lines and a nonzero gradient of the dependent variable normal to the flow exists. The QUICK differencing scheme of Leonard [13] generally reduces false diffusion. Rhode et al [14] have previously implemented QUICK into an axisymmetric computer code from which this program was developed. The three–point interpolation expression for the west face of the control volume on a uniform grid is shown in Figure 3 and is calculated by

$$\psi_w = \frac{1}{2}(\psi_P + \psi_W) - \frac{1}{8}(\psi_E - 2\psi_P + \psi_W) \tag{13}$$

if U_W is negative and

$$\psi_w = \frac{1}{2}(\psi_P + \psi_W) - \frac{1}{8}(\psi_P - 2\psi_W + \psi_{WW}) \tag{14}$$

if U_W is positive. The interpolation functions were modified for any non–uniform grid. Substitution of these interpolation functions into Eq. 12 , or use of the hybrid differencing scheme yields

$$\psi_P = \frac{\sum_i A_i \psi_i + Su}{\sum_i A_i - Sp} \tag{15}$$

where i =E,W,N,S,T,B,EE,WW,NN,SS and the last four neighbors are not needed in the hybrid scheme.

As is done in the TEACH code [15], the variables were stored on a system of four staggered grids. The values of pressure, turbulent kinetic energy, turbulence dissipation, and enthalpy were stored at the intersection points of the primary grid, whereas each velocity component was stored on a separate grid.

Wall functions were used to determine the appropriate shear stress near a wall. A radially unifrom profile of axial velocity, circumferential velocity,

turbulence kinetic energy, and turbulence dissipation was prescribed at the inlet. The circumferential variation of each was determined from a preliminary computer run. For that run, the inlet value of each variable, except pressure and swirl velocity, was set equal to the corresponding outlet value from the previous iteration. This case corresponds to a fully developed, i.e. streamwise periodic cavity. The inlet circumferential velocity profile was also uniform in the radial direction. At the circumferential location of largest clearance, this quantity was specified according to the problem of interest. All other circumferential locations were given an inlet value such that the swirl velocity conserved mass in the circumferential direction. Pressure was prescribed at one point in the domain.

The solution strategy employed is the well documented SIMPLER procedure. A line solver is used to solve for each variable of interest. This line solver is applied in the θ–direction in the cylindrical coordinate system and in the ϕ–direction in the modified bipolar coordinate system. The re–entrant or cyclic boundary condition is utilized. The assembled equations are written in the form

$$-\mathrm{A_T}\psi_\mathrm{T} + (A_\mathrm{P} - \mathrm{S_P})\psi_\mathrm{P} - \mathrm{A_B}\psi_\mathrm{B} = S_u + \sum_i \mathrm{A}_i\psi_i \qquad (16)$$

where i =N,S,E,W,NN,SS,EE,WW. Application of Eq. 16 to each grid circle leads to a matrix that is solved using a CTDMA algorithm. Each grid circle throughout the domain is solved in this manner.

DISCUSSION

Figure 4 shows the cavity and the relevant dimensions. Minimizing the grid nonuniformity was desireable in aiding convergence. The eccentricity of the rotor was three percent of the clearance c in this analysis.

TheFlowfieldsConsidered

Three different inlet swirl cases were investigated: 30,60, and 90 percent of the rotational speed of the cavity. The rotational speed of the rotor was 5,000 cpm and the working fluid was air at 3.0 atm. and 294 K at the inlet. The axial Reynolds number $\mathrm{Re}_x = 2U_{in}c/\nu$ in all cases was 19,200, which corresponds to a Mach number near 0.2. The inlet conditions were identical for each case except for swirl velocity. Each swirl case was considered with no whirl as well as half-speed forward whirl at 2,500 cpm.

A grid of 22x22x17 nodes in the x–, r–, and θ–directions, was found in a grid–dependence study to be sufficient to simulate the flowfield for this problem. A considerably finer grid is required, however, for higher Mach number cases. In order to conserve computer resources, the number of grid nodes used in the axial and radial directions, 22x22, was determined in conjuction with previous grid dependence testing [16] at the same Mach number.

For the present computer runs, it was found that the radial component of the net force was much larger than the tangential component. Inasmuch as the tangential component is a very small value here, it meandered somewhat (approximately $\pm$ 8 percent) with further iterations beyond the point of convergence for other quantities.

Results

The rotor in actual turbomachines has frequently become unstable with the

shaft whirling at a frequency approximately half of the rotational frequency. Results for this important case of half-speed whirl are considered here. The net tangential force acting on the eccentric whirling shaft is of considerable interest because it is the driving force for the whirl phenomenon. In Figure 5 the effect of inlet swirl strength on the net tangential force can be seen. The total net tangential force contains contributions from both pressure and shear forces. As expected from the literature, increasing swirl increases the driving force behind the rotordynamic whirl.

The contribution of shear forces to the total net tangential force is seen in Figure 6. From the quantitative result in Figures 5 and 6 it is obvious that the shear component of the net tangential force is less than one percent. The other 99 percent is from the net pressure force due to the circumferential pressure distribution around the cavity. Observe that the south wall(cavity base) contribution is less than zero and the others are greater than zero. This gives a cancellation and a small total shear force. Also, note that the south wall shear was the only one significantly influenced by a change in inlet swirl.

While a positive tangential force is a whirl driving force, a negative radial force is a restoring force. The effect of inlet swirl on the total net radial force can be seen in Figure 7. The radial force generally decreases slightly with increasing swirl. It is about four times larger than the tangential force. Note that the force is not restoring the rotor to its original position, but is actually pushing it to larger eccentricities. These same general trends were measured by Leong [17] at small eccentricities.

It was determined from Figures 7 and 8 that the net shear stress contribution to the total net radial force is less than one percent, as is the case with the net tangential force. Figure 8 also shows that all radial shear force components were invariant with swirl, except at the south wall. As expected, the shear contribution

to the radial force there was a minimum when $W_{in}^{*} = 0.6$ because this is near the asymptotic value in which case there was negligible $\tau_{r\theta}$ stress on the south wall.

Since the pressure force virtually determines the net forces acting on a seal, the variation of pressure (relative to a reference of 306,000 Pa) in the circumferential direction at two locations along the rotor are plotted. In Figure 9 the pressure values are taken at the middle of the south wall of the cavity. Symmetry about the axis through θ=180 degrees is observed indicating a very small contribution to F_t, and swirl had little effect on this. In Figure 10 the pressure distribution on the downstream tooth is given. Observe that here the pressure distribution is not symmetric at all through this axis, contributing substantially to F_t. Higher inlet swirl values produced this lack of symmetry, which caused an increase in the tangential force.

The case of no whirl has also been studied previously. The current results for the non-whirling case are very similar to those shown for half-speed whirl. This was expected since for such small eccentricities the boundary conditions are nearly the same.

The development of circumferential velocity within a bank of labyrinth cavities has been of interest for some time because, as shown above, swirl has a substantial influence on the forces generated by an eccentric seal. The circumferential variation of swirl at the inlet and exit for the case of lowest inlet swirl is given in Figure 11. The swirl increased in this case from the inlet to exit by about seven percent. This was expected since the inlet swirl was below the fully developed (i.e. asymptotic) value. Notice that the peak of the distribution shifted circumferentially nearly 25 degrees. This is attributed to the eccentricity and swirl development. For the intermediate inlet swirl case of $W^{*} = 0.6$, the swirl velocity increased by four

percent. Since this value of inlet swirl is closer to the asymptotic limit, there was less of an increase. The peak value shifted only about 12 degrees, in this instance. For the largest inlet swirl case, the swirl changed little in magnitude and shifted about 12 degrees.

The development of axial velocity through the cavity was also examined. This development for all three inlet swirl cases is presented in Figure 12. In each case the axial velocity inlet profile was exactly identical, and all three cases produced the same exit axial velocity. The exit axial velocity was almost symmetric about an axis through θ =180 degrees. For the present inlet Mach number, the velocity increased by about two percent from inlet to exit.

The velocity, pressure, turbulence energy and turbulence dissipation distributions give additional insight into the flowfield within the cavity which is useful to the developers of of simpler models. Reference [18] contains profile plots of these quantities. These plots are for the intermediate inlet swirl case with half-speed whirl. The velocity distributions within the cavity were quite similar to those produced by Rhode and Sobolik [14] for a concentric-rotor seal. The velocity did not vary greatly circumferentially. This can be expected since the eccentricity was only three percent. The axial velocity component shows significantly more circumferential variation than the other two velocity components.

Although they do not contribute significantly to the force components, shear stress distributions are needed in the development of simpler models. Shear stresses are plotted along each wall as well as the free shear layer for θ=0 in Reference [11]. The corresponding circumferential variation of these quantities at a location midpoint along each surface is given here. Thus the two sets of figures together can be used to approximate the entire three-dimensional shear stress distribution along

the cavity walls and the free shear layer.

The circumferential variation of the above shear stresses for a location midway along each respective plane is shown in Figures 13 through 16. The stresses in Figure 13 are for the midpoint along the south wall of the cavity. Stress τ_{rx} is independent of inlet swirl and exhibits a minimum at θ=180 degrees due to the lower axial velocity at that θ-location (most of the leakage flow is near θ=0). Stress $\tau_{r\theta}$ was fairly invariant with θ, but swirl affected the magnitude of $\tau_{r\theta}$ as found in the previous figures.

The shear stresses midway along the free shear layer are plotted in Figure 14. As with the corresponding south wall stresses in Figure 13, component τ_{rx} is independent of the inlet swirl and has a minimum at θ=180 degrees. Stress $\tau_{r\theta}$ was very sinusoidal and decreasing inlet swirl increased the magnitude of the stress, as expected.

The circumferential variation of east and west wall midpoint shear stresses can be observed in Figures 15 and 16. For both walls τ_{rx} is again independent of inlet swirl, and exhibits a minimum at θ=180 degrees. Stress $\tau_{x\theta}$ is nearly uniform with *theta* and decreases with increasing inlet swirl.

CONCLUSIONS

It has been shown that rotordynamic forces on an eccentric whirling labyrinth seal can be calculated using this numerical approach. A qualitative comparison of forces with Leong [17] gave good agreement. Although measurements of the rotordynamic forces on a single theeth-on-rotor cavity are not available for quantitative comparisons, numerical simulations of multi-cavity domains in the near future will allow this.

The current computational results serve to provide the seal designer with

more complete information about pressure circumferential variation within a cavity. Specifically, the included results quantify the dependence of the tangential and radial force components on the level of inlet swirl. For the cases considered here, an increase in inlet swirl re–distributed the pressure field to give an increased tangential force and a decreased radial force. Further, the circumferential pressure distributions presented reveal details concerning the large variation of those force components with axial location from the mid–cavity location to that of the downstream tooth.

It was further found that, while there is definitely a net fluid shear force acting on the rotor, the combined effect of all stresses tend to cancel, giving less than a one percent contribution to each force component. The circumferential variation of both wall and "free" shear stresses is presented in order to allow the developers of simpler flow models to refine their shear stress modeling. The same stress components are quantified in reference [11] as a function of position along each surface at a fixed θ–location so that an approximate three–dimensional stress field can be constructed from the two sets of stress data together.

ACKNOWLEDGEMENT

The financial support of AFOSR is gratefully acknowledged.

REFERENCES

1 Alford, J. S., "Protecting Turbomachinery From Self-Excited Rotor Whirl," *Transactions of ASME, Journal of Engineering for Power*, vol. 87, pp. 333–344, 1965.

2 Kostyuk, A. G., "A Theoretical Analysis of the Aerodynamic Forces in the Labyrinth Glands of Turbomachines," *Teploenergetika*, vol. 419(11), pp. 29–33, 1972.

3 Iwatsubo, T., "Evaluation of Instability Forces of Labyrinth Seals in Turbines or Compressors," in *Rotordynamic Instability Problems in High Performance Turbomachinery*, Texas A&M University, May 12–14 1980.

4 Iwatsubo, T., Matooka, N., and Kawai, R., "Flow Induced Force and Flow Pattern of Labyrinth Seal," in *Rotordynamic Instability Problems in High Performance Turbomachinery*, Texas A&M University, May 10–12 1982.

5 Childs, D. W., and Scharrer, J. K., "An Iwatsubo Based Solution for Labyrinth Seals: A Comparison to Experimental Results," *ASME Journal of Engineering for Gas Turbines and Power*, vol. 108, pp. 325–331, April 1986.

6 Childs, D. W., and Scharrer, J. K., "Experimental Rotordynamic Coefficient Results for Teeth-On-Rotor and Teeth-On-Stator Labyrinth Gas Seals," in *ASME 86-GT-12 at the 31st International Gas Turbine Conference and Exhibit*, Dusseldorf, FRG, 1986.

7 Dietzen, F. J., and Nordman, R., "Calculating Rotordynamic Coefficients of Seals by Finite Difference Techniques," in *Rotordynamic Instability Problems in High Performance Turbomachinery*, Texas A&M University, 1986.

8 Wyssman, H. R., "Flow In Labyrinth Seals And It's Influence On Rotor Stability Of Turbocompressors," in *Von Karman Institute Lecture Series 1987*, Von Karman Institute For Fluid Dynamics, Jan. 19–23, 1987.

9 Wyssman, H. R., Pham, T. C. and Jenny, R. J., "Prediction of Stiffness and Damping Coeficients for Centrifugal Compressor Labyrinth Seals," in *ASME 84-GT-86 at the 29th International Gas Turbine Conference and Exhibit*, Amsterdam, June 4–7, 1984.

10 Tam, L. T., et al, "Numerical And Analytical Study Of Fluid Dynamic Forces In Seals And Bearings," in *ASME Biennial Conference on Mechanical Vibrations and Noise*, Boston, 1987.

11 Rhode, D. L., and Hensel, S. J., "Three Dimensional Computation Of Rotordynamic Force Distributions In A Labyrinth Seal," in *ASME/AIAA/ASCE/SIAM/APS First National Fluid Dynamics Congress*, Cincinnati, July 24–28, 1988.

12 Pope, S. B., "The Calculation of Turbulent Recirculating Flows in General Orthogonal Coordinates," *Journal of Computational Physics*, vol. 26, pp. 197-217, 1978.

13 Leonard, B. P., "A Stable and Accurate Convective Modelling Procedure Based on Quadratic Upstream Interpolation," *Computational Methods Appl. Mech. Engr.*, vol. 19, pp. 59-98, 1979.

14 Rhode, D. L., and Sobolik, S. R., "Simulation Of Subsonic Flow Through A Generic Labyrinth Seal," in *ASME International Gas Turbine Conference*, Houston, Texas, 1985.

15 Gosman, A. D. and Pun, W. M., "Calculation of Recirculating Flows," *Research*

Report, Report no. HTS/74/2, Dept. of Mech. Eng., Imperial College, London, England, 1974.

16 Rhode, D. L. and Nail, G. H., "Computation Of Cavity-BY-Cavity Flow Development In Generic Labyrinth Seals," in *ASME International Computers In Engineering Conference*, San Francisco, July 31 - Aug. 3, 1988.

17 Leong, Y.M.M.S., "Experimental Forces Induced by Flow Through Model Labyrinth Glands," *Research Report*, Ph.D. Dissertation, Heriot-Watt University, Edinburgh, June 1983.

18 Hensel, S. J., "Calculation of Rotordynamic Forces On Labyrinth Seals," *Research Report*, M.S. Thesis, Texas A&M University, College Station, Texas, 1986.

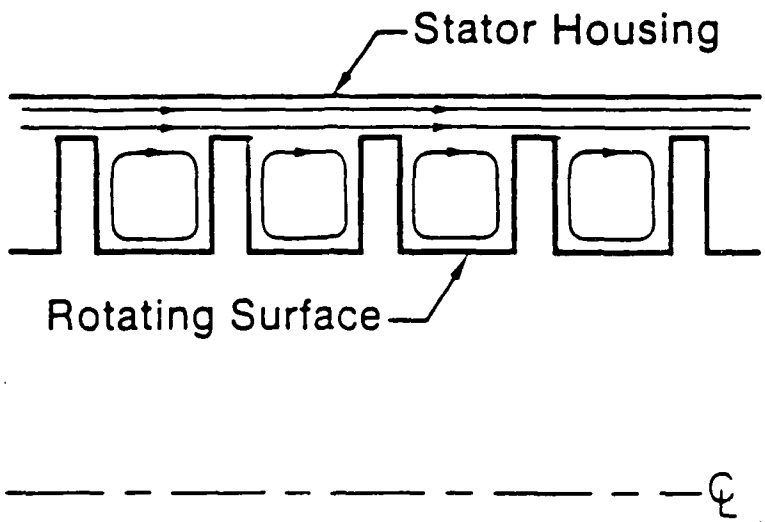

Fig. 1 Resulting streamlines due to leakage flow in a labyrinth seal

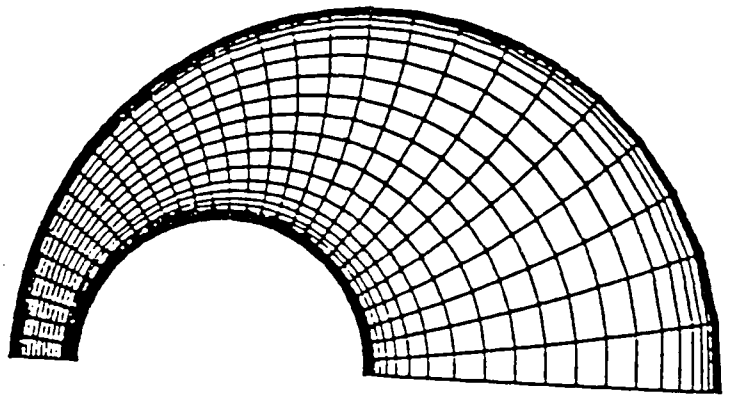

Fig. 2 An example of a finite difference grid in the eccentric region of the seal

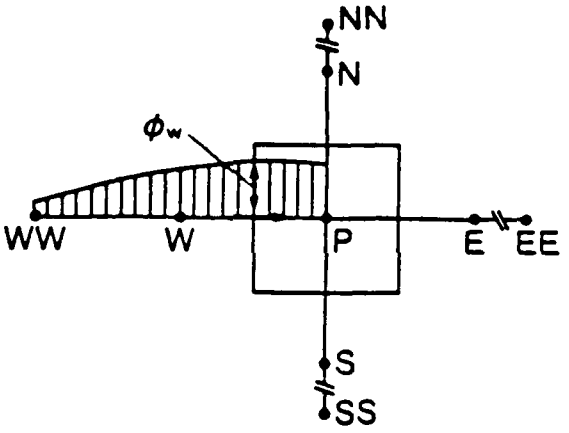

Fig. 3 Three-point interpolation for the west face of the control volume on a uniform grid using QUICK

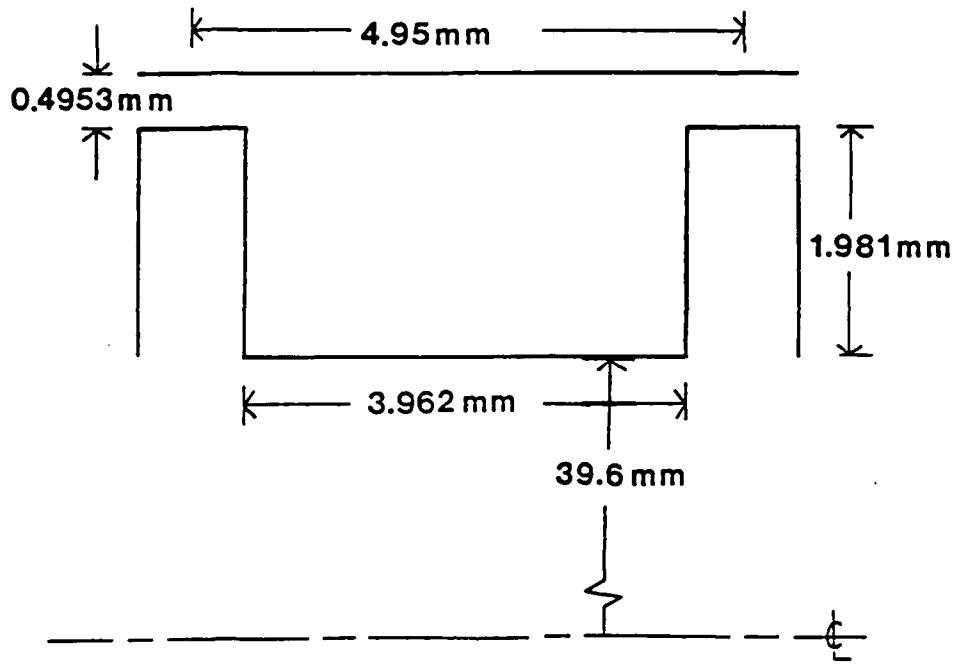

Fig. 4 The seal cavity investigated and its dimensions

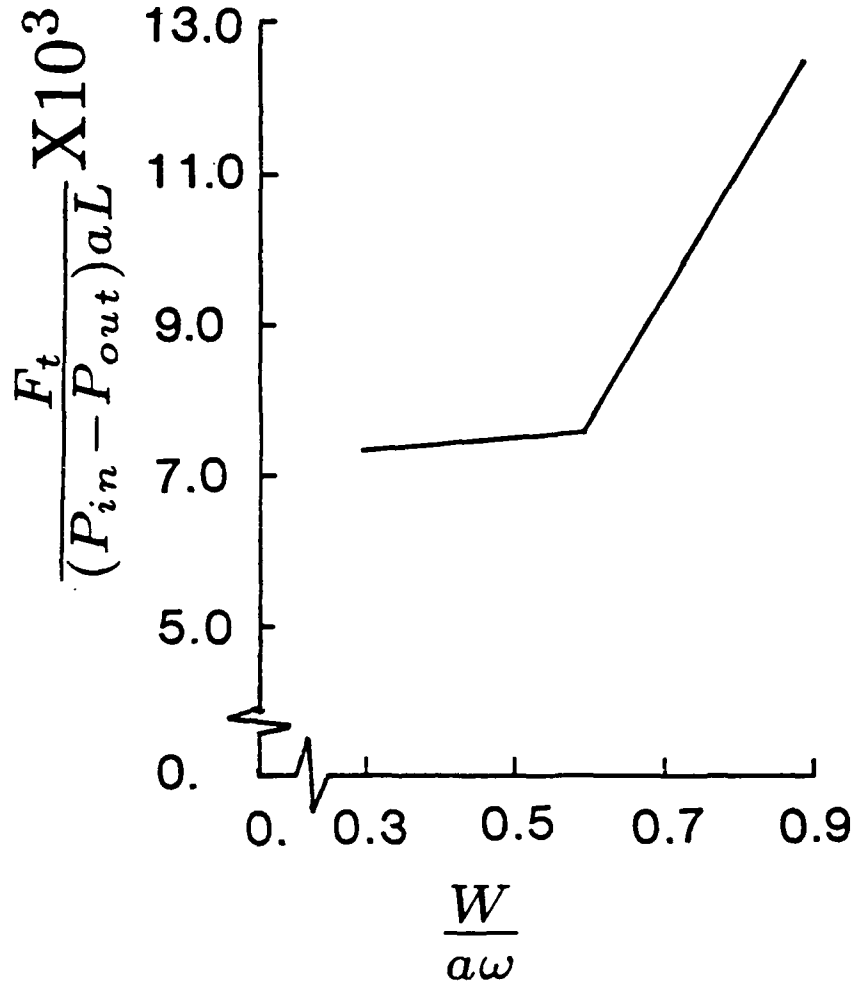

Fig. 5 Effect of inlet swirl on the
total tangential force for half-speed whirl

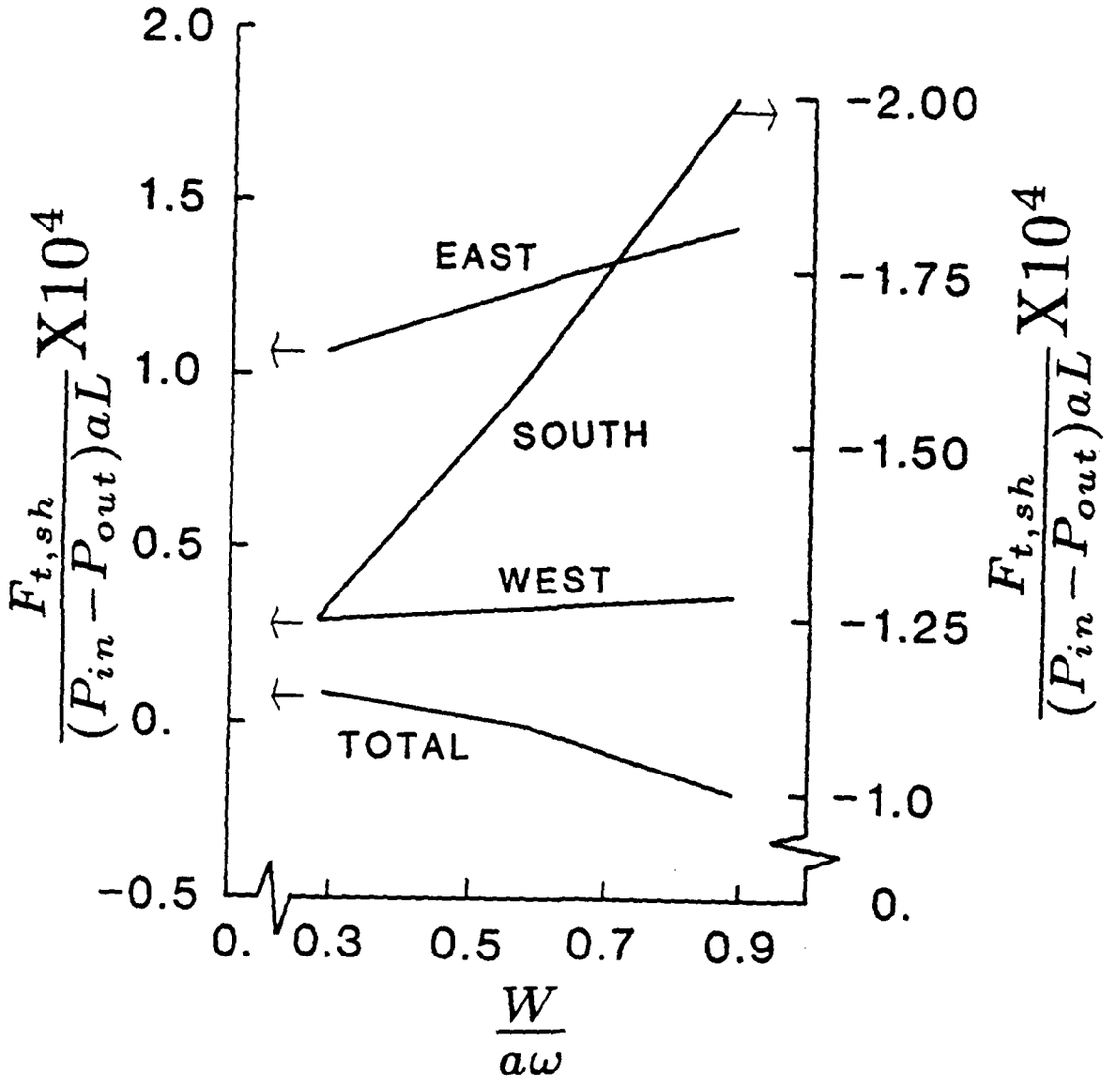

Fig. 6 Effect of inlet swirl on the shear stress contribution to the total tangential force on the cavity walls for half-speed whirl

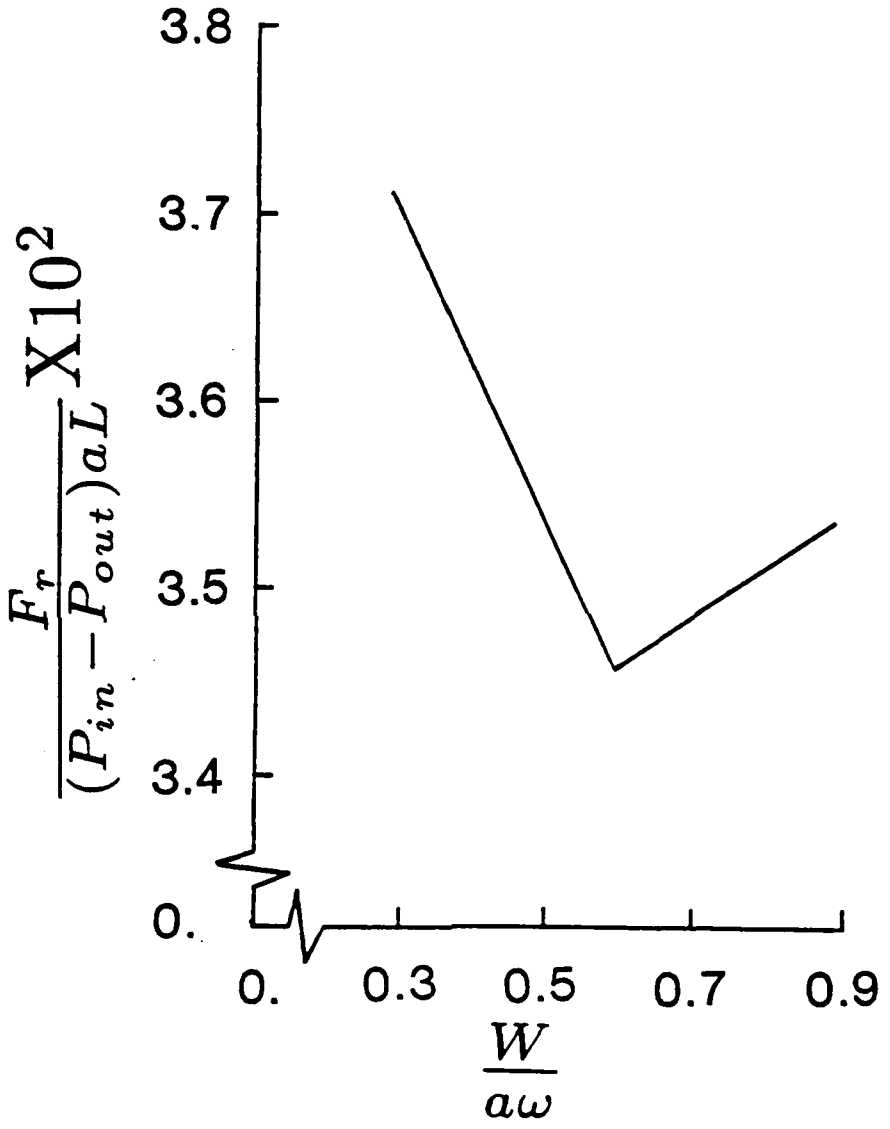

Fig. 7. Effect of inlet swirl on the total radial force for half-speed whirl

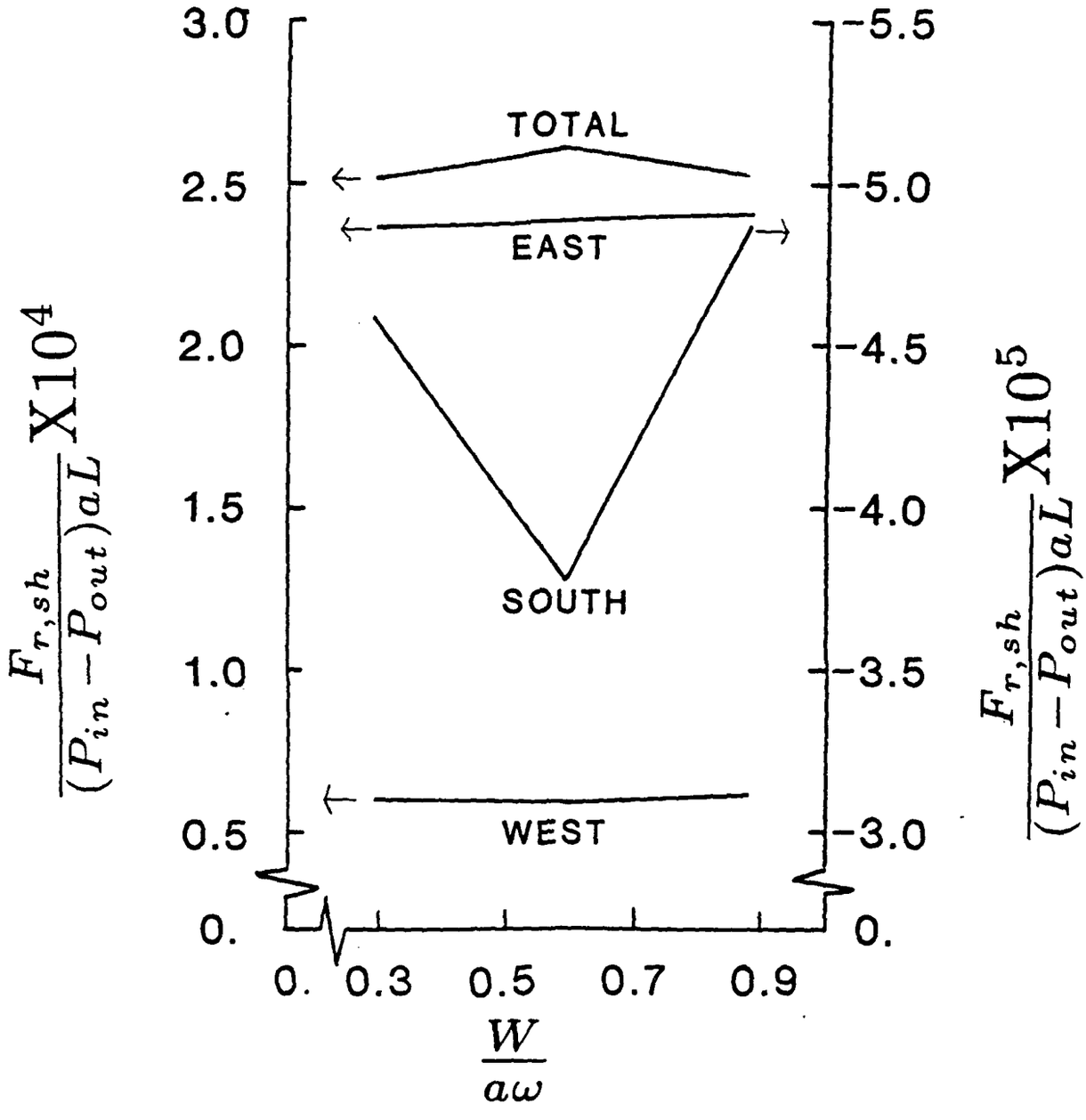

Fig. 8 Effect of inlet swirl on the shear stress contribution to the total radial force on the cavity walls for half-speed whirl

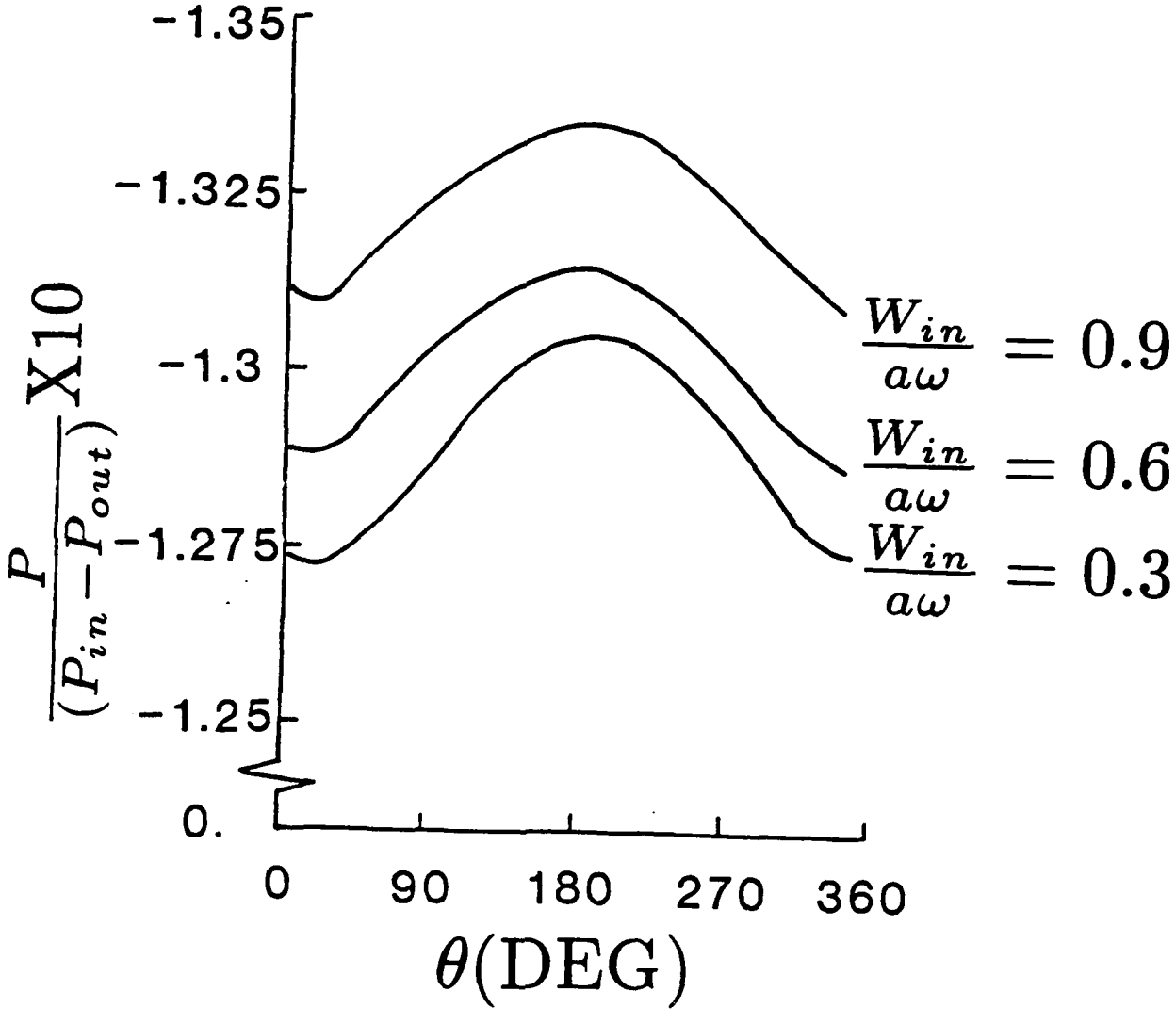

Fig. 9 Variation of relative pressure around the periphery of the rotor at mid-cavity for three inlet swirl cases at half-speed whirl

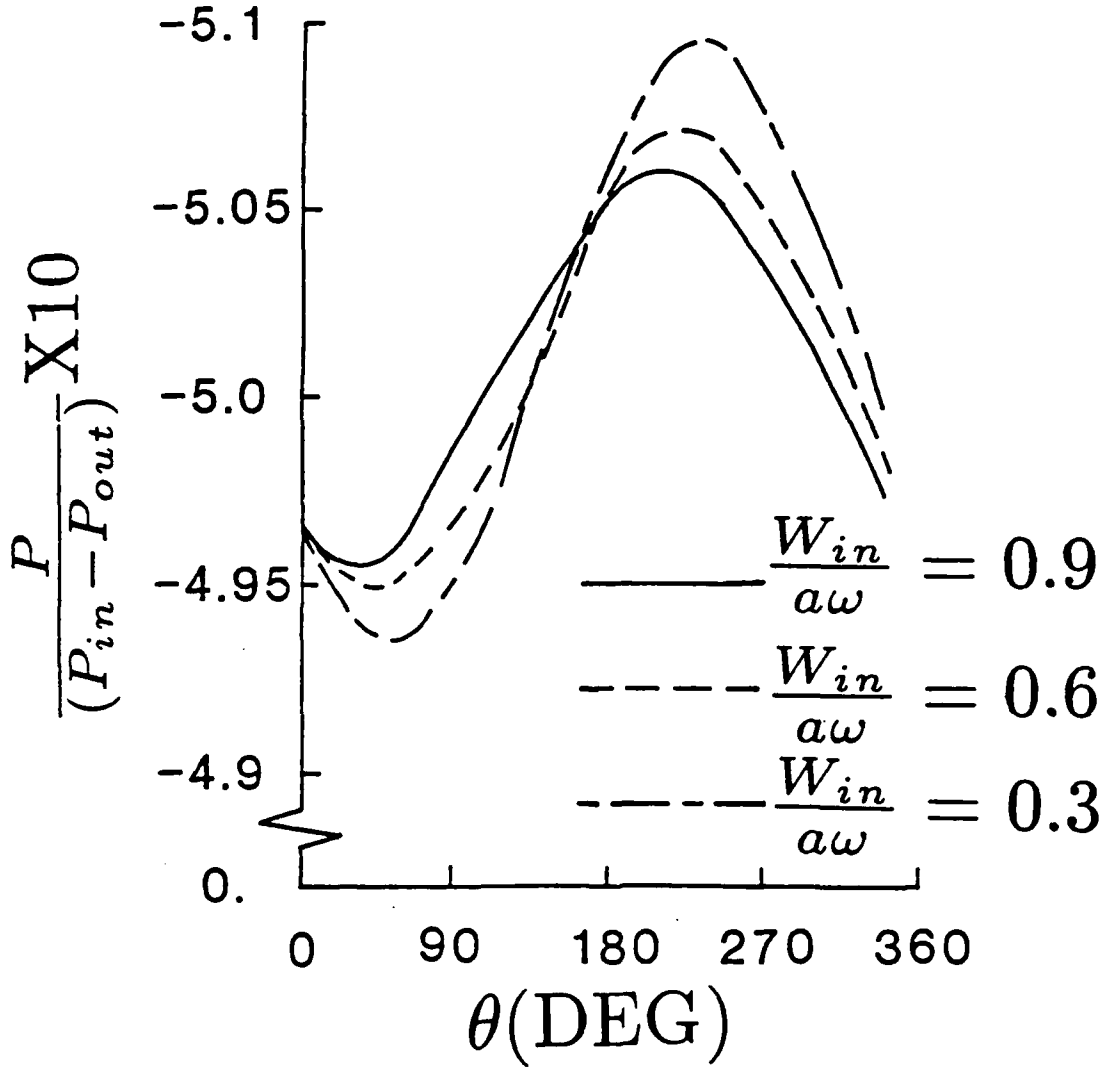

Fig. 10 Variation of relative pressure around the periphery of the downstream tooth for three inlet swirl cases at half-speed whirl

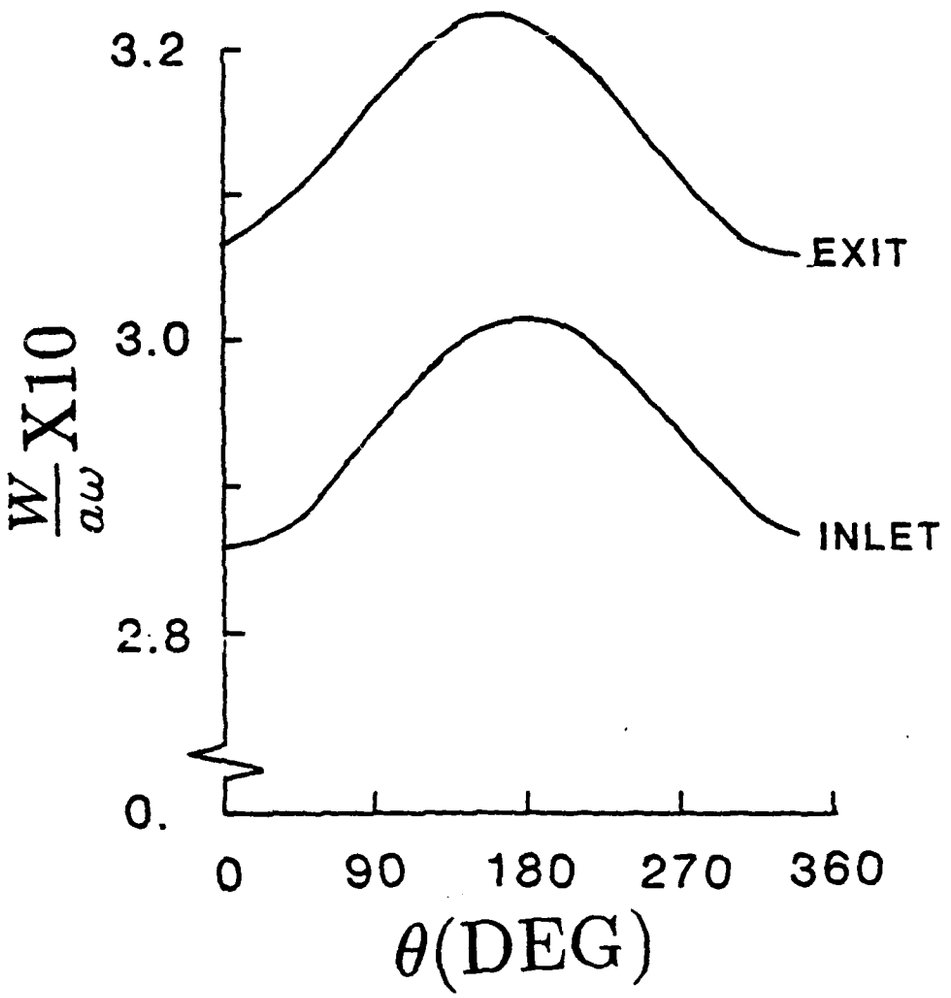

Fig. 11 Circumferential variation of spatially averaged swirl velocity component at the cavity inlet and outlet for $W_{in}^{*} = 0.3$ and half-speed whirl

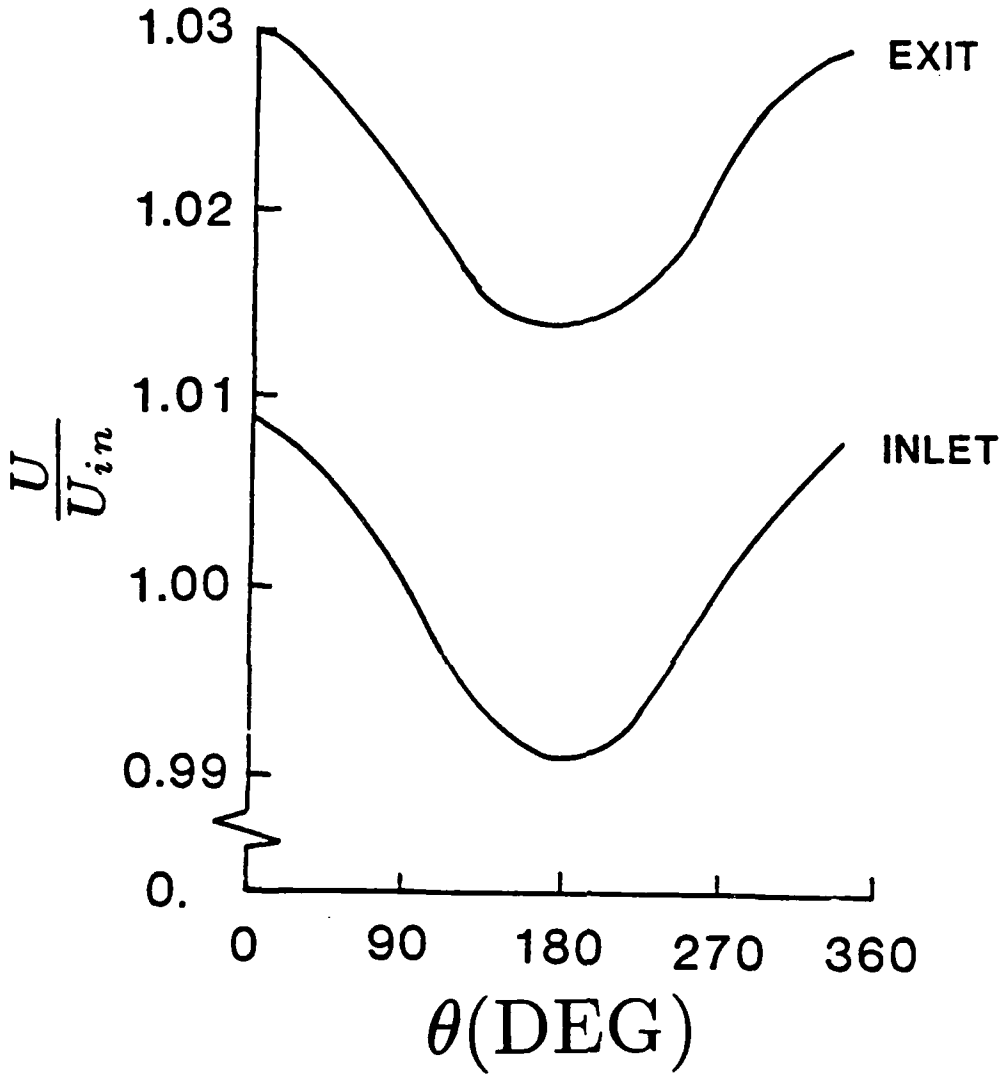

Fig. 12 Circumferential variation of spatially averaged axial velocity component at the cavity inlet and outlet for all three inlet swirl cases (W_{in}^{*} = 0.3,0.6, and 0.9) at half-speed whirl

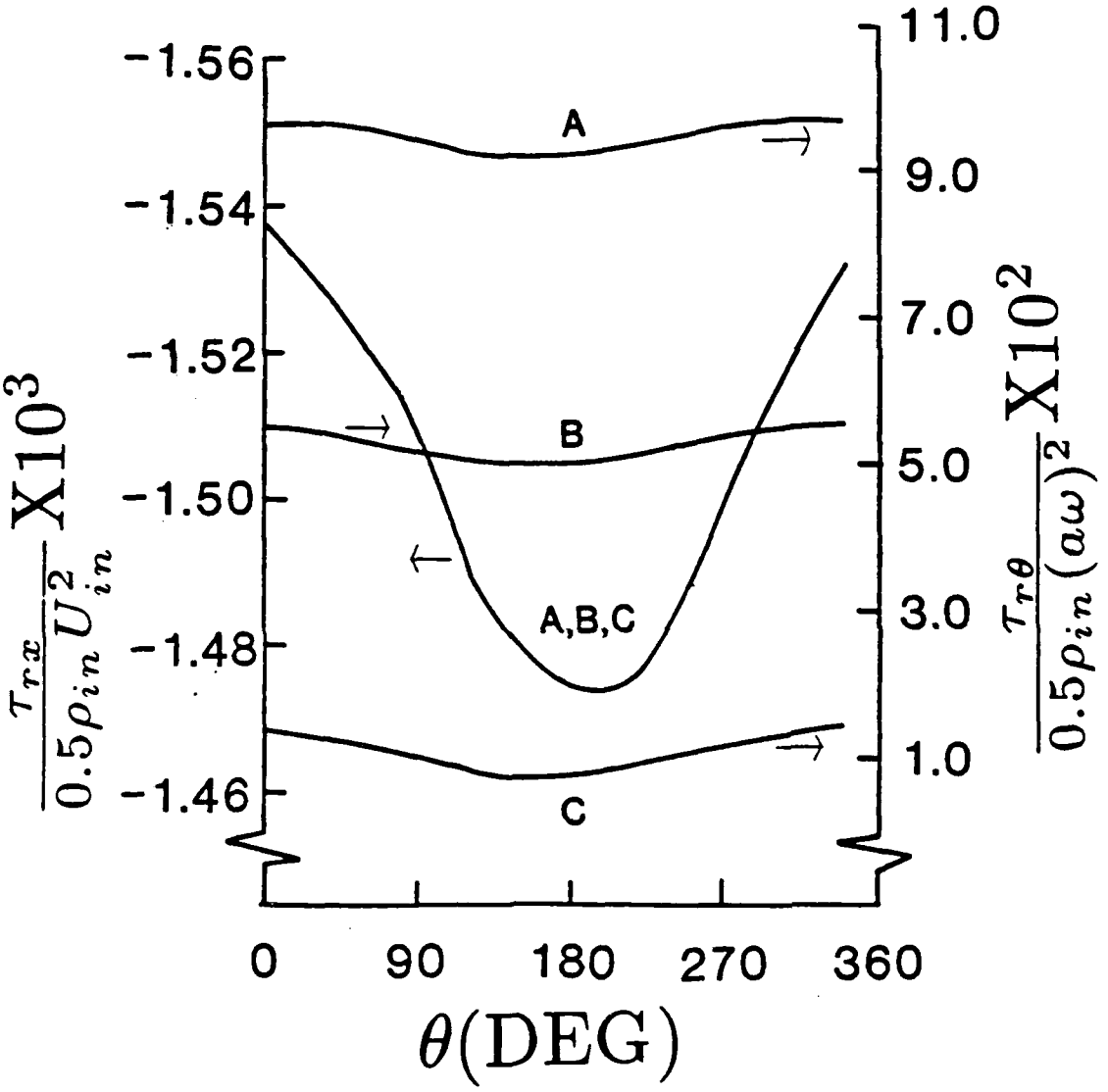

Fig. 13 Circumferential variation of rotor surface shear stresses at mid-cavity for cases A,B, and C (W_{in}^* =0.3,0.6, and 0.9 respectively) at half-speed whirl

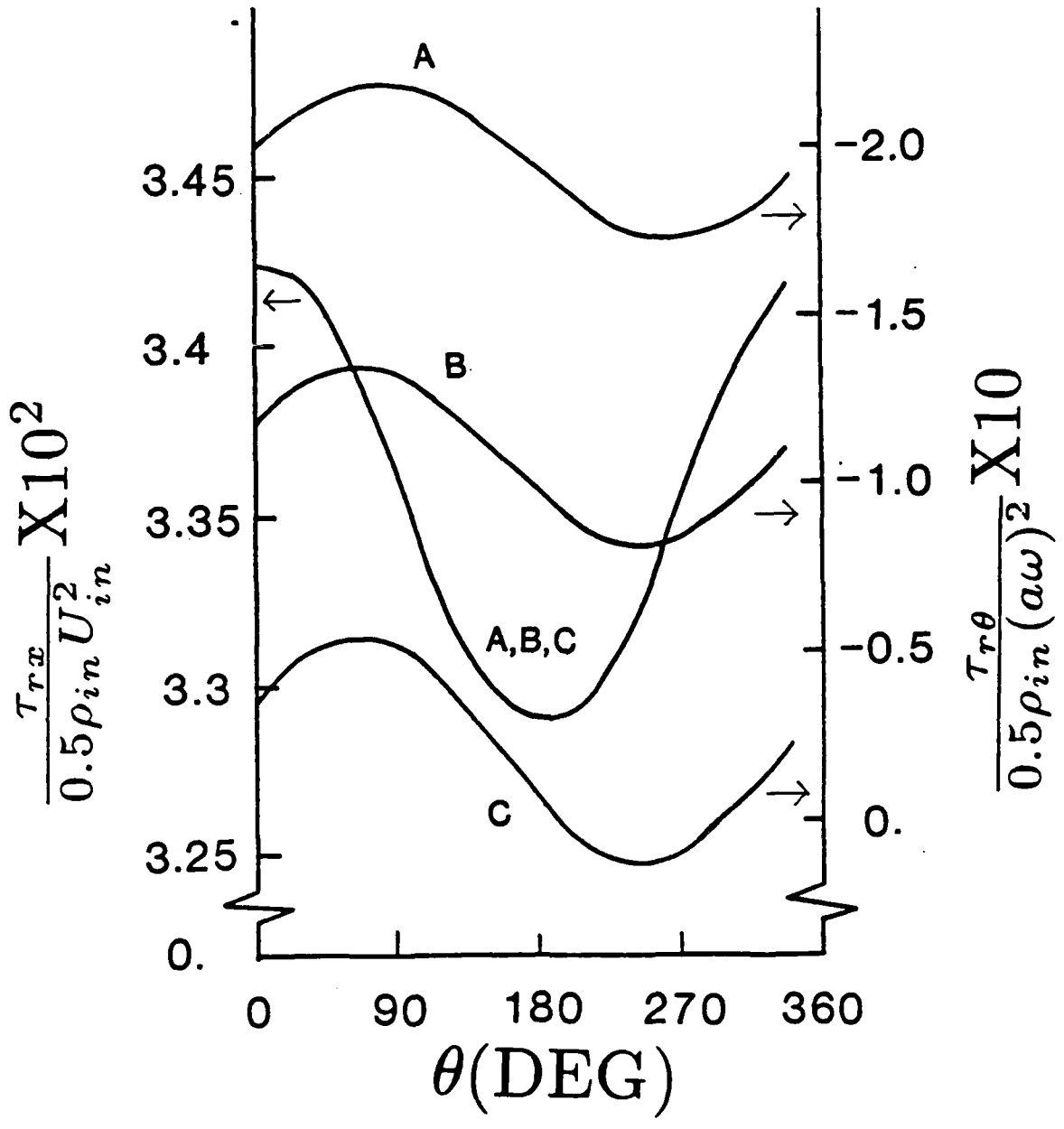

Fig. 14 Circumferential variation of free shear layer shear stresses at mid-cavity for cases A,B, and C (W_{in}^* =0.3,0.6, and 0.9 respectively) at half-speed whirl

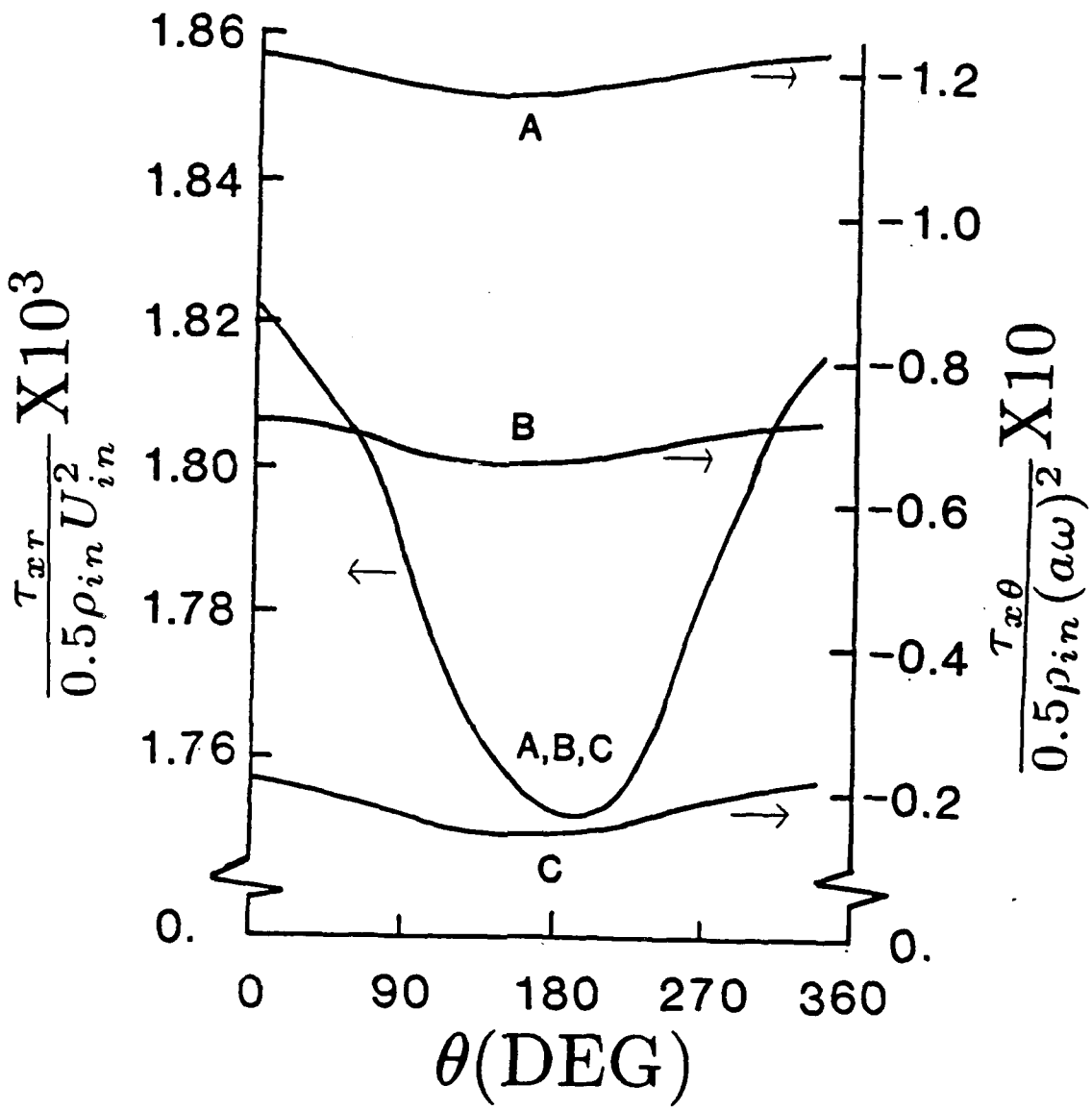

Fig. 15 Circumferential variation of tooth shear stresses at the midpoint along the downstream tooth for cases A,B and C (W_{in}^* =0.3,0.6, and 0.9 respectively) at half-speed whirl

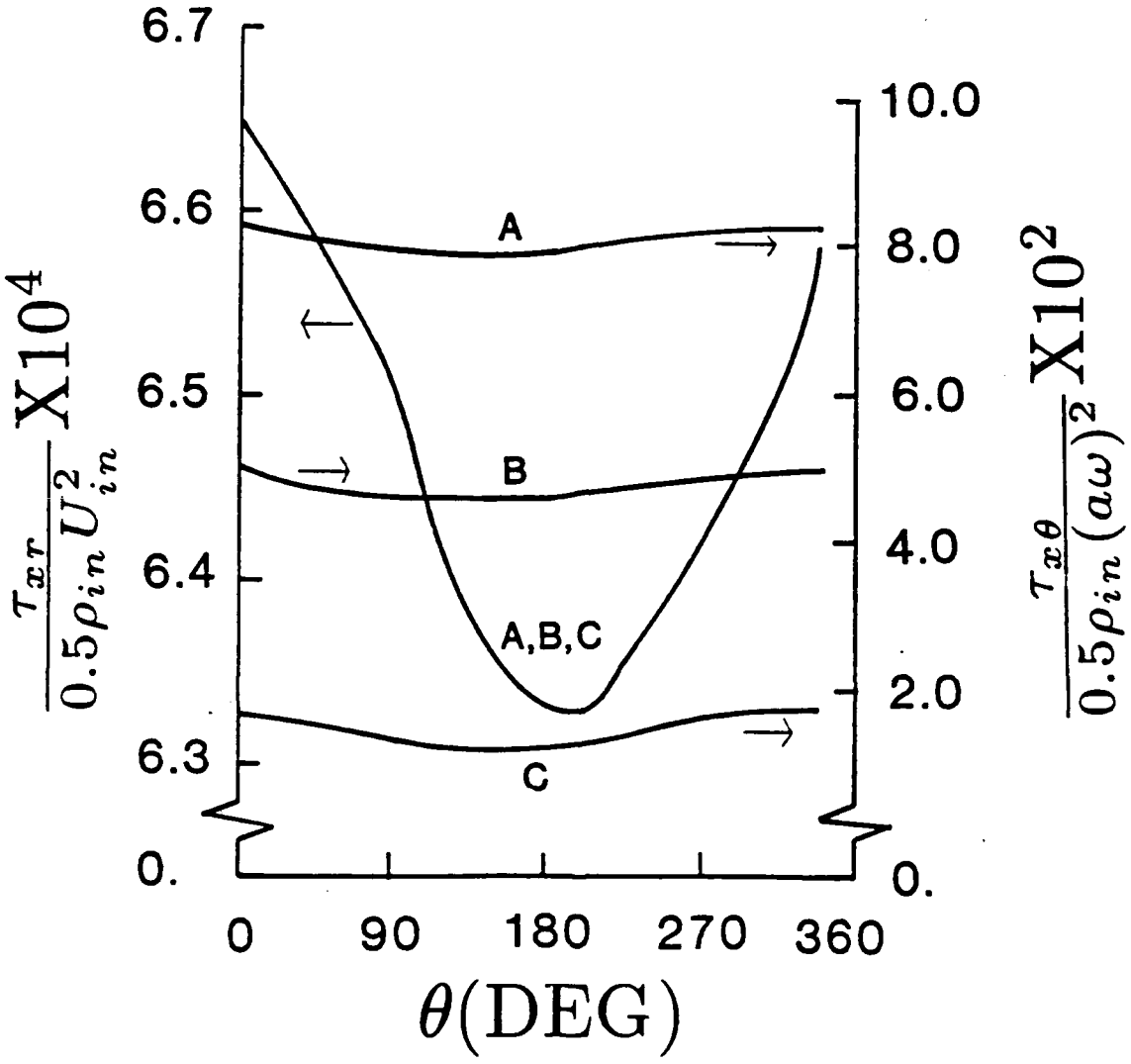

Fig. 16 Circumferential variation of shear stresses
at the midpoint along the upstream tooth for cases A,B, and C
(W_{in}^* = 0.3,0.6, and 0.9 respectively) at half-speed whirl

COMPUTATION OF CAVITY-BY-CAVITY FLOW DEVELOPMENT IN GENERIC LABYRINTH SEALS

D.L. Rhode* and G.H. Nail**
Turbomachinery Laboratories
Mechanical Engineering Dept.
Texas A&M University
College Station, TX 77843

---

* Associate Professor
** Graduate Student

NOMENCLATURE

a_p	point coefficient
a_j	neighbor coefficient
A	leakage flow area
A_e	area of east face of control volume
A_n	area of north face of control volume
A_w	area of west face of control volume
c	clearance
D^u	diffusion coefficient
ϵ	turbulence kinetic energy dissipation rate
Γ	diffusion coefficient
k	ratio of specific heats
κ	turbulence kinetic energy
l	turbulence length scale
$\dot{m}$	leakage mass flow rate
M	Mach number
μ	absolute viscosity
μ_{eff}	effective viscosity
μ_T	turbulent viscosity
P	static pressure
P'	pressure correction
Pe	Peclet number
$\overline{P}$	bulk averaged pressure
r	radial coordinate
R	outer stator radius
Re	Reynolds number
ρ	density
$\overline{\rho}$	bulk averaged density
S_u	source term
S_ϕ	general source term
Ta	Taylor number
u	axial velocity component
$\overline{U}$	bulk averaged axial velocity component
v	radial velocity component
v	specific volume
w	swirl velocity component
x	axial coordinate

Subscripts

e	cavity exit, east face of control volume
E	eastern neighbor control volume
EE	eastern neighbor of eastern neighbor
i	cavity inlet
n	north face of control volume
N	northern neighbor control volume
NN	northern neighbor of northern neighbor
P	center control volume
p	center of control volume
ϕ	general flow variable
r	radial
s	south face of control volume
S	southern neighbor control volume
SS	southern neighbor of southern neighbor
sh	shaft
θ	circumferential
w	west face of control volume
W	western neighbor control volume
WW	western neighbor of the western neighbor
x	axial

Superscripts

*	nondimensionalized, uncorrected value
/	correction value

ABSTRACT

A recently developed version of a swirl-flow finite difference computer program was improved and employed in predicting the compressible flow of air through labyrinth seals. The substantial effect of inlet leakage Mach number on grid sensitivity of the solution is investigated. Further, cavity-by-cavity development of the flowfield is computed and the distribution of various field variables are presented. Results are for straight-through seals of both teeth-on-stator and teeth-on-rotor types. The teeth-on-rotor seal gives less leakage than the equivalent teeth-on-stator design. However, it exhibits a greater tendency to generate self excited rotordynamic forces due to higher swirl velocities. Also, previously unavailable predictions of swirl velocity development are provided for the refinement of simple models for rotordynamic forces.

INTRODUCTION

Labyrinth seals are most commonly used in rotating machinery such as pumps, compressors and turbines. C. A. Parsons [1] apparently was the first to introduce the labyrinth seal in his development of the steam turbine near the turn of the century. Figure 1 shows a straight-through, teeth-on-rotor labyrinth seal.

The sealing objective is to present a highly frictional flow path between high- and low-pressure regions by means of a series of non-contacting restrictors and separating chambers. When the fluid enters a seal, it flows through a small constriction at the first tooth and part of the pressure head is converted into mean flow kinetic energy. Seals are designed so that a large portion of this kinetic energy is lost via turbulence dissipation in the chamber immediately downstream. Other constrictions and chambers follow downstream, where the process is repeated.

Numerous investigators have proposed empirically based relations utilizing characteristics of the overall flowfield for estimating the leakage rate. Experimental data such as total pressure drop has been recorded and used to develop these relationships. Leakage has been expressed as a function of overall pressure drop, friction factor, seal clearance, tooth thickness, cavity width, shaft speed and number of teeth. Resulting predictions from these formulas are successful when applied to seals which are very similar to those which were empirically studied. However, any significant difference in seal geometry can give considerable error. Therefore, a more widely applicable method has been sought for seals of arbitrary geometry, shaft speed, pressure drop, etc.

A numerical algorithm for solving the Navier-Stokes equations is widely applicable for seals. Furthermore, such a computational tool does not require extensive empirical data as a user input. However, this approach and can be quite expensive.

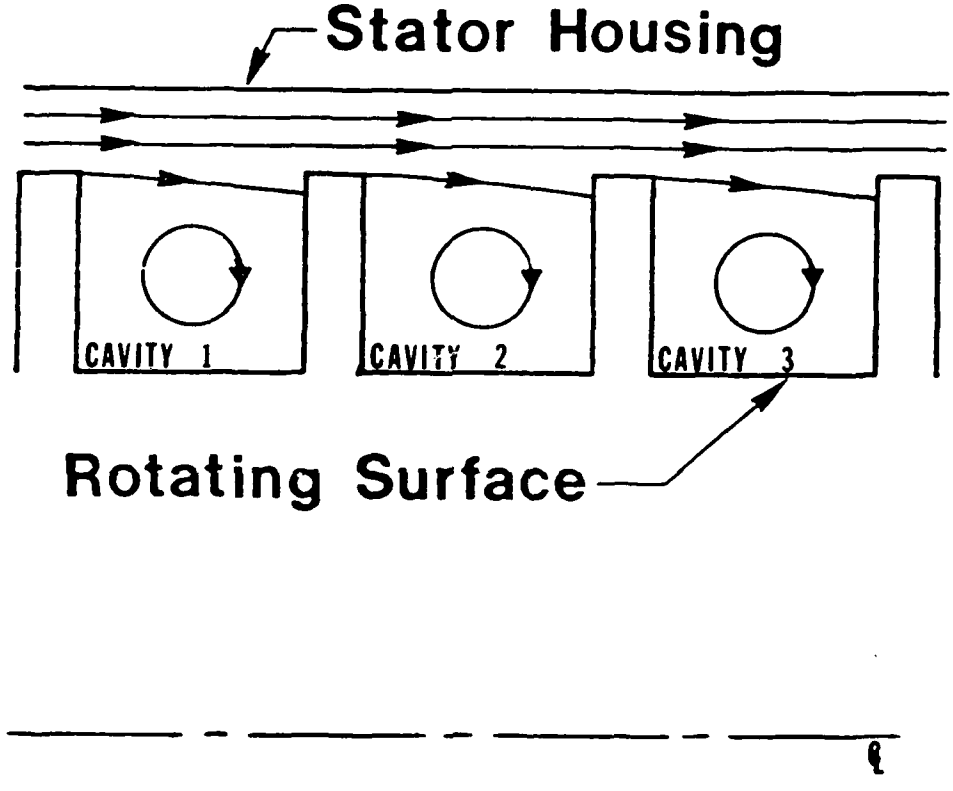

Fig. 1 Basic configuration and expected streamline pattern for a generic straight-through labyrinth seal

Stoff's investigation [2] of incompressible flow in seals was the first attempt at such a numerical solution. His work involved an extension of the TEACH computer program [3], which constitutes the basic approach used in this study also. Some of the more recent numerical results are those of Rhode and Sobolik [4] and Sobolik [5] involving subsonic compressible flow. The current study builds upon that work.

The primary objective of the present research is to predict the flowfield development from cavity to cavity along a labyrinth seal. Secondary objectives include comparison of swirl velocity and other quantities for corresponding teeth-on-stator and teeth-on-rotor generic labyrinth seals. The computer code of Sobolik [5] was extended in various ways in order to achieve these objectives.

PREVIOUS WORK

Most of the leakage oriented research has been aimed at developing simple empirical relationships between the leakage flow rate and the overall pressure drop, seal geometry, shaft speed and Reynolds number. Details such as velocity profiles have only very recently become the objective of experimental researchers.

Work done on labyrinth seals can be classified into compressible fluid leakage, incompressible fluid leakage and rotordynamic instability studies. The paper by Sneck [6] and the theses by Cogan [7] and Sobilik [5] were invaluable in compiling this review. The topic of instability is not addressed in this paper, and thus related studies are not included.

Compressible Fluid Leakage Studies

Martin [8], Stodola [9], Gercke [10], Egli [11], Dolin and Brown [12], Hodkinson [13], Kearton and Keh [14], Zabriskie and Sternlicht [15], Vermes [16], Rao and Narayanamurthi [17], Deich, et al. [18] and Benvenuti [19] are examples of early work with compressible flow seals. These studies drew conclusions based on gross overall characteristics of the flowfield. These researchers made assumptions such as constant flow area, uniform axial velocity profile or negligible turbulent kinetic energy carry-over. These assumptions greatly simplify the problem. However, models developed in this way have been very limited in application.

The first to take detailed measurements of compressible flow in labyrinth seals was Hauck [20]. He measured the axial and swirl components of velocity in straight-through and stepped seals. Velocity profiles were measured both in the cavity as well as in the leakage region. Hauck's test facility operated at both 4000 and 5000 CPM, and allowed for rotor eccentricity up to 75 percent of the clearance for a

concentric rotor.

Apparently the first to present a detailed numerical solution for the compressible flowfield within a labyrinth seal were Rhode and Sobolik [4]. A finite difference method was used employing Patankar's [21] SIMPLE (Semi-Implicit Method for Pressure-Linked Equations) algorithm. Converged solutions were obtained using each of two different finite differencing schemes: the Hybrid scheme developed by Spalding [22], and the QUICK scheme developed by Leonard [23]. Zimmermann and Wolff [24] developed an analytical model for correlation of leakage and pressure-drop. Previously obtained numerical solutions were used to integrate cavity exit velocity profiles and compute standard loss coefficients for each cavity.

Kirk [25] developed a relatively simple computer program to calculate the circumferential swirl and pressure distribution. He computed a nondimensionalized tangential velocity ratio and compared with previously obtained experimental results. The experimental data reveals a reduction of swirl, as the flow moves radially inward, that was not predicted. However, predicted and experimental results for swirl never differed by more than 25 percent.

Nordmann, et al. [26] also used a finite difference program to simulate flow in straight-through labyrinth seals. The effort was directed toward the fluid forces and rotordynamic coefficients. But they also plotted leakage as a function of pressure ratio, comparing against previous obtained experimentally results.

Incompressible Fluid Leakage Studies

Jerie [27], Bell and Bergelin [28], Nikitin and Ipatov [29] and Han [30] are examples of earlier studies dealing with gross overall characteristics. The conclusions reached by these researchers developed the application of flow and velocity carry-over coefficients, critical Reynolds number for transition to turbulence

and friction coefficients.

Three recent studies constitute the first investigations pertaining to detailed characteristics of velocity and pressure throughout a seal cavity. One was conducted by Stoff [2]. He used a finite difference computer program descended from the TEACH program to solve the Reynolds-averaged Navier-Stokes equations along with those of the $\kappa - \epsilon$ turbulence model. Predictions as well as experimental measurements of water in a large scale straight-through seal facility were obtained. He compared predictions of a single radial profile of mean swirl velocity and rms swirl velocity with corresponding experimental measurements for an axial station midway between adjacent teeth.

Rhode, et al. [31] is the second detailed study. That paper reports comparison predictions of two cavity configurations for a straight-through seal. A more recent version of a swirl-flow finite difference computer program, also descended from TEACH, was employed. Detailed radial profiles of the three velocity components, pressure and turbulence kinetic energy were shown. In addition, a recent convective differencing scheme was evaluated for numerical stability and accuracy.

Finally, Demko [32-34] conducted a study using both computational and experimental methods. He presented corresponding predictions and measurements of selected quantities such as axial and radial velocity and pressure. By investigating flow at relatively high Taylor numbers (typically Ta$> 10^4$) he was able to computationally and experimentally verify the existence of a double recirculation zone pattern. He presented his results in the form of a flow map which one can use to predict the existence of either a single versus a double recirculation zone within the cavity.

COMPUTATIONAL APPROACH

General Methodology

The compressible flow program for flow in labyrinth seals is a descendant of the TEACH program [3]. Seven simultaneous, partial differential equations are solved. These are: (a) the compressible, axisymmetric form of the Reynolds-averaged equations for conservation of momentum (with x, r, and θ time-mean velocity components u, v, w), (b) the two turbulence transport equations constituting the $\kappa - \epsilon$ turbulence model, (c) the energy equation, and (d) a pressure equation which determines the pressure field and enforces conservation of mass. Each of these can be divided into convection, diffusion and source term components and cast in the general form

$$\frac{1}{r}[\frac{\partial}{\partial x}(\rho u r \phi) + \frac{\partial}{\partial r}(\rho v r \phi)$$

$$-\frac{\partial}{\partial x}(r\Gamma_\phi \frac{\partial \phi}{\partial x}) - \frac{\partial}{\partial r}(r\Gamma_\phi \frac{\partial \phi}{\partial r})] = S_\phi \qquad (1)$$

Phi is the general dependent variable and Γ_ϕ is the diffusive coefficient respective to each equation. For example, in the x-momentum equation ϕ = u and $\Gamma = \mu_{eff}$. The effects of turbulence are incorporated through modification of the laminar-flow momentum diffusion coefficient μ. The turbulent viscosity μ_T is added to μ giving an effective viscosity μ_{eff} which is given by

$$\mu_{eff} = \mu_T + \mu \qquad (2)$$

The two-equation $\kappa - \epsilon$ model [35] was utilized to evaluate μ_T.

Figure 2 shows the staggered grid system on which the finite difference equations are solved. Values for all variables except u and v are stored at the intersections of the illustrated grid lines, such as point P. The axial and radial velocity components are stored at locations denoted by arrows. Different control volumes C, U and V for the variables stored at the p, w and s locations are shown in Fig. 2. An example of the computational domain that has been chosen for a labyrinth seal can be seen in Fig. 3.

Each ϕ has a corresponding finite-difference equation which was obtained from Eqn. 1 by applying the Gauss Divergence Theorem and expressing the result in terms of neighboring grid point values. The incorporation of the differencing schemes is discussed in Rhode, et al. [31]. As an example, the axial momentum equation from which u^*, a velocity estimate, is computed is

$$a_p^u u_p^* = \sum_j a_j^u u_j^* + A_w(P_w^* - P_p^*) + S_u^* \tag{3}$$

To satisfy conservation of mass locally, the values for u^* and v^* must undergo a correction. This correction is accomplished using the pressure-correction P' values. The equation for this quantity is derived from conservation of mass and momentum and is explained in further detail in a subsequent section. The expression for the corrected axial velocity formulation is

$$u_p = u_p^* + D^u(P_w' - P_p') \tag{4}$$

$$D^u = \frac{A_w}{a_p^u}$$

The radial velocity is corrected similarly. The P' equation takes the form

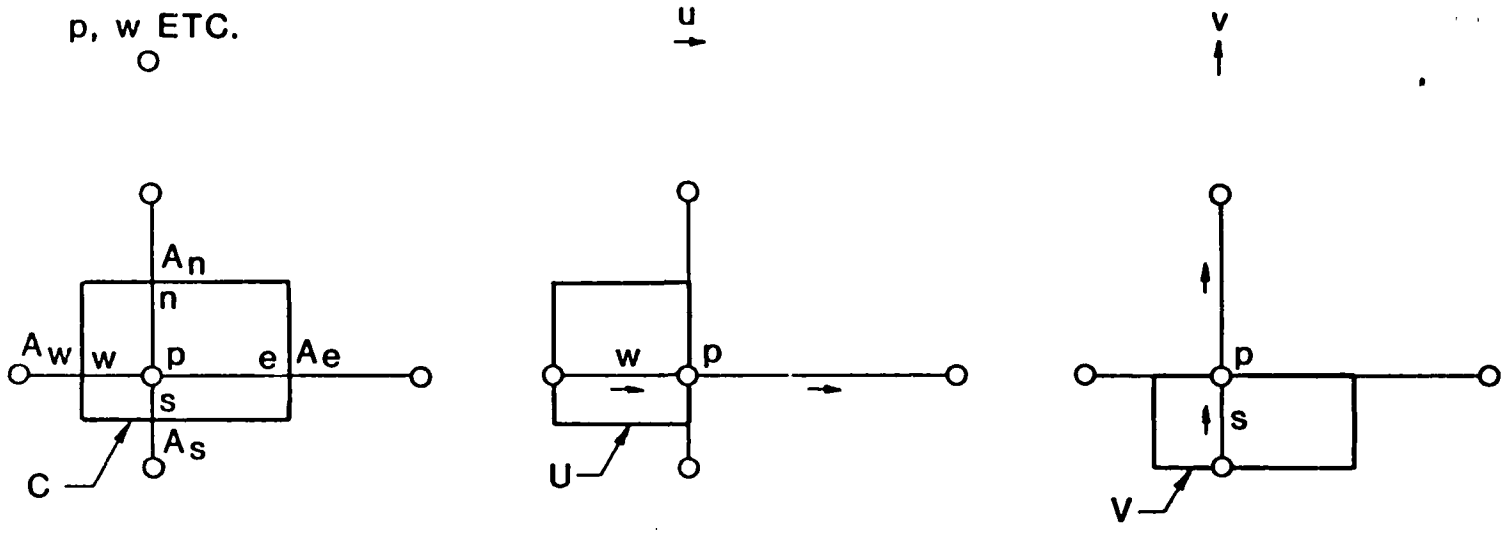

Fig. 2 Typical control volume showing staggered u and v cells

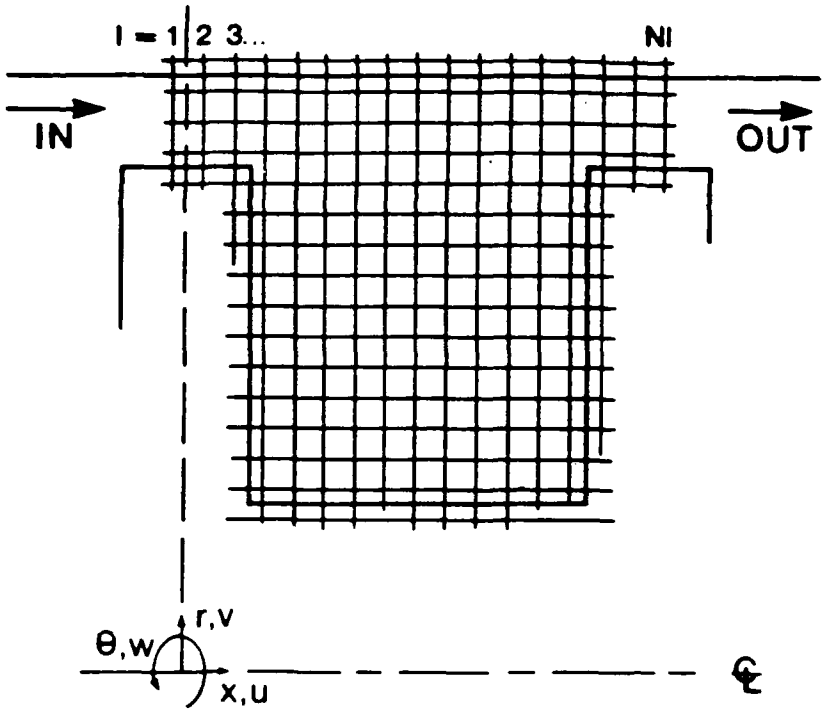

Fig. 3 Computational domain for a labyrinth seal cavity showing a uniform coarse grid

$$a_p^p P_P^l = \sum_j a_j^p P_j^l + S_u^p \tag{5}$$

as discussed in Patankar [21].

For the previously considered incompressible flow cases [31], the flow could be considered streamwise periodic. Thus, cavity inlet boundary conditions for all variables excepting pressure were set equal to the newly calculated exit values at the conclusion of each iteration. Flow at the cavity outlet is strongly convective in nature, and thus the upwind differencing used there requires no outlet boundary conditions. For the present compressible flow grid independence cases, the inlet values resulting from the above procedure were adopted in dimensionless form. Alternately, the cavity-by-cavity development computations used the exit values from the previous successive cavity as the corresponding inlet values. Further, the empirically-based law of the wall was used to evaluate normal derivatives of velocity tangent to a given wall.

False Diffusion

The upwind differencing scheme has been used extensively, however, it can introduce false diffusion. This truncation error occurs predominantly in flows where convection dominates (i.e., where the grid Peclet number $|Pe| = \frac{|V|\Delta}{\Gamma_\phi}$ exceeds 2.0) with substantial streamline-to-grid skewness and substantial diffusion normal to the streamlines.

False diffusion can cause an overly diffusive solution. Recirculating flows are particularly susceptible to the effects of false diffusion because of the certainty of considerable velocity gradients and streamline-to-grid skewness. The QUICK (Quadratic Upstream Interpolation for Convective Kinematics) scheme of Leonard

[23] was derived with the intention of reducing false diffusion. It employs a three-point, upwind-shifted interpolation formula. Predictions for turbulent flows by Leschziner and Rodi [36] and Han et al. [37] have indicated distinct advantages over the Hybrid upwind/central differencing scheme. Moreover, comparisons between the Hybrid and QUICK schemes for incompressible flow in labyrinth seal cavities by Rhode, et al. [31] for example, showed that the QUICK scheme yielded grid-independent solutions on considerably coarser grids than for the Hybrid scheme.

QUICK has been used in formulating the convective terms of the momentum equations only. Leschziner and Rodi [36] showed the κ and ϵ solutions are not significantly affected by alternative differencing schemes because of the source-term dominance of the corresponding transport equations. The κ and ϵ source terms contain the large generation and dissipation effects.

Computational Devolopments

An improved version of the compressible-flow P' equation was developed and tested. The essence of the modifications are best understood after reviewing a derivation of the P' equation for a simple case of one-dimensional axial flow. The derivation begins with the discretized form of the steady flow mass conservation equation

$$(\rho u)_e - (\rho u)_w = 0 \tag{6}$$

Lower case subscripts refer to values at control volume faces. A typical control volume for P' is shown in Fig. 2 as the C control volume. The mass flux through the east face, for example, where the $\rho'_e u'_e$ term has been neglected is

$$(\rho u)_e = (\rho^* + \rho')_e(u^* + u')_e = \rho_e^* u_e^* + \rho_e^* u_e' + \rho_e' u_e^* \tag{7}$$

The quantities ρ^* and u^* are the latest estimates to be corrected via ρ' and u' in order to satisfy the mass conservation equation.

The previous version of the program used a formulation for the ρ' terms using the ideal gas equation of state which gives

$$\rho_e' = \frac{1}{2}(\rho_E' + \rho_P') = \frac{1}{2}(\frac{P_E'}{RT_E} + \frac{P_P'}{RT_P}) \tag{8}$$

Note that the expression for ρ_e' in Eqn. 8 is the simple arithmetic mean. It was found in the present study that expressing ρ_e' in this way contributed to numerical instabilities during the iterative solution algorithm. This effect was more pronounced when the grid lines were non-uniformly distributed within the flow domain. An alternative formulation of ρ_e' that reduced numerical instabilities when using non-uniform grids was sought. Several variations were numerically tested for a labyrinth cavity flowfield. Evaluation of ρ directly from the ideal gas equation of state without using a ρ' quantity was an improvement over the $\rho = \rho^* + \rho'$ approach. This led to an algorithm that is less susceptible to numerical instabilities. The expression replacing Eqn. 7 is

$$(\rho u)_e = \rho_e(u^* + u')_e = \rho_e u_e^* + \rho_e u_e' \tag{9}$$

here ρ_e is formulated using the harmonic mean expression

$$\rho_e = \frac{2\rho_P \rho_E}{\rho_P + \rho_E} \tag{10}$$

From the axial momentum equation, one finds the following expressions [21] for velocity corrections

$$u'_e = D^u_e(P'_P - P'_E) \tag{11}$$

$$u'_w = D^u_w(P'_W - P'_P)$$

$$D^u_e = \frac{A_e}{a^u_P}$$

$$D^u_w = \frac{A_w}{a^u_P}$$

Upon appropriate east and west face mass flux substitutions into Eqn. 6 the following difference equation is obtained for P'

$$[A_E + A_W]P'_P = A_E P'_E + A_W P'_W + \Delta\dot{m}^* \tag{12}$$

$$A_E = \rho_e D^u_e$$

$$A_W = \rho_w D^u_w$$

$$\Delta\dot{m}^* = \rho_w u^*_w - \rho_e u^*_e$$

The P' equation used in the current computer program was derived from the two-dimensional flow mass conservation equation in cylindrical coordinates. The

procedure exactly parallels that given here. Appropriately, $P' = 0$ along boundaries was utilized for boundary conditions.

The TDMA (Tri-Diagonal Matrix Algorithm) is used to solve for the dependent variable of each finite difference equation in a line-by-line fashion. The previous version of the code solved for one vertical column at a time, beginning at the west boundary and sweeping line-by-line to the east boundary. This procedure causes the inlet boundary condition, usually at the west boundary, to be felt quickly by interior points of the calculation domain. This desirable effect is greatly enhanced if the fluid flow is in the same direction as the line-by-line sweeping motion of the TDMA.

The previous method of solving for vertical columns while sweeping from west to east tends to work very well in the predominantly straight-through west to east leakage flow region. It does not, however, efficiently incorporate the effect of boundary conditions within the recirculation zone of the cavity. For this reason an ADI sweeping procedure was implemented. It alternates between west-east and north-south sweeps, solving for vertical columns and horizontal rows, respectively. In this way, information from the boundary conditions is efficiently transmitted to all regions of the flow domain.

RESULTS AND DISCUSSION

The Seals Considered

In order to investigate the cavity-by-cavity distribution of various quantities, a TOS and also a TOR seal were simulated. The TOS cavities had a shaft radius of 0.0725 m, shaft centerline-to-cavity base radius of 0.07609 m and shaft centerline-to-tooth periphery radius of 0.07291 m. The TOR cavities had a shaft radius of 0.0725 m, a shaft centerline-to-stator radius of 0.07609 m, and shaft centerline to tooth periphery radius of 0.07568 m. Both seals had a cavity width of 0.002825 m and a tooth width of 0.00035 m.

Grid Independence

Figure 4 illustrates the effect of inlet leakage Mach number on grid independence. A uniform inlet temperature of $293^{o}K$ was assumed. After an inlet leakage Mach number M_i was selected, the inlet stator wall pressure was set to a value yielding an inlet leakage Reynolds number of $Re_x = \frac{\rho \overline{U_i} 2c}{\mu} = 2.60 \times 10^4$. Axial velocity and turbulence kinetic energy profiles were computed from a fourth-order curve fit of an incompressible flow problem previously simulated [31]. The shaft rotational speed was set to 8000 CPM and the radial distribution of inlet swirl velocity was taken from the measurements of Stoff [2]. This gives an inlet $Re_\theta = \frac{\rho \overline{W_i} 2c}{\mu} = 2.39 \times 10^4$ and 6.99×10^3 for the TOS and TOR cavities, respectively, at $M_i = 0.2$. The respective values at $M_i = 0.5$ are 9.55×10^3 and 2.19×10^3.

The variation of cavity bulk pressure drop ΔP^* with inlet Mach number M_i is shown in Fig. 4 for the teeth-on-stator (TOS) seal design. As expected, $M_i = 0.2$ possesses less grid size dependence than $M_i = 0.5$. The solution obtained using a

35x45 (x and r direction) grid is essentially grid independent near $M_i = 0.2$. The change in ΔP^* at $M_i = 0.2$ was approximately five percent in changing from the 20x30 to the 35x45 grid. This will be substantially less for a similar comparison using 35x45 and 50x60 grids. Observe the increased dependency on grid spacing at $M_i = 0.5$. This is attributed to the much higher pressure gradients, and in turn, density gradients at the higher Mach numbers.

Almost identical behavior was found for the teeth-on-rotor (TOR) design, which is not shown here. However, the value from the 65x75 grid at $M_i = 0.5$ for the TOR design is 0.474, whereas the corresponding value for the TOS design is 0.429. This indicates that the TOR design provides around 10.5 percent greater flow resistance. Stated differently, for a given ΔP^*, the TOR seal is expected to give less leakage. This agrees with a corresponding experimental comparison where both seals contained fifteen cavities of the present design.

Figure 5 shows the streamline pattern in a TOS generic labyrinth seal for $M_i = 0.5$. It is similar to that for incompressible flow in a similar generic seal in the paper by Rhode et al. [31]. The reattachment stagnation point in close proximity to the high speed leakage flow region gives rise to large velocity gradients just upstream of the downstream tooth.

Cavity-by-Cavity Flowfield Development

The following results were obtained by utilizing the finite difference code to simulate the flowfield development through a labyrinth seal, one cavity at a time. Figure 1 illustrates the cavity numbering scheme which is utilized in the following discussion. At the inlet to the first cavity a leakage Mach number of 0.3 was assumed. A uniform temperature profile of $300^o K$ was used as well as a uniform

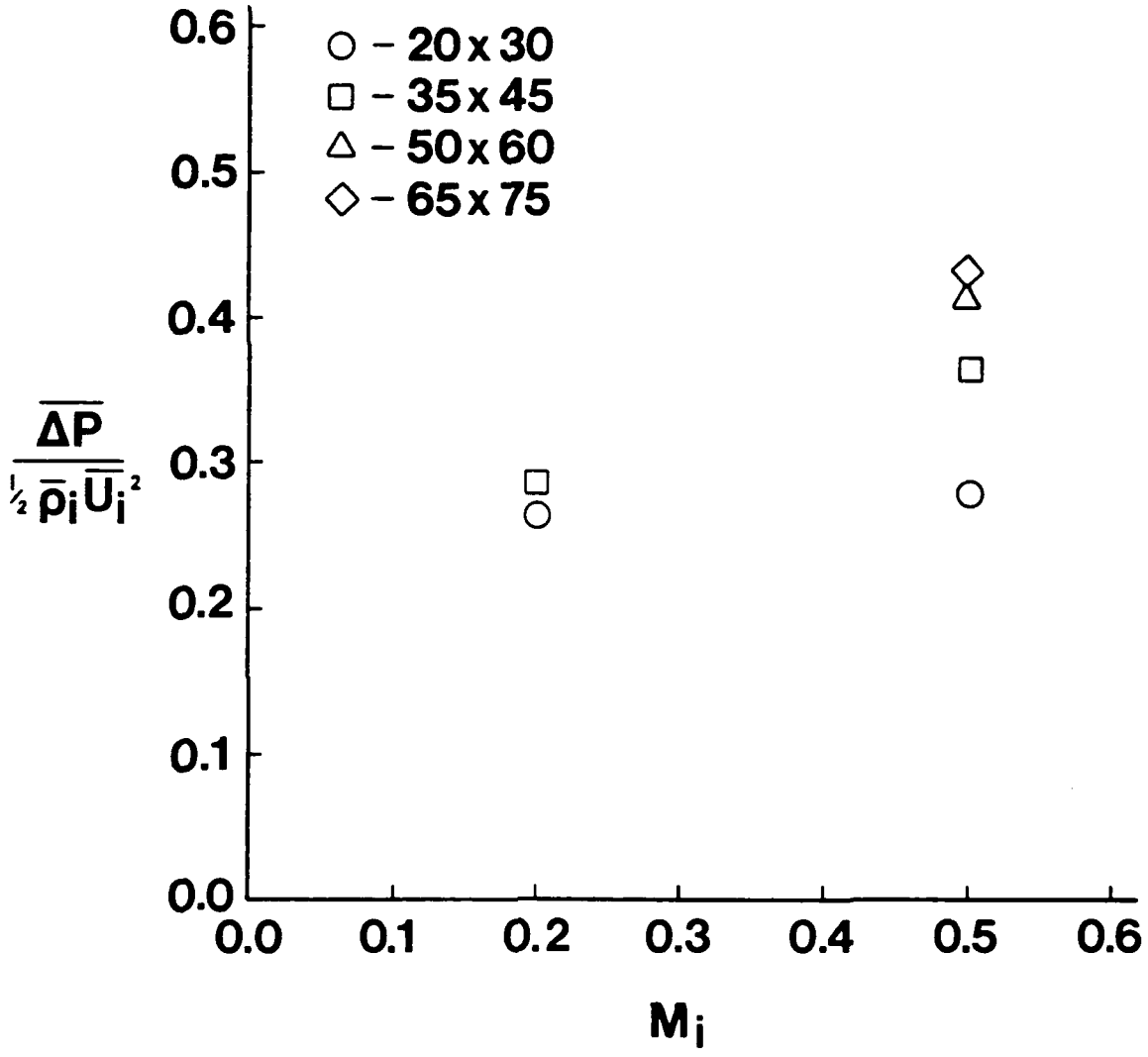

Fig. 4 Dimensionless pressure drop ΔP^* at $M_i = 0.2$ and 0.5 for different grids, TOS

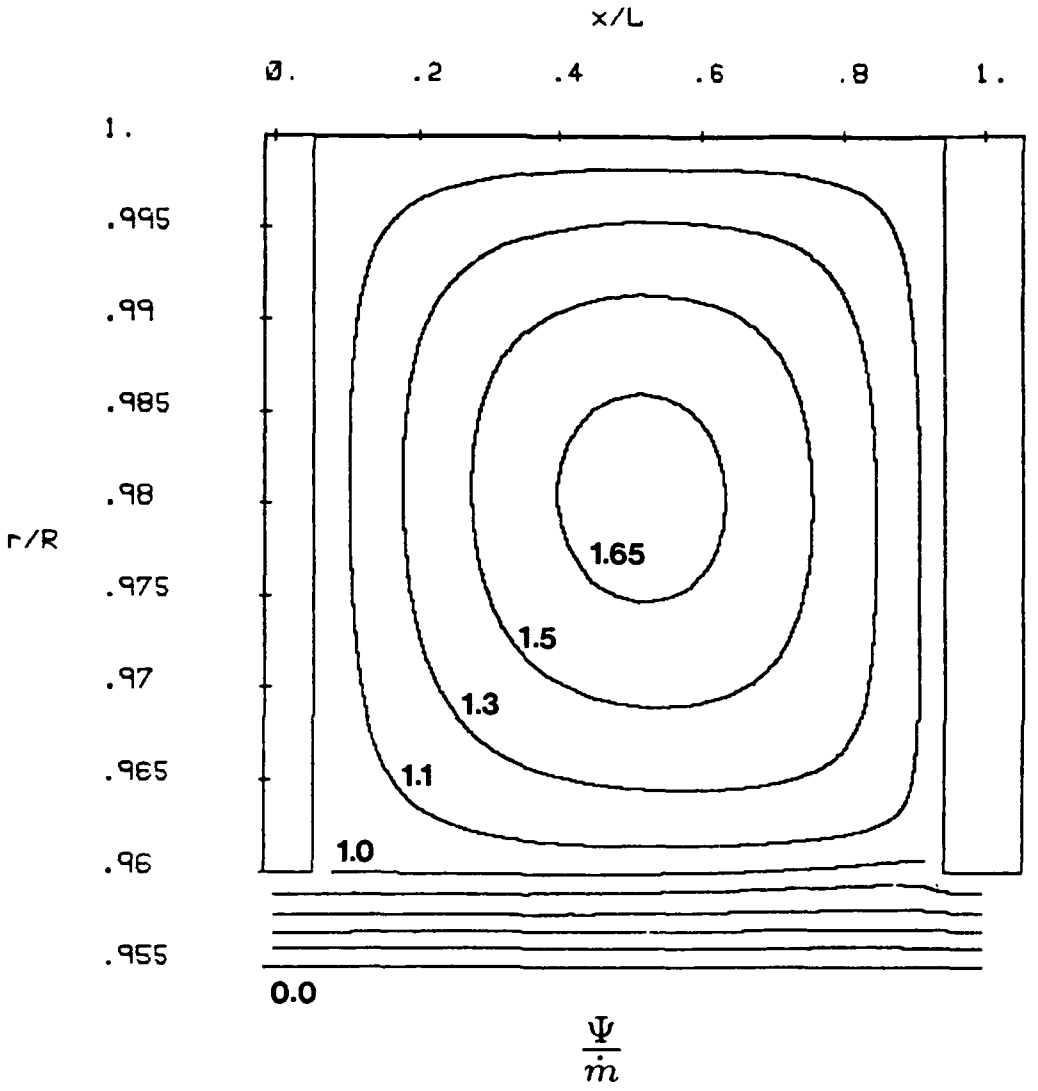

Fig. 5 Dimensionless streamline pattern at $M_i = 0.5$ for TOS

axial velocity profile. The inlet radial component of velocity was assumed to be zero. An inlet axial leakage Reynolds number of 32,000 was assumed. A uniform inlet profile of turbulence kinetic energy was used and a value of 3 percent of the mean flow kinetic energy was specified. The shaft speed was set to 9500 RPM.

Results were obtained using two different values of non-dimensional bulk swirl velocity W_i^* for comparison. The TOS cases were run at W_i^* of 0.0 and 0.58, while the TOR cases had W_i^* of 0.0 and 0.49. These non-zero inlet swirl cases give an Re_θ of 1.29×10^5 and 1.14×10^5, respectively. These values of W_i^* were selected as estimates of the inlet swirl resulting from rotating machinery upstream of the seal.

After obtaining a converged solution for the first cavity, the field variable values at the cavity exit plane are used as inlet values for the next cavity. Thus it was possible to simulate the flow development along the labyrinth seal by approximating inlet conditions for the first cavity and then proceeding downstream one cavity at a time.

For the TOS case of zero inlet swirl, Fig. 6 shows the increase of W_i^* with an almost constant slope. This result will be useful to the developers of simple flow models for calculating the net rotordynamic force which arises when the rotor is eccentric with respect to the housing. It is particularly noteworthy in this regard that the calculation of correct rotordynamic forces is sensitive to the correctly simulated distribution of W_i^*. Further there are no previous measurements or predictions of this distribution so that the developers of simple models have been unable to verify this aspect of their modeling. Thus it is significant that Fig. 6 shows a slow rate of growth of W_i^*. In fact, such generic TOS seals with as many as fifteen cavities never even approach the asymptotic value which is expected to be slightly less than 0.5. Figure 7 shows a linear decrease for the TOS case of

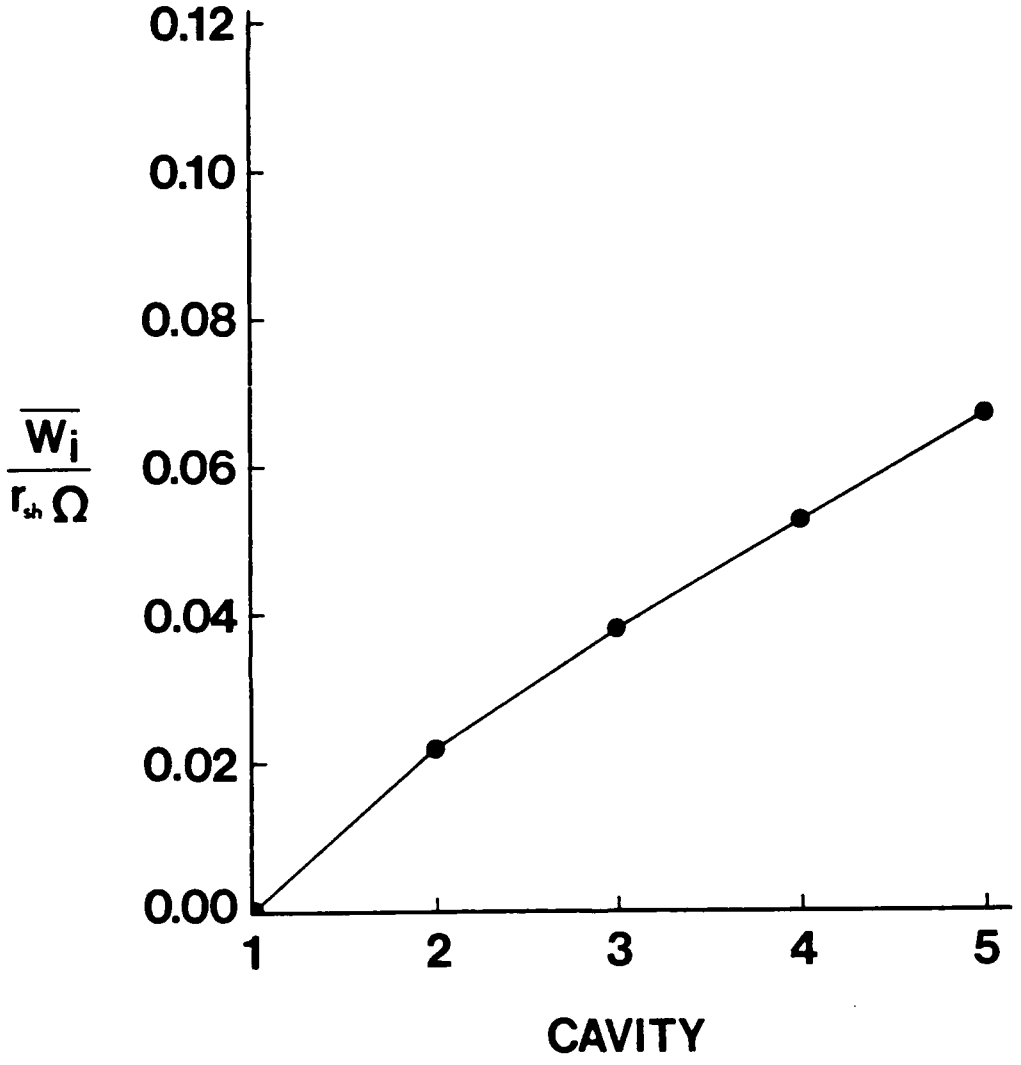

Fig. 6 Cavity-by-cavity development of dimensionless inlet swirl W_i^* for TOS with $W_i^* = 0.0$ at the first cavity

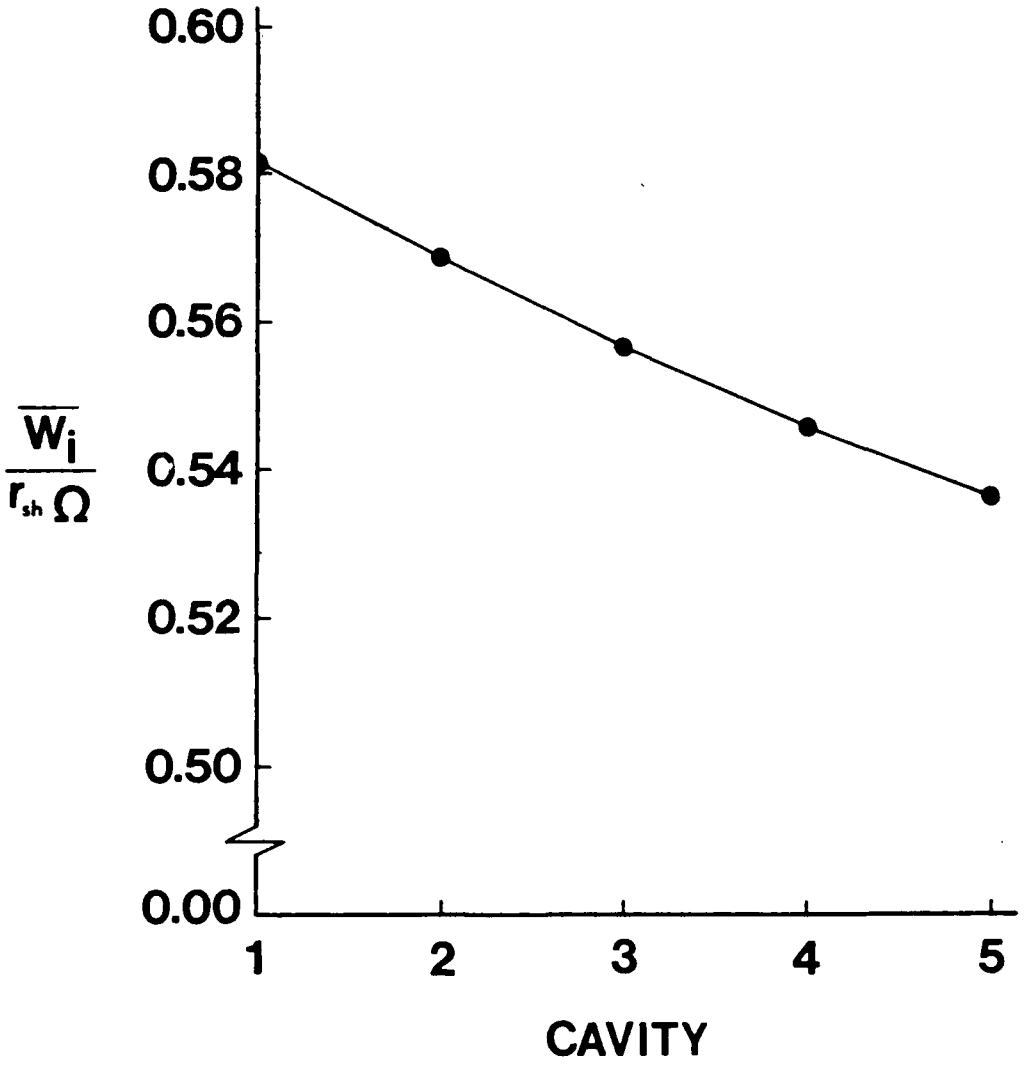

Fig. 7 Cavity-by-cavity development of dimensionless inlet swirl W_i^* for TOS with $W_i^* = 0.58$ at the first cavity

$W_i^* = 0.58$ and thus indicates an asymptotic value for W_i^* which is slightly less than 0.5.

The distributions shown in Figs. 8 through 10 reveal changes in the field variables as the flow proceeds cavity-by-cavity downstream. The axial velocity distributions of Fig. 8 indicate that this quantity has become essentially streamwise periodic within the third cavity. Even though Figs. 6 and 7 showed an almost linear development of W_i^*, the detailed distributions in Fig. 9 show a significantly non-linear rate of increase within the recirculation zone in the cavity region. The large turbulent shear stress $\tau_{r\theta}$ on the shaft gives rise to the shape of each radial profile near the shaft. Finally, Fig. 10 shows the effect of radial turbulent diffusion on turbulence energy development in the leakage region. This is most clearly shown for the developing profile in the first cavity. Although not shown here, the radial velocity profiles showed very little change.

The leakage Mach number increased from a value of 0.30 at the inlet of the first cavity to 0.33 at the exit of the fifth. By locating $M_i = 0.33$ on Fig. 4, one can determine that the 35x45 grid used for the swirl growth investigation was fine enough to avoid grid independence problems.

The TOR results for the W_i^* development shown in Figs. 11 and 12 are very similar to those for the corresponding TOS cases. One important difference however, is the much higher growth rate for the TOR case. The slow linear growth exhibited in Fig. 12 indicates that W_i^* is close to its asymptotic value which from these predictions is apparently near 0.55. This result is somewhat different from that for incompressible flow through a similar cavity by Rhode, et al. [31] indicating an asymptotic W_i^* value of 0.65.

Figures 13 through 15 correspond to Figs. 8 through 10 for the TOS cases and

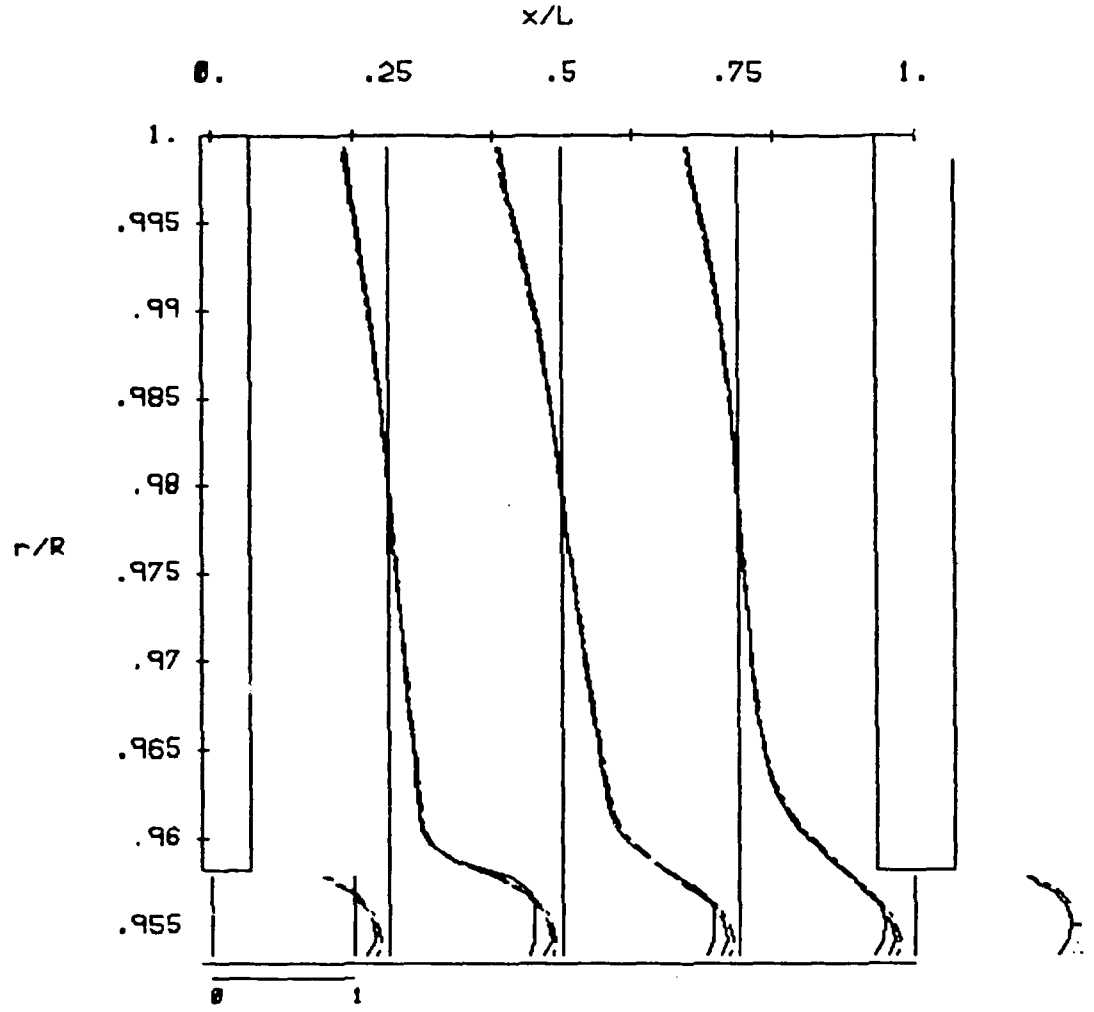

Fig. 8 Cavity-by-cavity dimensionless axial velocity distribution for TOS showing the first cavity(————), third cavity(—— ——) and fifth cavity(—— - ——)

AD-A197 185 THE MEASUREMENT AND PREDICTION OF ROTORDYNAMIC FORCES 1/3
FOR LABYRINTH SEALS (U) TEXAS A AND M UNIV COLLEGE
STATION TURBOMACHINERY LABS D W CHILDS ET AL MAR 88
UNCLASSIFIED AFOSR-TR-88-0662 F49620-82-K-0033 F/G 13/7 NL

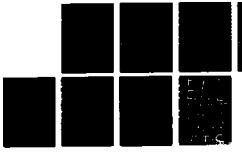

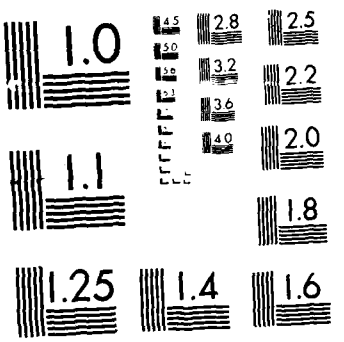

MICROCOPY RESOLUTION TEST CHART
NATIONAL BUREAU OF STANDARDS-1963-A

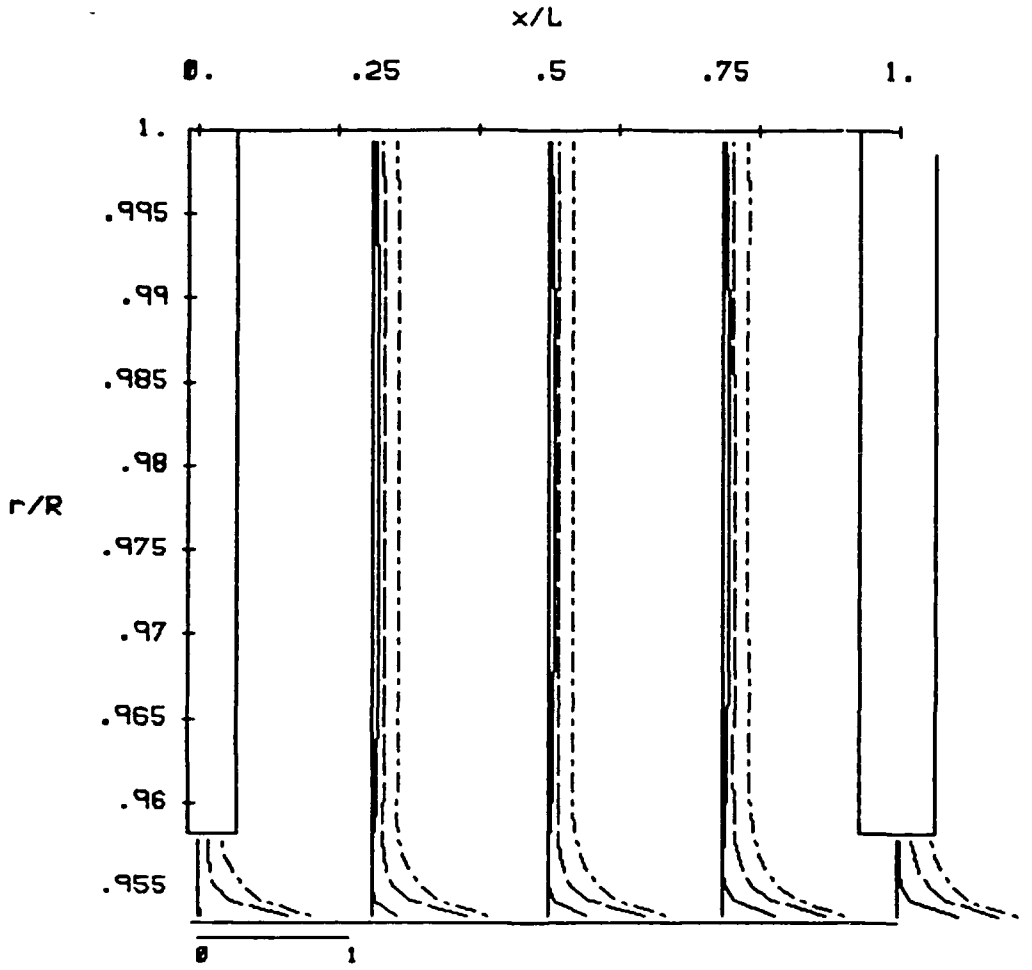

Fig. 9 Cavity-by-cavity dimensionless swirl velocity distribution for TOS showing the first cavity(————), third cavity(—— ——) and fifth cavity(—— - ——)

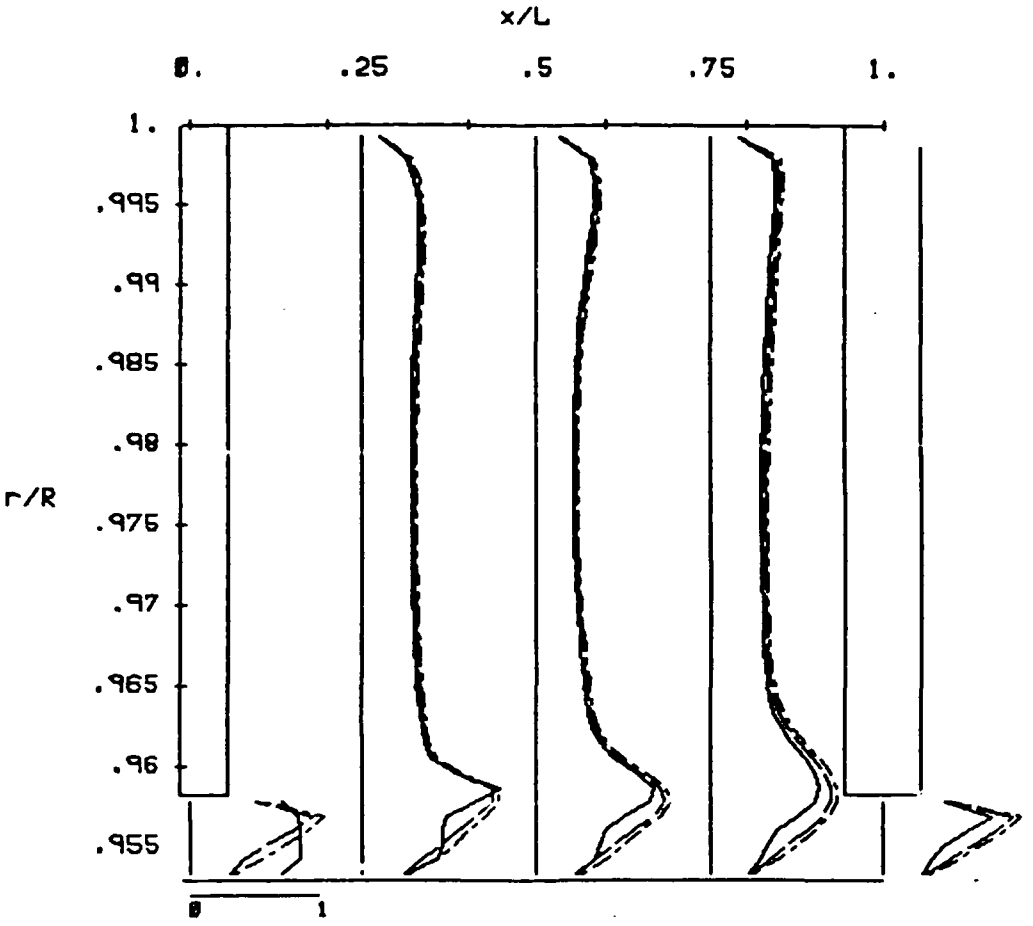

Fig. 10 Cavity-by-cavity dimensionless turbulence kinetic energy distribution for TOS showing the first cavity(————), third cavity(—— ——) and fifth cavity(—— - ——)

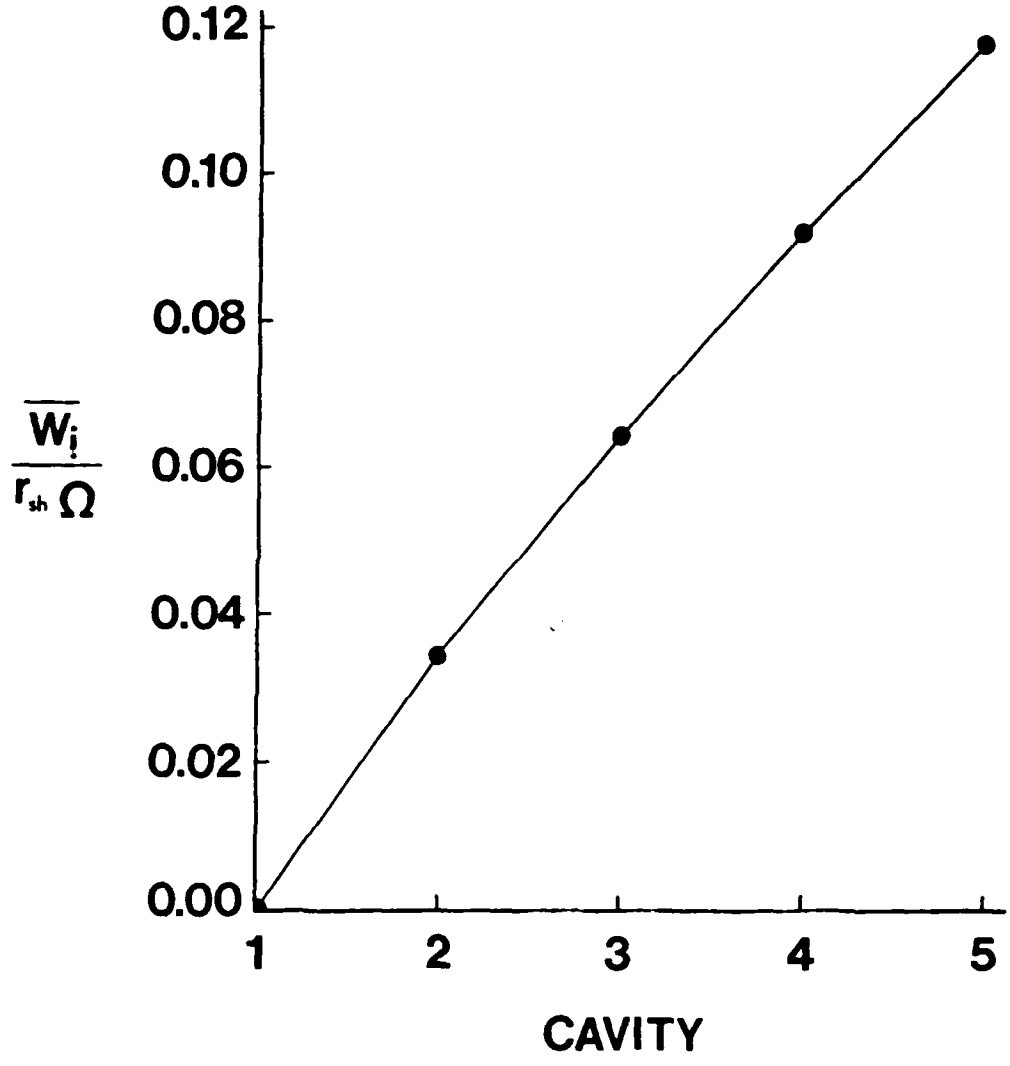

Fig. 11 Cavity-by-cavity development of dimensionless inlet swirl W_i^* for TOR with $W_i^* = 0.0$ at the first cavity

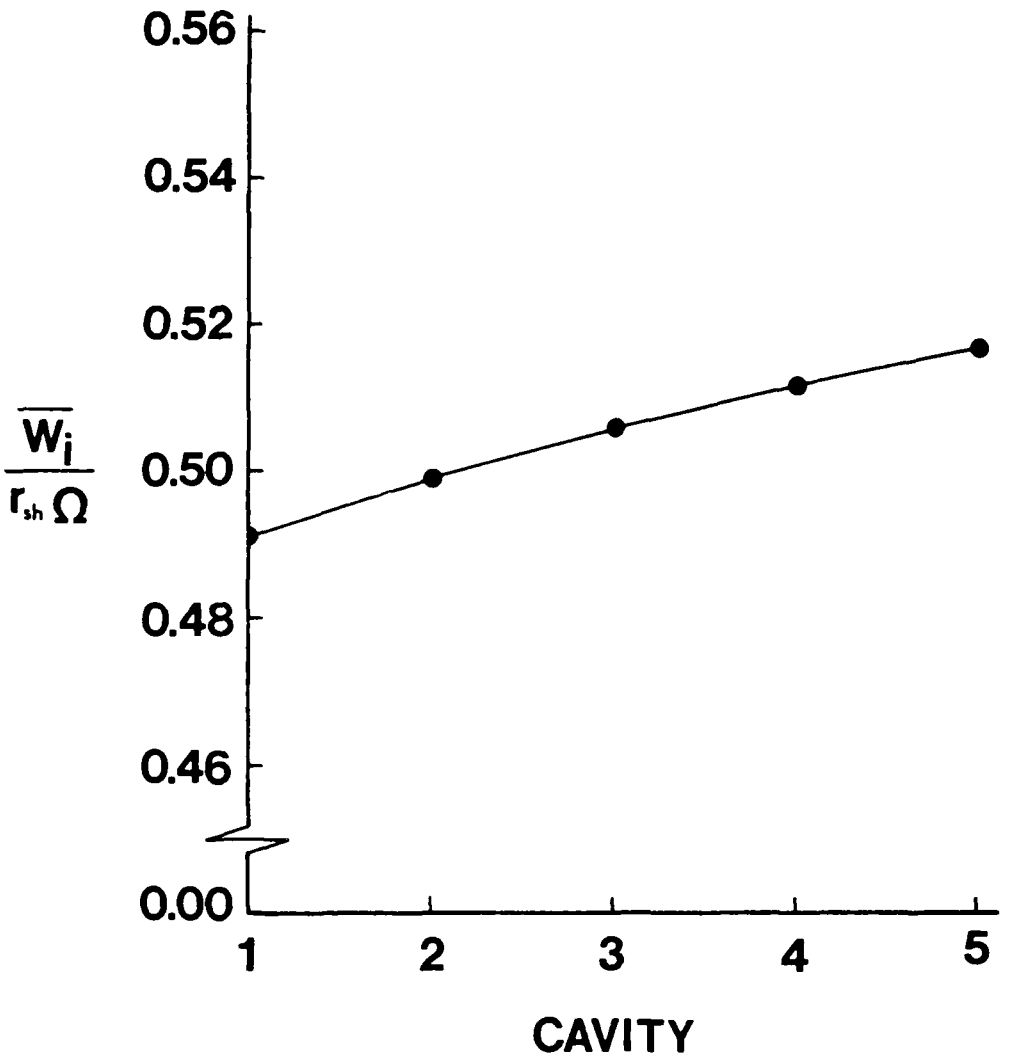

Fig. 12 Cavity-by-cavity development of dimensionless inlet swirl W_i^* for TOR with $W_i^* = 0.49$ at the first cavity

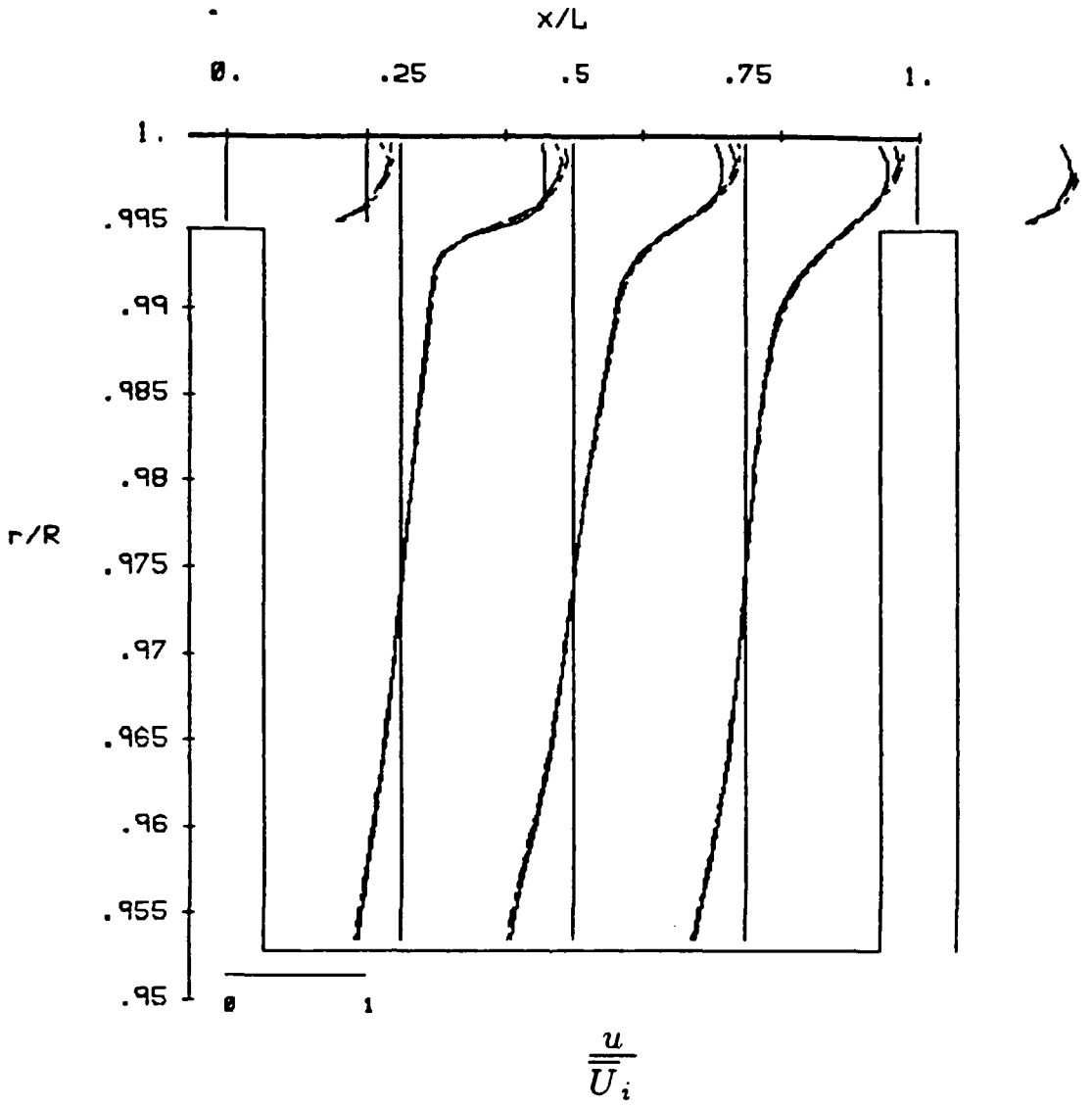

Fig. 13 Cavity-by-cavity dimensionless axial velocity distribution for TOR showing the first cavity(————), third cavity(—— ——) and fifth cavity(—— - ——)

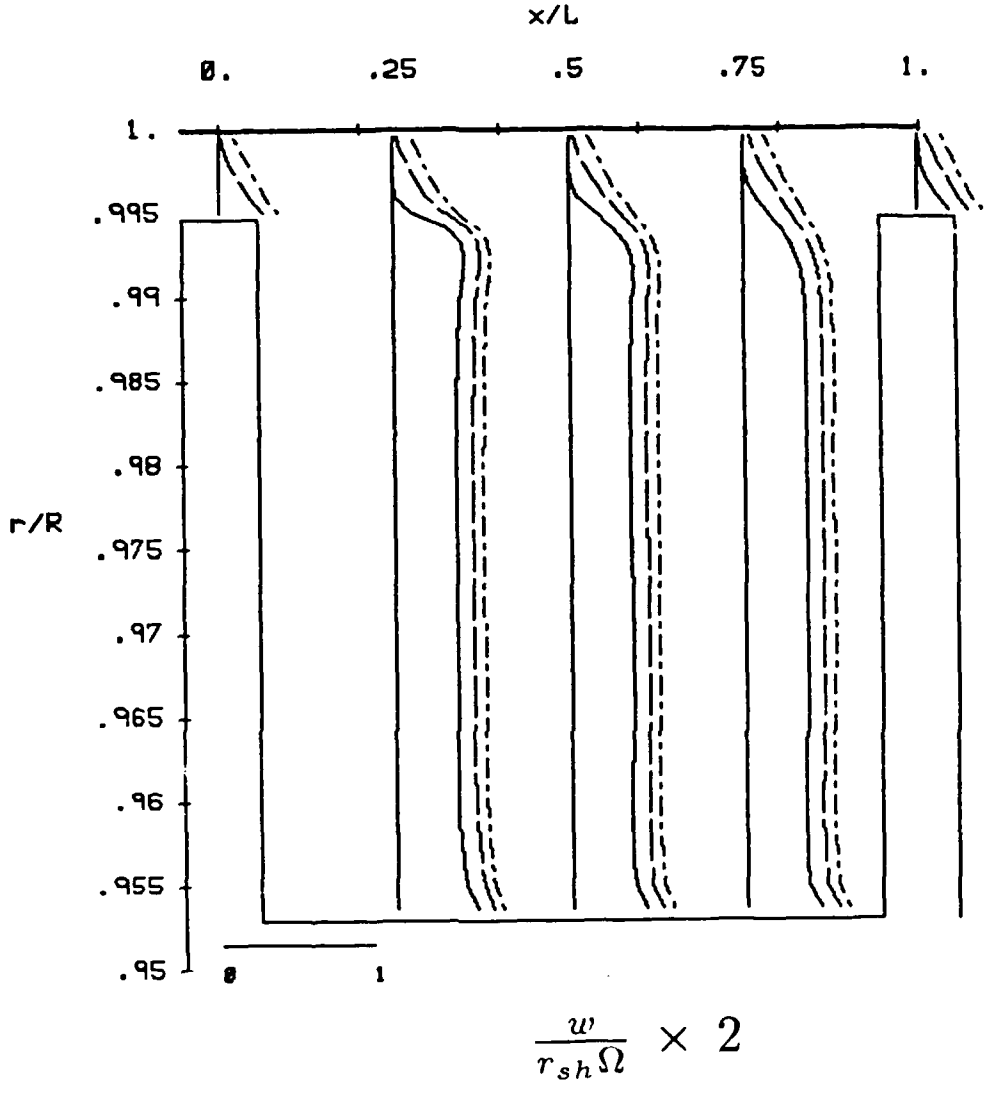

Fig. 14 Cavity-by-cavity dimensionless swirl velocity distribution for TOR showing the first cavity(————), third cavity(—— ——) and fifth cavity(—— - ——)

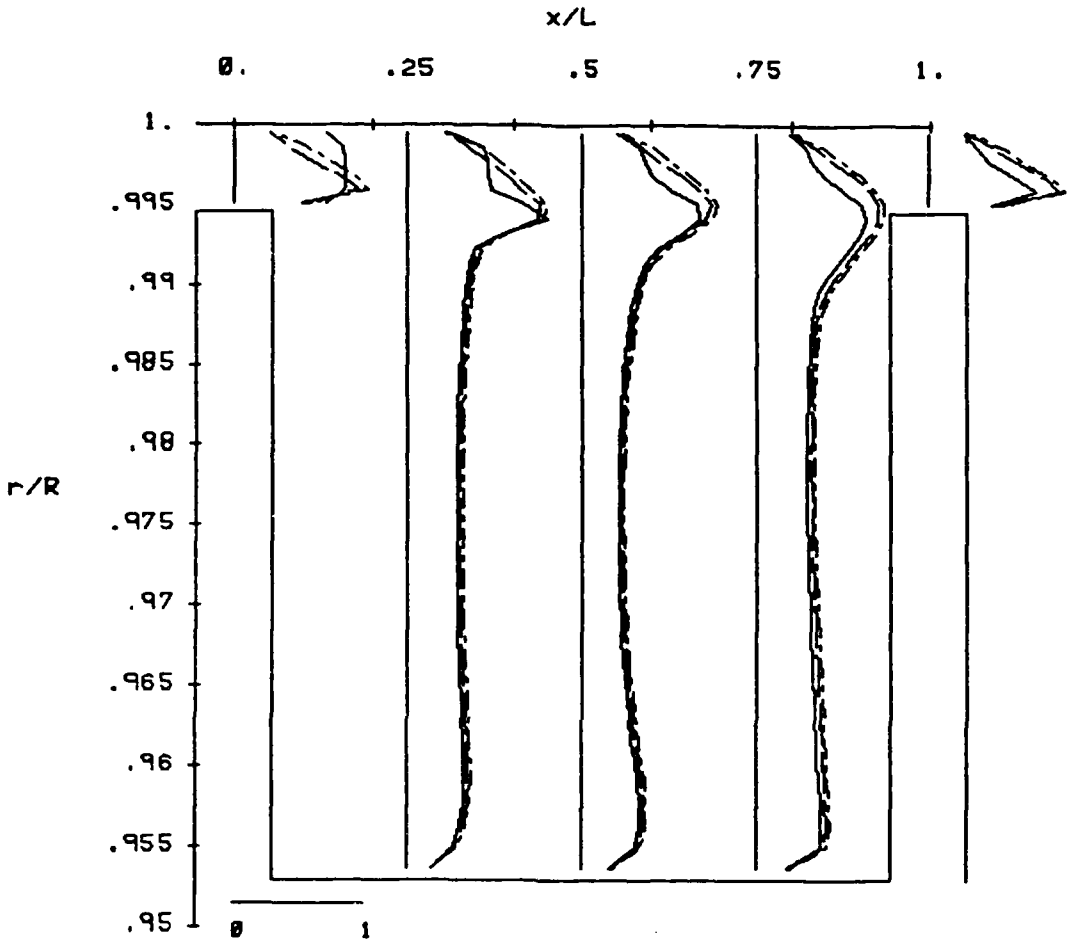

Fig. 15 Cavity-by-cavity dimensionless turbulence kinetic energy distribution for TOR showing the first cavity(————), third cavity(—— ——) and fifth cavity(—— - ——)

most of the results are nearly identical to those for TOS. Major items of interest again are approximate streamwise periodicity for axial velocity at the third cavity and swirl profile development. One difference between corresponding TOS and TOR cases is the swirl velocity profile in the leakage flow region. For the TOS case, Fig. 9 shows a larger $\frac{\partial w}{\partial r}$ than does Fig. 14 for TOR. This is due to the fact that the large shear stress $\tau_{r\theta}$ on the shaft acts on the leakage flow over the entire length from cavity inlet to outlet for the TOS case.

Figure 16 clearly contrasts the faster swirl growth rate of TOR over TOS. This leads to a higher asymptotic swirl velocity for TOR. Again, this is of significance to designers interested in analyzing rotordynamic forces on the shaft.

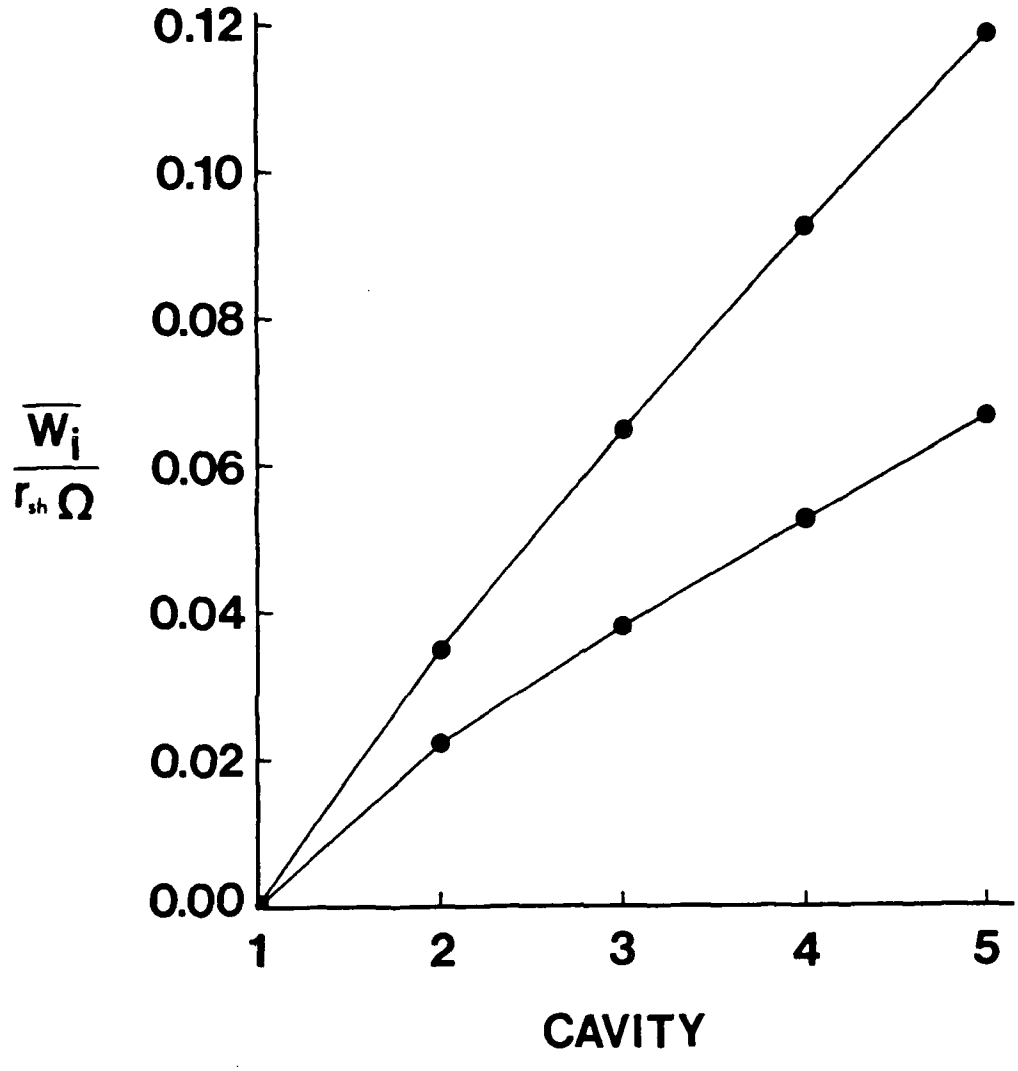

Fig. 16 TOS and TOR comparison of
cavity-by-cavity dimensionless inlet swirl development

CLOSURE

A finite difference computer program for predicting compressible, axisymmetric flow in labyrinth seals was used in investigating cavity-by-cavity growth of swirl velocity and leakage Mach number effect on grid independence. Due to a current lack of experimental data from compressible flow labyrinth seals, the results of this computational study cannot be verified.

The Fanno flow behavior computed herein for the compressible flow in labyrinth seals is well known. The steady increase in Mach number from one cavity to the next translates into a significant decrease in density and pressure. These in turn were found to give rise to a considerable grid dependence sensitivity at Mach numbers above approximately 0.4. Furthermore, predictions for corresponding TOR and TOS cavity designs with the same flow area and leakage rate showed that the TOR cavity had approximately ten percent greater dimensionless pressure drop than the TOS cavity. Thus, for a given pressure drop the TOR cavity is expected to leak less.

Several conclusions concerning the cavity-by-cavity flowfield development can also be drawn from the predictions presented. For example, it was clearly shown that the cavity-by-cavity swirl velocity development is fairly slow. It is anticipated that these values will prove helpful to the developers of simple models for predicting the rotordynamic fluid forces on such seals when the rotor is eccentric relative to the stator. Specifically, such previously unavailable values may serve as a swirl development prediction test case for such models, as the forces are sensitive to swirl velocity. Moreover, the TOS seals develop swirl velocity at a considerably slower rate than do TOR seals. This indicates that TOS seals are less likely to have significant destabilizing fluid forces which drive the rotor in the detrimental whirling

motion. Thus, the greater leakage tendency of TOS seals offsets this advantage of slower swirl velocity development.

In addition, the prediction of cavity-by-cavity flow development for Mach numbers near 0.3 indicates that, except for swirl velocity, most quantities are essentially streamwise periodic after the second cavity.

ACKNOWLEDGEMENT

The financial support of AFOSR is greatly appreciated.

REFERENCES

[1] Parsons, C. A., "The Labyrinth Packing," *Engineer*, vol. 165, No. 4280, pp. 23-84, Jan. 21, 1938

[2] Stoff, H., "Incompressible Flow in a Labyrinth Seal," *Journal of Fluid Mechanics*, vol. 100, pp. 817-829, 1980.

[3] Gosman, A. D. and Pun, W. M., "Calculations of Recirculating Flows," *Research Report*, Rept. No. HTS/74/2, Department of Mechanical Engineering, Imperial College, London, England, 1974.

[4] Rhode, D. L. and Sobolik, S. R., "Simulation of Subsonic Flow Through a Generic Labyrinth Seal," *ASME Journal of Engineering for Gas Turbines and Power*, vol. 108, pp. 674-680, 1986.

[5] Sobolik, S. R., "Prediction of Compressible Flow Within Concentric-Rotor Labyrinth Seals," M. S. Thesis, Texas A&M University, 1984.

[6] Sneck, H. J., "Labyrinth Seal Literature Survey," ASME Paper No. 73-Lub-12, 1973.

[7] Cogan, Kevin C., "Leakage Prediction of Incompressible Fluids in Labyrinth Seals," M. S. Thesis, Texas A&M University, College Station, Texas, December 1982.

[8] Martin, H., "Labyrinth Packings," *Engineering*, vol. 85, pp. 35-38, Jan. 10, 1908.

[9] Stodola, A., *Steam and Gas Turbines*. New York: McGraw-Hill, 1927.

[10] Gercke, M., "Flow Through Labyrinth Packing," *Mechanical Engineer*, vol. 56, pp. 678-680, 1934.

[11] Egli, Adolf, "The Leakage of Steam Through Labyrinth Seals," *Transactions ASME*, vol. 57, pp. 115-122, 1935.

[12] Dollin F., and Brown, W. S., "Flow of Fluids Through Openings in Series," *Engineering*, pp. 223-224, Aug. 27, 1937.

[13] Hodkinson, B., "Estimation of the Leakage Through a Labyrinth Gland," *Proc. of Inst. Mech. Eng.*, vol. 141, pp. 283-286, 1939.

[14] Kearton, W. and Keh, T., "Leakage of Air Through Labyrinth Glands of Staggered Type," *Proceedings of the Institute of Mechanical Engineers*, vol. 166, pp. 180-194, 1952.

[15] Zabriskie, W. and Sternicht, B., "Labyrinth Seal Leakage Analysis," *ASME Journal of Basic Engineering*, vol. 81, pp. 332-340, Sept. 1959.

[16] Vermes, G., "A Fluid Mechanics Approach to the Labyrinth Seal Leakage Problem," *ASME Journal of Engineering for Power* ,pp. 161-169, Apr. 1961.

[17] Rao, K. V. and Narayanamurthi, R. G., "An Experimental Study of the Performance Characteristics of Labyrinth Seals," *India Engineering Journal-ME*, vol. 52, pp. 277-281, July 1973.

[18] Deich, M. Y., Shkvar, A. Ya, and Solomko, V. I., "Investigation of Straight-Through Labyrinth Seals," *Izvestiya Akademii Nauk SSSR. Energetika i Transport*, vol. 16, pp. 146-152, 1978.

[19] Benvenuti, E., "Analytical and Experimental Development of Labyrinth Seals for Process Centrifugal Compressors," presented at the 25th Annual International Gas Turbine Conference and Exhibition, New Orleans, LA, March 9-13, 1980.

[20] Hauck, L., "Measurement and Evaluation of Swirl-Type Flow in Labyrinth Seals of Conventional Turbine Stages," presented at the Workshop on Rotordynamic Instability Problems in High-Performance Turbomachinery, Texas A&M University, May 10-12, 1982.

[21] Patankar, S. V., *Numerical Heat Transfer and Fluid Flow.* United States: Hemisphere Publishing Company, McGraw-Hill, 1980.

[22] Spalding, D. B., "A Novel Finite-Difference Formulation for Differential Expressions Involving both First and Second Derivatives," *Int. J. Num. Methods Eng.*, vol. 4, pp. 551, 1972.

[23] Leonard, B. P., "A Stable and Accurate Convective-Modelling Procedure Based on Quadratic Upstream Interpolation," *Comp. Meths. Appl. Mech. Eng.*, vol. 19, pp. 59-98, 1979.

[24] Zimmermann, H. and Wolff, K. H., "Comparison Between Empirical and Numerical Labyrinth Flow Correlations," presented at the Gas Turbine Conference and Exhibition, Anaheim, California, May 31-June 4, 1987.

[25] Kirk, R. G., "A Method for Calculating Labyrinth Seal Inlet Swirl Velocity," presented at the ASME 11th Biennial Conference on Mechanical Vibrations and Noise, Boston, Massachusetts, September 27-30, 1987.

[26] Nordmann, R., Dietzen, F. J. and Weiser, H. P., "Calculation of Rotordynamic Coefficients and Leakage for Annular Gas Seals by Means of Finite Difference Techniques," presented at the ASME 11th Biennial Conference on Mechanical Vibrations and Noise, Boston, Massachusetts, September 27-30, 1987.

[27] Jerie, J., "Flow Through Straight-Through Labyrinth Seals," *Proceedings of the Seventh Int. Cong. of Appl. Mech.*, vol.2, pp. 70-82, 1948.

[28] Bell, K. J., and Bergelin, O. P., "Flow Through Annular Orifices," *Transactions of the ASME*, vol. 79, pp. 593-601, April 1957.

[29] Nikitin, G. A. and Ipatov, A. M., "Design of Labyrinth Seals in Hydraulic Equipment," *Russian Engineering Journal*, vol. 53, pp. 26-30, 1973.

[30] Han, J. T., "A Fluid Mechanics Model to Estimate the Leakage of Incompressible Fluids Through Labyrinth Seals," ASME Paper no. 79-FE-4 , 1979

[31] Rhode, D. L., Demko, J. A., Traegner, U. K., Morrison, G. L. and Sobolik, S. R., "Prediction of Inompressible Flow in Labyrinth Seals," *ASME Journal of Fluids Engineering*, vol. 108, No. 19, pp. 19-25, March 1986.

[32] Demko, J. A., "The Prediction and Measurement of Incompressible Flow in a Labyrinth Seal," Ph. D. Dissertation, Texas A&M University, 1986.

[33] Demko, J. A., Morrison, G. L., and Rhode, D. L., "Effect of Shaft Rotation on the Incompressible Flow in a Labyrinth Seal," Proceedings of the 5th International Conference on Numerical Methods in Laminar and Turbulent Flows, Montreal, Canada, 7/6/87-7/10/87 (also accepted for publication in the *AIAA Journal of Propulsion and Power*) 1986.

[34] Demko, J. A., Morrison, G. L. and Rhode, D. L., "The Prediction and Measurement of Incompressible Flow in a Labyrinth Seal," AIAA paper 88-0190 presented at the 26th Aerospace Sciences Conference, Reno, Nevada, January 1988 (also accepted for publication by the *ASME Journal of Engineering for Gas Turbines and Power*).

[35] Launder, B. E., and Spalding, D. B., "The Numerical Computation of Turbulent Flows," *Comp. Meth. in Appl. Mech. and Engr.*, vol. 3, pp. 269-289, 1974.

[36] Leschziner, M. A. and Rodi, W., "Calculation of Annular and Twin Parallel Jets Using Various Discretization Schemes and Turbulence-Model Variations," *ASME Journal of Fluids Engineering*, vol. 103, pp. 352-360, 1981.

[37] Han, T., Humphrey, J. A. C., and Launder, B. E., "A Comparison of Hybrid and Quadratic-Upstream Differencing in High Reynolds Number Elliptic Flows," *Comp. Meths. Appl. Mech. Eng.*, vol. 29, pp. 81-95, 1981.